$H_2^{18}O$ and $H_2^{16}O$ Observations of Intermediate Mass Star Formation Regions

by

Mollie E. Conrad

A thesis
presented to the University of Waterloo
in fulfillment of the
thesis requirement for the degree of
Master of Science
in
Physics

Waterloo, Ontario, Canada, 2018

© Mollie Conrad 2018

I hereby declare that I am the sole author of this thesis. This is a true copy of the thesis, including any required final revisions, as accepted by my examiners.

I understand that my thesis may be made electronically available to the public.

Abstract

While the process of low mass (LM) star formation is a well studied area of astrophysics, the formation of high mass (HM) stars is much more complicated. The study of intermediate mass (IM) star formation is expected to shed some light on the clustered high mass regime. In this thesis, observations of 6 intermediate mass star formation regions were obtained with the Heterodyne Instrument for the Far Infrared (HIFI) aboard the Herschel Space Observatory (HSO) as part of the Water In Star-Forming regions with Herschel (WISH) project. Observations of all regions were decomposed into Gaussian components. NGC 7129 FIRS 2 is the main focus for this thesis as water observations for this source also include $H_2^{18}O$. This isotopologue in conjunction with $H_2^{16}O$ allow for tighter constraints to be placed on the star formation regions.

Modelling of the emission components corresponding to the IM YSO envelope was conducted with a radiative transfer program called RATRAN. This program allows for constraints to be placed on the chemical and physical parameters of the star formation region and the determination of the abundance of $H_2^{18}O$ and $H_2^{16}O$ present. The best-fit RATRAN models assume a freeze-out temperature of 100 K and a free-fall infall velocity towards a central mass of $1.1 M_\odot$. Three different power-law density profiles are considered with indices of $\alpha = 1.4$, $\alpha = 1.5$, and a hybrid of the two.

The narrow -7.8 km s^{-1} component of the 547 GHz (1_{10}-1_{01}) $H_2^{18}O$ ortho line was determined to have an outer envelope abundance of $3.5 \pm 0.3 \times 10^{-11}$ with respect to H_2 and an outer turbulent velocity of 2.25 km s^{-1} for the $\alpha = 1.4$ density profile. The inner envelope $H_2^{18}O$ abundance and turbulent velocity could not be constrained due to a larger optical depth (greater than 1.0) in this region. The higher energy state $H_2^{18}O$ lines (995 GHz/2_{02}-1_{11} and 1096 GHz/3_{12}-3_{03}) were not detected; this was confirmed by RATRAN modelling. The $H_2^{16}O$ ortho outer abundance was determined to be $X_{out} = 1.5 \pm 0.5 \times 10^{-8}$ for the hybrid density profile, and the para outer abundance was determined to be $X_{out} = 4.5 \pm 0.3 \times 10^{-9}$. This yields a total $H_2^{16}O$ abundance of $1.95 \pm 1.0 \times 10^{-8}$. The water abundance value is consistent with that of the low-mass and high-mass WISH teams ($\sim 10^{-8}$), and the turbulent velocity is consistent with that of the high-mass WISH team (2.0–2.5 km s^{-1}). The water abundances derived for the other density profiles are also consistent with this conclusion. This analysis determined an abundance ratio consistent with that of Herpin et al. (2016) (a HM study). The least useful molecular lines proved to be the ortho and para $H_2^{16}O$ ground state lines; these are not suggested as ideal probes of star formation regions. That being said, the most useful lines proved to be the $H_2^{18}O$ ground state ortho 547 GHz line and the $H_2^{16}O$ para 988 GHz line.

This study of water in intermediate mass star formation regions is to be considered alongside studies in the low and high mass regimes; this will allow for increased understanding of the overall star formation process.

Acknowledgements

I would like to extend my sincerest gratitude to my supervisor Dr. Michel Fich. This degree would not have been possible without his patience, mentoring, and wisdom.

I would like to thank my graduate instructors; Dr. Mike Hudson, Dr. Niayesh Afshordi, and again Dr. Michel Fich, for their teaching excellence and patience with my after-lecture questions.

Thank you Dr. Mike Hudson for offering me the best piece of advice, "Always remember the bigger picture".

I want to thank my committee members; Dr. Michael Balogh and Dr. James Taylor for their continued support and motivation. Also, thank you to Dr. Avery Broderick for providing invaluable feedback during my defence.

I would also like to thank all my peers and friends for their advice and support; George Bobotsis, Adrian Vantyghem, Nicole Drakos, Rufus Ni, Issac Spitzer, Paul Charlton and Saoussen Mbarek.

Finally, I would like to thank my mother Penny Conrad for often volunteering to drive 3 hours just to clean my laundry and watch me obsess over RATRAN models. "You the real MVP".

Dedication

I can't even begin to decide who to dedicate well over two years of my life to. There are so many people responsible for getting me where I am today. I think I will leave it at this: I dedicate this thesis to my parents for raising me to value hard work, to Mike Fich for presenting me with the opportunity to strive for more, and to my partner Chris Praill for always being in my corner.

In loving memory of my late Nanny and Poppy Dyer.

Table of Contents

List of Tables

xi

List of Figures

xiv

List of Symbols

$\mathbf{A}_{jk}$ Einstein Spontaneous Emission Coefficient; 48

A Convolution Constant; 55

$\mathbf{B}_{jk}$ Einstein Simulated Emission Coefficient; 48

B_ν Planck Function; 23

$\mathbf{C}_{jk}$ Collision rate causing an energy state transition from i to j; 48

C_s Sound Speed; 4

ΔV Linewidth; 21

$\Delta \nu$ Frequency Resolution of the Receiver; 37

$\mathbf{E}_n$ Energy of state n; 48

F Flux; 55

$\mathbf{G}$ Gravitational Constant; 5

$\mathbf{H}_2^{16}\mathbf{O}$ Water Molecule; 2

$\mathbf{H}_2^{18}\mathbf{O}$ Heavy Water Isotopologue; 2

I_ν Specific intensity; 22

I Moment of Inertia; 6

J_{KC} Rotational Energy Level; 21

J_ν Average Intensity; 23

K Kinetic Energy; 6

L_{bol} Bolometric Luminosity; 33

$L_\odot$ Solar Luminosity: 3.9×10^{33} erg s^{-1}; 12

L Path Length; 4

$\mathbf{M}_{H218O}$ Water Isotopologue Mass: 20.01504 amu; 239

$\mathbf{M}_{H2O}$ Water Molecule Mass: 18.01528 amu; 239

M_J Jeans Mass; 8

$M_\odot$ Solar Mass: 1.99×10^{33} g; 2

M Mass; 5

$\mathbf{N}_\ell$ Column density of particles; 21

Φ_g Gravitational Potential; 7

Φ Magnetic Flux; 5

R_e Reynolds Number; 4

S_ν Source Function; 22

$\mathbf{T}_A^*$ Smoothed Antenna Temperature; 39

$\mathbf{T}_B$ Brightness Temperature; 53

$\mathbf{T}_{MB}$ Main Beam Temperature; 77

$\mathbf{T}_{RMS}$ RMS Noise; 37

$\mathbf{T}_R$ Radiation Temperature; 53

$\mathbf{T}_{abs}$ Absorption Spectral Intensity in terms of Temperature; 73

$\mathbf{T}_{bg}$ Background Temperature; usually taken as the temperature of the CMB; 53, 239

$\mathbf{T}_d$ Dust Temperature; 62

$\mathbf{T}_{ex}$ Excitation Temperature; 52

h Planck Constant; 6.626×10^{-27} ergs $\cdot$ s;

$\int T_A dv$ Velocity Integrated Intensity;

j_ν Emission Coefficient;

κ_ν Dust Emissivity;

κ Opacity;

k_B Boltzmann Constant: 1.38065×10^{-16} ergs/K;

λ Wavelength;

m_H Hydrogen Mass: 1.67×10^{-24} g;

B Magnetic Field;

$\mathcal{M}$ Magnetic Field Energy;

$\mathcal{T}$ Bulk Motion Kinetic Energy;

$\mathcal{U}$ Random Thermal Kinetic Energy;

$\mathcal{W}$ Gravitational Potential Energy;

μ Mass to Flux Ratio;

$\mathbf{n}_i$ Number density of particles; population;

ν_m Molecular Viscosity;

ν Frequency;

ϕ Doppler Turbulent Broadening;

$\mathbf{p}$ p-value;

ρ_{dust} Dust Density;

ρ Density;

r_i Inner Radius;

r_o Outer Radius;

\- T.S Eliot, *A Little Gidding*

We shall not cease from exploration
And the end of all our exploring
Will be to arrive where we started
And know the place for the first time.

Chapter 1

Introduction

Stars are beautifully luminous, large gravitationally bound spheres of gas existing at temperatures high enough to sustain fusion reactions. They are one of the fundamental objects of astrophysics as they are ubiquitous in the universe and constitute one of the most basic building blocks of galaxies, to which they provide most of the luminous energy. Their luminosity is responsible for illuminating the Milky Way as well as other galaxies. We are able to study other galaxies because stars light up the overall structure and highlight less luminous features (i.e large molecular clouds). Stars allow us to generate a more complete picture of how gravity acts on large scales and some may also have ideal conditions to host habitable and life-sustaining planets.

Giant molecular clouds (GMC) act as stellar nurseries. Forces within the cloud engage in a balancing act, internal pressures supporting the cloud and gravitational forces causing collapse. Once this balance becomes unstable, the GMC collapses isothermally, radiating energy until the density is so large that the cloud becomes optically thick. Collapse is then slowed, the region halts the release of heat via radiation, and thus becomes more adiabatic and therefore increases in temperature. That is, less heat and matter are exchanged with the environment. At this point the condensed material, known as the core, is still able to radiate energy; this allows the interior to cool and collapse further. Meanwhile, the exterior matter continues infall and accretion onto the core, acting as a "lid" containing the core's radiation. The phase of star-formation where this accretion dominates the observed luminosity is known as a protostar, or a pre-main-sequence star. Once the core density is high enough to ignite nuclear fusion within the core (now known as a main-sequence (MS) star) and has generated enough radiation, the pressure is strong enough to break-out and overcome accretion. For higher mass stars, this outflow of radiation blows away and disperses the remaining dusty gaseous envelope, revealing the final stellar object.

The study of star-formation is important to the astronomical community for many reasons. Two of the main observable differences between low and high-mass stars are the presence of outflows and circumstellar disks in LM YSOs. It is possible that planets may form from the disks; modelling the environment and determining the physical and chemical conditions required for planet formation could give researchers an idea of what to look for when searching for exoplanets. Another reason why the study of star-formation is so important is the determination of a dependence on the metallicity and radiation field could allow us further insight into our galactic history.

Our knowledge of the low-mass $(< 2M_\odot)$ star formation process is much more developed than that of their high-mass counterparts ($> 10 M_\odot$). Low-mass stars are seen to form in groups or in isolation all over the universe, including nearby Earth. Additionally, the time scales for low-mass stellar evolution are much longer. Because of this, higher resolution observations are obtainable. Researchers are able to study low-mass star formation more thoroughly as low-mass stars at various stages of evolution are available. High-mass stars, while much more luminous, are seen to form in clusters at much further distance from the Earth, thus the spatial resolution is poorer. Currently, two ideas of high-mass star-formation have been made popular: the first being the method of faster clumpy accretion, the second being the merger of multiple high-mass cores. Observations of high-mass stars up to masses of >50 $M_\odot$ have been discovered; that being said, the method of single core accretion has an upper limit of $\sim$ 11 $M_\odot$ due to fragmentation and radiation pressure from the protostar. It is clear that further investigation is required to complete the picture of high-mass star-formation. One approach to this is looking into the intermediate-mass regime $(2\text{--}10M_\odot)$.

This thesis is an investigation into the physical and chemical properties of NGC 7129 FIRS 2. This object is one of six candidates included in the Water In Star-forming regions with Herschel (WISH) Intermediate Mass program. Molecular line emission of the $H_2^{18}O$ and $H_2^{16}O$ water molecules were measured using the Herschel Space Observatory (HSO). Radiative transfer models were used to simulate the emission lines observed. The goal is to use the models and observational data to constrain physical parameters such as the velocity field of the molecular cloud and chemical properties including the molecular abundances throughout the region. An attempt will be made to constrain additional chemical properties such as the $H_2^{16}O$ to $H_2^{18}O$ abundance ratio and the ratio of ortho to para water, the two spectroscopic forms of the molecule. Ortho and para water will be defined in §1.4.

1.1 Star Formation

As mentioned, the study of star-formation can be broken up into three mass regimes; while low-mass (LM) stars are fairly abundant in the local universe, intermediate-mass (IM) and high-mass (HM) stars are more scarce locally. We are able to study non-local HM stars mostly due to their high luminosity, with the trade-off being poorer resolution. Because of the scarcity of IM stars, the study of this mass regime is still in its infancy. IM stars are much less common than LM stars but also much less luminous than HM stars. This combination makes them rare and very few are known.

Star formation processes begin in dusty and gaseous giant molecular clouds (GMC), which are gravitationally bound objects with a complex substructure. Internal forces such as radiation pressure (turbulence, magnetic support) balance the inward pull of gravitational forces. The Virial Theorem, presented below, determines when this balance is upset and when subsequent near-isothermal cloud collapse occurs.

A general star-formation overview will be given and the differences in stellar mass regimes will be discussed.

1.1.1 Giant Molecular Cloud Substructure

Most star-formation actively takes place within giant molecular clouds (GMC) (Zuckerman & Palmer, 1974; Burton, 1976), which usually contain a molecular mass between 10^5 and 3×10^6 M$_\odot$, and a size on the order of 10 parsecs (Solomon, Sanders, & Scoville, 1979). Spectral observations, primarily of the CO molecule, have shown that GMCs have substructure clumping with clump masses ranging from $\sim 10^3$ to 10^4 M$_\odot$, sizes from 2 to 5 parsecs, densities of n$_H \sim 10^{2.5}$ cm^{-3}, and temperatures around 10 K (Sargent, 1977; Evans, 1978; Blitz, 1978; Rowan-Robinson, 1979) (see Figure 1.1 for an example of GMC substructure clumping). Cores are deeply embedded within these clumps; as such, protostar identification is conducted via infrared (IR) spectral energy distributions (Adams & Shu, 1986; Adams, Lada, & Shu, 1987; Myers et al. 1987) as optical light absorbed by the surrounding dust is re-radiated in the sub-mm and IR.
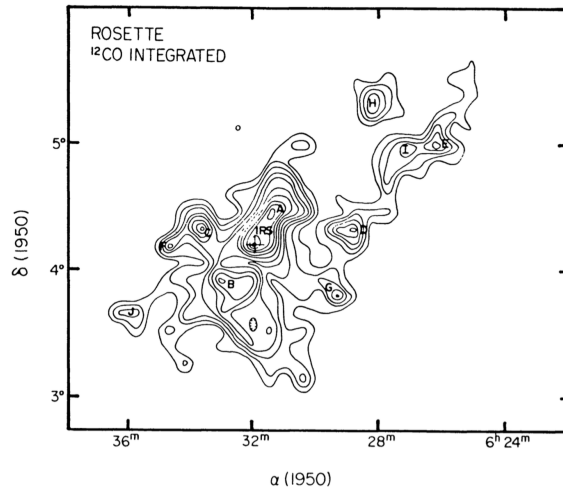
Figure 1.1: Molecular cloud clumping substructure observed in ^{12}CO within the Rosette Nebula. A hot core as been identified at the position of the cross. (From Blitz & Thaddeus, 1980).

Initial collapse in these clumps occurs when the supporting forces, turbulence and magnetic support, give way to the gravitational forces. The Virial Theorem can be used to ascertain when the cloud will become gravitationally unstable. Molecular cooling (energy removed from the system via de-excitation radiation) then allows for further collapse.

1.1.2 Turbulence

Giant molecular clouds have intrinsic instabilities, interpreted as turbulence (Bonnell et al. 2006). The dimensionless Reynolds number, referred to as R_e, plays a prominent role in foreseeing turbulence patterns in a fluid. Specifically, R_e is the ratio of the inertial to the viscous forces. Turbulence can condense material to form "knots" of large mass and is usually generated if the Reynolds number (Equation 1.1), R_e, is greater than some critical value (depends on the situation, but usually a few tens of thousands). Here, $v =$ typical velocity, $L =$ typical length, $\nu_m =$ molecular viscosity, $C_s =$ sound speed, and $\sigma_m =$ particle scattering cross-section ($\sim 10^{-15}$ cm^2 for neutral particles). For a molecular cloud, $R_{e,cloud} \gg R_{e,crit}$.

$$R_e = \frac{vL}{\nu_m} = \frac{vL}{C_s \lambda_m} = \frac{vLn\sigma_m}{C_s} \qquad (1.1)$$

4

While turbulence acts to condense cloud material, when coupled with magnetic fields, it also acts as the main support for GMCs, as long as they have sufficient strength (Gritschneder et al. 2009; Bodenheimer, 2011; Takahira, Tasker, & Habe, 2014; Christie, Wu, & Tan, 2017). Turbulence usually decays after a certain length of time and thus has to be driven by some mechanism, such as SN or outflows, to maintain support (Gritschneder et al. 2009). Defining the turbulence amplitude as σ_T, or the velocity dispersion, it can be related to the shock Mach number through $M \equiv \sigma_T/C_s$, where C_s is the sound speed.

Takahira, Tasker, & Habe (2014) determined that when turbulence is present, clouds remain in a static position for a relatively short amount of time because the cloud is supported against cooling. Their simulations showed turbulence causes pre-shocked cloud gas to have a filamentary structure, causing the shock propagation to become more complicated. The filaments then create thin shell instabilities, generating ripples that fragment into multiple cores. Without turbulence, the cloud is condensed by the shock force and by its own gravity, generating a single core.

Although usually a method of support, complicated shock waves due to turbulence randomly generate highly compressed regions. If these regions last long enough, they can trigger star-formation (Bodenheimer, 2011). Turbulence is included as a parameter in the radiative transfer models of water line emission produced in this thesis.

1.1.3   Ambipolar Diffusion

As mentioned in §1.1.1, magnetic support of GMCs is one of the mechanisms that resists infall or collapse. The measure of support provided by the magnetic field is given by the mass to flux ratio μ (Equation 1.2), where Φ is the magnetic flux, M is the mass, and G is the gravitational constant. A ratio value of $\mu = 1.0$ usually represents the critical value (Christie, Wu, & Tan, 2017), where $\mu < 1$ is the condition for stability against collapse (Mouschovias & Spitzer, 1976).

$$\mu = \frac{M/\Phi}{1/\sqrt{63G}} \tag{1.2}$$

One of the ways this support breaks down is through ambipolar diffusion (Shu, Adams, & Lizano, 1987; Vanhala & Cameron, 1998; Stahler & Palla, 2005; Christie, Wu, & Tan, 2017), which is the ion dispersion out of a GMC due to the interactions with magnetic and electric fields. This sets the timescale for contraction since gravity is allowed to compress the gas without overbearing opposing magnetic forces (Stahler & Palla, 2005).

Christie, Wu, & Tan (2017) showed a stronger magnetic field has a greater effect on ambipolar diffusion, and thus the star-formation rate since the surface density becomes more dense along the collision front. The neutral particles are left to condense onto the central core, which will grow until it becomes gravitationally unstable and collapses inside-out under its own self-gravity (Shu, Adams, & Lizano, 1987; Stahler & Palla, 2005).

1.1.4 Collapse Criterion

The simplest way to approximate when the gravitational instability and subsequent cloud collapse occurs is using the Virial Theorem. This states that a system's time averaged kinetic energy, K, would be equal to half of the potential energy of the force acting upon it, $-U/2$ (Carroll & Ostlie, 2007). The cloud would be gravitationally stable if $U + 2K = 0$, where K is the internal kinetic energy and U is the gravitational potential. If this relation were to become less than zero, the particles within the system would not have enough kinetic energy to support against the gravitational potential; cloud collapse would occur (i.e, loss of energy due to radiative cooling). The virial theorem is given by

$$\frac{1}{2}\frac{\partial^2 I}{\partial t^2} = 2\mathcal{T} + 2U + \mathcal{W} + \mathcal{M} - \int (P + \frac{B^2}{8\pi})r \cdot n \ d^2x + \frac{1}{4\pi}\int (r \cdot B)B \cdot n \ d^2x \qquad (1.3)$$

Simplifying this version of the virial theorem by ignoring surface integrals, including one representing the effect of any external pressure:

$$\frac{1}{2}\frac{\partial^2 I}{\partial t^2} = 2\mathcal{T} + 2U + \mathcal{W} + \mathcal{M} \qquad (1.4)$$

where I resembles the moment of inertia, and is defined as

$$I \equiv \int \rho |r|^2 d^3x \qquad (1.5)$$

where ρ is density and r is radius. Looking at the right-hand terms of Equation 1.4, $\mathcal{T}$, the total kinetic energy in bulk motion $\mathcal{T}$ is defined as:

$$\mathcal{T} \equiv \frac{1}{2}\int \rho |u|^2 d^3x \qquad (1.6)$$

where u is the fluid velocity. $\mathcal{U}$ is the energy contained in random thermal motion:

$$\begin{aligned} \mathcal{U} &\equiv \frac{3}{2}\int nk_B T d^3x \\ &= \frac{3}{2}\int P d^3x \end{aligned} \qquad (1.7)$$

6

where n is the number of particles, k_B is the Boltzmann constant, and T is temperature. $\mathcal{W}$ is the gravitational potential energy:

$$\mathcal{W} \equiv \frac{1}{2} \int \rho \Phi_g d^3 x \tag{1.8}$$

where Φ_g is the gravitational potential, and finally, $\mathcal{M}$ is the magnetic field energy:

$$\mathcal{M} \equiv \frac{1}{8\pi} \int |B|^2 d^3 x \tag{1.9}$$

where B is the magnetic field. Integrals for U, $\mathcal{M}$, and $\mathcal{T}$ are all positive while the integral for $\mathcal{W}$ is negative. If none of the positive terms balance $\mathcal{W}$, then a typical GMC would be in a state of gravitational collapse (Stahler & Palla, 2005).

Jeans Mass

In 1902, James Jeans considered the conditions required for an interstellar gas cloud to collapse and form stars. His derivation does not consider effects such as rotation, turbulence, external pressure, or magnetic fields, but focuses on thermodynamics and gravitation. Although his treatment of collapse is overly simplified, it provides useful insight into the development of protostars. To derive the Jeans mass, we begin with considering a uniform density cloud. The gravitational potential $\mathcal{W}$ is defined as:

$$\begin{aligned} \mathcal{W} &= -\int_0^M \frac{GM(r)dM}{r} \\ &= -\int_0^R \frac{G(4\pi\rho r^3/3)(4\pi r^2 \rho dr)}{r} \\ &= -\frac{3}{5}\frac{GM^2}{R} \end{aligned} \tag{1.10}$$

and the kinetic energy is defined as:

$$\begin{aligned} 2K &= 3Nk_B T \\ &= \frac{3Mk_B T}{\mu m_H} \end{aligned} \tag{1.11}$$

7

where G is the gravitational constant, M is the enclosed mass, R is the cloud radius, μm_H is the mass of Hydrogen, T is the temperature, and k_B is the Boltzmann constant. Considering now the Virial Theorem to determine collapse, where $R = (3M/4\pi\rho_0)^{1/3}$:

$$
\begin{aligned}
0 &> U + 2K \\
\frac{3}{5}\frac{GM^2}{R} &> \frac{3Mk_BT}{\mu m_H} \\
M &> \frac{5Rk_BT}{\mu m_H G} \\
M &> \left(\frac{5k_BT}{\mu m_H G}\right)^{3/2}\left(\frac{3}{4\pi\rho_0}\right)^{1/2}
\end{aligned}
\tag{1.12}
$$

Arriving at the Jeans mass M_J:

$$
M_J = \left(\frac{5k_BT}{\mu m_H G}\right)^{3/2}\left(\frac{3}{4\pi\rho_0}\right)^{1/2}
\tag{1.13}
$$

Free-Fall Time

In order for a region to collapse and form a star, the gravitational potential must greatly exceed the cloud-supporting forces. At this point, Equation 1.3 can be reduced to

$$
\frac{1}{2}\frac{\partial^2 I}{\partial t^2} \approx -\frac{GM^2}{R}
\tag{1.14}
$$

where R is the radius or a cloud of mass M, and G is the gravitational constant. If I is further approximated as MR^2, the free fall time t_{ff} is given as approximately

$$
t_{ff} \approx \left(\frac{R^3}{GM}\right)^{1/2}
\tag{1.15}
$$

Or, more conventionally, the collapse time for a homogeneous sphere with zero internal pressure (Stahler & Palla, 2005).

$$
t_{ff} \equiv \left(\frac{3\pi}{32G\rho}\right)^{1/2}
\tag{1.16}
$$

1.1.5   Heating & Cooling

As mentioned previously, for cloud collapse to occur the mass must be close to or exceeding the Jeans mass, a shock must be in the proper velocity range, and the cooling must be effective. Cooling is a required condition of star-formation collapse (Boss et al. 2008; Boss et al. 2010; Bodenheimer, 2011; Gritschneder et al. 2012; Dale & Bonnell, 2012; Zhou et al. 2015) and is usually caused by the rotational and vibrational transitions of optically thin, warm molecular gas (i.e., H_2O, CO, H_2, C^+, O) (Boss et al. 2010; Bodenheimer, 2011). Molecules have more energy levels available (as compared to atoms) because they also have rotational and vibrational energy transitions; specifically, the big advantage of molecules is that the rotational energy transitions are so low that they are in the same range as the temperatures of the interstellar medium. Therefore, there is enough energy in collisions to excite the non-vibrational rotation lines, allowing them to be ideal probes of these low temperatures. The effective cooling of molecules results in nearly isothermal free-fall collapse. It has been suggested that an inability to cool may lead to a higher internal temperature and a higher Bonnor-Ebert core mass (Zhou et al. 2015). The dominant cooling processes include:

1. collisional excitation of atoms, molecules, electrons, etc.; then rapid decay and release of photon.

2. dust grain cooling - colliding with grains transfers energy from the gas and heats the grains; this results in a loss of thermal energy from the gas, effectively cooling it.

The dominant heating sources include:

1. photodissociation of H_2 by interstellar photons

2. photoionization of C by interstellar radiation

3. ionization of H and H_2 by low energy cosmic rays

4. production of photoelectrons liberated from grains by UV photons.

1.1.6   From GMC to Protostar

Stars actively form in giant molecular clouds (GMC). Once the molecular cloud has reached the Jeans mass limit by one form or another and begins collapse, the density climbs until the cloud becomes too optically thick to its own cooling radiation. This shifts the system into an adiabatic phase (Tielens, 2005; Carroll & Ostlie, 2007). The internal pressure increases, slowing down infall. The accreted material releases energy by radiating in the infrared (IR), effectively cooling itself and building up onto the core until it reaches hydrostatic equilibrium. This allows a release of internal energy from the core, causing further condensation and core mass gain while rising in temperature. Once the temperature reaches 2000 K, molecular hydrogen dissociation occurs. The temperature continues to slowly rise past this point until most of the molecular hydrogen in the core is dissociated. Further gravitational collapse can then occur. The central object at this stage is known as the protostar (Stahler & Palla, 2005) - this is the stage of star-formation that this thesis will be focusing on.While the deeply embedded protostar is forming within the cloud of dust and molecules, matter from the parent cloud is still accreting. The central temperature continues to rise until about 10^6 K, when nuclear fusion commences. At this point, the star will begin to produce a radiation pressure strong enough to disperse all of the surrounding material and halt accretion. The final pre-main sequence star will then be visible (Stahler & Palla, 2005; Carroll & Ostlie, 2007).

Identifying the stage of stellar evolution is difficult. Dust and gas within the cloud absorb optical light emitted by the protostar and accretion. This light is re-emitted at much longer wavelengths (mm - IR). Observing at these wavelengths is key to understanding YSO evolution.

Class 0 stars like that studied in this thesis are identified as very red deeply embedded sources and are considered to represent an earlier phase of protostellar evolution (Stahler & Palla, 2005). In terms of the structure, this protostar is surrounded by a nebular disk, which in turn is encompassed by a spherical envelope. When the protostellar radiation pressure is strong enough against the pressure generated by the infalling material, outflows will be present as well. This structure is discussed further in the next section.

1.1.7   Star Formation Overview
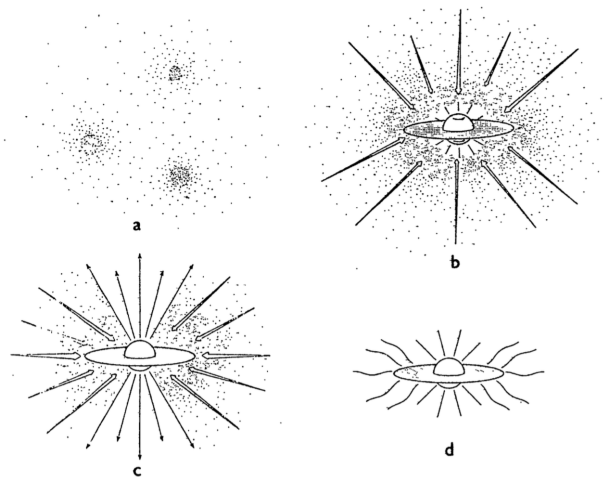
Figure 1.2: The four stages of star-formation, from Shu, Adams, & Lizano (1987).
(a) Formation of cores within molecular clouds as a result of loss of support.
(b) Protostar and surrounding nebular disk forms at collapsing cloud center (LM stars).
(c) Stellar wind break-out into bipolar outflow.
(d) Termination of infall, leaving newly formed star with circumstellar disk.

As described in Shu, Adams, & Lizano (1987), stars follow the same overall formation process, with a few differences across the mass regimes (see Figure 1.2 for schematic of this process):

1. **Slowly rotating cloud core:** Low-mass cloud envelopes experience a slow leakage of support. High-mass envelopes may also fragment during contraction.

2. **Inside out collapse:** The contracting cloud reaches a point of instability; the innermost envelope radii begin to collapse, with the outermost following suit in a domino-like manner. The material falling onto the embedded protostar will pass through an accretion shock, generating a considerable amount of the observed luminosity. Ram pressure of the infalling material onto the protostellar surface acts as a "lid", containing the stellar wind. Eventually, a sizable amount of infalling material will accrete onto the disk instead of the protostellar surface, weakening this lid at the rotational poles and allowing for a stellar wind to breakout, thus forming collimated jets or bipolar outflows.

3. **Bipolar outflows:** The bipolar outflows eventually sweep out over all 4π steradians.

4. **YSO:** The previous stage allows for the reveal of a young stellar object (YSO) and its remnant nebular disk (in the low-mass case). High-mass YSO's sometimes have disks as well.

5. **Disk disappearance:** Nebular disk disappears, forming into planets or stellar companions. At this point, LM YSO's enter pre-main sequence phase, while HM YSO's join the main sequence during the accretion phase.

The above seems like quite a generalization of star-formation; while it may be an adequate generalization for LM star-formation, in reality HM star-formation is fairly complicated. Masses exceeding 8 $M_\odot$ produce a radiative pressure that is far greater than the gravitational pressure, which should effectively halt the accretion process. This clearly isn't the case as stellar masses as great as >50 $M_\odot$ have been discovered. This suggests that HM star-formation is not a simple gravitationally driven process (Crimier et al. 2010). Clearly, other mechanisms are at play.

High-mass star-formation has been observed in tight clusters (Hillenbrand & Hartmann, 1998), while LM stars are able to form in isolation or loose groups (i.e., few objects per cubic parsec) (Gomez et al. 1993). Intermediate-mass star-formation has also been observed in clusters (Testi & Sargent, 1999; Neri et al. 2007; Fuente et al. 2007); stars around 3.5 $M_\odot$ are seen to form in loose clusters, indicating a smooth transition from LM to HM (Testi & Sargent, 1999). Crimier et al. (2010) find physical characteristic evidence of a smooth transition across all three mass regimes, indicating consistent trigger sources and formation processes. Further study of IM star-formation, including that of this work, is expected to help clarify some of the complicated grey areas across the mass regimes (Crimier et al. 2010; Fich et al. 2010; Johnstone et al. 2010).

1.1.8 Stellar Mass

In this work, the different masses of Young Stellar Objects (YSOs) are classified by luminosity since this can be directly measured. The standard delineation of mass ranges follows from a variety of models of the star-formation process: Low-Mass (LM) < 100 $L_\odot$, 100 $L_\odot$ ≤ Intermediate-Mass (IM) ≤ 10^4 $L_\odot$ (corresponding to 2 - 8 $M_\odot$), and High-Mass (HM) > 10^4 $L_\odot$. The spectral line profiles for each of the mass regimes have similar features: broad components ($\sim$ 20 km s^{-1}) corresponding to stellar outflows, medium components ($\sim$ 5 - 20 km s^{-1}) corresponding to jets or the protostar itself, and narrow components (< 5 km s^{-1}) corresponding to protostellar envelopes. Sometimes absorption features are

seen, which are attributed to the absorption by the outer envelope. Due to the similar nature of these components, it has been assumed that the processes by which these features interact with the environment is similar across a wide range of luminosity and mass. It has been seen that outflows dominate in the low and intermediate-mass regimes; envelope contributions are more prominent for HM.

Low-mass stars have been found forming in isolation and in loose groups of a few objects per cubic parsec (Gomez et al. (1993)). This mass regime is well studied thanks to the large number of LM stars in the local galaxy. Some examples of LM Class 0 studies include Jørgensen et al. (2002) (7 YSOs) and Shirley et al. (2002) (11 YSOs). Intermediate-mass stars have often been found in clustered environments (similar to HM) (e.g. Testi & Sargent, 1998; Neri et al. 2007; Fuente et al. 2007) with a smooth transition towards the loose LM regime for stellar masses of $\sim 3.5 M_\odot$ (Testi et al. 1999). These stars are located locally, making them observable on a similar scale like the LM regime (Fuente et al. 2012). It been seen that IM stars are also dominant sources of FUV field (e.g., Habing, 1968, Gondhalekar & Wilson, 1975). This FUV field regulates phases in the galactic ISM and therefore the overall galactic star-formation and history (Crimier et al. 2010). Studies of IM stars are performed to bridge the understanding between mass regimes. Some examples of studies conducted on IM star-formation include Hogerheijde et al. (1999), Schreyer et al. (2002), Fuente et al. (2007), Neri et al. (2007), Crimier et al. (2010), Fich et al. (2010), Johnstone et al. (2010), and Tisi (2013). High-mass stars are usually found to form in tight clusters (e.g. Hillenbrand & Hartmann, 1998). Their mass accretion rates are seen to be orders of magnitude greater than that of their low-mass counterparts (Stahler & Palla, 2005). This requires a higher sound speed C_s and temperature. Higher densities may also be required. HM stars are scarcer and are located at further distances from Earth; this makes them difficult to observe at high spatial resolution. Adding to the difficulties, HM stars quickly disperse their surroundings once formed, hindering the study of their environment. Some examples of HM protostellar studies include Mueller et al. (2002) (31 YSOs), Hatchell & van der Tak (2003) (10 YSOs), Williams et al. (2005) (32 YSOs), and van der Tak (2000) (9 YSOs).

Considering the above studies, we see a luminosity range of $1 < L_\odot < 22$ and $1 \times 10^3 < L_\odot < 2 \times 10^6$, and thus a luminosity and knowledge gap between $22 < L_\odot < 1 \times 10^3$ (Crimier et al. 2010). IM observations are necessary as they provide a link between LM and HM (Di Francesco et al. 1997; Mannings & Sargent, 1997, 2000). Although highly important in regards to connecting the low and high stellar mass regimes, the overall study of IM star-formation is still very much in its infancy.

1.2 Herschel Space Observatory & HIFI

The Herschel Space Observatory launched May 14, 2009 with the purpose of learning more about the physics and processes governing the interstellar medium (Pilbratt et al. 2010). Three instruments on board the 3.5 m Cassegrain telescope operating in the 55 - 672 micron range (Ott et al. 2010) (0.45 - 5.4 THz or 15-180 cm^{-1}; van Dishoeck et al. 2011) include the Heterodyne Instrument for the Far Infrared (HIFI) (de Graauw et al. 2010), the Photodetector Array Camera and Spectrometer (PACS) (Poglitsch et al. 2010) and the Spectral and Photometric Imaging Receiver (SPIRE) (Griffin et al. 2010).

The HIFI instrument provides many observational benefits, including resolving power of R $= \lambda/\Delta\lambda > 10^7$ (where λ is wavelength), high spectral resolution (0.03 – 300 km s^{-1}) over a wide range of frequencies (480 – 1250 GHz and 1410 – 1910 GHz), using a combination of the heterodyne radio technique and near quantum-noise limited sensitivity. Amongst other benefits, HIFI is specially optimized for observations of water lines. (de Graauw et al. 2010).

The instrument offers four observing modes, a.) dual beam switch (DBS), b.) frequency switch (FS), c.) load chop (LC), and d.) position switch (PS). As explained in de Graauw et al. (2010) and Roelfsema et al. (2012), the DBS observing mode moves an internal mirror that in turn moves the light beam to a reference OFF-target position on the sky, but still within 3 arcminutes of the ON-target position. This mode runs the risk of incurring standing waves. The FS observing mode allows for observation by shifting the local oscillator frequency a few (90 - 300) MHz to keep the lines of interest observable. This mode is beneficial as it reduces baseline ripples. The LC observing mode uses the HIFI internal cold source as a reference and the chopping mirror bounces between the target on the sky and the internal load. This mode is useful when non-emission-free regions pollute the target area. The final PS mode bounces between a target position and at a reference position, where the reference position is typically chosen to be nearby and devoid of emission in the employed band.

The majority of the water observations used in this work are obtained in DBS observing mode; a few are obtained using load chop, and the remainder use position or frequency switch. This is outlined in Table 2.1.

Spectral observations made with the HSO would have poor spatial resolution; multiple line emissions used together with radiative transfer analysis is required for understanding physical and chemical processes in the star-formation region (Tisi, 2013; van Dishoeck et al. 2011; Hillier, 2008; van der Tak et al. 2005).

1.3 WISH Team

Water plays an important role in star-formation as it is an abundant molecule with multiple observed rotational transition spectral lines. The Water In Star-Forming regions with Herschel (WISH) program (van Dishoeck et al. 2011) is a key program on the Herschel Space Observatory, designed to probe the physical and chemical dynamics of star-formation regions using gas-phase water and related molecules. This program also follows the water abundance throughout different phases of star-formation. Approximately 80 sources (disks, pre-stellar cores, LM YSOs, IM YSOs, HM YSOs) with luminosities ranging from <1 $L_\odot$ to $>10^6$ $L_\odot$ were targeted; these include candidates studied by the intermediate-mass YSO team: NGC 7129 FIRS 2, NGC 2071 IR (IRAS 08448-4343), VelaIRS17 (IRAS 08470-4321), VelaIRS19, L1641 S3MMS 1, AFGL 490). These, and briefly one HM candidate (NGC 6334) are studied in this work, with a focus on NGC 7129 FIRS 2. These observations were obtained with HIFI.

Of the six IM YSO's studied by the IM team, Crimier et al. (2010) and Johnstone et al. (2010) presented preliminary results for NGC 7129 FIRS 2. IM YSO candidates Vela IRS 17 and Vela IRS 19 were rigorously studied by Tisi (2013). See §1.7 for further information regarding NGC 7129 FIRS 2.

1.3.1 Spectral Line Profile

Spectral lines show a multitude of features. Molecular lines must have emission or absorption features appearing against the continuum. The continuum represents a collection of indistinguishable interactions between many atoms, ions, or molecules spread out across the spectrum. Sources of continuum may include a hot core or dust emission. Spectral observations of star-formation regions show similar features corresponding to different processes involved (see Figure 1.3): broad components (~ 20 km s^{-1}) corresponding to strong outflows, medium components (~ 5 - 20 km s^{-1}) corresponding to jets or the protostar itself, and narrow components (< 5 km s^{-1}) corresponding to protostellar envelopes. Sometimes absorption features are seen, which are attributed to the absorption by the outer envelope. If additional absorption features are seen at a velocity away from the associated V_{LSR}, the presence of a foreground cloud is possible.

The shape of the spectral line profile may reveal a great deal about the dynamics of the star-formation region. Beals (1953) studied the spectra of the P Cygni stars and stressed their similarity to Novae and Wolf-Rayet stars, attributing their similar features to ejection of stellar material (panel I of Figure 1.4). Today the P-Cygni profile is attributed to line profiles that have strong emission lines towards the line center with a corresponding

15

blueshifted absorption. Sometimes a double peak structure is created when the absorption is superimposed on a broad symmetric emission line. The latter is produced by material moving away from the interior star and toward Earth, while the emission comes from other parts of the expanding envelope, or stellar outflow. An inverse P-Cygni profile is characterized by an inversion of the line profile about the V_{LSR}; i.e, instead of a redshifted asymmetry (panel III of Figure 1.4), a blueshifted asymmetry is present. This profile is attributed to cold protostellar envelope (absorption) infalling towards a central core (emission). The velocity of the free-fall region v_{ff} can be derived from invoking conservation of energy such that the kinetic energy gained by the infalling mass m is equal to the change in gravitational potential energy:

$$
\begin{aligned}
\frac{mv^2}{2} &= \frac{GMm}{r} \\
v^2 &= \frac{2GMm}{rm} \\
v_{ff} &= \sqrt{\frac{2GM_*}{r}}
\end{aligned}
\tag{1.17}
$$

or, alternatively:

$$
V = 1 \text{ km s}^{-1} \left[\left(\frac{M_*}{M_\odot} \right) \left(\frac{1000\text{AU}}{r} \right) \right]^{0.5}
\tag{1.18}
$$

Asymmetry due to infall becomes more pronounced as optical depth and infall speed increase (Myers et al. 1996). This information will be considered during the radiative transfer modelling of the Herschel HIFI line spectra.
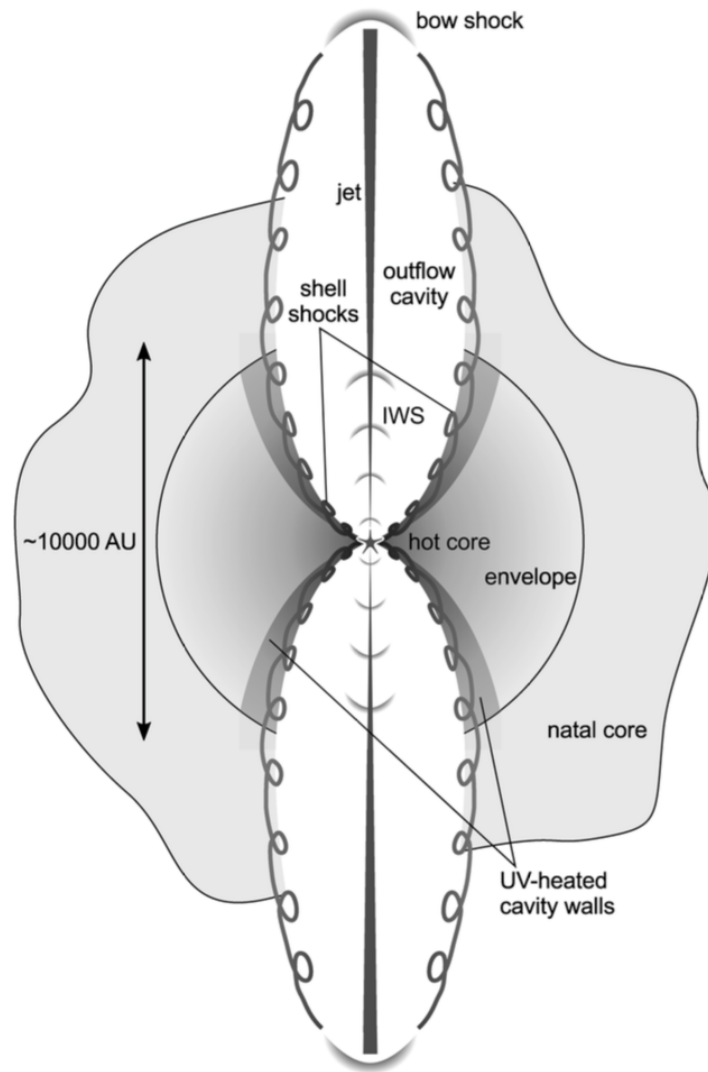
Figure 1.3: Illustration of a protostellar envelope with the different physical components and their nomenclature indicated. IWS stands for internal working surfaces. The indicated scale is appropriate for a low-mass YSO. On this scale, the ∼100 AU radius disk surrounding the protostar is not visible. From van Dishoeck et al. (2011).
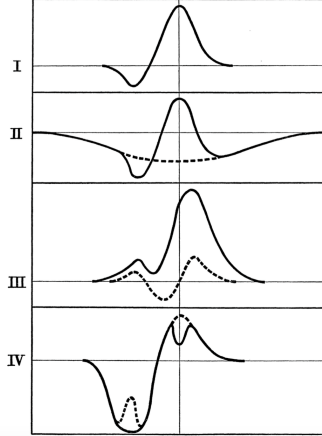
Figure 1.4: Spectra of P-Cygni stars obtained by Beals (1953).

1.4 Water

Water and its isotopolgues (different versions of water with heavier oxygen atoms, ^{17}O and ^{18}O) are nearly-impossible to observe from ground-based instruments due to the absorption by the Earth's atmosphere. The first detection of water was made by Cheung, Rank, & Townes in 1969 with the twenty foot radio telescope at the Hat Creek Observatory; they observed the 22 GHz 6_{16} - 5_{23} transition from the directions of Sgr B2, the Orion Nebula and the W49 source. While this line can be used to trace areas of high excitation around star-formation regions, not much information about water and its role in these environments can be obtained from this line at large spatial scales (Cernicharo & Crovisier, 2005). Alternatively, lower transition water lines can have significant advantages in the study of protostellar environments (see Cernicharo & Crovisier, 2005 and Melnick, 2009 for reviews). These lines can be used as unique diagnostics of molecular gas clouds due to high variability in abundance across large temperature ranges. Water acts as a marker of star-formation similar to the 22 GHz line as this molecule in a gaseous state is sensitive to energy deposited in the region around it. Water is an ideal tracer compared to CO; it has a large dipole moment of 1.85 D, nearly 20 times larger than that of CO (Stahler & Palla, 2005). Because of this large dipole moment (measure of system's polarity), water has high A rotation constants ($A = \hbar^2/2I$; I = moment of inertia, $\hbar = h/2\pi$); thus, the energy spacing between lower levels is larger than that for heavier molecules like CO (Takahashi et al. 1983; van Dishoeck et al. 2011. Additionally, water has a plethora of observed transitions due to its hyperfine structure (discussed below), and is optically thinner.

18

The formation of water occurs through many chemical processes (Stahler & Palla, 2004; van der Tak et al. 2005; Hillier, 2008; van Dishoeck et al. 2011). Neutral reactions occur in hot environments, while ion-molecule reactions occur in cooler environments. At ~ 250 K, gaseous oxygen is driven into water by reactions of oxygen and OH with hydrogen. The reaction in Equation 1.19 is endoergic (absorbs energy) by 2000 K (Elitzur & Watson, 1978; Charnley, 1997) and the reaction in Equation 1.20 is exothermic with an energy barrier of ~ 2100 K (Atkinson et al. 2004). This temperature range is representative of shocked cloud regions. The major sequence is

$$H_2 + O \rightarrow OH + H \tag{1.19}$$

$$OH + H_2 \rightarrow H_2O + H \tag{1.20}$$

These neutral-neutral reactions don't occur within cold (~ 10 K), dark clouds. Here, ion-molecule reactions dominate. Oxygen and hydrogen combine on dust grains to form ice that evaporates around ~ 100 K. The formation of water in this environment involves the chain

$$H_3^+ + O \rightarrow H_2 + OH^+ \tag{1.21}$$

$$OH^+ + H_2 \rightarrow OH_2 + H \tag{1.22}$$

$$OH_2 + H_2 \rightarrow H_3O^+ + H \tag{1.23}$$

$$H_3O^+ + e^- \rightarrow H_2O + H \tag{1.24}$$

The last reaction proceeds very quickly given an adequate supply of free electrons.

Oxygen (O) is the most abundant element in the universe after hydrogen (H) and helium (He). The cosmic abundance of O relative to H is $\sim 5.6 \times 10^{-4}$ (Neufeld, Lepp, & Melnick, 1995; Pinsonneault & Delahaye, 2009). If all available oxygen is converted into water, we obtain an upper limit of H_2O/H_2 of $2 \times 5.6 \times 10^{-4}$. If only the reaction in Equation 1.20 drives all available gaseous O into water, we receive an upper limit of 3×10^{-4} (van Dishoeck et al. 2011). Of course, not all oxygen is converted into water; some of the oxygen can be in other forms like CO. Three-micron absorption spectroscopy of solid water towards YSOs indicates that iced water abundances can be as high as $\sim 10^{-4}$, much higher than results from freeze-out of gas phase water (i.e, Whittet et al. 1988; Pontoppidan et al. 2004). Near protostars, grain temperatures rise above ~ 100 K; all iced water thermally desorbs on very short timescales (Fraser et al. 2001). This leads to an upper limit of gaseous water abundance as high as the ice abundances (van Dishoeck et al. 2011). In short, the upper limit of water should be more like $\sim 10^{-4}$ for a temperature of ~ 100 K, and 3×10^{-4} for a temperature of > 250 K. Gas phase chemical model predictions
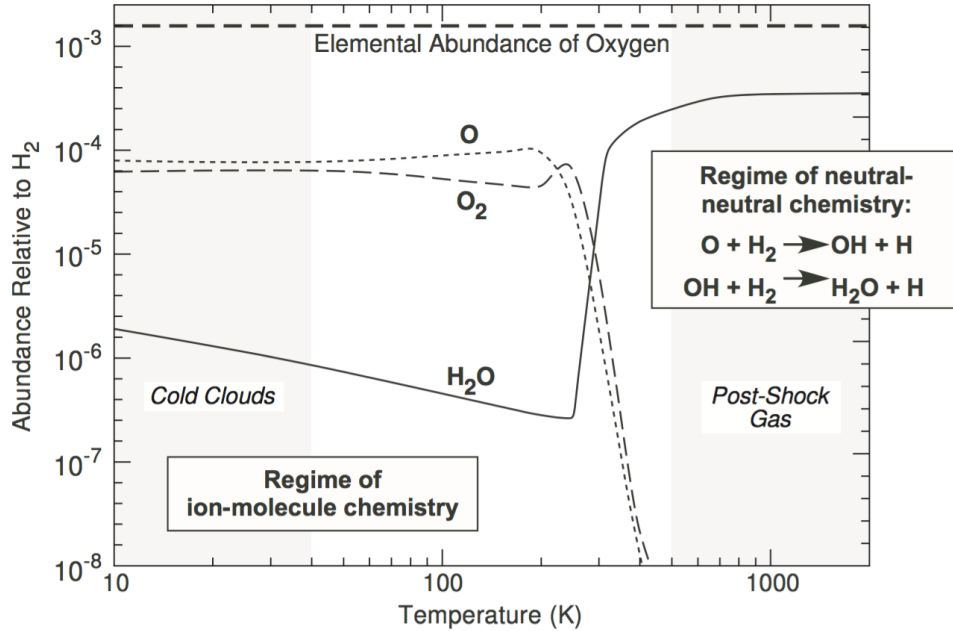
Figure 1.5: Gas phase chemical model predictions of O, O_2, and H_2O as a function of gas temperature for $n(H_2) = 10^5$ cm^3 (after Neufeld, Lepp & Melnick, 1995)

of O, O_2, and H_2O as a function of gas temperature are given in Figure 1.5 for a molecular hydrogen density of 10^5 cm^3. Pure gas phase chemistry gives a lower limit of $\sim 10^{-7}$, but effects of dust-grain freeze-out allows for a much lower abundance relative to H_2, since H_2 does not freeze-out (van Dishoeck et al. 2011). The modelling procedure outlined later in this thesis considers these upper and lower limits.

The excitation of the rotational energy levels of water and the eventual radiative decay allows the molecule to act as a coolant for shock-heated clouds, thereby playing a critical role in the evolution of warm molcular clouds (Neufeld & Kaufman, 1993; Neufeld, Lepp, & Melnick, 1995; Melnick, 2009; van Dishoeck et al. 2011). The molecule heats through infrared (IR) absorption and relaxes through collisional and radiative de-excitation (van Dishoeck et al. 2011). The most important colliders in these reactions are ortho- and para-H_2.

Water is an asymmetric top molecule; this rotates differently than more simple molecules such as CO. It has three unequal moments of inertia along its principle axes. The complexity of its rotation allows for many different transitions between rotational states. This complexity is further increased by the hyperfine structure of water. The magnetic moments of the protons around H-atoms could be aligned/parallel (ortho-hydrogen) or anti-
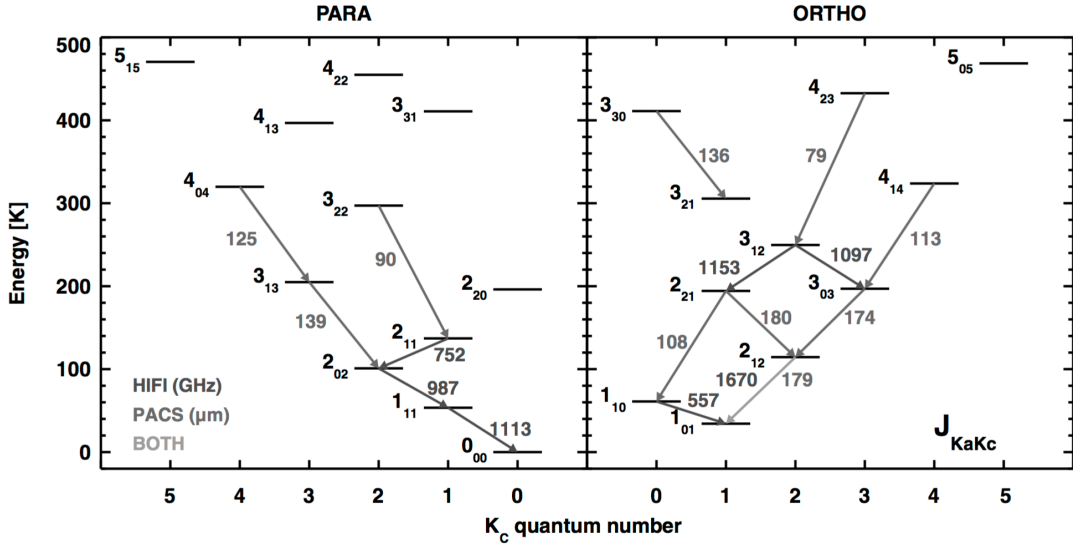
Figure 1.6: Figure 1 from van Dishoeck et al. (2011). Energy levels of ortho- and para-H2O, with HIFI transitions (in gigahertz) and PACS transitions (in microns) observed in WISH indicated.

aligned/anti-parallel (para-hydrogen). (Stahler & Palla, 2005). This means that water has two sets of rotational state lines and that there are numerous rotational energy levels available. The rotational states for water are labelled with three numbers in the form J_{KC}. Ortho-water states can be distinguished from the J_{KC} nomenclature when the sum of K and C equal an odd number; an even sum of K and C corresponds to para states of water. The rotational energy transitions for water observed with Herschel HIFI can be seen in Figure 1.6; these observations will be studied in this thesis. Each rotational state has a number of sublevels equal in energy corresponding to the spins of the 2 hydrogen nuclei. This degeneracy is three times greater for ortho than para (hence, an expected ortho to para ratio of 3:1). (Stahler & Palla, 2005). Transitions cannot occur across the ortho-para ladders except through chemical reactions that exchange a hydrogen nucleus.

Water has high line opacities due to high transition frequencies and its large dipole moment (van Dishoeck et al. 2011). For example, considering the ground state ortho-$H_2^{16}O$ 1_{10}-1_{01} (557 GHz) line, $\tau = 2.0 \times 10^{13}$ $N_\ell(H_2O)\Delta V$ where $N_\ell \sim oH_2O$ column density and ΔV = FWHM (van Dishoeck et al. 2011). Because of this large optical depth, its heavier isotopologue $H_2^{18}O$ makes a great alternative for studying the physics and chemistry of star-formation regions. This molecule is of particular interest as it is 200-500 times less abundant than regular water (therefore having a much smaller optical depth).The frequency

coverage (0.45 - 5.4 THz) of Hershel allows for both high and low excitations of $H_2^{16}O$ and $H_2^{18}O$ to be observed. Studies on $H_2^{18}O$ in relation to star-formation are limited, making this an exciting thesis topic.

1.5 Radiative Transfer

Analysis of star-formation regions that determines the density, temperature, velocity, etc., must take into account the absorption and reemission of photons by atoms, molecules, and dust grains (Spitzer, 1978). The change in specific intensity I_ν resulting from interaction with matter is governed by the equation of transfer, derived by considering the flow of energy in and out of a cylinder of length ds and the absorption and emission coefficients α_ν and j_ν, where ν is the photon frequency. Assuming photons travel in straight lines, the change in specific intensity along distance ds then corresponds to:

$$\frac{dI_\nu}{ds} = -\alpha_\nu I_\nu + j_\nu \tag{1.25}$$

or equivalently with $d\tau_\nu \equiv \alpha_\nu ds$ (Spitzer, 1978; Hogerheijde & van der Tak, 2000; Hillier, 2008; Tisi, 2013), where $\tau_\nu = 0$ at the observer and increases towards the star-formation region

$$\frac{dI_\nu}{d\tau_\nu} = -I_\nu + S_\nu \tag{1.26}$$

The above expressions have the following units: α_ν i in cm^{-1} and j_ν in erg s^{-1} cm^{-3} Hz^{-1} sr^{-1}. From Equation 1.26, we can define the source function $S_\nu \equiv j_\nu/\alpha_\nu$. Both molecules and dust particles will be considered as sources of emission and absorption during the radiative transfer modelling process, found later in this thesis:

$$\begin{aligned} j_\nu &= j_\nu(\text{dust}) + j_\nu(\text{gas}) \\ \alpha_\nu &= \alpha_\nu(\text{dust}) + \alpha_\nu(\text{gas}) \end{aligned} \tag{1.27}$$

The dust components are given by:

$$j_\nu(\text{dust}) = \alpha_\nu(\text{dust})B_\nu(T_{\text{dust}}) \tag{1.28}$$

$$\alpha_\nu(\text{dust}) = \kappa_\nu \rho_{\text{dust}} \tag{1.29}$$

where $B_\nu(T_\text{dust})$ is the Planck function at the dust temperature

$$B_\nu(T) = \frac{2h\nu^3}{c^2} \frac{1}{e^{h\nu/kT} - 1} \qquad (1.30)$$

ρ_{dust} is the density of the dust, κ_ν is the dust opacity in cm^{-2} per unit dust mass, h is the Planck Constant, k_B is the Boltzmann constant, and c is the speed of light. The opacity used in the radiative transfer program RATRAN (Hogerheijde & van der Tak, 2000), discussed later in this work, was the program default "jena,thin,e6", corresponding to the Jena dust models (Ossenkopf & Henning, 1994) with thin mantles and 10^6 years of coagulation.

The gas components depend on the rotational transitions:

$$j_\nu^{ul}(gas) = \frac{h v_0}{4\pi} n_u A_{ul} \phi(\nu) \qquad (1.31)$$

$$\alpha_\nu^{ul}(gas) = \frac{h v_0}{4\pi} (n_l B_{lu} - n_u B_{ul}) \phi(\nu) \qquad (1.32)$$

where u and l correspond to the upper and lower states, respectively, and ϕ accounts for Doppler turbulent broadening, assumed to be Gaussian:

$$\phi(\nu) = \frac{c}{b\nu_0} \exp\left(-\frac{c^2(\nu - \nu_0)^2}{v_0^2 b^2} \right) \qquad (1.33)$$

where c is the speed of light and b is broadening parameter in km s^{-1}, related to the full width at half maxiumum (FWHM) by

$$\frac{b}{\text{FWHM}} = \frac{1}{2\sqrt{\ln 2}} = 0.60 \qquad (1.34)$$

The Einstein coefficients A$_{ul}$, B$_{lu}$ and B$_{ul}$ are the probabilities for spontaneous emission and absorption and stimulated emission, respectively. These are dependent on the molecule, and are discussed further in Section §3.1, along with population level densities n_u and n_l.

The local mean intensity of the radiation field is given as

$$J_\nu = \frac{1}{4\pi} \int I_\nu d\Omega \qquad (1.35)$$

where J_ν is the average intensity received from all solid angles $d\Omega$, and I_ν is the solution of Equation 1.25. The spectral intensity (Spitzer, 1978), can be defined as

$$\int j_\nu d\nu = \frac{h\nu_{lu} n_u(X^{(r)}) A_{ul}}{4\pi} \qquad (1.36)$$

23

where ν_{ul} is the frequency at the line center, the quantity $n_u(X^{(r)})$ is the particle density for molecules of species X, ionized r times and in the energy level u. Further derivations and numerical testing are conducted in Chapter 3.

1.6   Modelling Overview

Before modelling can take place, the observations obtained with Herschel HIFI need to be downloaded from the observatory's archive via the Herschel Interactive Processing Environment (HIPE, version 15.0). The observational data for NGC 7129 FIRS 2, NGC 2071 IR, Vela IRS17, Vela IRS19, L1641 SMMS3 1, and AFGL 490 will be obtained using observation IDs, outlined later in this thesis (Chapter 2). This data will then be processed such that any standing waves will be removed, the baseline will be removed, and the frequency scale will be converted to a velocity scale relative to the IM YSO's V_{LSR}. Because the spectral line profiles we are modelling are the result of emission and absorption from many features in the star-formation region, we will apply Gaussian fitting in attempt to disentangle the origins. Gaussian line profiles will be applied to the molecular lines of each IM YSO candidate; among these include a broad, medium, and narrow contribution. It is expected that the narrow contribution is attributed to the envelope as these regions shouldn't have a large radial velocity, if any at all. This narrow component will be the focus of the modelling procedure outlined below.

To model the emission spectra obtained with Herschel HIFI, radiative processes throughout the dusty and molecular envelope must be calculated. An isothermal density and temperature profile has an index of $\alpha = 1.5$. An H_2 density and temperature profile is calculated by Crimier et al. (2010) with a program called DUSTY. They use a power-law index $\alpha = 1.4$. The DUSTY program solves the radiative transfer equations defined in §1.5 and §3 through a spherically symmetric dust cloud and returns the temperature profile. The DUSTY modelling allows for fitting of physical parameters such a size, density, and optical depth of the cloud. These two density profiles, and a hybrid density profile combining the density profile of $\alpha = 1.4$ and the temperature profile of $\alpha = 1.5$, are used in this work. These structural envelope models (including oH_2 density, pH_2 density, and temperature profile) are input into an accelerated Monte Carlo radiative transfer program called RATRAN (Hogerheijde & van der Tak, 2000) for spectral line modelling.

RATRAN models line emission spectra through a spherical region. As such, we will only be modelling the envelope contribution of the star formation region. Other components such as the outflow are not spherical in nature and might be better modelled with a program that handles the proper geometry, such as RADEX (van der Tak et al. 2007).

RATRAN assumes a 1D geometry along the line of sight due to the symmetry of the spherical environment. A dust to gas ratio of 100:1 and a shared profile are assumed. The program takes as input a signal-to-noise ratio (SNR), an initial number of photons, dust emissivity (in this case, Jena dust models; Ossenkopf & Henning, 1994), molecular data and collisional rate coefficients [H_2O; Daniel et al. 2011], and a source model. This model consists of the Crimier density and temperature profile, collider density (ortho and para H_2), target molecule density ($H_2^{16}O$ and $H_2^{18}O$), and a velocity field (turbulent and infall/expanse velocity). Turbulent velocity is input in the form of the Doppler broadening parameter, which is related to the width of the envelope contribution to the spectral line by Equation 1.34. If modelling the envelope (or a portion of the envelope) in free-fall, the radial velocity is defined as Equation 1.17. The density of water is calculated by taking the sum of the oH_2 and pH_2 density, and dividing by some value within the upper and lower limits defined in Section §1.4. This value is the abundance of the molecule with respect to H_2. In short, population densities of rotational energy levels are calculated with the RATRAN sub-program AMC and are then used to produce emission spectra via ray tracing with a second sub-program SKY. The details of the RATRAN code will be elaborated in a later chapter.

In the source model for NGC 7129 FIRS 2, the spherical envelope is broken up into regions of nested shells, ranging in distance from the core between 1.496×10^{13} m (100 AU) to 2.69×10^{15} m (18000 AU), and in temperature from 288.5 K to 15.8 K. A freeze-out radius is assumed at T $\sim$ 100 K; out to this radius water is gaseous, beyond this it is frozen onto dust grains (van Dishoeck et al. 2011). The inner region is defined as the radii interior to the freeze-out radius ($<5.4 \times 10^{13}$ m), and the outer region is defined as the radii exterior($\geq 5.4 \times 10^{13}$ m). The outer envelope is much larger in size compared to the inner envelope and is expected to contribute the majority of the emission/absorption features observed due to the optical depth of $H_2^{16}O$ and the low abundance of $H_2^{18}O$. DUSTY and RATRAN are the tools we use with the Herschel HIFI data to place constraints on the size, density, velocity field, and the abundance of $H_2^{16}O$ and $H_2^{18}O$ relative to H_2 in the inner and outer regions of the NGC 7129 FIRS 2 envelope.

1.7 Previous Studies: NGC 7129 FIRS 2

This thesis focuses on the IM star formation region NGC 7129, selected for this work as observations for both $H_2^{16}O$ and $H_2^{18}O$ are available, the additional molecule allowing for tighter constraints on radiative transfer models of the region. NGC 7129 is a reflection nebula located in a complex and active molecular cloud (Hartigan & Lada, 1985; Miranda et al. 1993) and possibly the youngest IM object known at present, NGC 7129 FIRS 2

(Crimier et al. 2010). The region contains several Herbig AeBe stars; these are responsible for the nebula illumination (Crimier et al. 2010).

NGC 7129 was first detected by Bechis et al. (1978) and Harvey et al. (1984) in the FIR; it is not seen in the optical or NIR wavelengths. Edwards & Snell (1983) detected a bipolar outflow with CO observations. This was confirmed by Fuente et al. (2001), where the morphology of the outflow was determined to be quadrapolar - a configuration of 2 outflows (FIRS 2-out 1 and FIRS 2-out 2). Eiroa et al. (1998) classified NGC 7129 FIRS 2 as an IM Class 0.

Shevchenko & Yakubov (1989) estimated a distance to NGC 7129 of d $\sim$ 1250 $\pm$ 50 pc from the sun by measuring BV photometry and 1D visually determined spectral classification. Straizys et al. (2014) determined this same measurement to be d $\sim$ 1150 $\pm$ 80 pc by measuring 7-colour photometry for 159 stars in a 13 arcminute by 13 arcminute region focused on NGC 7129. They determined this measurement by analyzing the extinction A_V due to dust, deduced the distance to the dust cloud TGU H645 P2, and inferred this as the distance to NGC 7129. This thesis will use the former as the distance to NGC 7129 FIRS 2 in order to maintain consistency with Crimier et al. (2010).

Since then, lots of exciting work has been conducted on the IM YSO candidate NGC 7129 FIRS 2. Looking back nearly a decade and a half ago, Fuente et al. (2005) compared NGC 7129 FIRS 2 to the Type I Herbig Be star LkHα 234 using the IRAM 30m telescope. These stellar objects are located in the same molecular cloud and have similar luminosities; any physical or chemical difference between the two should only be due to evolutionary phase. Their results suggested two ideas: 1.) As a YSO becomes visible, the protostellar envelope is dispersed and heated; and, 2.) bipolar outflows eventually fade or disappear before the YSO even becomes visible. Most importantly, Fuente et al. (2005) presented the first detections of a hot core in any IM YSO. They deduced the size of this hot core to be roughly 600 AU by 800 AU.

Crimier et al. (2010) examined 5 different IM YSO's including NGC 7129 FIRS 2. The observations were obtained with the Long Wavelength Spectrometer (LWS) aboard the Infrared Space Observatory (ISO) (45 micron - 200 micron range). Additional LWS grating spectra were obtained from the ISO data archive. These authors used 450 μm, 850 μm and 1300 μm continuum emission maps to obtain brightness profiles and Spectral Energy Distributions (SED) for NGC 7129 FIRS 2; these maps are given in Figure 1.7.

The comparison between the computed and observed 450 μm, 850 μm and 1300 μm brightness profiles (specifically the brightness versus the distance from the centre of the envelope) and SED allows one to constrain the density profile and the temperature profile of the envelope. The envelope density and temperature profile is derived by giving input
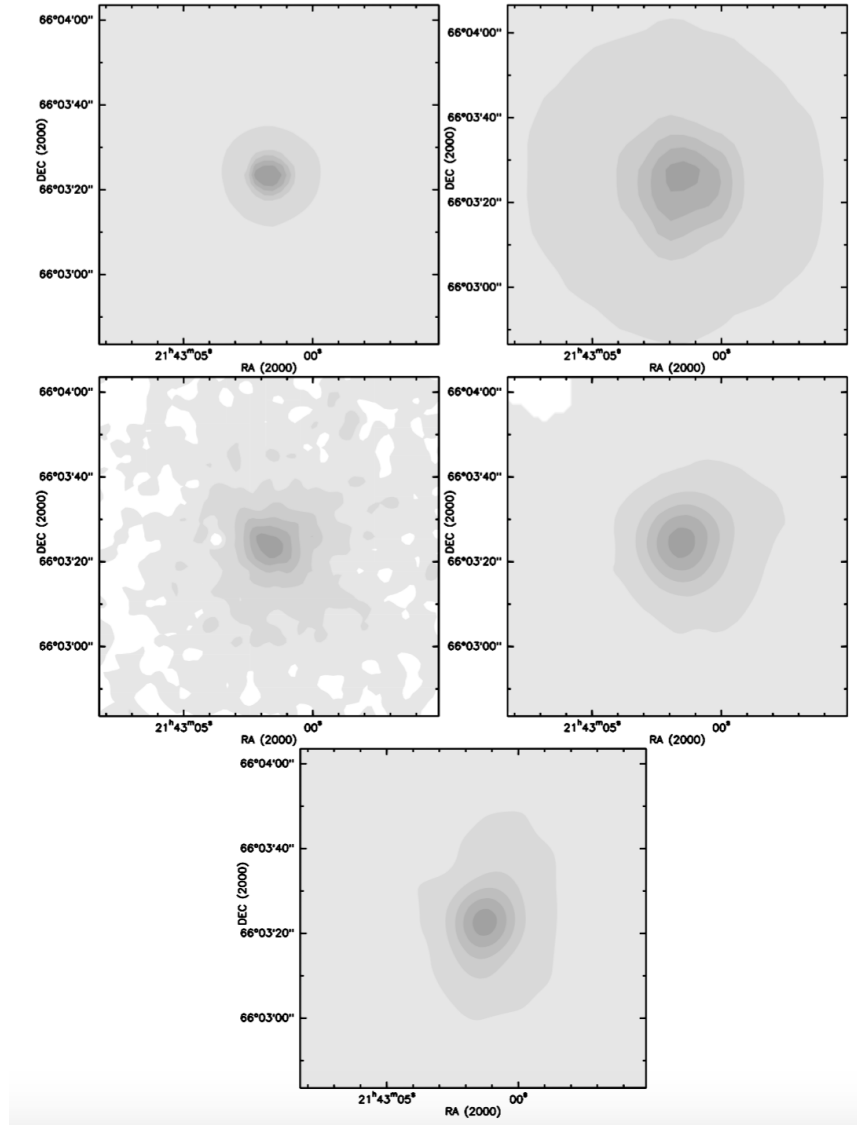
Figure 1.7: Continuum Emission maps around NGC 7129 FIRS 2 at 24 μm (upper left), 70 μm (upper right), 450 μm (middle left), 850 μm (middle right), and 1300 μm (below center). Grey contours mark the continuum flux from 10% to 90% peak emission, in 20% increments. Taken from Crimier et al. (2010).

as the temperature, size of the central object, and dust density profile to the 1D radiative transfer code DUSTY. They used their results to compare the density profile power law index, size, mass, average density, density (1000 AU), and density (10 K) of the IM YSO envelopes to that of LM and HM. They deduced that the parameter transition appears smooth across all 3 mass regimes, suggesting that formation processes and triggers do not substantially differ. This thesis uses the Crimier density and temperature profile for NGC 7129 FIRS 2. The best-fit model has an envelope mass of 50 $M_{\odot}$, an optical depth at 100 μm of 2.3, an inner radius of 100 AU and an outer radius of 18,600 AU. The temperature at the inner radius is 300 K and this falls to 100 K at a radius of 373 AU where the H_2 density is 4.4×10^7 cm^{-3}. The density varies as a power-law with index 1.4.

Shortly after, Fich et al. (2010) used Herschel PACS to study NGC 7129 FIRS 2. They obtained 26 good detections of H_2O, CO, OH, O I, and C II. They noted that most of the lines are substantially stronger than predicted by the spherical envelope models, typically by orders of magnitude. They chose to focus on CO; studies of the highest energy CO lines should reveal more about the warmest innermost regions. The authors use RATRAN to estimate the strength of CO emission by using a Crimier density and temperature profile for CO. Simply modelling the envelope contribution falls below the low to mid-J CO observed emission. The authors then use a second, more general radiative transfer program RADEX (van der Tak et al. 2007) to model the CO emitting slabs. This extends the line profile into the higher-J CO lines, and the emission begins to fit the observations with increasing energy. The unexpected line strength of high-J CO lines requires high temperature and relatively high diesties immediately surrounding FIRS 2. The slab model fits the high-J CO lines, but a more complex model is required to fit all lines simultaneously.

Johnstone et al. (2010) examined the $H_2^{16}O$ and $H_2^{18}O$ lines obtained with Herschel HIFI (the same observations as studied in this thesis). The authors noted that the molecular lines of each molecule share the same morphology: a narrow ~ 6 km s^{-1} component slightly redshifted and a blueshifted much broader ~ 25 km s^{-1} component. They suggest the former component is caused by the envelope surrounding the IM YSO, while the latter component is likely associated with powerful outflows, and the self absorption is likely caused by cold water in the envelope. Johnstone et al. (2010) used the one-dimensional radiative transfer code RATRAN to model the observed line emission and scaled the Green et al. (1993) H_2O-He collisional cross-sections by 1.348 for collisions with H_2. They assumed an ortho to para ratio of 3 and assumed the Crimier density and temperature profile for NGC 7129 FIRS 2. They assumed a freeze-out temperature of 100 K. The final constraints were deduced as follows: turbulent velocity of 2 km s^{-1}, an infall radial velocity of $V = \sqrt{2GM_*/R}$ where $M_* = 1.1 M_{\odot}$, an outer envelope ortho-$H_2^{18}O$ abundance of 3 ± 1 $\times 10^{-10}$, and an inner envelope ortho-$H_2^{18}O$ abundance of $3 \times 10^{-7} - 1 \times 10^{-5}$. An abundance

ratio of $H_2^{16}O/H_2^{18}O$ was assumed to be 550. Ultimately, the majority of the line profile shapes were not reproduced by modelling the envelope alone.

Fuente et al. (2012) models $C^{18}O$ and HDO lines in NGC 7129 FIRS 2. These authors focused on $C^{18}O$ $3 \to 2$ (observed with JCMT) and HDO 3_{12} - 2_{21} (observed with IRAM 30m) lines, hoping to constrain the abundance in the protostellar envelope and in the hot core. Using the radiative transfer code DATACUBE, these authors placed the following constraints on the IM YSO: radial infall velocity of $V = 41.8R(AU)^{-0.5}$ km s^{-1}, turbulent velocity of 1.2 km s^{-1}, HDO abundance of $\sim 0.4 - 1 \times 10^{-7}$ in the hot core (similar to NGC 1333 IRAS 2A), and $C^{18}O$ abundance $\sim 1.6 \times 10^{-8}$. The latter value is a factor of 10 lower than the reference value.

Shortly after, Fuente et al. (2014) aimed to determine the chemical composition of the IM hot core within NGC 7129 FIRS 2. Using radiative transfer and molecular excitation code MADEX (Cernicharo, 2012), they modelled a total of ~ 300 spectral lines, obtained with the IRAM Plateau de Bure Interferometer (PdBI) between 218200 MHz and 221 800 MHz. Interestingly in the context of this thesis, their rotational diagrams (Figure 1.8) indicate excitation temperatures for the hot core that are similar to the innermost radius of our density and temperature model for the envelope of NGC 7129 FIRS 2 (i.e, center panels indicating $T_{rot} = 265^{+39}_{-69}$ K (A- and E-CH$_3$OCHO) and $T_{rot} = 260^{+4}_{-5}$ K (HNCO)).

Lastly, this thesis also models the HM YSO NGC 6334 I(N) in effort to gain confidence in the modelling procedure. This YSO was previously studied by van der Tak et al. (2013), and 3 years later by Herpin et al. (2016). The velocity profiles of the low-excitation H2O lines toward a HM sample of YSOs have been presented by van der Tak et al. (2013), without detailed modelling. They decomposed HIFI water line spectra into three distinct physical components: (i) dense cores (protostellar envelopes) usually seen as medium or narrow absorption/emission; (ii) outflows seen as broader features; and (iii) absorptions by foreground clouds along the line of sight. Similar to this thesis, Herpin et al. (2016) focuses on the analysis of the water observations toward the mid-IR quiet massive protostars of the WISH sample. Using the HIFI instrument they studied molecular gas dynamics, estimated infall and turbulent velocities present in the protostellar envelopes, and derived H$_2$O abundances in these YSOs. As in this thesis, these authors also used RATRAN and the Daniel et al. (2011) water collisional cross-sections, and comparison of our NGC 6334 I(N) radiative transfer models with theirs should supply confidence in the integrity of our models. This is expanded in §4.4.
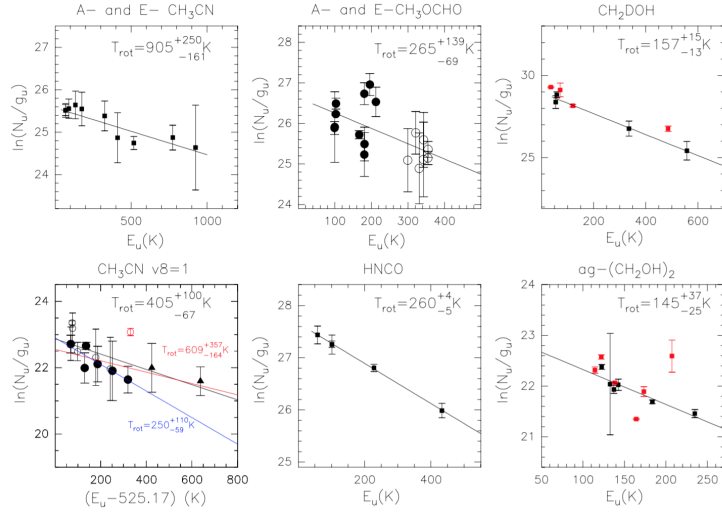
Figure 1.8: Rotational diagrams for the NGC 7129 FIRS 2 hot core. Figure extracted from Fuente et al. (2014). Rotational excitation temperatures ranging from $T_{rot} = 145^{+37}_{-25}$ K to $T_{rot} = 905^{+250}_{-161}$ K.

1.8 Thesis Outline

The goal of this thesis is to place tighter constraints on the physical and chemical parameters of the IM YSO NGC 7129 FIRS 2 using Herschel HIFI observations of $H_2^{18}O$ and $H_2^{16}O$. This thesis will use the up-to-date collisional cross-sections of Daniel et al. (2011) and an updated version of the radiative transfer code RATRAN to model spectral line emission for this IM YSO. The chemical and physical parameters include the envelope abundance, turbulent velocity, radial infall, $H_2^{16}O/H_2^{18}O$ abundance ratio, freeze-out temperature, and the H_2O ortho-to-para ratio. These parameters have been previously constrained, but the derived values are not consistent with that of the low- and high-mass regimes. This thesis aims to bring the intermediate-mass parameter values into harmony with that of the other mass regimes.

Herschel HIFI Observations and data reduction techniques are discussed in Chapter 2. Radiative transfer equations are further outlined and tested in Chapter 3. Chapter 4 discusses the modelling techniques involving radiative transfer program RATRAN and Chapter 5 discusses the same for the radiative transfer program RADEX. Modelling results are also discussed in both of these chapters. A discussion is given in Chapter 6, Conclusions are given in Chapter 7, and Future Work is outlined in Chapter 8.

30

Chapter 2

Observations

This chapter presents molecular line emission observations of 6 intermediate-mass star formation regions and one high-mass star formation region. All observations were obtained under the WISH program. The single HM region, NGC 6334 I(N), has already been studied by van der Tak et al. (2013) and Herpin et al. (2016). We include this HM region in our studies to ensure our radiative transfer modelling outputs are consistent with their findings, allowing confidence in the modelling of intermediate-mass sources. This will be explained further in §4.4.

Fifty water spectral observations were obtained with Herschel HIFI (de Graauw et al. 2010). The descriptions of each observing mode are given in Section §1.2; these modes along with the observation IDs (obsids) are outlined in Table 2.1 for each of the studied spectra. Physical properties of the WISH targets, such as the mass regime, location, and V_{LSR}, are outlined in Table 2.2 and a summary of the NGC 7129 FIRS 2 water transitions studied in this work is given in Table 2.3. See Appendix A, *Other IM WISH Candidates*, for the other IM WISH candidate parameters. There, a water observation summary is given in Table A.2 and A.3, baseline removed observations are shown in Figures A.1 - A.6, Gaussian fit parameters are given in Tables A.4 - A.8, and the corresponding fits are plotted in Figures A.7 - A.15. These sources are excluded from the main study as $H_2^{18}O$ observations are either non-detections, weren't observed, or time constraints wouldn't allow it. Acquiring this data and subsequent reduction was carried out with the Herschel Interactive Processing Environment (HIPE). In short, HIPE was used to convert the wave scale, remove the baseline and any standing waves, convert to ASCII, and fit Gaussians.

Table 2.1: Observation ID and Observing Mode: Intermediate, High, and Low Mass YSOs. **Boldface** = Load Chop, *Italic* = Frequency Shift, Plainfont = DBS, `Typewriter` = Position Switch. "OTF" = On the fly.

Source	NGC 7129 FIRS 2	NGC 2071 IR	VelaIRS17 (IRAS 08448-4343)	VelaIRS19 (IRAS 08470-4321)	L1641 S3MMS1	AFGL490 I(N)	NGC 6334	NGC 1333 IRAS2A
Transition				Observation ID				
$H_2^{16}O$ 1_{10}-1_{01}	**1342198329**	**1342205274**	**1342198316**	**1342198314**	**1342203754**	**1342214346**	1342205282[OTF]	1342202067
$H_2^{18}O$ 1_{10}-1_{01}	1342192362	1342194490	*1342198317*	*1342198315*	*1342203755*	*1342214347*	1342205282[OTF]	1342192207
$H_2^{16}O$ 1_{11}-0_{00}	134219176	1342194790	**1342197984**	**1342197985**	**1342206122**	**1342217724**	1342206383	
$H_2^{16}O$ 2_{02}-1_{11}	1342191613	1342204503	1342197951	1342197952	1342203147	1342204511	1342204519	
$H_2^{16}O$ 2_{11}-2_{02}	1342191747	1342194682	1342201541	1342201540	1342203220	1342217717	1342205847	
$H_2^{16}O$ 3_{12}-2_{21} & CO (10-9)	1342198347	1342206128	1342198357	1342198358	1342203260	1342217731		
$H_2^{18}O$ 2_{02}-1_{11}	1342191614						1342204518	
$H_2^{16}O$ 3_{12}-3_{03}	1342191677						1342206384	
$H_2^{18}O$ 3_{12}-3_{03}	1342227393	1342227395					1342206384	

Table 2.2: WISH Target Information: Intermediate and High Mass YSOs.

Source/ Property	NGC 7129 FIRS 2	NGC 2071 IR	VelaIRS 17	VelaIRS 19	L1641 S3MMS1	AFGL 490	NGC 6334 I(N)
Regime	IM	IM	IM	IM	IM	IM	HM
RA (h m s)	21 43 01.7	05 47 04.4	08 46 34.7	08 48 48.5	05 39 55.9	03 27 38.4	17 20 55.2
dec (° ' ")	+66 03 23.6	+00 21 49.0	-43 54 30.5	-45 32 29.0	-07 30 28.0	+58 47 08.0	-35 45 04
V_{LSR} (km s^{-1})	-9.8	9.6	3.9	12.2	5.3	-13.5	-7.7
L_{bol} (L$_{\odot}$)	430	520	715	776	70	2000	1.1×10^{5}
d (pc)	1250	422	700	700	465	1000	1700
Outflow	B(+60, +60), R(+60, -60)	P0(+32, +63), P5(-128, -97)	-	-	-	-	-
Reference	35, 44, 98	65, 125	48, 71, 101	71, 101	106, 125	78, 102	95

Table 2.3: List of NGC 7129 FIRS 2 Observed Water Lines. Beamsize calculated using Equation 3.18 (Roelfsema et al. (2011)).

Molecule	Transition	Line	ν (GHz)	E_{up} (K)	Band	Integration (s)	Resolution (MHz)	Date	θ_{beam} (")
o-H$_2^{16}$O	1_{10}-1_{01}	o001	556.936	61.0	1a	405	1.022	15-06-10	38.074
p-H$_2^{16}$O	1_{11}-0_{00}	p001	1113.343	53.4	4b	2431	1.135	05-03-10	19.046
p-H$_2^{16}$O	2_{02}-1_{11}	p002	987.927	100.8	4a	1271	1.022	03-03-10	21.464
p-H$_2^{16}$O	2_{11}-2_{02}	p004	752.033	136.9	2b	922	1.139	07-03-10	28.197
o-H$_2^{16}$O	3_{12}-2_{21}	o006	1153.127	249.4	5a	598	1.020	15-06-10	18.389
p-H$_2^{16}$O	3_{12}-3_{03}	o007	1097.365	249.4	4b	1803	1.018	05-03-10	19.323
o-H$_2^{18}$O	1_{10}-1_{01}	o001	547.676	61.0	1a	3599	1.139	20-03-10	38.718
p-H$_2^{18}$O	2_{02}-1_{11}	p002	994.675	100.8	4a	2265	1.022	03-03-10	21.318
o-H$_2^{18}$O	3_{12}-3_{03}	o007	1095.627	249.4	4b	6495	1.119	25-08-11	19.354

2.1 Data Reduction

2.1.1 HIPE

The Herschel Interactive Processing Environment (HIPE) was created as a user friendly version of the Herschel Data Processing System (Ott, 2010). The benefit of HIPE is that the environment is more concerned with the data as opposed to the language, thus allowing Java-inexperienced users ease of access. Observations obtained by Herschel are processed into data products of different reduction levels through pipelines on the European Space Astronomy Centre (ESAC) computing grid (Ott, 2010). These levels include:

- Level 0 products: Raw telemetry data as measured by the instrument. Potential of minimal formatting.

- Level 1 products: Detector readouts calibrated and converted to physical units, within principle instrument. Observatory independent.

- Level 2 products: Level-1 data products further processed to absolutely calibrated images, spectral cubes and spectra such that scientific analysis can be performed.

These data products are then input into the Herschel Science Archive (HSA), where they can be retrieved via HIPE. The spectral observations included in this thesis were obtained from the HSA with HIPE 15.0.0 using their observation IDs and the following input prompts:

```
HIPE > obsid = 1342198329
HIPE > data = getObservation(obsid = obsid, useHsa = True)
```

Using HIPE's Observation Viewer the level 2.0 data products were then selected for baseline removal. Standing waves and spurs were observed through the ground state o-$H_2^{18}O$ 1_{10}-1_{01} spectral lines of AFGL 490 and Vela IRS 19. These observations were discarded upon unsuccessful standing wave removal (HIPE routine `fitHifiFringe`).

The minor HIPE tasks such as converting to ASCII formatting or changing the wavescale are carried out within the spectrum toolbox. The former task is labelled `ExportSpectrumtoAscii` and the latter is labelled `ConvertWavescale`.

Baseline Removal

(a) $H_2^{16}O$ Observations.

(b) $H_2^{18}O$ Observations.
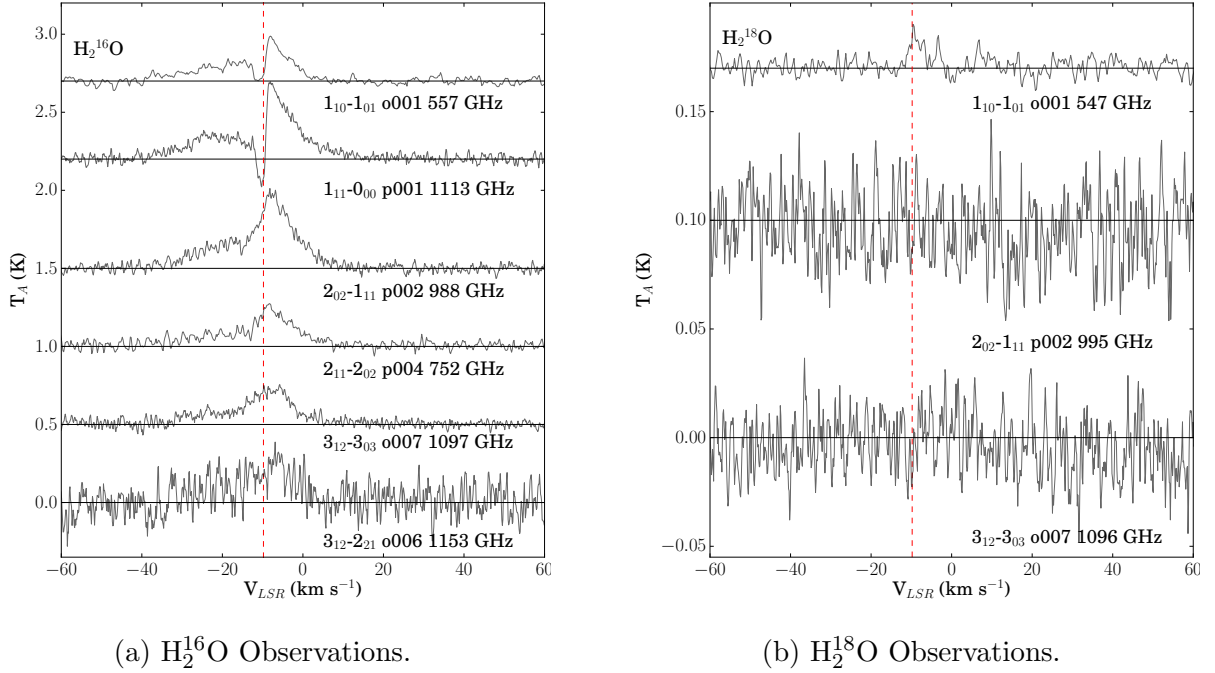
Figure 2.1: NGC 7129 FIRS 2 Observations. System V_{LSR} located at -9.8 km s-1 (red dashed line). Absorption feature near the system V_{LSR} tends to lessen with increased transition energy, indicating the absorption feature occurs due to a colder region. The $oH_2^{16}O$ 006 3_{12}-2_{21} line is quite noisy as this dataset also observed a much more intense CO 10-9 line. The $oH_2^{18}O$ excited lines are considered non-detections. $H_2^{18}O$ ground state emission peak ~ 0.02 K, $H_2^{16}O$ ground state emission peak ~ 0.3 K.

HIPE 15.0.0 was used to remove the baselines from the observations; linear baselines were removed for the majority of the data, although some second order polynomials and higher were required for baseline correction. The input prompts for this are as follows:

```
HIPE > sds_out = fitBaseline(data = sds_in)
```

where **sds_in** is the path of the level 2 data product (data > level 2 > WBS_H_USB > box_001 > 0001).

Several issues were encountered during baseline removal. Spurs were present in the ground state ortho-water lines of Vela IRS19 and AFGL 490, resulting in their removal from further analysis. Spurs were also present in the ground state ortho $H_2^{16}O$ and $H_2^{18}O$ L1641 S3MMS1 lines, but in the preceeding sub-band (redshifted from V_{LSR} by $\sim 200 - 800$ km s^{-1}). The $H_2^{18}O$ spur had amplitudes of $T_A \sim 1000$ K, making the entire spectra unusable for further analysis. Finally, the $H_2^{16}O$ 2_{02}-1_{11} p002 line and 2_{11}-2_{02} p004 line for all 6 IM WISH candidates were located between two sub-bands. These data were stitched and averaged prior to baseline removal. The results of the baseline removal can be seen in Figures 2.1a,b. See Appendix A for other 5 IM WISH candidate baseline removal.

Gaussian Spectral Fitting

Gaussians are fit to spectral line data so that it is possible to assess different physical components of star formation region. A narrow Gaussian component (< 5 km s^{-1}) is thought to be produced by a heated envelope with very little turbulence. A medium Gaussian component is thought to be related to turbulent regions in the mid-range of the envelope, while a broad Gaussian component (> 20 km s^{-1}) is associated with high velocity outflow from the embedded protostar, with emission originating from shocks along cavity walls (Tisi, 2013).

HIPE 15.0.1 was used to fit the spectral lines with Gaussians. Once the baselines were removed from the datasets and the spectra were stitched together, the `Spectrum Fitter GUI` was used to fit the IM WISH candidate spectral lines. The automatic fitting routines employed by HIPE enable multiple simultaneous fits. For NGC 7129 FIRS 2, four different Gaussian components were initially applied. The errors associated with the total fit were too great and the data didn't support the fourth component, a narrow absorption, at -10 km/s, even considering the residuals of NGC 7129 FIRS 2 o-$H_2^{16}O$ 1_{10}-1_{01} and p-$H_2^{16}O$ 1_{11}-0_{00} (see residuals in Figure 2.2). When fine-tuning this absorption component, the HIPE automatic spectral fitting routines alternately increased the amplitude of a nearby overlapping emission component, then the absorption component, to the point where the two essentially cancelled. Three components were used instead (Figure 2.2), omitting the -10 km/s narrow absorption; the three component associated errors were in better agreement with the data. It must be emphasized that once an acceptable fit had been made to the ground state $H_2^{16}O$ 1_{10}-1_{01} lines of each IM candidate with the automatic fitter GUI, the positions were made constant for the following excitation lines. It is expected that if star formation region features contribute to all the spectral lines included in our data set, they should appear in each line at the same velocity.

The fitted Gaussian parameters for each of the three components are listed in Table 2.4

for each of the studied water transitions. Listed here are the transition lines, RMS noise σ_{RMS}, the ID used during the Gaussian fitting process, the line colour in Figures 2.2 and 2.3, the component classification (broad, medium, or narrow), the V_{LSR} of the component, the width of the component, the peak antenna temperature, the velocity integrated intensity, and the FWHM. Gaussian parameters fit to the other 5 IM WISH candidates, Vela IRS 17, Vela IRS 19, L1641 S3MMS 1, and AFGL 490 can be found in Appendix A.

Noise

Following the Gaussian fitting in HIPE, the residual spectrum and the noise associated with this residual was determined at the 3σ level with Python. The noise was determined from the following equations and is indicated at the 3σ level in Figures 2.2 - 2.4 for each of the IM WISH candidates.

Calculation of the mean μ, where the antenna temperature T_A is summed and divided by the length for a specific velocity range:

$$\mu = \frac{\sum\limits^{n} T_A}{n} \tag{2.1}$$

The variance σ^2 is calculated using this mean:

$$\sigma^2 = \frac{\sum\limits^{n}(T_A - \mu)^2}{n} \tag{2.2}$$

The root mean square noise σ_{RMS} is then the square-root of the variance.

$$\sigma_{RMS} = \sqrt{\sigma^2} \tag{2.3}$$

The expected noise T_{RMS} for each spectra can be determined by:

$$T_{RMS} = \frac{T_{sys}}{\sqrt{\Delta\nu t}} \tag{2.4}$$

where T_{sys} is the the temperature sum of the sky and the receiver, $\Delta\nu$ is the frequency resolution of the receiver ($\sim 1.1 \times 10^6$ Hz for HIFI, see Table 2.5), and t is the integration time in seconds.

Table 2.4: Spectral Fits to Water Data: NGC 7129 FIRS 2

Transition	σ_{RMS} (K)	ID	Colour	Component	V_{LSR} (km s^{-1})	Width (km s^{-1})	T_A (K)	$\int T_A dv$ (K km s^{-1})	FWHM (km s^{-1})
o-H$_2^{16}$O	0.02	G1	Green	Broad	-19.7	9.0 ± 0.5	0.1 ± 0.003	2.2 ± 0.66	21.17
1$_{10}$-1$_{01}$		G2	Red	Narrow	-7.8	2.4 ± 0.3	0.1 ± 0.007	0.8 ± 0.06	5.68
		G3	Cyan	Narrow	-3.6	1.0 ± 0.08	0.2 ± 0.02	0.6 ± 0.06	2.46
p-H$_2^{16}$O	0.04	G1	Green	Medium-Broad	-19.7	7.7 ± 0.3	0.1 ± 0.004	2.6 ± 0.10	18.05
1$_{11}$-0$_{00}$		G2	Red	Medium	-7.8	3.2 ± 0.09	0.3	2.1	7.631
		G3	Cyan	Narrow	-3.6	0.9 ± 0.03	0.3	0.8	2.141
p-H$_2^{16}$O	0.02	G1	Green	Narrow	-19.7	8.1 ± 0.3	0.2 ± 0.004	3.0 ± 0.06	1.908
2$_{02}$-1$_{11}$		G2	Red	Medium	-7.8	5.4 ± 0.2	0.2 ± 0.006	2.6 ± 0.08	12.81
		G3	Cyan	Medium	-3.6	2.7 ± 0.09	0.3 ± 0.007	1.8 ± 0.04	6.307
p-H$_2^{16}$O	0.02	G1	Green	Broad	-19.7	11.6 ± 0.6	0.08 ± 0.003	2.2 ± 0.08	27.50
2$_{11}$-2$_{02}$		G2	Red	Medium	-7.8	5.5 ± 0.4	0.08 ± 0.007	1.1 ± 0.1	12.95
		G3	Cyan	Medium	-3.6	2.7 ± 0.2	0.1 ± 0.007	9.1 ± 0.64	6.264
o-H$_2^{16}$O	0.02	G1	Green	Medium	-19.7	6.7 ± 1.9	0.1 ± 0.02	1.9 ± 0.38	15.86
3$_{12}$-2$_{21}$		G2	Red	Medium	-7.8	4.3 ± 1.5	0.1 ± 0.04	1.1 ± 0.44	10.12
		G3	Cyan	Medium	-3.6	4.0 ± 1.1	0.2 ± 0.05	1.5 ± 0.37	9.377
o-H$_2^{16}$O	0.09	G1	Green	Broad	-19.7	9.3 ± 0.6	0.07 ± 0.004	1.7 ± 0.1	21.95
3$_{12}$-3$_{03}$		G2	Red	Medium	-7.8	6.6 ± 0.7	0.05 ± 0.008	0.8 ± 0.13	15.64
		G3	Cyan	Medium	-3.6	3.9 ± 0.2	0.2 ± 0.007	1.5 ± 0.05	9.275
o-H$_2^{18}$O	0.004	G2	Red	Narrow	-3.4 ± 0.1	0.6 ± 0.1	0.01 ± 0.002	0.02 ± 0.004	1.31
1$_{10}$-1$_{01}$		G3	Cyan	Narrow-Medium	-8.6 ± 0.21	1.9 ± 0.2	0.01 ± 0.001	0.06 ± 0.006	4.38
p-H$_2^{18}$O	0.02	-	-	-	-	-	-	-	-
2$_{02}$-1$_{11}$		-	-	-	-	-	-	-	-
o-H$_2^{18}$O	0.01	-	-	-	-	-	-	-	-
3$_{12}$-3$_{03}$		-	-	-	-	-	-	-	-

T_{sys} can be obtained for each sub-band from

```
data > trendAnalysis > Tsys > TsysTrendTable.
```

The median T_{sys} for concatenated sub-bands is obtainable from the meta data for the level 2.0 data product. The noise values for NGC 7129 FIRS 2 can be found in Table 2.5 and plotted in Figure 2.5. Generally it is observed in this work that the actual noise calculated for these lines is greater than the expected noise by on average a factor of ~ 2.0. The outlier with noise ratio ~ 0.3 corresponds to the 1153 GHz line.

Compared to noise calculations of the same data in Johnstone et al. (2010), those in this work are slightly larger (Table 2.6). For example, the $H_2^{16}O$ p002 2_{02}-1_{11} observation has a calculated noise of 0.023 K, while Johnstone et al. (2010) calculates 0.020 K. The larger result in this work is likely due to a wider velocity range; Johnstone et al. (2010) uses a velocity range of 1 km s^{-1}, while this work uses a range from -60 km s^{-1} to $+60$ km s^{-1} with respect to the YSO V_{LSR}. The larger velocity range is likely causing a larger calculated noise as it might be considering some real emission as noise. In hindsight, this velocity range should have been moved to $[-120, -60]$ km s^{-1}; this would ensure that none of the actual signal is included in the noise calculation.

2.1.2 Spectral Smoothing

During the radiative transfer modelling process, it is imperative that fits are only made to the contributions made by water molecules and not to noise. To aid this effort, the spectra was smoothed using `astropy.convolution.Box1DKernel` in Python. Boxcar smoothing is equivalent to converting the T_A signal into a new signal T_A^*, where each new data point is the average of w adjacent data points. In this thesis (seen plotted in Figure 2.6), a width of w = 11 has been used, but as an example, for $T_A^*[13]$ with a width of 5,

$$T_A^*[13] = \frac{T_A[11] + T_A[12] + T_A[13] + T_A[14] + T_A[15]}{5} \tag{2.5}$$
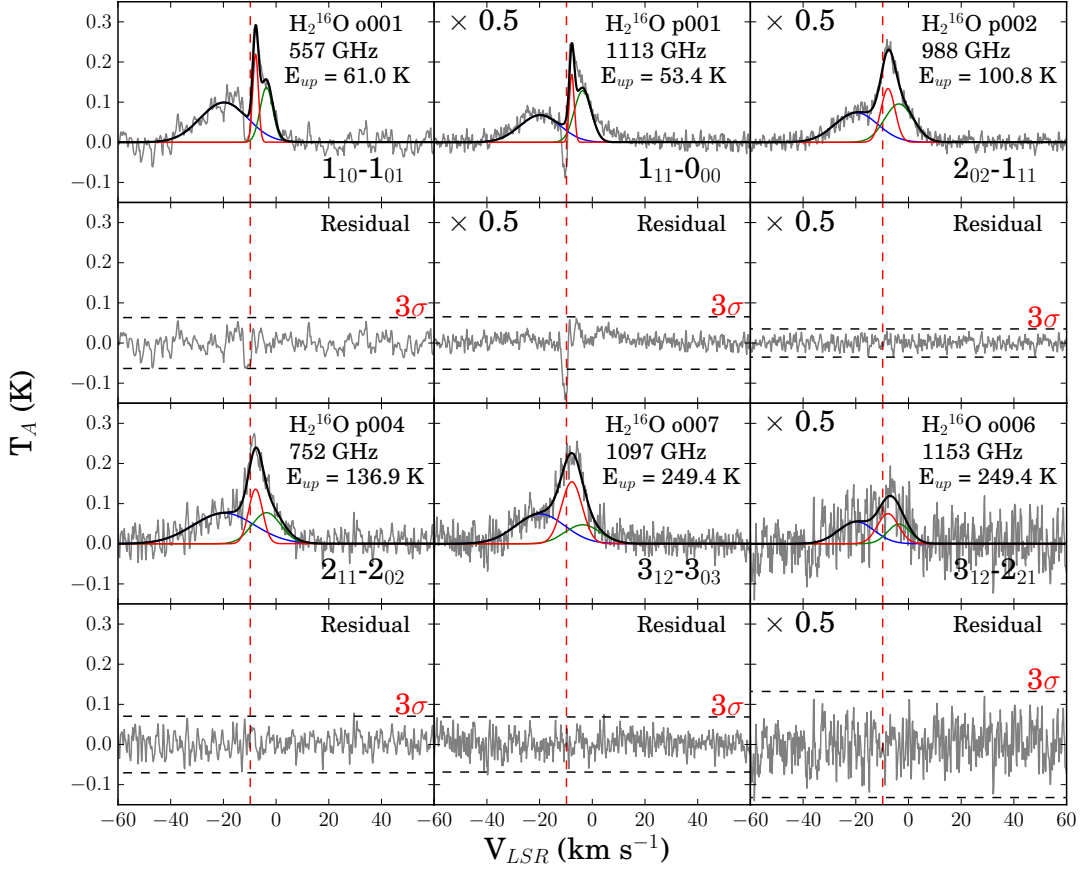
Figure 2.2: NGC 7129 FIRS 2: $H_2^{16}O$ Gaussian Fits contrasted with $H_2^{16}O$ HIFI data. Medium feature located at -19.7 km s^{-1} (blue), narrow feature at -3.6 km s^{-1} (green), and second medium feature at -7.8 km s^{-1} (red). The total fit is outlined in black. Gaussians are fit at the same position in each transition, but at varying widths. See Table 2.4 for further details. Local $V_{LSR} = -9.8$ km s^{-1}. Gaussian fits are subtracted from the HIFI data, yielding the residuals in the bottom panels. The 3σ boundaries around the residuals represent the goodness of fit of the Gaussians. The majority of fits are well encased by these boundaries; the para and ortho ground state lines appear to have some unfitted features. The absorptions seen in this data were not fit. Some lines are scaled by 0.5: p001, p002, and o006.

40
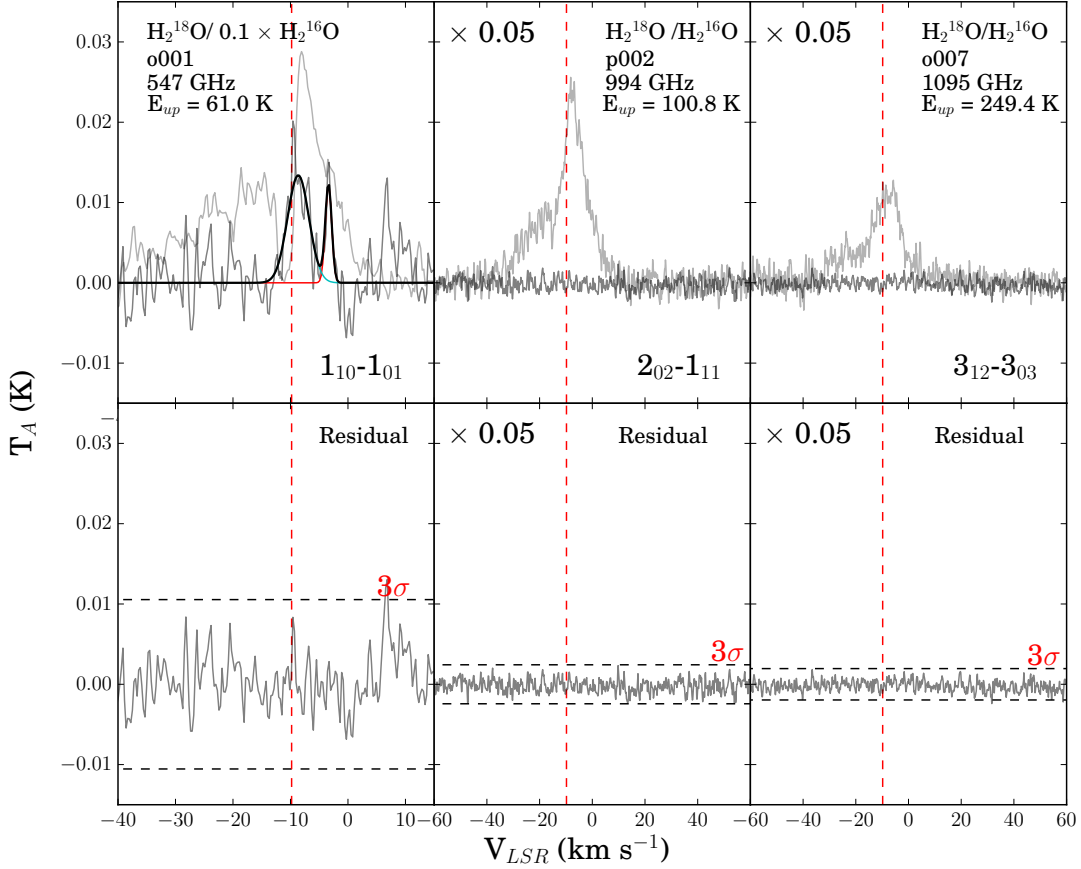
Figure 2.3: NGC 7129 FIRS 2 $H_2^{18}O$ Gaussian Fits, contrasted with $H_2^{18}O$ and $H_2^{16}O$ HIFI data (reduced to 10 % for ground state line o001). Medium feature located at -8.6 km s^{-1} (green) and narrow feature at -3.4 km s^{-1} (red). The total fit is outlined in black. Gaussians are fit for the ground state line, while the excited lines appear to be non-detections. See Table 2.4 for further details. The -3.4 feature is likely to be a non-associated feature, such as a foreground cloud. The ground state line is shown in the following Figure 2.4. Local $V_{LSR} = -9.8$ km s^{-1}. Gaussian fits are subtracted from the HIFI data, yielding the residuals in the bottom panels. The 3σ boundaries around the residuals represent the goodness of fit of the Gaussians. The majority of fits are well encased by these boundaries.

41
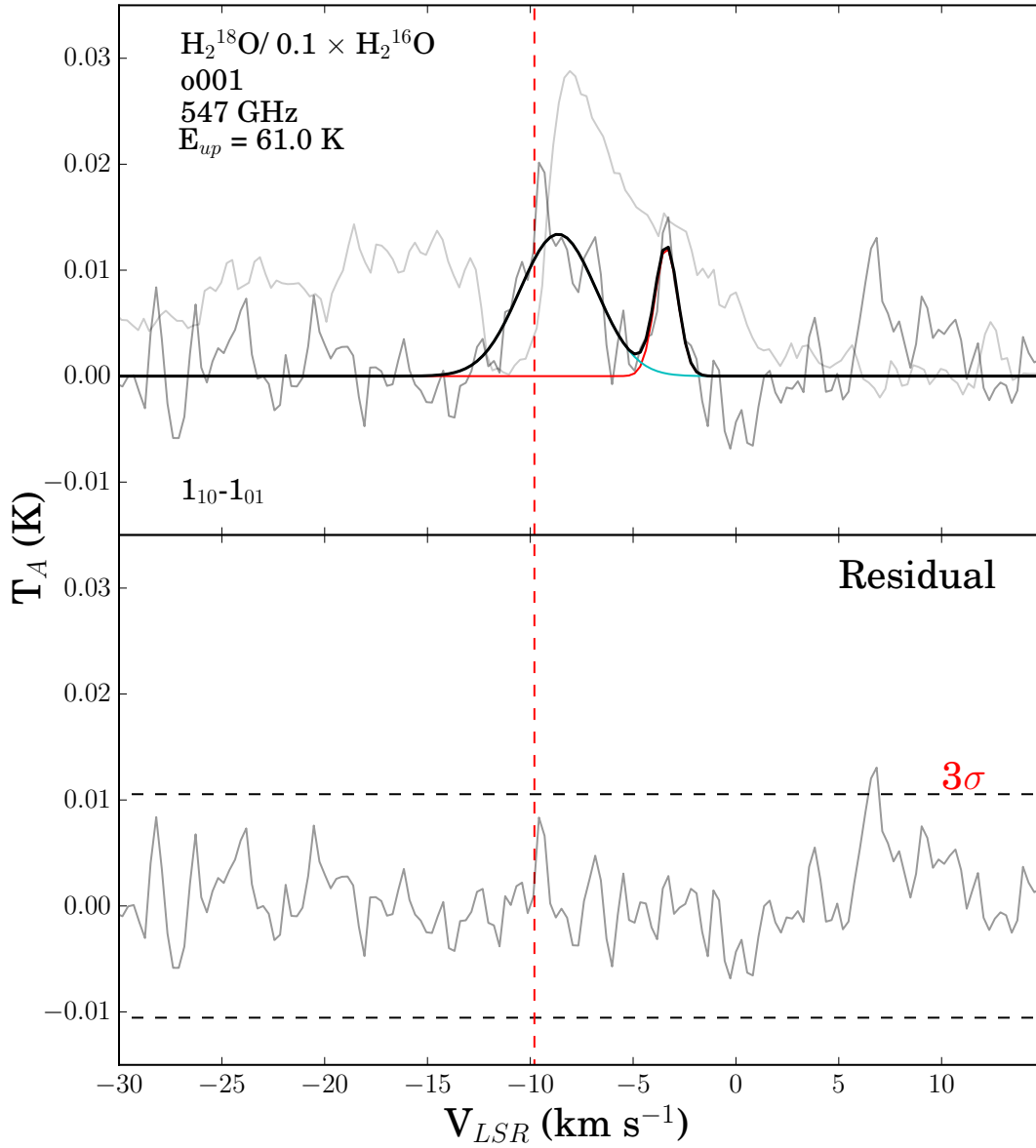
Figure 2.4: NGC 7129 FIRS 2 fits, contrasted with $H_2^{18}O$ and $H_2^{16}O$ HIFI data (reduced to 10 %). Medium feature located at -8.6 km s^{-1} (cyan) and narrow feature at -3.4 km s^{-1} (red). The total fit is outlined in black. The -3.4 feature is likely to be a non-associated feature, such as a foreground cloud. Local $V_{LSR} = -9.8$ km s^{-1}.
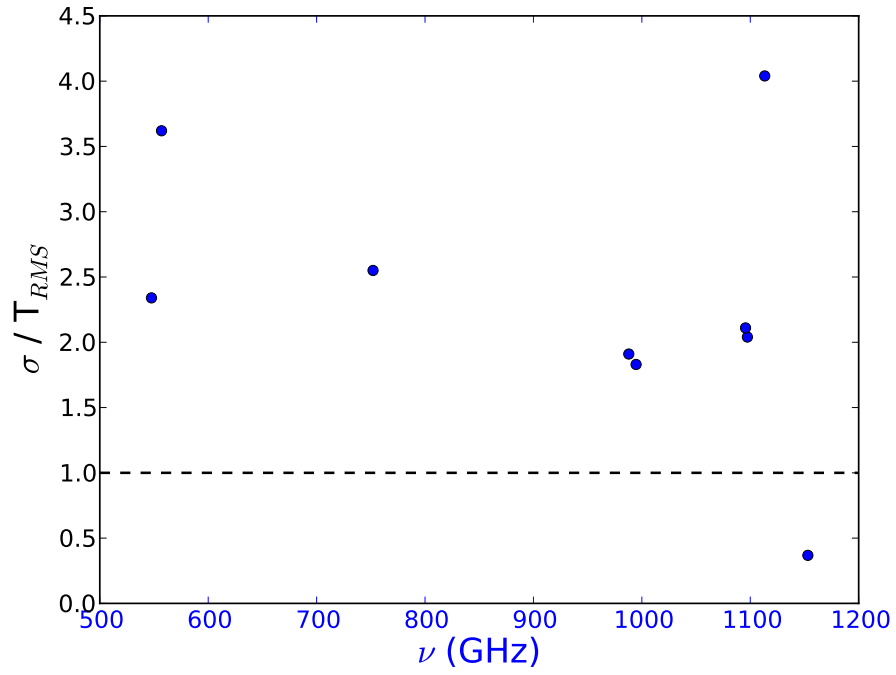
Figure 2.5: Calculated vs. Expected RMS Noise for NGC 7129 FIRS 2 Water Transitions. Generally it is observed in this work that the actual noise calculated is greater than the expected noise by a factor of ~ 2.0. The outlier with noise ratio ~ 0.3 corresponds to the 1153 GHz line.

Table 2.5: NGC 7129 FIRS 2 RMS noise: comparing observed noise (obs) to noise expected (exp) by receiver for each of the observed water lines.

Molecule	Transition	Line	Line ν (GHz)	Integration (s)	T_{sys} (K)	Resolution (MHz)	obs T_{rms} (mK)	3σ (mK)	exp T_{rms} (mK)	obs/exp
o-H$_2^{16}$O	1_{10}-1_{01}	o001	556.936	138.2	69.33	1.022	21	63	5.8	3.62
p-H$_2^{16}$O	1_{11}-0_{00}	p001	1113.343	1100.16	380.95	1.135	44	130	11	4.04
p-H$_2^{16}$O	2_{02}-1_{11}	p002	987.927	550.08	290.82	1.022	23	70	12	1.91
p-H$_2^{16}$O	2_{11}-2_{02}	p004	752.033	423.36	202.31	1.139	23	70	9.2	2.55
o-H$_2^{16}$O	3_{12}-2_{21}	o006	1153.127	266.4	721.59	1.020	88	264	44	0.368
o-H$_2^{16}$O	3_{12}-3_{03}	o007	1097.365	806.4	321.86	1.018	23	69	11	2.04
o-H$_2^{18}$O	1_{10}-1_{01}	o001	547.676	1657.6	65.147	1.139	3.5	11	1.5	2.34
p-H$_2^{18}$O	2_{02}-1_{11}	p002	994.675	1036.8	285.854	1.022	16	50	8.8	1.83
o-H$_2^{18}$O	3_{12}-3_{03}	o007	1095.627	2900.8	351.790	1.119	16	49	6.2	2.11

Table 2.6: Comparing σ_{RMS} as derived by this work and Johnstone et al. (2010)

Molecule	Transition	Line	J(2010) (mK)	This Work (mK)
H$_2^{16}$O	1_{11}-0_{00}	p001	16	44
H$_2^{16}$O	2_{02}-1_{11}	p002	20	23
H$_2^{16}$O	3_{12}-3_{03}	o007	16	23
H$_2^{18}$O	1_{10}-1_{01}	o001	5	3.5
H$_2^{18}$O	2_{02}-1_{11}	p002	5	16

2.1.3 Observations: Summary

The study of molecular emission lines is very useful in the investigation of star formation. This chapter presented molecular line emission observations of 6 intermediate-mass star formation regions and one high-mass star formation region. Reduced data was presented for NGC 7129 FIRS 2, as well as the corresponding Gaussian fits.

The spectral lines show a self-absorption by the envelope, seen in the ortho and para ground state lines. The residuals of these lines show similarities to P-Cygni profiles, indicating expansion. The 557, 752, 988, 1097, and 1113 GHz lines appear quite similar when ignoring absorption features; in terms of width, the 557, 752, and 1097 GHz lines appear to be similar while the 988 and 1113 GHz lines are slightly broader. Additionally, The 752 and 988 GHz line are found to be identical when multiplied by a scaling factor. The 1153 GHz line while similar in shape displays high noise, a consequence of the observational set-up.

Three Gaussians were fit, a narrow component (<5 km s^{-1}) corresponding to the envelope contribution, a medium component corresponding to the hot core and/or collimated jets, and a broad component (>20 km s^{-1}) associated with out-flowing gas. The positions of these remain constant (-7.8, -3.6, -19.7, respectively), while the velocity widths and intensities are allowed to vary. Of these, our focus will be on the narrow component as the radiative transfer program used in the following chapter, RATRAN (Hogerheijde & van der Tak, 2000), models only the emission contribution of the envelope.

Once the baselines were removed and Gaussians were fit, the noise was measured across a velocity range of $[-60, 60]$ km s^{-1}. It was ensured that no additional spectral features were included in this velocity range. Comparing these calculated RMS noise values to those derived for the same spectral dataset by Johnstone et al. (2010) we see a slight increase in our measurements. The main difference between the two is that Johnstone et al. (2010) used a much smaller velocity range of 1 km s^{-1} vs. 120 km s^{-1} (as mentioned in §2.1.1).
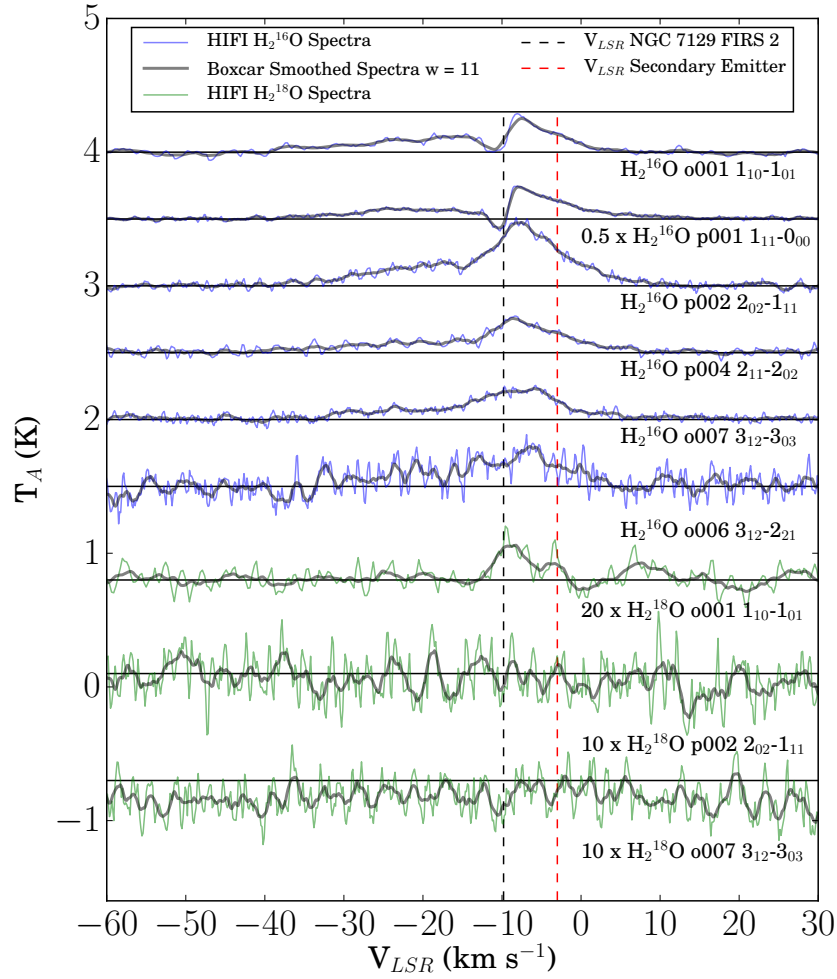
Figure 2.6: NGC 7129 FIRS 2 $H_2^{16}O$ and $H_2^{18}O$ observations obtained with Herschel HIFI, overlaid by spectra smoothed with a Boxcar convolution with width 11 (black). $V_{LSR} = -9.8$ km s^{-1} (black dashed line), velocity of secondary emission feature is ~ 3.0 km s^{-1} (red dashed line). The $H_2^{18}O$ (green) spectra are scaled larger to enhance emission features for better comparison with $H_2^{16}O$ (blue).

Chapter 3

Overview of Model Techniques

Modelling the radiative transfer expected in molecular clouds allows insight into the dynamics and properties of star formation regions. This chapter presents the radiative transfer equations employed in the modelling codes RATRAN and RADEX. These equations are outlined and manually tested, the results of which are then compared to RADEX output in order to gain confidence in the model calculation results.

3.1 Radiative Transfer Equations: Testing Model Results

Input parameters for both radiative transfer codes can be found in Appendix B and C. These combined with the constants in Table D.1 and the equations seen in this section (§ 3.1) make up the total code input. A variety of useful information specific to the line transitions of a given molecule (i.e. $H_2{}^{16}O$ and $H_2{}^{18}O$) is then output. RATRAN outputs the expected brightness temperature, which is then convolved with HIFI beam sizes to obtain spectral line profiles. RADEX outputs numerical line information including the transition ($J_{K_A K_C, u}$-$J_{K_A K_C, l}$), the upper state energy, the line frequency, level populations, the excitation temperature, the optical depth, and the expected flux. RADEX output is manually confirmed using the following calculations and Python 2.7 prior to modelling. Some of these equations have been seen already in the introduction section §1.5.

Three different ideal molecule systems are considered when verifying energy level populations output by RADEX:

- a 2-level energy system,

- a 3-level restricted energy system (levels 2 and 3 non-interacting),

- and a 3-level semi-restricted energy system (levels 2 and 3 only interacting collisionally)

Where the collision rates C_{ul} for transitions between levels 1-3 are defined as:

$$C_{21} = C_{12}\frac{g_1}{g_2}\exp\left[\frac{\Delta E_{21}}{kT}\right] \tag{3.1}$$

and

$$C_{31} = C_{13}\frac{g_1}{g_3}\exp\left[\frac{\Delta E_{31}}{kT}\right] \tag{3.2}$$

where g is the statistical weight of the quantum level, ΔE_n is the change in energy between states, k is the Boltzmann constant, and T is temperature.

3.1.1 Determining Population: Overview

To calculate the quantum state populations, the radiative and collisional probabilities of idealized molecules must be determined, then the simultaneous equations solved on a computer (Spitzer, 1978). We can calculate the statistical equilibrium, or the balance of molecules moving in and out of each state collisionally and radiatively, with the following state equation:

$$n_j\left[\sum_k(n_cC_{jk} + B_{jk}U_\nu) + \sum_{k<j}A_{jk}\right] = \sum_k n_k(n_cC_{kj} + B_{kj}U_\nu) + \sum_{k>j}n_kA_{kj} \tag{3.3}$$

where n_i is the population in state j, n_c is the population of the collider, C_{jk} is the collision rate for a transition from j to k, B_{jk} is the simulated emission coefficient, U_ν is the radiant energy density ($U_\nu = c^{-1}\int I_\nu d\omega$), and A_{jk} is the spontaneous emission coefficient. For the purpose of the following sections, the simulated emission terms ($B_{jk}U_\nu$) are omitted. These state equations are then used as a system of linear equations solved with Python 2.7 using various methods. These methods include substitution, non-square left-inverse,

and square inverse with NumPy (Damgaard et al. 1992). The matrix methods derive the inverse in the following manner:

$$A^{-1} = \begin{bmatrix} a & b & c \\ d & e & f \\ g & h & i \end{bmatrix}^{-1} = \frac{1}{det(A)} \begin{bmatrix} A & B & C \\ D & E & F \\ H & I & J \end{bmatrix}^{T} = \frac{1}{det(A)} \begin{bmatrix} A & D & G \\ B & E & H \\ C & F & I \end{bmatrix}$$

where:

Table 3.1: Matrix Determinant

A =	(ei - fh)	B =	-(di - fg)
C =	(dh - eg)	D =	-(bi - ch)
E =	(ai - cg)	F =	-(ah - bg)
G =	(bf - ce)	H =	-(af - cd)
I =	(ae- bd)		

and det(A) = aA + bB +cC

2 - Level Energy System

We consider the simplest energy system with molecules entering and exiting only two energy states. If we assume statistical equilibrium, the number entering must equal the number exiting for each state. It is reasonable to assume statistical equilibrium for this system as the number of particles are not drastically changing over time.

Table 3.2: Balancing molecules entering and molecules exiting each state.

State	Entering	Exiting
Ground	$n_1 n_c C_{12}$	$n_2 A_{21} + n_2 n_c C_{21}$
2nd	$n_2 n_c C_{21} + n_2 A_{21}$	$n_1 n_c C_{12}$

The total number of molecules in each state:

$$n = n_1 + n_2 \tag{3.4}$$

First considering these equations in matrix form with $A^{-1}x = B$:

$$\begin{bmatrix} n1 \\ n2 \end{bmatrix} = \begin{bmatrix} n_c C_{12} & -(A_{21} + n_c C_{21}) \\ (A_{21} + n_c C_{21}) & -(n_c C_{12}) \\ 1 & 1 \end{bmatrix}^{-1} \begin{bmatrix} 0 \\ 0 \\ n \end{bmatrix}$$

Immediately it is evident that to include all relevant equations, the coefficient matrix will be non-square. Due to this shape, two different methods were used to deduce the inverse matrix:

- The left inverse matrix $A^{-1}A = I$ was determined with *Python 2.7*,

- One of the state equations was removed, thus forcing the shape to become square. With a square matrix, manual hand calculations can be carried out, or NumPy can be employed to speed up the process. (See Damgaard, et al. 1992)

These two methods were compared; the results were consistent within 5 decimal places. The system of linear equations can also be solved algebraically with the method of substitution.

3 - Energy Level Restricted System

We now consider molecules entering and exiting three levels, with the second and third non-interacting:

Table 3.3: 3-State System - Balancing molecules entering and molecules exiting each state.

State	Entering	Exiting
Ground	$n_1 n_c C_{12} + n_1 n_c C_{13}$	$n_2 A_{21} + n_2 n_c C_{21} + n_3 A_{31} + n_3 n_c C_{31}$
2nd	$n_2 n_c C_{21} + n_2 A_{21}$	$n_1 n_c C_{12}$
3rd	$n_3 n_c C_{31} + n_3 A_{31}$	$n_1 n_c C_{13}$

The total number of molecules in each state:

$$n = n_1 + n_2 + n_3 \tag{3.5}$$

Considering these equations in matrix form $A^{-1}x = B$:

$$
\begin{bmatrix} n1 \\ n2 \\ n3 \end{bmatrix} = \begin{bmatrix} n_c(C_{12} + C_{13}) & -(A_{21} + n_cC_{21}) & -(A_{31} + n_cC_{31}) \\ (A_{21} + n_cC_{21}) & -(n_cC_{12}) & 0 \\ (A_{31} + n_cC_{31}) & 0 & -(n_cC_{13}) \\ 1 & 1 & 1 \end{bmatrix}^{-1} \begin{bmatrix} 0 \\ 0 \\ n \end{bmatrix}
$$

Due to the non-square shape of the coefficient matrix, the same methods as the 2-level system were used to deduce the inverse matrix.

3 - Energy Level Semi-Restricted System

We again consider molecules entering and exiting each level, the second and third now interacting only collisionally (no radiative transfer between states 2 and 3). Considering this, the spontaneous emission terms between levels 2 and 3 will be zero:

Table 3.4: 3-State System - Balancing molecules entering and molecules exiting each state.

State	Entering	Exiting
Ground	$n_1 n_c C_{12} + n_1 n_c C_{13}$	$n_2 A_{21} + n_2 n_c C_{21} + n_3 A_{31} + n_3 n_c C_{31}$
2nd	$n_2 n_c C_{21} + n_2 A_{21} + n_2 n_c C_{23} + n_2 A_{23}$	$n_1 n_c C_{12} + n_3 n_c C_{32} + n_3 A_{32}$
3rd	$n_3 n_c C_{31} + n_3 A_{31} + n_3 n_c C_{32} + n_3 A_{32}$	$n_1 n_c C_{13} + n_2 n_c C_{23} + n_2 A_{23}$

The total number of molecules in each state:

$$n = n_1 + n_2 + n_3 \tag{3.6}$$

Considering these equations in matrix form $A^{-1}x = B$:

$$
\begin{bmatrix} n1 \\ n2 \\ n3 \end{bmatrix} = \begin{bmatrix} n_c(C_{12} + C_{13}) & -(A_{21} + n_cC_{21}) & -(A_{31} + n_cC_{31}) \\ (A_{21} + n_cC_{21}) & -(n_cC_{12}) & n_cC_{32} \\ (A_{31} + n_cC_{31}) & n_cC_{23} & -(n_cC_{13}) \\ 1 & 1 & 1 \end{bmatrix}^{-1} \begin{bmatrix} 0 \\ 0 \\ n \end{bmatrix}
$$

Results from the 2 methods produced results in agreement.

Statistical Equilibrium Results

The results from these systems can be found in Table 3.5. Here, the kinetic temperature was taken as 25.0 K. At this temperature, $A_{21} = 3.458 \times 10^{-3}$ s^{-1}, $A_{31} = 5.593 \times 10^{-2}$ s^{-1}, ortho $C_{12} = 2.97 \times 10^{-10}$ cm^3 s^{-1}, $C_{13} = 1.19 \times 10^{-10}$ cm^3 s^{-1}, $C_{23} = 1.17 \times 10^{-10}$ cm^3 s^{-1}, para $C_{12} = 3.33 \times 10^{-11}$ cm^3 s^{-1}, $C_{13} = 3.41 \times 10^{-11}$ cm^3 s^{-1}, $C_{23} = 1.62 \times 10^{-11}$ cm^3 s^{-1}, corresponding to energies of $E_1 = 23.794$ eV, $E_2 = 42.371$ eV, and $E_3 = 79.496$ eV. It is apparent from the values listed that for a high H$_2$ collider density the population ratios approach those seen in Local Thermodynamic Equilibrium (LTE). This is due to the fact that at this point collisional de-excitation dominates over radiative de-excitation (Spitzer 1978). Population results as derived by RADEX will be compared to that computed by the AMC sub-program of RATRAN in Section §5.4.

Table 3.5: Comparing 2 and 3 Level Radiative Transfer Systems: Water population levels from the above idealized systems.

Model		n_2 / n_1	n_3 / n_1
2 - Level	Para	0.34332794	-
	Ortho	0.34332794	-
3 - Level Restricted	Para	0.34331978	0.06756116
	Ortho	0.34332702	0.06756472
3 - Level Unrestricted	Para	0.34331762	0.06756157
	Ortho	0.343327644	0.06756501
Boltzmann (LTE)		0.34332794	0.06756615

3.1.2 Other Radiative Transfer Equations

In addition to the state equations solved above, the radiative transfer codes consider the following equations in its calculations (Hogerheijde & van der Tak, 2000; van der Tak et al. 2007):

Excitation Temperature T_{ex}:

$$T_{ex} = \left[\frac{-k_B}{E_2 - E_1} \ln \left(\frac{f_2}{f_1} \frac{g_1}{g_2} \right) \right]^{-1} \tag{3.7}$$

where $f_j = n_i/n$, the fractional state population, and g_u and g_u correspond to the statistical weights. Optical Depth τ:

$$\tau_o = \frac{A_{21}}{8\pi\tilde{\nu}^3} \frac{N}{1.065\Delta V} \left[f_1 \frac{g_2}{g_1} - f_2 \right] \tag{3.8}$$

where $\tilde{\nu}$ is the wavenumber, N is the column density, and ΔV is the linewidth. Antenna Temperature T_R:

$$T_R = T(1 - e^{-\tau_\nu}) + T_{bg} e^{-\tau_\nu} \tag{3.9}$$

where τ_ν is the optical depth and T_{bg} is the temperature of the background radiation. Deriving Brightness Temperature T_B beginning with the integrated intensity (Spitzer 1978):

$$\int I_\nu dv = \int \frac{f_u A_{ul} h \nu_{ul}}{4\pi} ds \tag{3.10}$$

where

$$\begin{aligned} n_{u_{H_2O}} &= \frac{n_{u_{H_2O}}}{n_{H_2O}} \frac{n_{H_2O}}{n_{H_2}} n_{H_2} \\ &= \left(\frac{n_u}{n} \right)_{H_2O} \mathcal{X} n_{H_2} \end{aligned} \tag{3.11}$$

substituting to give:

$$\int I_\nu dv = \frac{n_u A_{ul} h \nu_{ul}}{4\pi} \left(\frac{n_u}{n} \right)_{H_2O} \mathcal{X} \int n_{H_2} ds \tag{3.12}$$

where n is the number density of molecules in the indicated state, h is the Planck constant, ν is the frequency, X is the abundance with respect to H_2, n_{H_2} is the density of H_2, and ds is the distance taken along the line of sight. Here,

$$d\nu = dv \frac{\nu}{c} \tag{3.13}$$

where v is velocity and c is the speed of light.

From the Rayleigh-Jeans Approximation,

$$I \equiv \frac{2kT_B}{\lambda^2} \tag{3.14}$$

Letting Eq. 3.12 = Eq. 3.14 and rearranging for the brightness temperature T_B:

$$T_B = \frac{\lambda^2 A_{ul} h\nu_{ul}}{8\pi k_B} \left(\frac{n_u}{n}\right)_{H_2O} \mathcal{X}\mathcal{N}_{H_2} \frac{c}{\nu} \frac{1}{\Delta v} \tag{3.15}$$

where $\mathcal{N}$ is the column density of H_2. To accurately determine antenna temperature with either radiative transfer program (RADEX or RATRAN), we need to know if the considered source would fill the beam (the telescopes field of view). To confirm, we must consider the angular diameter of the region as well as the angular resolution. For NGC 7129 FIRS 2, the diameter of cloud is $d_{cloud} \sim 37200$ AU, and the distance to the cloud is $D_{cloud} = 1250 \pm 50$ pc $= 2.58 \times 10^8 \pm 1.03 \times 10^7$ AU (Shevchenko & Yakubov, 1989). Where D $\gg$ d, the angular diameter of the region θ_{src} is defined as:

$$\begin{aligned}\theta_{src} &= \frac{d_{cloud}}{D_{cloud}} \\ &= 1.44 \times 10^{-4} \pm 2.89 \times 10^{-5} \\ &= 29.76 \pm 5.96''\end{aligned} \tag{3.16}$$

Now estimating angular resolution θ_{beam} considering the diameter of the Herschel Telescope (3.28 m) and a wavelength of 538.3 microns (557 GHz, ground state line frequency of $H_2^{16}O$):

$$\begin{aligned}\theta_{beam} &= 1.22\frac{\lambda}{d} \\ &= 2.00 \times 10^{-4} \\ &= 41.28''\end{aligned} \tag{3.17}$$

From Roelfsema et al. (2011), the beamwidth for Herschel HIFI is more precisely calculated with

$$\begin{aligned}\theta_{beam,R} &= \frac{2}{\pi}(1.6 + 0.021T_e)\frac{\lambda}{D} \\ &= 38.074''\end{aligned} \tag{3.18}$$

where $T_e = 7.94 \pm 0.82$ is the measured edge taper, D (Herschel) = 3.28 m, and λ is the wavelength in m. Considering the above equations and solutions showing $\theta_{src} \geq \theta_{beam}$, our source would not fill the beam completely for the ortho ground state line (1_{10} - 1_{01}, o001). The antenna temperature would therefore not be equivalent to the brightness temperature output by RATRAN and RADEX, and must be calculated for this line. Convolving the brightness temperature T_B to obtain antenna temperature, T_A:

$$
\begin{aligned}
T_A &= \left(\frac{\Omega_s}{\sqrt{\Omega_s^2 + \Omega_b^2}} \right) T_B \\
&= \left(\frac{\theta_s^2}{\sqrt{\theta_s^4 + \theta_b^4}} \right) T_B \\
&= A T_B
\end{aligned}
\tag{3.19}
$$

where Ω_s is the solid angle of the source, Ω_b is the solid angle of the beam, and θ is the angular resolution. This convolution assumes a Gaussian source and Gaussian beam. We will let $A = \theta_s^2 / \sqrt{\theta_s^4 + \theta_b^4}$ for simplicity. This value is calculated for each of the water lines included in this work and tabulated in Table 3.6, alongside calculated beamwidths of both Equations 3.17 and 3.18. Considering this with RATRAN, once the ray-tracing sub-program SKY is executed, the output brightness temperature is convolved to obtain spectra in terms of antenna temperature. During this process, the continuum generated by hot dust temperatures in the model file is removed by averaging the first and last channels, then subtracting this value from each of the channels. The baseline value removed for each water line is also tabulated in Table 3.6.

Finally, the RADEX program defines Flux (F) (ergs/cm^2/s) as:

$$
F = 1.0645 \cdot 8\pi k_B \Delta v T_A \tilde{\nu}^3
\tag{3.20}
$$

and flux in terms of K km/s:

$$
F = 1.0645 \cdot \Delta V T_A
\tag{3.21}
$$

The goodness of fit of the final RATRAN modelling results will be calculated using the chi-squared test χ^2:

$$\chi^2 = \sum_{i=1}^{N} \frac{(T_{A,HIFI_i} - T_{A,RATRAN_i})^2}{\sigma^2} \qquad (3.22)$$

while the reduced chi-square χ_R^2 can be calculated from:

$$\chi_R^2 = \frac{\chi^2}{\nu} \qquad (3.23)$$

where ν is the degrees of freedom, equal to the number of evaluated points minus the number of varied parameters. Seen later, chi-square grid models alter 2 parameters while holding the others constant. The standard deviation σ is taken as the HIFI RMS noise. A statistical probability parameter p called the p-value will then be computationally determined. The p-value is used to determine the confidence of the model; a small p-value (typically ≤ 0.05) indicates strong evidence against the null hypothesis, so it is ruled out. A large p-value (> 0.05) indicates weak evidence against the null hypothesis, so you fail to reject the null hypothesis. In other words, the p-value gives the significance of the reduced chi-squared.

3.2   Results

A comparison was made between the manual calculations above and RADEX output; the RADEX input used can be found in Table 3.7 and the output can be found in Table 3.8. These results use an H_2 ortho-to-para ratio that is built-in to the code; this takes the form of the LTE ortho-to-para ratio seen plotted in Figure 4.34 later in this work. A summary of the numerical comparison can be found in Table 3.9. The majority of calculated parameters are remarkably in agreement, save for the upper and lower populations. The manual calculations were carried out with non-square idealized systems of equations, so the differences of 7.5% (upper population) and 3.5% (lower population) are acceptable. Additionally, population levels in the manual calculations are very approximate since it is assumed that there are only a few possible levels; a perfect match is not expected.

Table 3.6: Herschel HIFI beamwidths for various water lines. Classically derived θ_{beam} given in radians and arcseconds, Roelfsema et al. (2011) $\theta_{beam,R}$ given in arcseconds. Whether the source fills the beam for each water line is indicated by (Y/N) under 'Fill'. A is the convolution factor between brightness temperature and antenna temperature, using the Roelfsema beamwidths. The continuum baseline removed from the RATRAN antenna temperature after convolution is also listed.

Molecule	Line	ν (GHz)	λ (10^{-4} m)	θ_{beam} (10^{-4} rad)	θ_{beam} ($''$)	$\theta_{beam,R}$ ($''$)	Fill (Y/N)	A	RATRAN Baseline (K)
	o001	557	5.38	2.00	41.276	38.074	N	0.121	2.871×10^{-2}
	o006	1153	2.59	0.96	19.871	18.389	Y	0.465	1.616×10^{-1}
$H_2^{16}O$	o007	1097	2.73	1.02	20.945	19.323	Y	0.427	1.484×10^{-1}
	p001	1113	2.69	1.00	20.638	19.046	Y	0.437	1.522×10^{-1}
	p002	988	3.03	1.13	23.246	21.464	Y	0.358	1.221×10^{-1}
	p004	752	3.98	1.48	30.535	28.197	Y	0.217	6.643×10^{-2}
	o001	547	5.47	2.03	41.966	38.718	N	0.117	2.784×10^{-2}
$H_2^{18}O$	p002	996	3.01	1.12	23.093	21.318	Y	0.362	1.479×10^{-1}
	o007	1095	2.73	1.02	20.945	19.354	Y	0.427	1.235×10^{-1}

Table 3.7: Example Input Variables used with RADEX

Variable	Label	Value
Kinetic Temperature	T_{kin}	25.0 K
Depth into Molecular Cloud	ds	1.496×10^{15} cm
Abundance of Water	X	10^{-8}
Number Density of Water	n_{H_2O}	1.0
Column Density of Water	N_{H_2O}	1.496×10^{16} cm^{-2}
Number Density of Collider H_2	n_{H_2}	10^8
Column Density of Collider H_2	N_{H_2}	1.496×10^{22} cm^{-2}
Wavelength	λ	0.05 cm
Line Width	ΔV	1.00 km s^{-1}

Table 3.8: RADEX Output using Input from Table 3.7

Variable	Label	Value
Line Transition		1_{10} - 1_{01}
Line Upper Level Energy	E_{up}	61.0 K
Frequency	ν	556.9361 GHz
Wavelength	λ	538.2888 μm
Excitation Temperature	T_{ex}	2.419×10^1 K
Optical Depth	τ	1.451×10^2
Radiation Temperature	T_R	1.323×10^1 K
Population in Upper Level	n_{up}	2.382×10^{-1}
Population in Lower Level	n_{low}	7.191×10^{-1}
Flux	F	1.409×10^1 K km/s
Flux	F	$3.134E \times 10^{-5}$ erg/cm^2/s

Table 3.9: Summary of Radex Calculations vs. Manual Calculations. From this table it is seen that the values are mostly in agreement.

Parameter	RADEX	Manual
T_{ex}	2.419×10^1K	2.419×10^1 K
τ	1.451×10^2	1.450×10^2
T_R	1.323×10^1 K	1.373×10^1 K
Pop_{up}	2.382×10^{-1}	Ortho: 2.556×10^{-1}
		Para: 2.556×10^{-1}
Pop_{low}	7.191×10^{-1}	Ortho: 7.444×10^{-1}
		Para: 7.444×10^{-1}
Flux	1.409×10^1 K km/s	1.408×10^1 K km/s
Flux	3.134×10^{-5} erg/cm^2/s	3.133×10^{-5} erg/cm^2/s

Chapter 4

RATRAN Modelling

We learn a great deal about star formation regions from their molecular line spectra. The 1D Monte Carlo radiative transfer code RATRAN (Hogerheijde & van der Tak, 2000) was developed to model the line spectra of the dense and cool interstellar medium via rotational radiative transfer (see Chapter §3) and molecular excitation calculations. This code is only capable of modelling protostellar envelopes - the outflow is not taken into consideration. As such, models produced by RATRAN can be compared to the envelope contribution of an observed spectral line (usually in the form of a Gaussian spectral fit). Deductions about the physical parameters of the envelope can be made from the best fit model; if a single model fits multiple radiative transitions of a molecule, in this case $H_2^{16}O$ or $H_2^{18}O$, constraints can be placed on these parameters. This is the ultimate goal.

Section §4.1 outlines how this radiative transfer program works, the limitations of RATRAN are given in §4.2, and the RATRAN modelling approach is detailed in §4.3. Finally, the RATRAN modelling results for NGC 6334 I(N) and NGC 7129 FIRS 2 can be found in §4.4 and §4.5 respectively. Modelling of NGC 6334 I(N) is conducted in order to solidify confidence in the RATRAN results of NGC 7129 FIRS 2.

4.1   How does RATRAN work?

RATRAN input models vary parameters in a spherical shell manner. The number of spherical shells may be altered; this work generally uses 22 shells, but also briefly investigates the effects of increasing to 42 and 62 shells. The optimal number of shells has been investigated by Hillier (2008); he suggested that while increasing the number of spherical

shells increases the precision of the resultant spectral line, the time required to run a single model also increases. The number 22 was selected as it optimizes both precision and computational time. Refer to Section §4.5.7 for further details on shell number.

Within RATRAN model shells, the following parameters are varied: the density of an exciting collider (n_{H_2}, ortho and para H_2), the density of a modelled species (n_{H_2O}, $H_2^{18}O$ and $H_2^{16}O$), dust temperature (T_d), kinetic temperature of both colliders (T_g), turbulent velocity (in the form of the Doppler broadening parameter b), and lastly the radial velocity (vr).

Collision rates obtained from Daniel et al. (2011) work together with the above RATRAN input to generate energy level populations in each of the spherical shells through the excitation solver Fortran program "AMC". This is unlike the majority of the previous intermediate-mass studies; these instead scaled helium collision rates from Green et al. (1993) to model collisions with H_2O. Refer to Section §4.5.9 for more on the effects of Collision Rates on spectral line modelling. AMC runs through the radiative transfer calculations given in §1.5 and §3. As so eloquently explained in Tisi (2013), this program initially estimates the level populations based on the input, then randomly assigns N number of photons to each radial shell. The photons are given a random frequency ν_r as $|\nu_0 - \nu_r| \leq 4.3b$, where b is the turbulent velocity defined above. A mean radiation field J_ν is calculated for each shell by summing attenuated rays along the shell boundaries, where ds is the distance from the origin of a ray to the shell boundary. These rays change direction randomly with each new shell. The mean radiation field is then used to calculate shell population. This changes emission and absorption rates and how rays are attenuated along the path to the next shell. The program alternates between J_ν and level population until the population difference between iterations is $\leq 10^{-6}$. This process is repeated until the level populations converge to a user-defined accuracy. In this process, both molecules and dust particles are considered as sources of emission and absorption, but scattering is ignored.

An example population output from AMC for n = 1, 2, 3, and 6 is plotted for both ortho and para $H_2^{18}O$ in Figure 4.1. Also plotted here is the freeze-out temperature, indicated by the black vertical dashed line. Colder regions have a higher fractional population for the ground state. As the temperature rises moving inward through the molecular cloud, the excited states increase in population. At ~ 250 K, most of the plotted populations sit around a fractional population of 0.1. Fractional population should always sum to 1.0; thus, this plot indicates that water is in a state higher than those plotted here in the inner envelope regions. This is the result of the final RATRAN model ($\alpha = 1.5$) for $H_2^{18}O$.
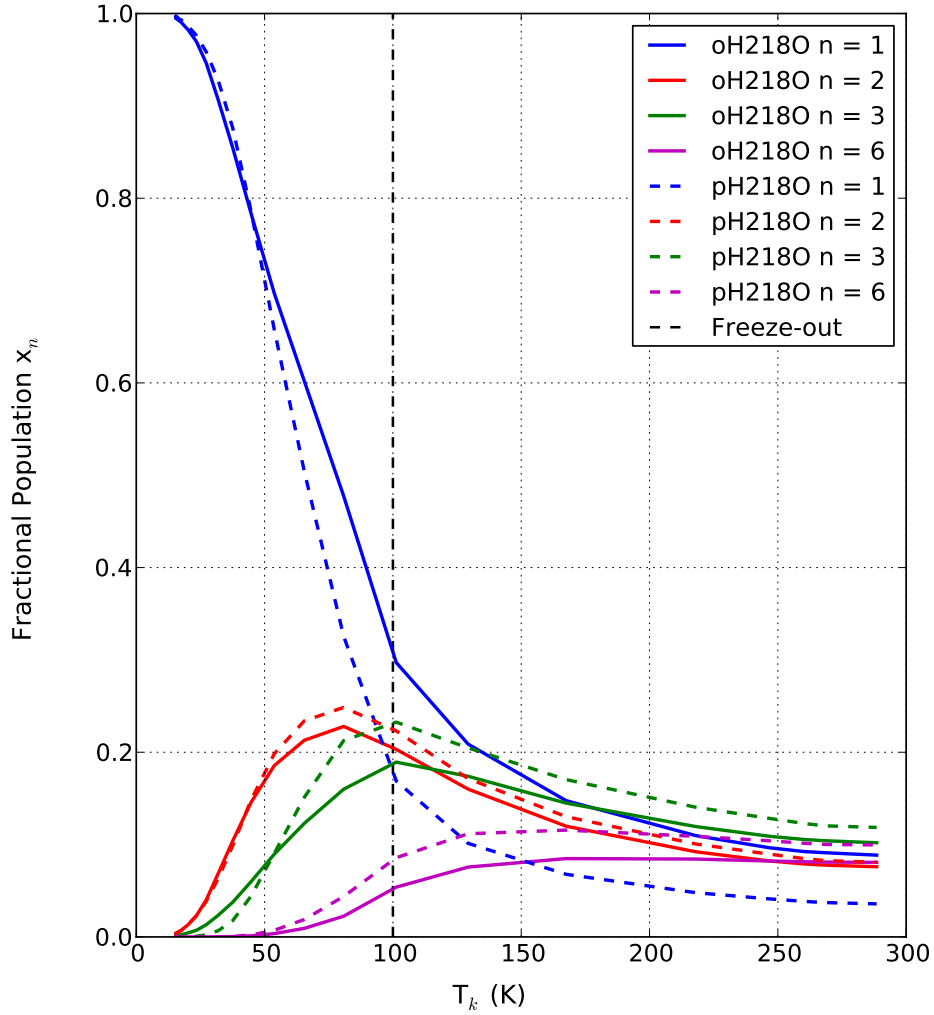
Figure 4.1: Fractional Population for H$_2^{18}$O as determined by RATRAN program AMC (n = 1, 2, 3, 6) for both ortho and para. n = 1 (blue), n = 2 (red), n = 3 (green), n = 6 (magenta). Freeze-out temperature is indicated by the vertical black dashed line. Colder regions (outer envelope) have a higher fractional population in the n = 1 ground state. As the temperature rises, moving inward through the envelope, the excited states increase in fractional population. By 250 K, most population levels plotted bounce around a population level of 0.1. Fractional population should always sum to 1.0; thus, this plot indicates that water is in a state other than those plotted here in the inner envelope regions. This AMC output is taken as input for the ray-tracer RATRAN program SKY.

The calculated AMC stellar envelope level populations are passed to the ray tracer Fortran program "SKY", which then produces line emission images based on input radiative transitions. More specifically, SKY outputs the brightness temperatures at different velocity slices into a FITS (Flexible Image Transfer System) image, containing 2 spatial dimensions and 1 velocity dimension. The SKY output images are then convolved with an additional program (written by Michel Fich) using HSO beamsizes (Roelfsema et al. 2012) for each respective transition. As previously mentioned, continuum baselines are subtracted in this convolution routine and are given in Table 3.6 for each transition. The resultant files are then passed to Python, where the simulated spectra are plotted.

4.1.1 Foundation RATRAN Models

In this particular work, a subset of the RATRAN input parameters are pre-defined and held constant. For NGC 7129 FIRS 2, the H_2 density (on_{H_2} and pn_{H_2}) and temperature (T_g and T_d) are obtained from a DUSTY model generated by Crimier et al. (2010) based on SCUBA continuum observations. This yields a best fit density power law index of $\alpha = 1.4$, although some calculations in this thesis model $\alpha = 1.5$. See Figure 4.7 for the Crimier et al. density and temperature model ($\alpha = 1.5$) and section §4.1.2 for a detailed explanation regarding the transition from DUSTY model to RATRAN model. For modelling of the high-mass star formation region NGC 6334 I(N), the density and temperature profile is extracted from van der Tak et al. (2013). The gas temperature T_g is taken to equal the dust temperature T_d for both sources. It was recently suggested that a higher gas temperature (perhaps 1.10 T_d) could be possible. This is further investigated in Section §4.5.5.

4.1.2 DUSTY Model to RATRAN Model

The Crimier et al. (2010) spherical envelope model for NGC 7129 FIRS 2 is labelled in this work as "B3". This DUSTY model has an inner radius $r_i = 1.496 \times 10^{15}$ cm (100 AU), outer radius r_o at 180 r_i, optical depth of $\tau = 2.3$ at 100 microns, and a power-law index α of 1.4. A power-law index of $\alpha = 1.5$ is also investigated; this is the isothermal model that is often invoked. Alongside these values, a gas to dust ratio of 100 and an opacity κ of 86.5 cm^2/g (100 μm) are assumed. Densities for H_2 can be calculated from DUSTY model parameters for use in RATRAN, and are derived like so: assuming the density in a spherical envelope follows a power law,

$$\rho_{dust} = \rho_0 r^{-\alpha} \tag{4.1}$$

Then the optical depth through the center of the spherical cloud is

$$
\begin{aligned}
\tau_\nu &= \int_{r_i}^{r_o} \rho_{dust} \kappa_\nu dr \\
&= \int_{r_i}^{r_o} \rho_0 r^{-\alpha} \kappa_\nu dr \\
&= \kappa_\nu \rho_0 \left[\frac{r^{-\alpha+1}}{-\alpha + 1} \right]_{r_i}^{r_o} \\
&= \frac{\kappa_\nu \rho_0}{-\alpha + 1} [r_o^{1-\alpha} - r_i^{1-\alpha}] \\
&= \frac{\kappa_\nu \rho_0}{\alpha - 1} [r_i^{1-\alpha} - r_o^{1-\alpha}]
\end{aligned}
\tag{4.2}
$$

where κ_ν is the absorption coefficient; a typical value at 100 microns is 86.5 cm^2 g^{-1}. The final line in derivation 4.2 can then be used to extract the density power law ρ_0 above. Rearranging,

$$
\rho_0 = \frac{\tau_\nu (\alpha - 1)}{\kappa_\nu} \frac{1}{r_i^{1-\alpha} - r_o^{1-\alpha}}
\tag{4.3}
$$

The density profile for molecular hydrogen can then be obtained from assuming a constant gas to dust mass density ratio, usually designated R and typically with a value of 100:

$$
\rho_{hydrogen} = R \rho_{dust}
\tag{4.4}
$$

Considering this, the molecular hydrogen density can be written as

$$
\rho_{H_2} = \frac{\rho_{hydrogen}}{2 m_H}
\tag{4.5}
$$

where m_H is the hydrogen mass (each molecule of H_2 weighs $2m_H$). Substituting previous Equations 4.4, 4.1, and 4.3, then simplifying, we derive an expression for ρ_{H_2}:

$$
\begin{aligned}
\rho_{H_2} &= \frac{\rho_{hydrogen}}{2m_H} \\
&= \frac{R\rho_{dust}}{2m_H} \\
&= \frac{R\rho_0 r^{-\alpha}}{2m_H} \\
&= \frac{Rr^{-\alpha}}{2m_H} \frac{\tau_\nu(\alpha-1)}{\kappa_\nu} \frac{1}{r_i^{1-\alpha} - r_o^{1-\alpha}} \\
&= \frac{R}{2m_H} \frac{\tau_\nu(\alpha-1)}{\kappa_\nu} \frac{r^{-\alpha}}{r_i^{1-\alpha} - r_o^{1-\alpha}} \ (\mathrm{cm}^{-3})
\end{aligned} \tag{4.6}
$$

where as mentioned, $R = 100$, $m_H = 1.67 \times 10^{24}$ g, $\tau_\nu(100\mu m) = 2.3$, $\alpha = 1.4$, $\kappa_\nu = 86.5$ cm^2 g^{-1} (100 μm), $r_i = 1.496 \times 10^{15}$ cm, $r_o = 180r_i$, and r is the shell radius.

The calculated radial number density is divided between ortho and para H$_2$ depending on the ortho-to-para ratio; in this work, it was usually taken as 3:1. A varying ortho-to-para ratio is also considered. These ortho and para H$_2$ radial number densities are taken as RATRAN input. The number density of the modelled species, H$_2^{16}$O and H$_2^{18}$O, are taken as a fractional abundance of the total H$_2$ density (sum of ortho and para), ranging anywhere from 10^{-4} – 10^{-11}n$_{H2}$. This will be described in §4.5. Lastly, the radial dust and gas temperatures are taken directly from the B3 DUSTY model, and the velocity field is user-defined. The RATRAN input column identifiers are summarized in Table C.1 of Appendix C.

4.2 Limitations

While RATRAN is a helpful tool when studying star forming molecular clouds, it doesn't come without limitations. This radiative transfer code assumes spherical symmetry due to its one-dimensional nature. It also assumes statistical equilibrium. This isn't necessarily applicable to all molecular clouds; depending on the stage of evolution, the cloud may be expanding or contracting. The envelope region of the molecular cloud could be increasing in temperature, or the local chemistry could be out of equilibrium. Additionally, the AMC subroutine considers both molecules and dust particles as sources of emission and absorption, but ignores scattering. Finally, RATRAN does not account for external radiation fields.

4.3   Modelling Approach: NGC 7129 FIRS 2

The RATRAN modelling process begins with the 547 GHz ground state ortho 1_{10} - 1_{01} line of $H_2^{18}O$. Considering the ratio of O^{16}/O^{18} and the upper abundance limit of oxygen with respect to H_2, we are able to make some initial water abundance estimates. An ortho to para ratio of 3:1 is assumed for the most part, although a temperature dependent ratio is also considered. Because of the relatively young age of the studied protostars, we expect the cloud to be either completely or partially infalling, allowing an initial estimate for the radial velocity to be a negative value ranging between 0 and the free-fall velocity towards a central mass. We also estimate an initial value for the turbulent velocity based on the width of the Gaussian fitted to the spectral line envelope component. Additionally, the envelope is segmented into two regions by a freeze-out radius; we expect water to freeze-out onto dust grains at 100 K. Radii interior to this radius is considered the "inner" envelope and radii exterior are considered the "outer" envelope.

The derived $H_2^{18}O$ model is then applied to the ground state 1_{10}-1_{01} 557 GHz line of ortho-$H_2^{16}O$ by multiplying the molecular density by an abundance ratio of 550 (or less if deemed necessary by RATRAN modelling results). The additional water transitions are modelled simultaneously with the ground state line for each molecule.

Within the above modelling process, specific input parameters are varied to determine their effect. The abundance ratio is investigated in §4.5.2, the radial velocity is investigated in §4.5.3, water abundance is detailed in §4.5.1, and the turbulent velocity is investigated in §4.5.4. Additional RATRAN models are produced to test the effects of altering the dust temperature (Crimier et al. 2010; §4.5.5), Freeze-out radius (§4.5.6), number of spherical shells (Hillier 2008; §4.5.7), ortho-to-para ratio (§4.5.8), and finally the collision rates (Daniel et al. 2011; §4.5.9).

Considering that multiple parameters contribute to the spectral line in the same manner (i.e, both the abundance and the radial velocity increase or decrease the amplitude) potential degeneracy in the models must be identified. To do this, hundreds of RATRAN models are run in a grid manner, investigating 2 input parameters at a time. A chi-squared test (Equation 4.7) is then applied to each model, measuring the goodness of fit to the observational data.

$$\chi_R^2 = \sum_{i=1}^{N} \frac{(T_{A,HIFI_i} - T_{A,RATRAN_i})^2}{\nu \sigma^2} \tag{4.7}$$

Here, T_{ratran} is the antenna temperature modelled by RATRAN, T_{obs} is the antenna temperature as measured by HIFI, ν is the degrees of freedom (number of data points minus

the number of varied parameters), and σ is the noise as listed in Table 2.4. Grids are typically created to aid the investigator in visualizing the results and making the dependence of the fit on various parameter selections more obvious. This allows constraints to be placed on the physical structure of the modelled molecular cloud.

Once an acceptable model is produced for $H_2^{18}O$, it is applied to $H_2^{16}O$ by multiplying by an abundance ratio. If the initial RATRAN result for $H_2^{16}O$ isn't a good enough fit, the above parameters are adjusted until an acceptable fit is obtained. In order to achieve this, the abundance ratio may have to be lowered from 550.

4.4 NGC 6334 I(N): a High-Mass Young Stellar Object

Table 4.1: NGC 6334I(N) source data. Obtained from van der Tak et al. (2013), Herpin et al. (2016), Sandell (2000), and Neckel (1978).

RA (J2000.0) (h m s)	17 20 55.2
Dec ($° \prime \prime\prime$)	-35 45 04
V_{LSR} (km s^{-1})	-3.3 km s^{-1}
$L_{bol}(L\odot)$	1.9×10^3
M_{env} (M$\odot$)	3826
d (kpc)	1.7

Often in astronomy, one looks to literature for motivation and validation. For increased confidence in the modelling process of this thesis, a literature review was conducted for water in high mass protostars. Through this review, it was determined that Herpin et al. (2016) also observed with the Heterodyne instrument for the Far-Infrared (HIFI) and used the Daniel et al. (2011) collision rates with the 1D radiative transfer code RATRAN (Hogerheijde & van der Tak, 2000). They also modelled both of the isotopologues studied in this thesis, $H_2^{18}O$ and $H_2^{16}O$.

Herpin et al. (2016) studied many HM sources; of these, their RATRAN model for NGC 6334 I(N), a mid-IR quiet high mass protostellar object, is replicated in this thesis. The main goal of this exercise is to reproduce the same emission features, absorption features, and asymmetries seen in their molecular line observations of water. The source data is given in Table 4.1, the transition lines studied are listed in Table 4.2, and the Gaussian fits are listed in Table 4.3. Note that the authors do not supply Gaussian amplitudes.

The Herpin et al. NGC 6334 I(N) envelope model is obtained via visual inspection of van der Tak et al. (2013) Figure C3 (Figure 4.2 of this work). It must be emphasized that this is done quite manually by visually extracting 22 values from the figure. Model parameters can be found in Table 4.4, obtained from Herpin et al. (2016). The extracted van der Tak NGC 6334 I(N) density and temperature model is plotted in Figure 4.3 and Table 4.5. From the slope of the plotted line, the density power law is determined to have an index of $\alpha = 1.3$. Their resultant RATRAN models (with added outflow contribution) are plotted in Figure 4.4. Here, the main isotopologue $H_2^{16}O$ is plotted in the right-side panels and $H_2^{18}O$ is plotted in the bottom left-side panels. These authors also model a third water isotopologue, $H_2^{17}O$. The intensity and width measurements associated with the Herpin et al. RATRAN model line spectra are listed in Table 4.6. These were obtained via inspection.

Different to the methods in this work, Herpin et al. keep the continuum (although they smooth to a factor of 0.2 and scale by 0.5) and add a outflow Gaussian contribution to their RATRAN envelope model. Their outflow parameters (intensity and width) come from the Gaussian fitting. Herpin et al. determined a best fit for the total line intensity by adjusting a combination of the abundance, turbulence, and outflow parameters. Similar to this thesis, their models assume an abundance jump at 100 K.

To begin the replication of their simulated spectral lines, the van der Tak envelope model is input into AMC. The eventual output from SKY is convolved with the HIFI beamsizes that were determined before launch. The final RATRAN results for this are plotted in Figure 4.5. By inspection it is seen that these results are similar to that in Herpin et al. (2016) (Figure 4.4). To go one step further, the same broad Gaussian components used in Herpin et al. (2016) (Table 4.3) are then added to the RATRAN models to further compare the two sets of results (Figures 4.6). The Gaussians are plotted with the supplied full-width half-max (FWHM) values and their positions v_{LSR} in the following manner:

$$f(x) = \frac{1}{\sigma\sqrt{2\pi}} \exp\left[\frac{-1}{2}\left(\frac{x-\mu}{\sigma}\right)^2\right] \tag{4.8}$$

where $\sigma \sim$ FWHM/2.355 and $\mu = v_{LSR}$. This function was scaled for each water line to match that plotted in Figure 4.4.

Table 4.2: Herschel HIFI observed water line transitions in NGC 6334 I(N).

Molecule	Line	ν (GHz)	Beam ('')
$H_2^{16}O$	p 111-000	1113.343	21.7
	o 110-101	556.936	43.5
	p 202-111	987.927	24.5
	o 212-101	1669.91	20.8
	p 211-202	752.033	32.2
	o 312-303	1097.37	22.1
$H_2^{18}O$	p 111-000	1101.70	21.7
	o 110-101	547.676	43.5
	p 202-111	994.675	24.5
	o 312-303	1095.63	22.1

Table 4.3: NGC 6334 I(N) Gaussian Components from Herpin et al. (2016). V is the Gaussian component peak velocity. ΔV is the velocity full width at half maximum (FWHM) of the narrow, medium, and broad components. [a] indicates absorptions.

Line	V_{nar}	ΔV_{nar}	V_{med}	ΔV_{med}	V_{broad}	ΔV_{broad}
$pH_2^{16}O$ 111-000			-3.9 ± 0.2^a	6.1 ± 0.3	-3 ± 2	30 ± 1
$oH_2^{16}O$ 110-101			-3.5 ± 0.1^a	5.8 ± 0.2	-2.0 ± 0.2	26.1 ± 0.6
$pH_2^{16}O$ 202-111	-3.0 ± 0.1^a	3.1 ± 0.1	-3.0 ± 0.2^a	10.0 ± 0.3	-5.7 ± 0.2	29.6 ± 0.5
$oH_2^{16}O$ 212-101			-3.9 ± 0.2^a	6.8 ± 0.4		
$pH_2^{16}O$ 211-202			-3.2 ± 0.1^a	7.3 ± 0.3	-4.4 ± 0.2	29.4 ± 0.7
$oH_2^{16}O$ 312-303			-1.9 ± 0.1^a	9.6 ± 0.3	-6.1 ± 0.3	27.6 ± 0.6
$pH_2^{18}O$ 111-000	-2.9 ± 0.2^a	4.5 ± 0.2				
$oH_2^{18}O$ 110-101			-3.8 ± 0.4^a	6 ± 1		
$oH_2^{18}O$ 312-303			-3.9 ± 0.4	6 ± 1		
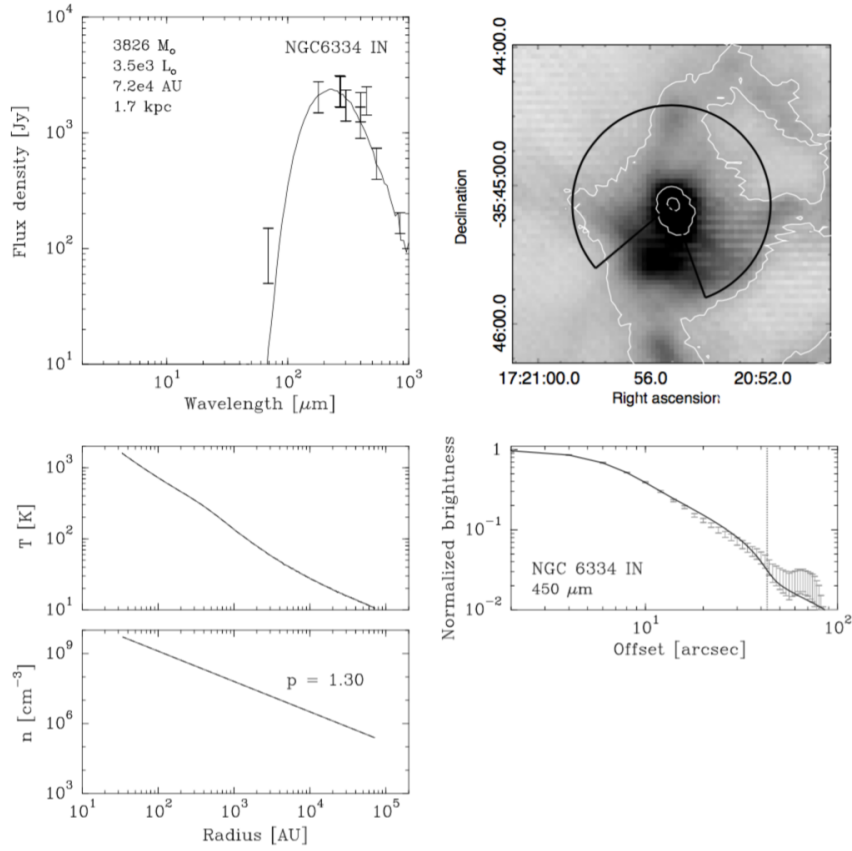
Figure 4.2: Figure C3 from van der Tak et al. (2013). Continuum model for NGC6334I(N). Top left: Spectral energy distribution. Top right: sub-millimeter image with 3σ contour marked in white and usable map sectors marked in black. Bottom left: Temperature and density structure as a function of radius. Bottom right: sub-millimeter emission profiles. The numbers in the top left panel are the modelled envelope mass, the modelled luminosity, the adopted envelope size, and the adopted distance. Values for the density and temperature with respect to radius were extracted from the bottom left manually.
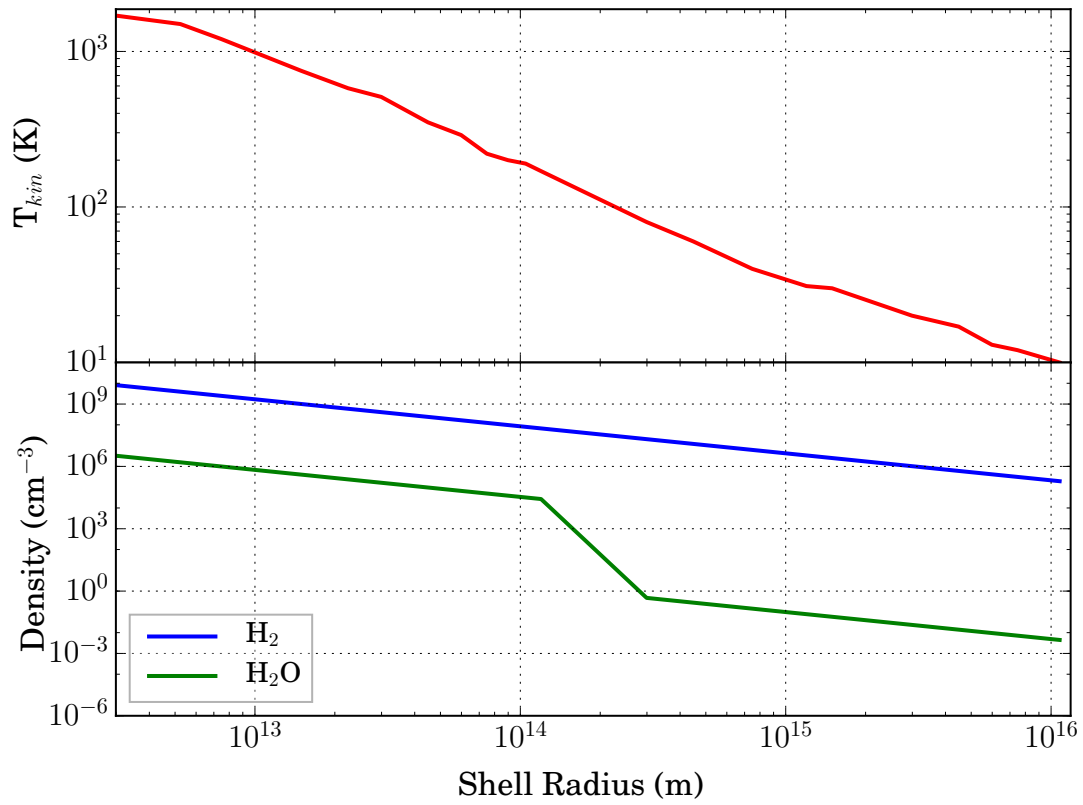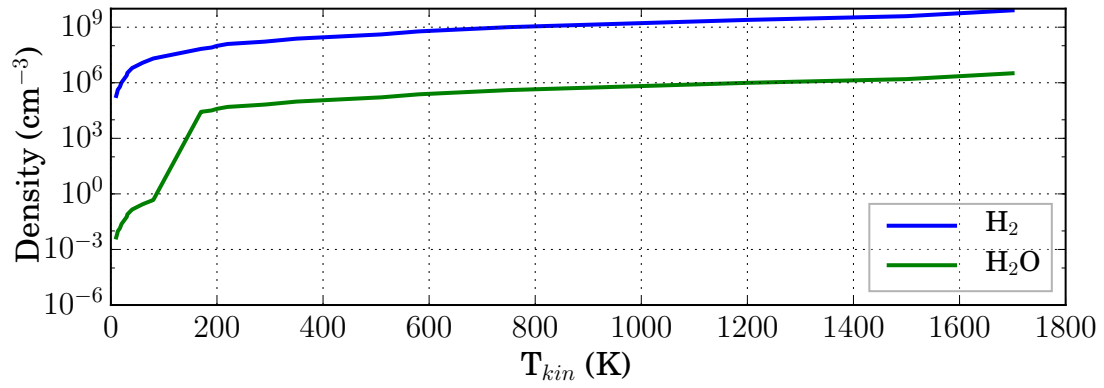
Figure 4.3: NGC 6334 I(N): RATRAN Density & Temperature Profile, obtained by eye from Figure 4.2. From the slope of the density line, $\alpha = 1.3$.

Table 4.4: NGC 6334I(N) Model Parameters from Herpin et al. (2016)

Model Parameter	Value
Infall Velocity	-0.7
Turbulent Velocity	2.5 km s^{-1}
Inner X_{H_2O}	0.4E-5
Outer X_{H_2O}	2.3E-8

Table 4.5: NGC 6334I(N) temperature and density profile from van der Tak et al. (2013) and turbulent velocity from Herpin et al (2016). Derived H$_2^{16}$O and H$_2^{18}$O abundances (n(H$_2^{18}$O) = n(H$_2^{16}$O)/550). Used as RATRAN input.

Radius (m)	T (K)	n_{H_2} (cm^{-3})	V_{turb} (km s^{-1})	$n_{H_2^{18}O}$ (cm^{-3})	$n_{H_2^{16}O}$ (cm^{-3})
2.992E12	1.7E3	8.0E9	2.0	5.92E3	3.26E6
7.480E12	1.2E3	4.0E9	2.0	2.86E3	1.57E6
1.496E13	6.0E2	1.0E9	2.0	1.80E3	9.90E5
2.244E13	5.5E2	7.0E8	2.0	7.31E2	4.02E5
2.992E13	5.1E2	6.8E8	2.0	4.31E2	2.37E5
4.488E13	3.5E2	6.0E8	2.0	2.97E2	1.63E5
5.984E13	2.9E2	3.0E8	2.0	1.75E2	9.64E4
7.480E13	2.2E2	1.1E8	2.0	1.21E2	6.63E4
8.976E13	2.0E2	1.0E8	2.0	9.02E1	4.96E4
1.047E14	1.9E2	9.0E7	2.0	7.11E1	3.91E4
1.197E14	1.7E2	8.0E7	2.0	5.82E1	3.20E4
2.992E14	8.0E1	5.0E7	2.0	4.89E1	2.69E4
4.488E14	6.0E1	2.0E7	2.5	8.55E-4	4.70E-1
7.480E14	4.0E1	1.0E7	3.0	5.05E-4	2.78E-1
1.197E15	3.1E1	8.0E6	3.0	2.60E-4	1.43E-1
1.496E15	3.0E1	5.0E6	3.0	1.41E-4	7.76E-2
2.992E15	2.0E1	2.0E6	3.0	1.10E-4	5.80E-2
4.488E15	1.7E1	9.0E5	3.0	4.29E-5	2.36E-2
5.984E15	1.3E1	8.0E5	3.0	2.53E-5	1.39E-2
7.480E15	1.2E1	7.0E5	3.0	1.74E-5	9.57E-3
1.077E16	1.0E1	5.0E5	3.0	1.30E-5	7.16E-3
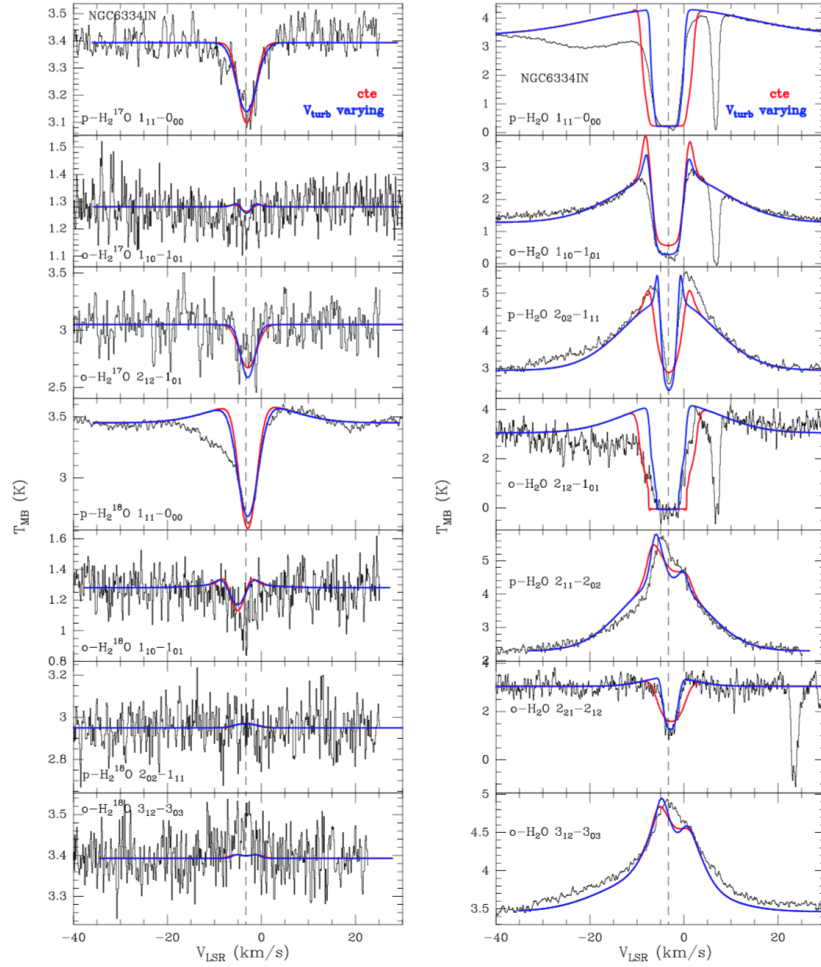
Figure 4.4: Figure 2 from Herpin et al. (2016). NGC 6334I(N) HIFI Spectra of $H_2^{17}O$ and $H_2^{18}O$ (left) and $H_2^{16}O$ (right) in black with continuum. Red lines correspond to models with constant parameters for infall and turbulent velocity = 2.5 km s^{-1}, the former outlined in Table 4.4. Blue lines correspond to models with varying turbulent velocities, outlined in Table 4.4. It must be noted that the models also include derived outflow data, not included in the scope of this thesis. Vertical dotted line indicates V_{LSR} = -3.3 km s^{-1}. Spectra have been smoothed to 0.2 km s^{-1} and the continuum divided by a factor of two. Evidence of foreground cloud seen in pH$_2$O 1$_{11}$-0$_{00}$, oH$_2$O 1$_{10}$-1$_{01}$, oH$_2$O 2$_{12}$-1$_{01}$, and oH$_2$O 2$_{21}$-2$_{12}$. Ground state lines are deeply absorbed. Blue asymmetries (i.e, inverse P-cygni profiles) seen in pH$_2$O 2$_{02}$-1$_{11}$ and pH$_2$O 2$_{11}$-2$_{02}$.

Table 4.6: Herpin et al. (2016) RATRAN spectral fits - intensities and widths for ortho and para $H_2^{18}O$ and $H_2^{16}O$, as determined by visual inspection. Asymmetry is listed as 'B' blueshifted or 'R' redshifted; those marked with * are just slight asymmetries. ΔT_{abs} indicates the full absorption depth; in the case of asymmetries, depth with respect to each emission peak is given.

Molecule	Transition	T_{peak} (K)	ΔV (km s^{-1})	Asymmetry	ΔT_{abs} (K)
$H_2^{16}O$	p 1_{11} - 0_{00}	0.8	70	-	4.1
	o 1_{10} - 1_{01}	2.15	45	B*	3.15
	p 2_{02} - 1_{11}	2.45	50	-	3.15
	o 2_{12} - 1_{01}	1.25	30	-	4.25
	p 2_{11} - 2_{02}	3.5	50	B	1.4/0.2 (B/R)
	o 2_{21} - 2_{12}	0.25	15	-	2.0
	o 3_{12} - 3_{03}	1.45	50	B	0.5/0.1 (B/R)
$H_2^{18}O$	p 1_{11} - 0_{00}	0.1	45	-	0.9
	o 1_{10} - 1_{01}	0.025	15	-	0.15
	p 2_{02} - 1_{11}	0.025	10	-	-
	o 3_{12} - 3_{03}	0.01	8	-	0.005

Table 4.7: Herschel HIFI observed water line transitions in NGC 6334 I(N). Convolution of RATRAN output with HIFI beam size uses the baseline removal seen below. Ray tracer SKY yields the opacity τ and line intensity before convolution.

Molecule	Line	ν	Beam	Baseline	τ	Intensity
		(GHz)	('')	(K)		(K)
$H_2^{16}O$	p 111-000	1113.343	21.7	1.8921	951.5	0.22
	o 110-101	556.936	43.5	0.6015	399.2	1.17
	p 202-111	987.927	24.5	1.6587	65.72	0.57
	o 212-101	1669.91	20.8	1.9657	2.04	24.45
	p 211-202	752.033	32.2	1.1084	37.46	3.96
	o 312-303	1097.37	22.1	1.8565	5.32	10.82
$H_2^{18}O$	p 111-000	1101.70	21.7	1.8921	2.67	4.04
	o 110-101	547.676	43.5	0.6015	1.21	9.08
	p 202-111	994.675	24.5	1.6587	0.25	23.23
	o 312-303	1095.63	22.1	1.8565	0.46	22.23
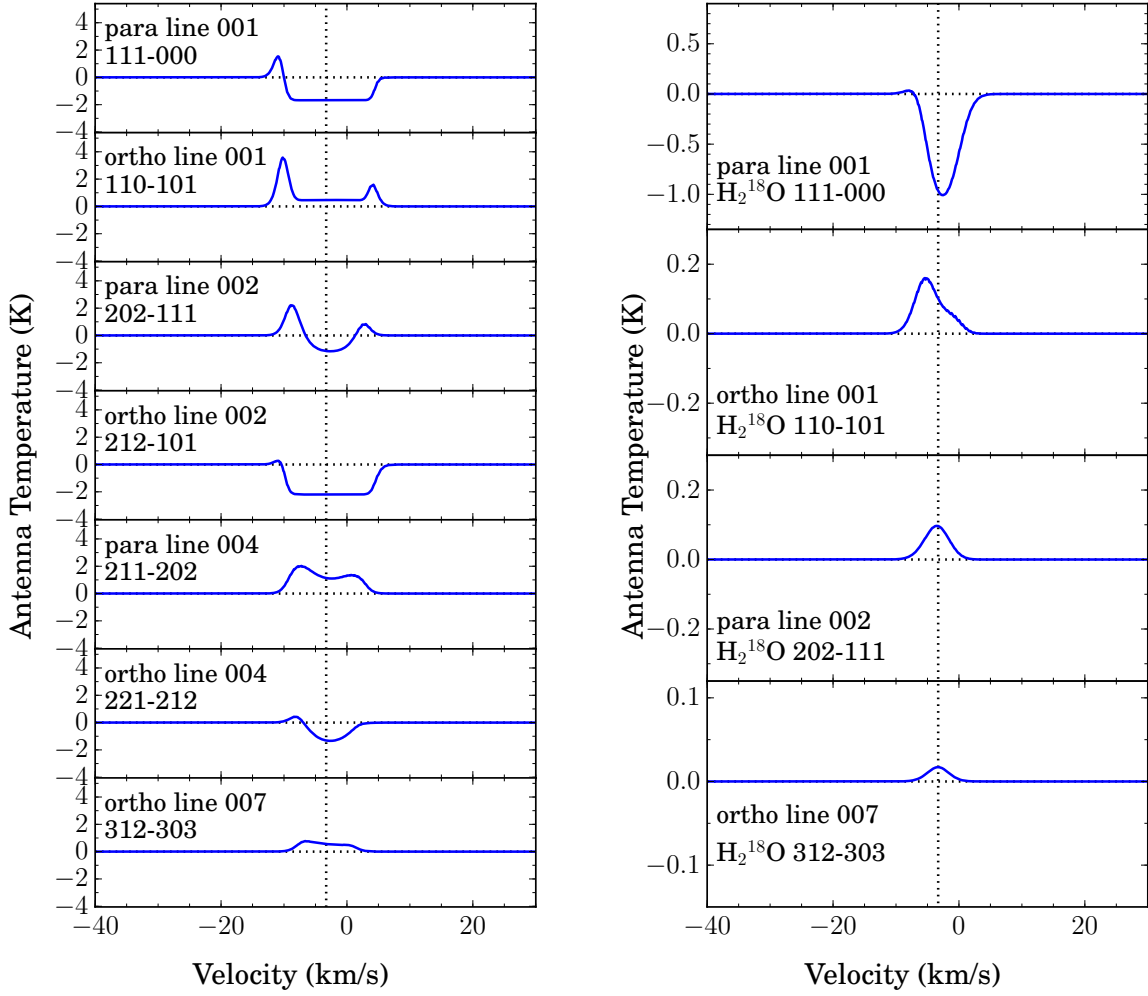
Figure 4.5: Reproduced RATRAN output for $H_2^{16}O$ (left) and $H_2^{18}O$ (right) in NGC 6334I(N). Vertical dotted line corresponds to V_{LSR} = -3.3 km s^{-1}. Similarities are seen when compared to the same lines in Herpin et al. (2016) where outflow Gaussians are added.
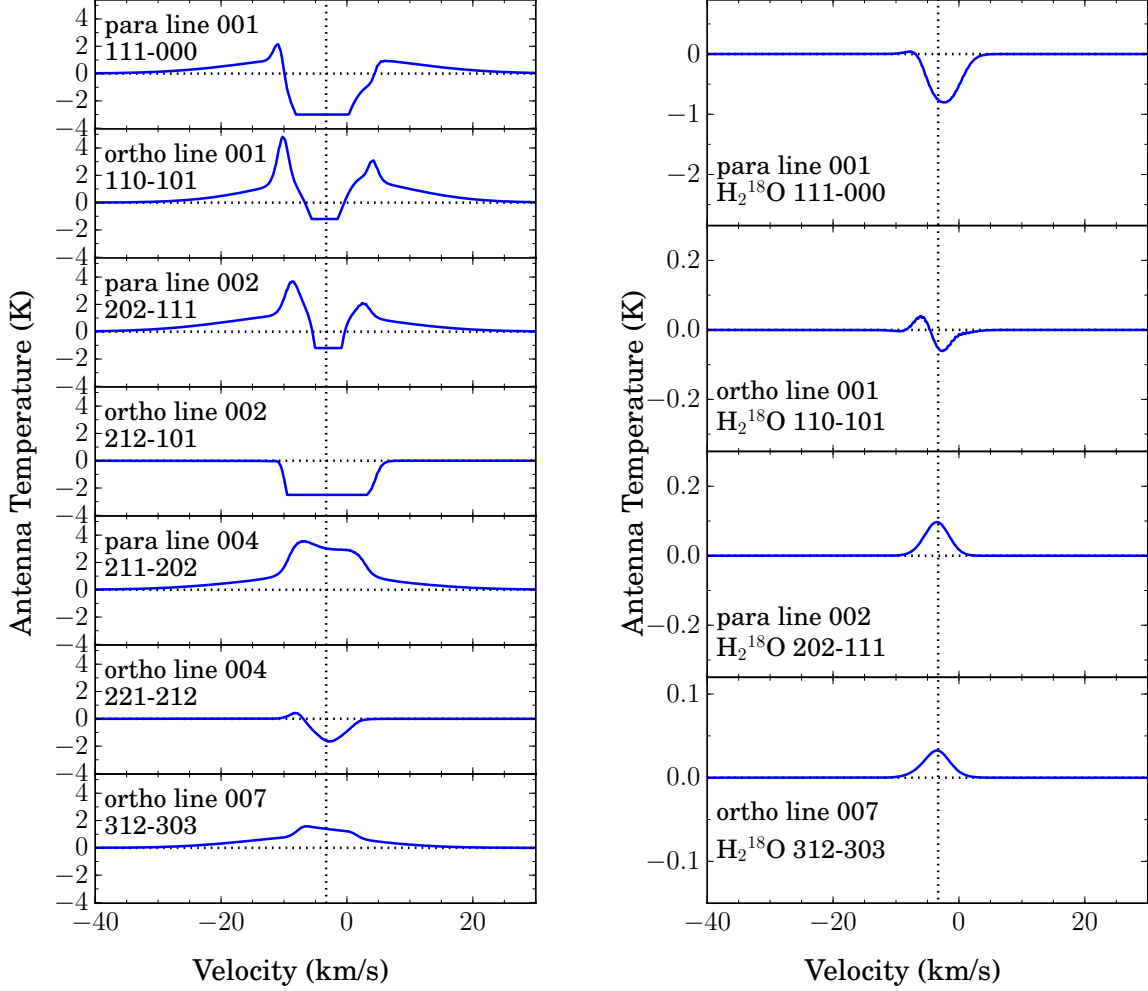
Figure 4.6: Reproduced $H_2^{16}O$ (left) and $H_2^{18}O$ (right) RATRAN output for NGC 6334I(N) with added Gaussian components. Gaussian parameters (σ, μ) were obtained from Herpin et al. (2016) and can be found in Table 4.3, while the Gaussian amplitude was inferred by inspection. Vertical dotted line corresponds to V_{LSR} = -3.3 km s^{-1}. Overall the total sum of the model and Gaussian components is very similar to the same published by Herpin et al. (2016), especially considering the NGC 6334I(N) RATRAN model was imprecisely obtained by hand and/or eye.

The para ground state line overall looks satisfactory. From Figure 4.6, $H_2^{16}O$ p-1_{11}-0_{00} (panel 1), o-1_{10}-1_{01} (panel 2), and p-2_{02}-1_{11} (panel 3) show an absorption and a blue asymmetry. Compared to the expected RATRAN lines, these are roughly the same line shape, although the current models produce a stronger asymmetry. The modelled line profile for o-2_{12}-1_{01} (panel 4) shows absorption like that in Herpin et al. , although it appears to be missing an emission feature similar to that of an outflow. That being said, this line did not have a broad emission Gaussian feature listed in Herpin et al. (2016). Molecular line p-2_{11}-2_{02} (panel 5) has a blue asymmetry and a slight absorption dip. The shape is similar to the Herpin et al. shape, although their absorption appears to be stronger. The o-2_{21}-2_{12} line (panel 6) has a slight blue asymmetry and an absorption; Herpin et al. also has a slight emission feature with the absorption, but equal in intensity on both the red and blue sides. This modelled line is consistent with the expected modelled line for the most part. The o-3_{12}-3_{03} line (panel 7) also has a blue asymmetry and a very slight absorption, similar to that in seen in Panel 5. Herpin et al. also shows consistency between these two lines.

From the right-side plot of Figure 4.6, $H_2^{18}O$, p-1_{11}-0_{00} (panel 1) and o-1_{10}-1_{01} (panel 2) appear in absorption like Herpin et al. (2016), with slight differences in the accompanying emission features. The expected modelled lines for p-2_{02}-1_{11} o-3_{12}-3_{03} are barely detectable, while the current lines return in detectable emission.

From this qualitative review, the reproduced line shapes are mostly as expected. It is also important to note that the linewidths of both sets of modelled water lines are consistent. Quantitatively, the current models are presented in antenna temperature T_A, while the Herpin et al. models are presented in main beam temperature T_{MB}. The conversion between these two values is as follows:

$$T_{MB} = \frac{\eta_\ell}{\eta_{MB}} T_A \tag{4.9}$$

where η_ℓ is the forward efficiency as defined in Roelfsema et al. (2012) and η_{MB} is the main beam efficiency. Refer to Table 4.8 for these values (Herpin et al. 2016). The peak temperature T_{peak}, total linewidth ΔV, and absorption depth ($|T_{max} - -T_{min}|$) for the current RATRAN models are also listed in this table for each water line. The temperature values are tabulated in T_A along with the efficiency ratio and corresponding main beam temperature conversion values. In the last two columns, a comparison is made between the intensities of the current models and the Herpin et al. models (refer to Table 4.6). This is carried out in the form of $(T/T_H)_{peak}$ and $(\Delta T/\Delta T_H)_{abs}$.

Table 4.8: NGC 6334 I(N) RATRAN spectral fits - intensities and widths for ortho and para $H_2^{18}O$ and $H_2^{16}O$, as determined by visual inspection. Asymmetry is listed as 'B' blueshifted or 'R' redshifted. ΔT_{abs} indicates the full absorption depth ($|T_{max} - T_{min}|$). Forward efficiency used in Herpin et al. to convert T_A to T_{mb} is η_ℓ = 0.96. $T_{mb} = (\eta_\ell / \eta_{mb}) T_A$.

| Molecule | Transition | T_A | | | | T_{mb} | | | | | |
		T_{peak} (K)	ΔV (km s^{-1})	Asymm.	ΔT_{abs} (K)	η_{mb}	η_ℓ/η_{mb}	T_{peak} (K)	ΔT_{abs} (K)	$(T/T_H)_{peak}$	$(\Delta T/\Delta T_H)_{abs}$
	p 1_{11} - 0_{00}	2.4	70	B	5.4	0.63	1.52	3.65	8.2	4.6	2.0
	o 1_{10} - 1_{01}	4.8	50	B	6.0	0.62	1.55	7.44	9.3	3.5	3.0
	p 2_{02} - 1_{11}	3.75	50	B	5.0	0.63	1.52	5.70	7.6	2.3	2.4
$H_2^{16}O$	o 2_{12} - 1_{01}	-3.3	20	-	-3.3	0.58	1.66	-5.5	-5.5	1.25/-5.5	1.3
	p 2_{11} - 2_{02}	3.5	50	B	0.5	0.64	1.50	5.25	0.75	1.5	0.5
	o 2_{21} - 2_{12}	0.5	15	B	2.0	0.58	1.66	0.83	3.3	3.3	1.7
	o 3_{12} - 3_{03}	1.5	50	B	-	0.63	1.52	2.28	-	1.6	-
	p 1_{11} - 0_{00}	0.05	12	B	0.7	0.63	1.52	0.08	1.1	0.8	1.2
$H_2^{18}O$	o 1_{10} - 1_{01}	0.05	15	B	0.8	0.62	1.55	0.08	1.2	3.2	8.0
	p 2_{02} - 1_{11}	0.1	12	-	-	0.63	1.52	0.15	-	6.0	-
	o 3_{12} - 3_{03}	0.03	15	-	-	0.63	1.52	0.046	-	4.6	-

While the RATRAN results for NGC 6334 I(N) produced in this thesis appear to be on average a few factors larger than that seen in Herpin et al. (2016), the similarities are promising considering the rough nature of this exercise.

Tangential to the topic of this exercise and somewhat similar to this work in general, Herpin et al. also employ RADEX to test physical parameters of NGC 6334 I(N). While this radiative transfer code is also used in this thesis to compare RATRAN results of an envelope, Herpin et al. use RADEX to roughly estimate the column density of water in the outflow components of each of their sources. This assumes an isothermal homogeneous material that shields envelope emission. They adopt $n_{H_2} = 3\times10^4$ cm^{-3} and T_k =200 K, like that in van der Tak et al. (2010), but also test neighbouring values. They determine that in order to reproduce the observed intensities, a water column density of $N_{H_2O} = 10^{17}$ is required for the NGC 6334 I(N) outflow. This is not modelled in this work.

Similarities and Differences with Herpin et al. (2016)

Table 4.9: Beamsizes used with NGC 6334 I(N) RATRAN models. Compared with those used in Herpin et al. (2016).

Line	This Work	H(2016)
o001	43.5	37.1
o007	22.1	19.9
o009	20.8	12.6
o002	14.5	12.6
p001	21.7	19.7
p002	24.5	21.3
p004	32.2	28.0

Overall, the general water line shapes are consistent with what is expected. We usually see absorptions and emissions where they should be. In contrast with Herpin et al., the same program is used (RATRAN), same collision rates (Daniel et al. 2011), same freeze-out radius (at 100 K), roughly same density and temperature profile (from van der Tak et al. (2013)), and same Gaussian widths and locations (Herpin et al. 2016).

Most often, the largest modelled differences are the blueshifted asymmetries. While the expected modelled lines show some of these asymmetries, they seem to occur in a majority of the current models. Additionally, the temperature measurements do not seem to be consistent. This is likely due to differences in beam size used during antenna temperature

convolution. At the time of modelling this exercise, the beam sizes tabulated in Table 4.9 were used; these are the pre-launch beamsizes. Later in this work, Roelfsema et al. (2012) beamsizes are used. The beam sizes used in this exercise are on average 1.17 times larger than that used in Herpin et al. (2016). Beamsize is discussed again later in 4.5.10.

Another potential source of error is the visual extraction of values for the density and temperature profile. The final extracted profile plotted in Figure 4.3 is not without flaws. The line reflects the rough nature of its retrieval. The number of points extracted (22 points) corresponds to the number of shells used in the RATRAN model. Herpin et al. (2016) did not define the number of shells used, presenting another potential source of error. As mentioned, Herpin et al. also did not supply amplitudes for their Gaussian fits. As such, these had to be visually estimated based on their final best fits to the water observations.

Considering the above similarities even with the rough nature of this exercise, we are now confident in moving forward with RATRAN modelling of this work's focus, NGC 7129 FIRS 2.

4.5 NGC 7129 FIRS 2: an Intermediate-Mass Young Stellar Object
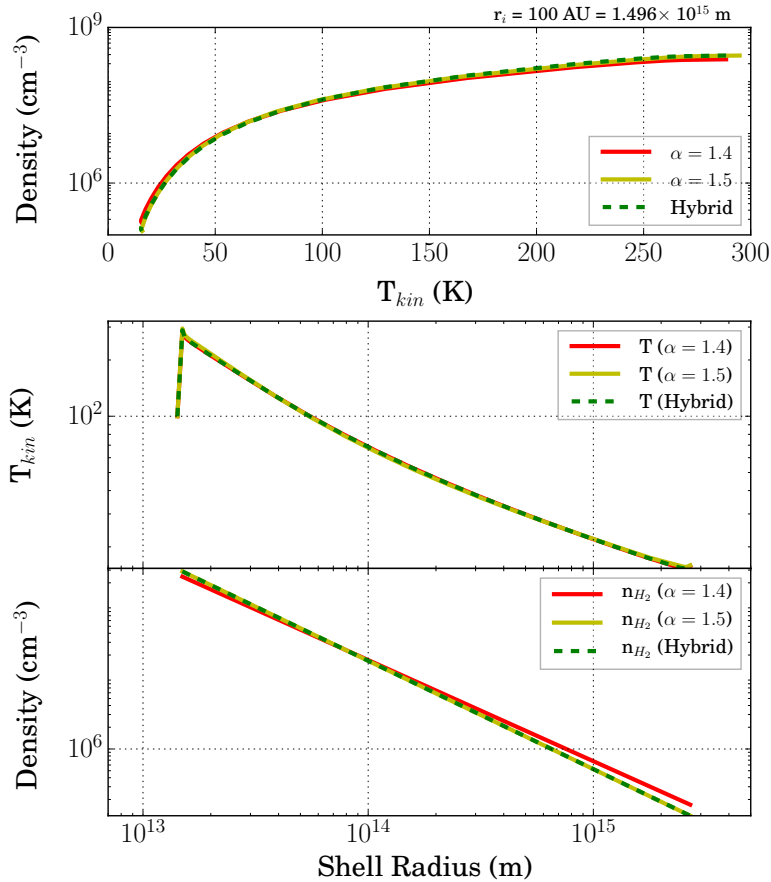
Figure 4.7: NGC 7129 FIRS 2: RATRAN Density & Temperature Profile, obtained from Crimier et al. (2010). Hybrid profile: density profile of $\alpha = 1.5$ and temperature profile of $\alpha = 1.5$. Inner radius r_i (envelope)= 100 AU = 1.496×10^{15}. Power law profile with $\alpha = 1.4$ (red), Hybrid (dashed green), and power law profile with $\alpha = 1.5$ (yellow).

Following the overall successful RATRAN exercise with the high-mass YSO NGC 6334 I(N) (§4.4), we are now confident in moving forward with modelling of intermediate-mass YSO NGC 7129 FIRS 2. The density and temperature profile for the envelope of NGC 7129 FIRS 2 is obtained from Crimier et al. (2010) and is plotted in Figure 4.7 for a density power law

index of $\alpha = 1.4$ and 1.5, and a hybrid profile using the density profile of $\alpha = 1.5$, and the temperature profile of $\alpha = 1.4$. The majority of this thesis uses the hybrid model, unless indicated otherwise. The radius, free-fall velocity, angular diameter, and beam dilution of each RATRAN shell are given in Appendix E, Table E.1. The radiative transfer modelling process with RATRAN begins with the ground state ortho 1_{10} - 1_{01} 547 GHz line of $H_2^{18}O$. Considering the ratio of $O^{16}/O^{18} \sim 550$, and the upper abundance limit of oxygen with respect to H_2 of $\sim 10^{-4}$, we should expect an inner abundance of $\sim 10^{-6}$ or less. Because of the age of the protostar, we also expect the cloud to be either completely or partially infalling. This allows an initial estimate for the radial velocity of a negative value ranging between 0 and the free-fall velocity towards a central mass of 1.1 $M_\odot$. We can also estimate an initial value for the turbulent velocity based on the width of the Gaussian fitted to the spectral line envelope component.

The following modelling analysis will investigate these input parameters to determine their effect. The radial velocity is investigated in §4.5.3, the turbulent velocity is investigated in §4.5.4, the water abundance is detailed in §4.5.1, and the abundance ratio is investigated in §4.5.2. Additional RATRAN models are produced to test the effects of altering the dust temperature (Crimier et al. 2010; §4.5.5), Freeze-out radius (§4.5.6), number of spherical shells (Hillier 2008; §4.5.7), ortho-to-para ratio (§4.5.8), and finally the collision rates (Daniel et al. 2011; §4.5.9).

4.5.1 Water Abundance

The water abundance is a measure of the water density relative to the H_2 density, thus simply another way of expressing the molecular density within the star formation region. As seen in 4.5.4, altering the abundance acts to alter the intensity T_A.

A grid model (P1 - P117) of ground state ortho (o001) $H_2^{18}O$ for a power law index of $\alpha = 1.5$ further investigates the effects on the spectral line due to the outer and inner envelope abundance and attempts to constrain this value. The input parameter values can be found in Table 4.10 and plotted in Figure 4.8. This grid model holds constant $b = 2.0$ km s^{-1}, and v_r = free-fall. The 95% and 90% confidence levels are indicated on the colour plot, at $\chi^2 = 0.593$ and $\chi^2 = 0.632$, respectively. Both confidence level contours seem to be well defined; with 95% confidence it can be said that the outer envelope abundance for $H_2^{18}O$ lies between $4.5 - 5.25 \times 10^{-11}$ for inner abundance $\gtrsim 1 \times 10^{-5}$, and between $5.25 - 6.0 \times 10^{-11}$ for inner abundance $\lesssim 1 \times 10^{-5}$. This is confirmed in the traditional plot of Figure 4.8. The tightest constraint this investigation makes for the outer abundance is between $4.5 - 5.0 \times 10^{-11}$, at confidence greater than or equal to 95%.

82
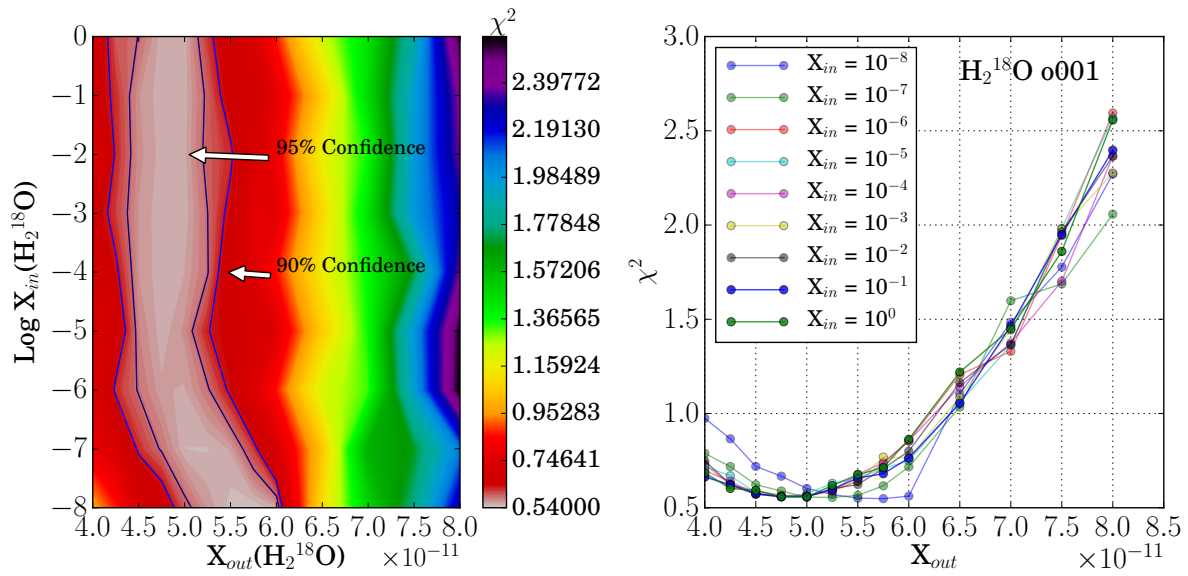
Figure 4.8: Varying X_{in} and X_{out} for o001 $H_2^{18}O$. Left plot presents colour plot of X_{in} and X_{out}. The 95% and 90% confidence levels are located at $\chi^2 = 0.593$ and $\chi^2 = 0.632$, respectively. Right plot presents χ^2 vs. Xout. Minima seen between 4.5–5.0$\times10^{-11}$.

Table 4.10: Running a series of models comparing two parameters (X_{out} vs. X_{in}) for the purpose of analysing their spectral fits via chi-sq tests. Models labelled P1 - P117. Plotted in Figure 4.8. $b = 2.0$ km s^{-1}, vr = FF.

X_{out} ($\times 10^{-11}$)	4.0	4.25	4.50	4.75	5.0	5.25	5.5	5.75	6.0	6.5	7.0	7.5	8.0
$X_{in} = 10^{-8}$	P1	P2	P3	P4	P5	P46	P47	P48	P49	P82	P83	P84	P85
$X_{in} = 10^{-7}$	P6	P7	P8	P9	P10	P50	P51	P52	P53	P86	P87	P88	P89
$X_{in} = 10^{-6}$	P11	P12	P13	P14	P15	P54	P55	P56	P57	P90	P91	P92	P93
$X_{in} = 10^{-5}$	P16	P17	P18	P19	P20	P58	P59	P60	P61	P94	P95	P96	P97
$X_{in} = 10^{-4}$	P21	P22	P23	P24	P25	P62	P63	P64	P65	P98	P99	P100	P101
$X_{in} = 10^{-3}$	P26	P27	P28	P29	P30	P66	P67	P68	P69	P102	P103	P104	P105
$X_{in} = 10^{-2}$	P31	P32	P33	P34	P35	P70	P71	P72	P73	P106	P107	P108	P109
$X_{in} = 10^{-1}$	P36	P37	P38	P39	P40	P74	P75	P76	P77	P110	P111	P112	P113
$X_{in} = 10^{\ 0}$	P41	P42	P43	P44	P45	P78	P79	P80	P81	P114	P115	P116	P117

Table 4.11: RATRAN: SKY Output for Final $H_2^{18}O$ Envelope Model; statistics at line and source center, prior to convolving with HIFI beamsizes.

Line	Opacity	Intensity (K)
o001	3.275E-01	3.262E+00
o006	8.386E-02	4.076E+00
o007	7.699E-02	3.962E+00
p001	2.956E-01	3.934E+00
p002	6.711E-02	3.745E+00
p004	3.958E-02	2.797E+00

The final modelled spectral line is plotted in Figure 4.9. This RATRAN model used an ortho $H_2^{18}O$ inner abundance with respect to H_2 of 1.0×10^{-7} (this is not a constrained parameter), an outer abundance of 4.8×10^{-11} (constrained), a turbulent velocity of 2.25 km s^{-1} (constrained for outer envelope), and free-fall velocity towards a central mass of 1.1 M$_\odot$ (not constrained). A para $H_2^{18}O$ inner abundance with respect to H_2 of 3.3×10^{-8} (this was not constrained by this model) and an outer abundance of 1.6×10^{-11} was used. The numerical output from SKY for this model is given in Table 4.11.
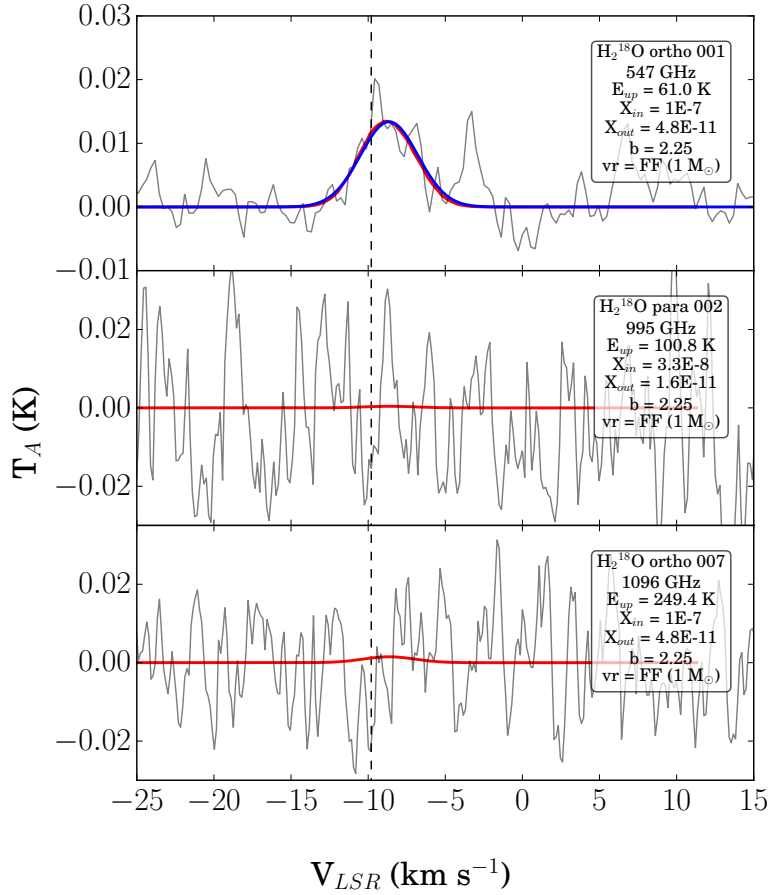
Figure 4.9: Final RATRAN model for $H_2^{18}O$ NGC 7129 FIRS 2. HIFI spectral observations (grey), fitted Gaussian for the envelope contribution (blue), and the RATRAN spectral model (red). Spectral lines of all $H_2^{18}O$ transitions appear to fit the data well.
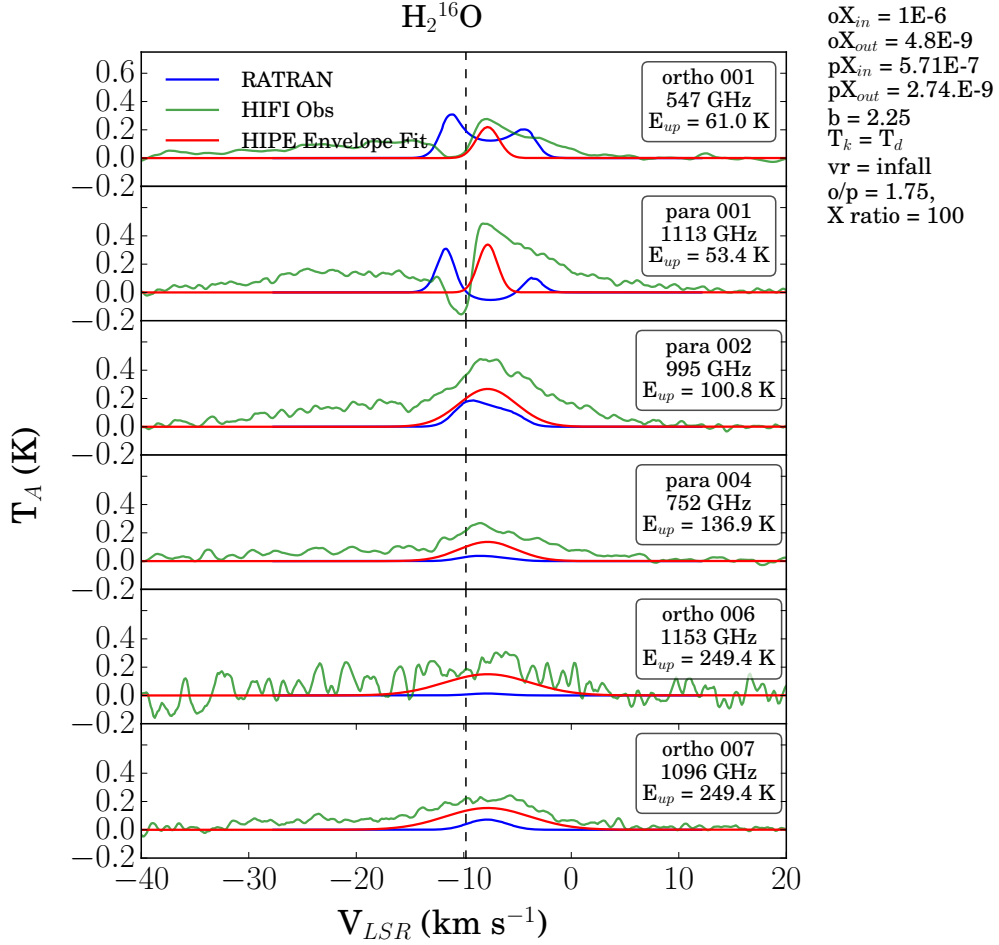
Figure 4.10: Final RATRAN model for $H_2^{16}O$ NGC 7129 FIRS 2 with abundance multiplied by 100. An ortho-to-para ratio of 1.75 is assumed. HIFI spectral observations (green), fitted Gaussian for the envelope contribution (red), and the RATRAN spectral model (blue). Spectral lines of excited $H_2^{16}O$ transitions appear to be more consistent with the data than the ground state lines. Deep absorptions arising from the cold outer envelope.

This model abundance was multiplied by 100 (instead of the expected 550) for a model of $H_2^{16}O$, with a ortho-to-para ratio for water of 1.75. The resultant molecular line can be found in Figure 4.10. The excited lines, while still falling short at this abundance, are most consistent with the HIFI observations than the ground state lines. Deep absorptions occur, likely due to the colder outermost envelope.

Summary: Water Abundance As seen in §4.5.4, altering the abundance increases or decreases the intensity T_A. Through the grid models in this section, we constrain the $H_2^{18}O$ outer abundance between $4.8 \pm 0.3 \times 10^{-11}$, at confidence greater than or equal to 95%.

4.5.2 Abundance Ratio X_{ratio}

Once an acceptable RATRAN model is fit to the envelope Gaussian of the $H_2^{18}O$ HIFI observational data, it is expected that this model should also apply to $H_2^{16}O$, but at an abundance approximately 550 times greater. In theory, if NGC 7129 FIRS 2 has this general abundance ratio, we should be able to simply multiply the molecular density of $H_2^{18}O$ by an abundance ratio ($X_{ratio}= X_{H_2^{16}O}/ X_{H_2^{18}O}$) of 550 and see a spectral line similar in integrated line intensity to that of the HIFI observed spectral line. This does not occur for the ground state lines; the modelling of $H_2^{16}O$ isn't as straightforward as originally expected. It is possible that the abundance ratio is less in NGC 7129 FIRS 2.

Table 4.12: NGC 7129 FIRS 2 RATRAN models. Varying abundance ratio ($X_{ratio} = X_{H_2^{16}O}/ X_{H_2^{18}O}$). The X_{in} and X_{out} tabulated are values of $H_2^{18}O$. The abundance values for $H_2^{16}O$ equal the $H_2^{18}O$ values multiplied by the tabulated ratio. Plotted in Figures listed. FF = Free-fall towards central mass of $1.1 M_\odot$.

Date/ID	Tested Parameter	X_{in}	X_{out}	b (km s^{-1})	vr (km s^{-1})	Figure
	$X_{ratio} = 550$	1×10^{-6}	5×10^{-11}	2.5	FF	4.11
	$X_{ratio} = 500$	1×10^{-6}	5×10^{-11}	2.5	FF	4.11
	$X_{ratio} = 450$	1×10^{-6}	5×10^{-11}	2.5	FF	4.11
	$X_{ratio} = 400$	1×10^{-6}	5×10^{-11}	2.5	FF	4.11
	$X_{ratio} = 350$	1×10^{-6}	5×10^{-11}	2.5	FF	4.11
	$X_{ratio} = 300$	1×10^{-6}	5×10^{-11}	2.5	FF	4.11
2018-01-06	$X_{ratio} = 250$	1×10^{-6}	5×10^{-11}	2.5	FF	4.11
OPQR16	$X_{ratio} = 200$	1×10^{-6}	5×10^{-11}	2.5	FF	4.11
	$X_{ratio} = 150$	1×10^{-6}	5×10^{-11}	2.5	FF	4.11
	$X_{ratio} = 100$	1×10^{-6}	5×10^{-11}	2.5	FF	4.11
	$X_{ratio} = 50$	1×10^{-6}	5×10^{-11}	2.5	FF	4.11
	$X_{ratio} = 20$	1×10^{-6}	5×10^{-11}	2.5	FF	4.11
	$X_{ratio} = 10$	1×10^{-6}	5×10^{-11}	2.5	FF	4.11
	$X_{ratio} = 5$	1×10^{-6}	5×10^{-11}	2.5	FF	4.11
	$X_{ratio} = 2$	1×10^{-6}	5×10^{-11}	2.5	FF	4.11

Models OPQR16 (Table 4.12) vary this abundance ratio from 2 to 550 at a constant $H_2^{18}O$ inner abundance of 1×10^{-6}, outer abundance of 5×10^{-11}, turbulent velocity of 2.5 km s^{-1}, and a free-fall infall velocity towards a central mass of $1.1 M_\odot$, for a power law index of $\alpha = 1.5$. The results of these models can be found in Figure 4.11. The ground state ortho (o001) $H_2^{16}O$ envelope Gaussian component is shown in thick blue, the HIFI observations are shown in faded black, and the local V_{LSR} = -9.8 km s^{-1} is shown in the vertical dashed line. In terms of peak T_A, an X_{ratio} between 50 and 100 seem comparable to the envelope Gaussian, although the radiative transfer model indicates we should be expecting red-shifted self absorption and a blue asymmetry at this abundance. This is not observed in the HIFI observational data, where the self absorption due to the envelope falls on the blue side of the V_{LSR}, and the emission is present in a red-shifted asymmetry. This plot helps solidify the conclusion that the $H_2^{16}O$ ground state ortho emission line isn't a reliable probe of star formation regions.

Summary: Abundance Ratio For the hybrid density and temperature model for NGC 7129 FIRS 2, the abundance ratio between $H_2^{16}O$ and $H_2^{18}O$ appears to be closer to a value of 100 as opposed to 550. This will be further constrained in Section §4.5.11

4.5.3 Radial Velocity v_r

An extensive investigation into the effects of varying the infall velocity of the NG 7129 FIRS 2 envelope is conducted for the power law profile $\alpha = 1.5$ while holding the other parameters constants.

RATRAN models for a free-falling molecular cloud towards a central mass of $1.1 M_\odot$ are compared to those of a static and constant infall velocity (models F1-F6, Table 4.13). The radial velocity v_r is varied from 0.0 to -4.0 km s^{-1} and compared to free-fall towards $1.1 M_\odot$ (FF), turbulent velocity b is held constant at 2.1 km s^{-1}, inner abundance X_{in} is held constant at 1×10^{-6}, and the outer abundance X_{out} is held constant at 5.25×10^{-11}. This is plotted in Figure 4.12. In terms of peak antenna temperature, the free-fall model (red) and the -2.0 km s^{-1} constant model (cyan) appear to fit the data the best, although tweaking in the width would be required to make a solid model confirmation. As the constant velocity models increase, the blueshifted emission tail increases in width. Thus, we can rule out constant velocity models v_r = -4.0 – -1.0 km s^{-1}. Considering optical depth later in this work, for both molecules, only the outer envelope is contributing to the models. That being said, the velocity in the outer envelope ranges from $\sim$ -2 to -0.34 km s^{-1}. Models with radial velocity in the lower range appear to fit the observational data sufficiently well.
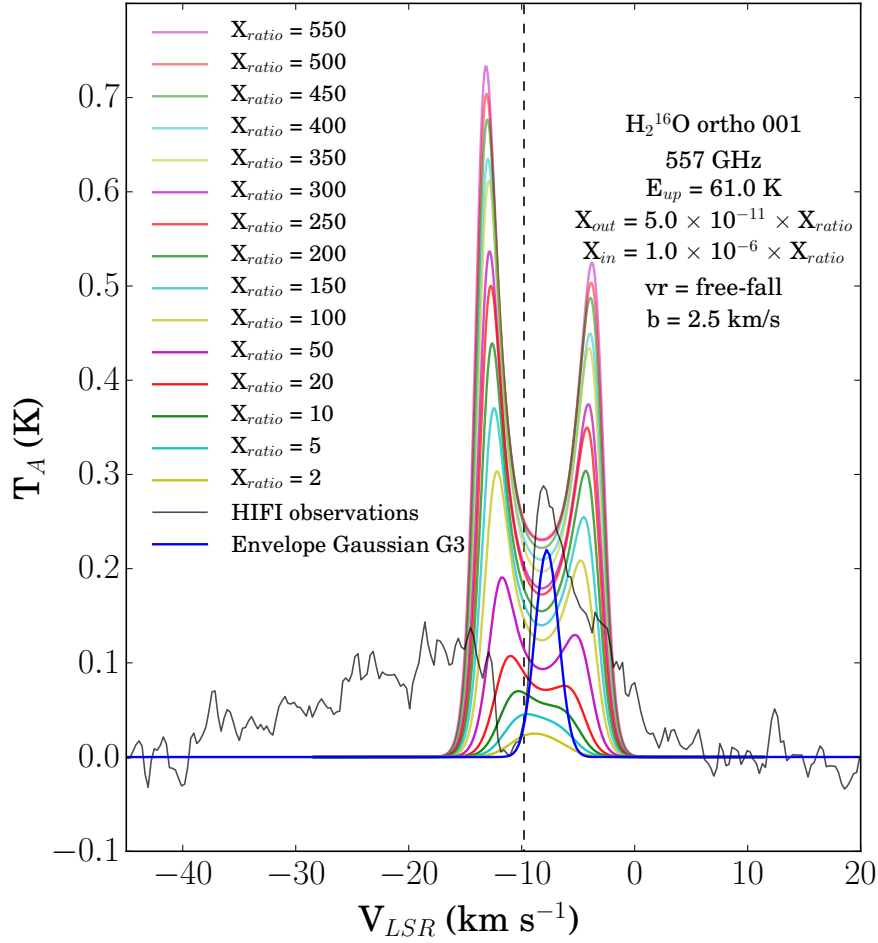
Figure 4.11: Varying $H_2^{16}O/H_2^{18}O$ X_{ratio}. It is expected that $X_{ratio} \sim 550$. The ground state ortho (o001) $H_2^{16}O$ envelope Gaussian component= thick blue, HIFI observations = faded black, and V_{LSR} = -9.8 km s^{-1} = vertical dashed line. An o001 $H_2^{18}O$ inner abundance of 1×10^{-6} and an outer abundance of 5×10^{-11} is assumed. These values are multiplied by the indicated X_{ratio} for o001 $H_2^{16}O$. b = 2.5 km s^{-1} and a free fall infall velocity towards a central 1.1 $M_{\odot}$ mass are assumed. In terms of temperature amplitude, an X_{ratio} between 50 and 100 would seem comparable to the envelope Gaussian.

Because the ground state residuals of the Gaussian subtracted HIFI data appear to be consistent with P-Cygni profiles (i.e., red asymmetry, Figures 6.2 and 6.3), possibly indicating expansion, a second investigation into the behaviour of the radial velocity is conducted. For both $H_2^{18}O$ and $H_2^{16}O$, the radial velocity is set to a constant $+4.0$ km s^{-1} and a constant -4.0 km s^{-1}. The $V_{LSR} = -9.8$ km s^{-1} for NGC 7129 FIRS 2.

Table 4.13: NGC 7129 FIRS 2 RATRAN models. Varying $H_2^{18}O$ infall velocity.

Date/ID	Tested Parameter	X_{in}	X_{out}	b (km s^{-1})	vr (km s^{-1})	Figure
	vr	1×10^{-6}	5.25×10^{-11}	2.1	FF	4.12
	vr	1×10^{-6}	5.25×10^{-11}	2.1	0.0	4.12
2018-02-12	vr	1×10^{-6}	5.25×10^{-11}	2.1	-0.5	4.12
F1-F6	vr	1×10^{-6}	5.25×10^{-11}	2.1	-1.0	4.12
	vr	1×10^{-6}	5.25×10^{-11}	2.1	-2.0	4.12
	vr	1×10^{-6}	5.25×10^{-11}	2.1	-3.0	4.12
	vr	1×10^{-6}	5.25×10^{-11}	2.1	-4.0	4.12

For this second radial velocity investigation, X_{in} is set to 4×10^{-6} (although this is greater than the availability of oxygen, this does not effect the resultant spectral line due to the thick optical depth) for $H_2^{18}O$, X_{out} is set to 4.8×10^{-11}, and b is set to 2.25 km s^{-1}. The $H_2^{18}O$ spectral models are plotted in Figure 4.13. The $+4.0$ km s^{-1} model is plotted in blue, the -4.0 km s^{-1} model is plotted in green, the HIFI spectral data is plotted in red, and the envelope Gaussian contribution is plotted in cyan. The first interesting effect noticed is the mirroring of the line about the envelope V_{LSR} (-8.6 km s^{-1} for $H_2^{16}O$, -7.8 km s^{-1} for $H_2^{18}O$) with the changing of radial velocity sign from positive to negative. Looking at the ortho ground state line in the top panel, the spectral line of the constant expanding envelope (blue) appears to fit the HIFI data better than the infalling case (green). Considering the minor differences in the plotted lines for $H_2^{18}O$, both models still fit the data well. No differences are seen in the excited p002 and o007 lines, as expected.

For $H_2^{16}O$, X_{in} is again arbitrarily set to 4×10^{-4}, the X_{out} is set to 4.8×10^{-9}, and b is set to 2.25 km s^{-1}. $X(H_2^{16}O/H_2^{18}O) = 100$ in this example. In the $H_2^{16}O$ Figure 4.14, the colour scheme is the same as that in Figure 4.13. Looking at the ground state lines in particular, the abundance ratio and/or the ortho-to-para ratio should be altered slightly for ortho-water, and appears to be consistent in height for para-water.

The o001 spectral data appears to be better fit by the infalling model if the central V_{LSR} of the RATRAN line is redshifted by $\sim$ 2-3 km s^{-1}; the redshifted tail seems to match the tail
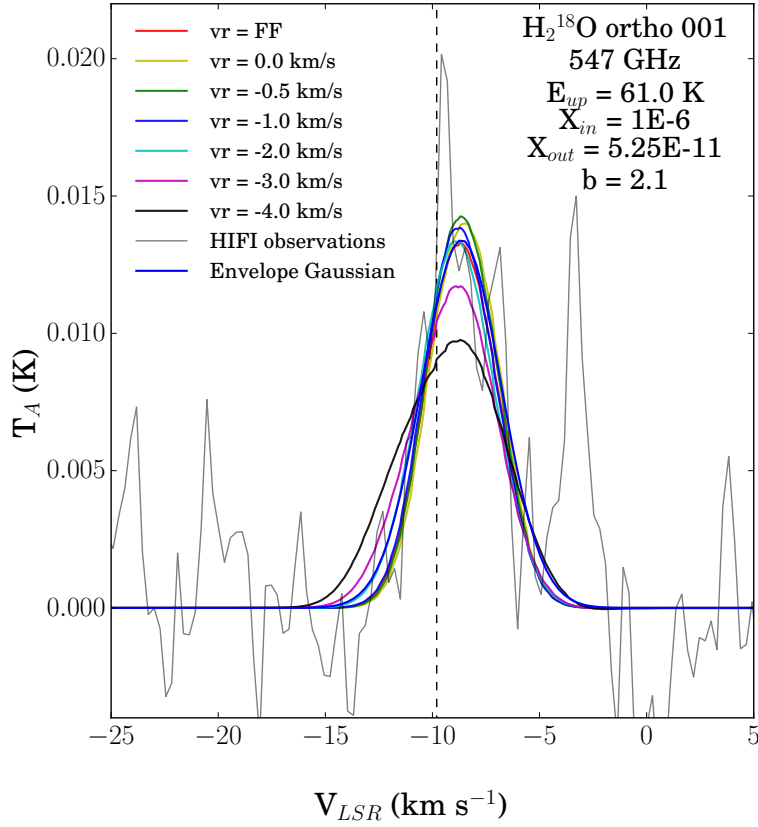
Figure 4.12: Radiative transfer models were run to test the effect of varying the infall velocity. A free-fall velocity towards a central mass of 1.1 $M_\odot$ was considered (red), alongside constant infall velocities ranging from -0.5 – -4.0 km s^{-1} (green – magenta), and a static model of 0.0 km s^{-1} (yellow). $b = 2.1$ km s^{-1}, $X_{in} = 1 \times 10^{-6}$, and $X_{in} = 5.25 \times 10^{-11}$. In terms of temperature amplitude, the free-fall model and the -2.0 km s^{-1} constant model appear to fit the data the best. The ground state ortho $H_2^{18}O$ envelope Gaussian component = thick blue, HIFI observations = faded black, and $V_{LSR} = -9.8$ km s^{-1} = vertical dashed line.

in the HIFI spectral data. Considering this tail is already fit by a Gaussian representing the outflow, this likely isn't a good fit. Looking at the expanding model instead, the blue "tail" aligns with the self absorption from the envelope. The para ground state line p001 shows a similar feature - the envelope contributes to the blueshifted absorption, and this matches the HIFI spectral data. The excited lines aren't greatly effected by the change in radial velocity, as is expected. The $H_2^{16}O$, like the $H_2^{18}O$ spectral observations appear more consistent with an expanding model than an infalling model, although the overall fit to the observations is not consistent for a constant $\pm$ 4.0 km s^{-1} model. Considering this, and due to the age of NGC 7129 FIRS 2 (Class 0), we don't expect this to be an expanding case. In addition to this, the poor spectral fits produced by the constant $\pm$ 4.0 km s^{-1} indicates that the radial velocity is likely not constant throughout the entire envelope; the infall velocity likely decreases with radius from the SFR center. This supports the claim that a free-falling infall velocity might be the best fit.

With that, we consider lowering the radial velocity for the outer envelope. A constant infalling -4.0 km s^{-1} $H_2^{16}O$ model is compared to a model with radial infall velocity of -4.0 km s^{-1} (shell 1-9), -2.0 km s^{-1} (shell 10-15), and -1.0 km s^{-1} (shell 16-22), moving from inner to outer envelope. These values are roughly similar to that of the free-fall infall velocity towards a $1.1M_\odot$ core. X_{out} is also reduced by a factor of 2 for both models in attempt to better fit the peak antenna temperature. The result is seen in Figure 4.15, where $H_2^{16}O$ ortho $X_{in} = 5\times10^{-4}$, para $X_{in} = 2.5 \times 10^{-4}$, ortho $X_{out} = 2.4 \times 10^{-9}$, para $X_{out} = 8 \times 10^{-10}$, $b = 2.25$ km s^{-2}. By decreasing the constant radial velocity with radius from the central YSO, the amplitude and width decreases, and the red-shifted tail increases into a stronger emission feature. This generates a redshifted absorption dip at the line center. It appears that as the radial infall velocity in the outer envelope decreases the redshifted emission increases. Perhaps less inner material is absorbed by the envelope when it is infalling slower. Both RATRAN models, the constant +4.0 km s^{-1} and the constant decreasing model, show complicated $H_2^{16}O$ structure from the envelope alone. This result suggests the notion that it is difficult to place constraints on NGC 7129 FIRS 2 with this molecule, however; some interesting effects are still being observed by manipulating these RATRAN input variables.

Summary: Radial Velocity   To summarize the above investigation on radial velocity with respect to RATRAN modelling results, altering the model from an infalling cloud to an expanding cloud mirrors the resultant molecular line about the envelope V_{LSR}. For a case where the constant velocity is decreased for the outer-envelope, the redshifted emission increases. Perhaps less inner material is absorbed by the envelope when it is infalling slower. The constant infall models can likely be ruled out, supporting the suggestion that

the envelope is collapsing under free-fall. These modelling results also contribute to the notion that it is difficult to place constraints on NGC 7129 FIRS 2 with $H_2^{16}O$.
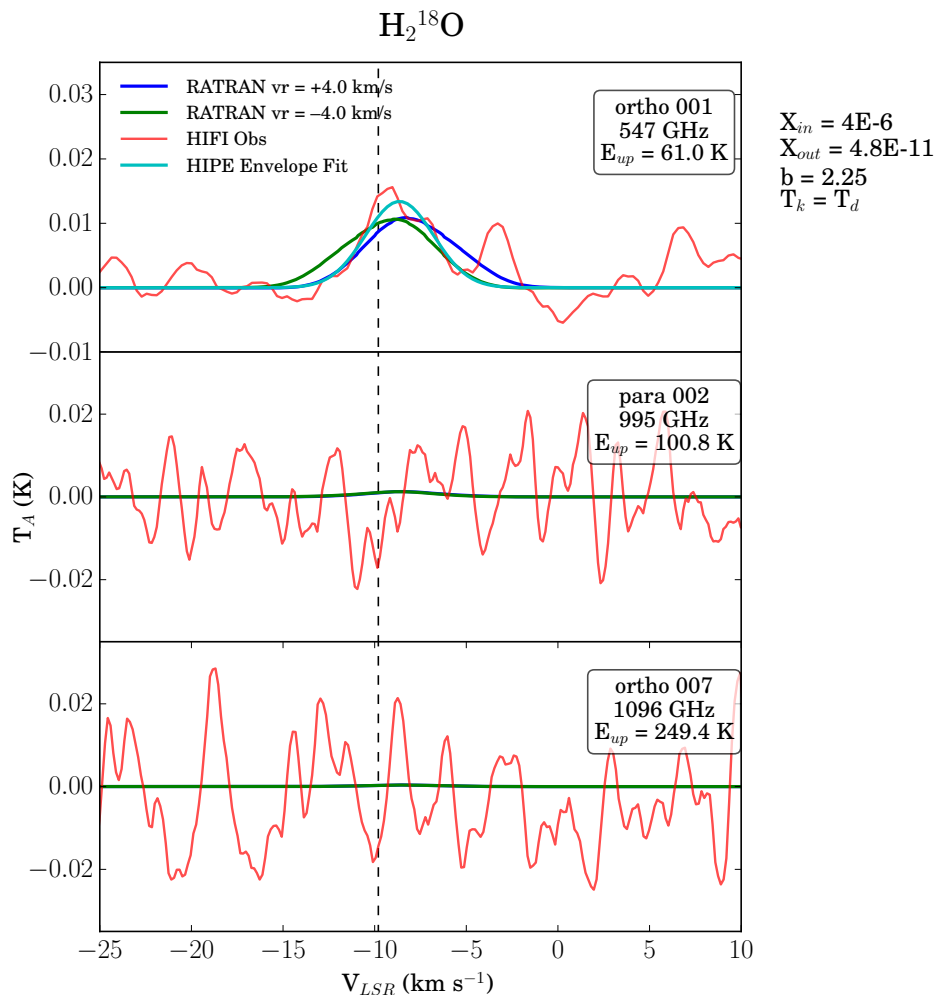
$$H_2^{18}O$$

Figure 4.13: RATRAN models of $H_2^{18}O$, for a constant expanding velocity of +4.0 km s^{-1} and constant infalling velocity of -4.0 km s^{-1}. The X_{in} = 4×10^6, X_{out} = 4.8×10^{-11}, and b = 2.25 km s^{-1}. The +4.0 km s^{-1} model = blue, the -4.0 km s^{-1} model = green, the HIFI spectral data = red, and the envelope Gaussian contribution= cyan.
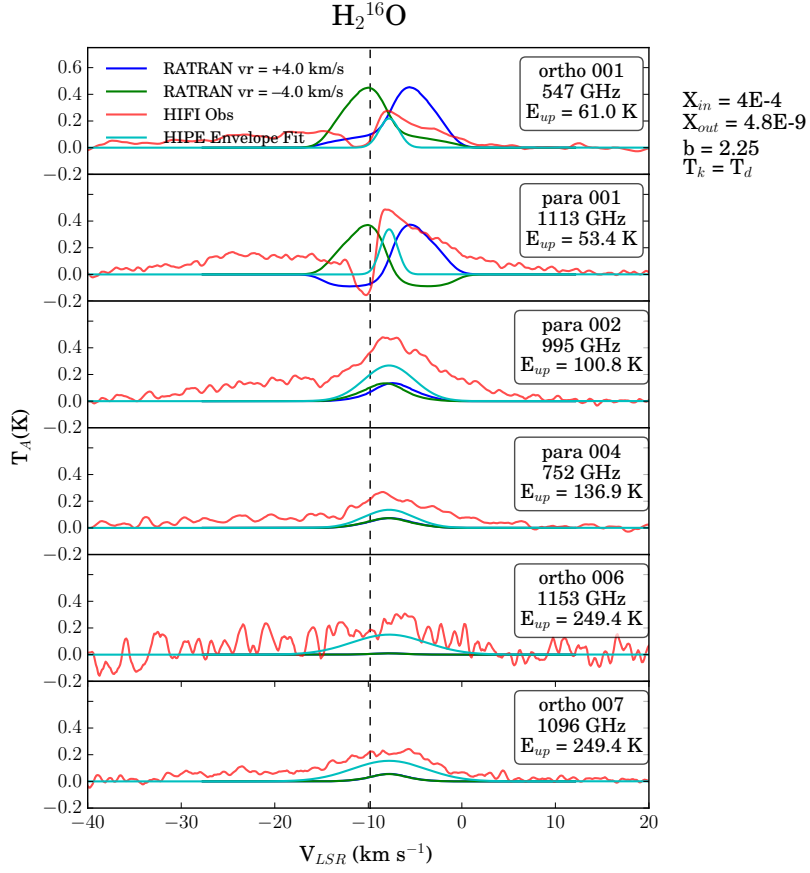
Figure 4.14: RATRAN models of $H_2^{16}O$, for a constant expanding velocity of +4.0 km s^{-1} (blue) and constant infalling velocity of -4.0 km s^{-1} (green). The inner abundance was set to 4×10^4, the outer abundance was set to 4.8×10^{-9}, and the turbulent velocity was set to 2.25 km s^{-1}. The abundance ratio of $H_2^{16}O/H_2^{18}O = 100$ in this example. The HIFI spectral data = red, and the envelope Gaussian = cyan.
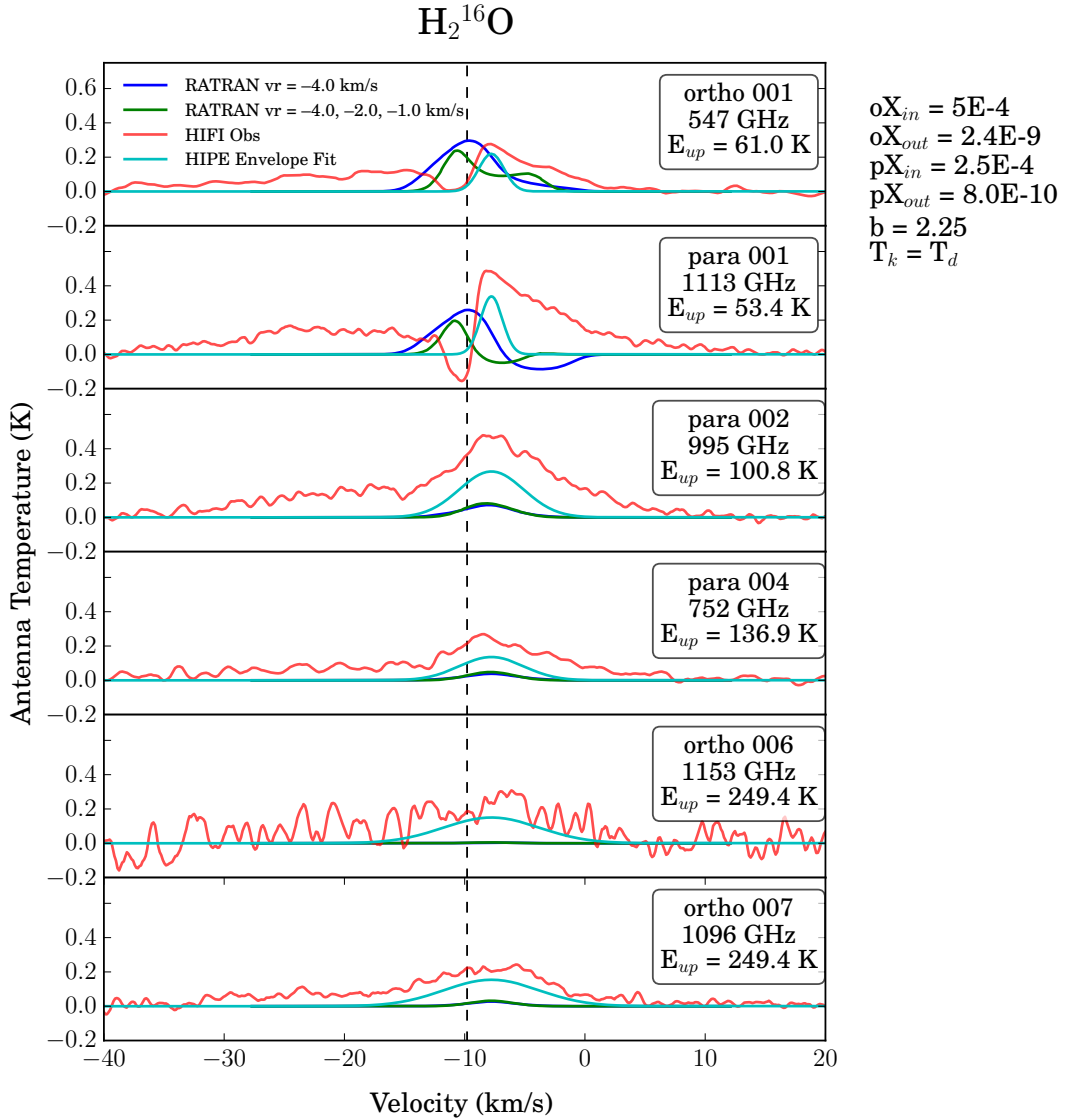
Figure 4.15: A constant infalling -4.0 km s^{-1} H$_2^{16}$O model was compared to a model with radial infall velocity of -4.0 km s^{-1} (shell 1-9), -2.0 km s^{-1} (shell 10-15), and -1.0 km s^{-1} (shell 16-22), moving from inner to outer envelope. Ortho inner abundance = 5×10^{-4}, outer abundance = 2.4×10^{-9} (a reduction of factor 2 from the previous models and Figure 4.14). Para inner abundance = 2.5×10^{-4}, outer abundance = 8.0×10^{-10}. Turbulent velocity $b = 2.25$ km s^{-1}.

4.5.4 Doppler Broadening Parameter db

An extensive investigation into the effects of varying the turbulent velocity is conducted for the power law profile $\alpha = 1.5$ while holding the other parameters constants. Only the abundance is allowed to vary across model sets.

The radial velocity v_r and the inner $H_2^{18}O$ abundance X_{in} are held constant at -0.5 km s^{-1} and 1×10^{-6} respectively for 24 RATRAN models (Table 4.14). In each of the 24 models, the turbulent velocity b is allowed to vary between $0.5 - 4.0$ km s^{-1}. In the first 8 (Models 9s), the outer $H_2^{18}O$ abundance is held constant at 1×10^{-10} (Figure 4.16); from these, it is apparent that both the velocity width and the temperature peak are too large. The outer abundance is then decreased to 1×10^{-12} (Models 10s) in attempt to lower the width and height of the produced line (Figure 4.17). This results in the line being much too weak. The last 8 models (Models 10.2s) hold the outer $H_2^{18}O$ abundance at a constant 1×10^{-11} (Figure 4.18). The height and width of the RATRAN produced lines are more consistent with the HIFI data at this outer abundance; further refinement of the turbulent velocity and outer abundance is now required.

From here, 4 more RATRAN models are produced with more specific parameters based on the findings of models 9s, 10s, and 10.2s. Labelled O25, P25, Q25, and R25 in Table 4.14, these models select $X_{out} = 5 \times 10^{-11}$, and vary X_{out} from 1×10^{-6} to 5×10^{-7}, and turbulent velocity from 2.50 to 2.75 km s^{-1}. The results of these models can be found in Figure 4.19. All four of these models appear to fit the HIFI observational data well, and model O25 (red line) seems to be the most consistent with the fitted Gaussian (thick blue line). The higher excitation lines either see a very slight emission or a non-detection, consistent with the HIFI observations.

A set of grid models, R1-R81 (Table 4.15), investigates the effects of varying the turbulent velocity of the inner and outer envelope. The models R1-R25 were run first; the rest were added for extra detail. The outer abundance is held constant at 4.8×10^{-11} (just deduced from Model O25), the inner abundance is held constant at 1×10^{-7} (arbitrarily selected), and the infall velocity is taken to be in free-fall towards a central mass of 1.1 M$_\odot$. The colour plot in Figure 4.20 compares the chi-squared values of these models for ground state ortho (o001) $H_2^{18}O$. The 95% and 90% confidence levels are indicated on the colour plot, at $\chi^2 = 0.593$ and $\chi^2 = 0.632$, respectively. The 95% confidence level indicates that the best fit radiative transfer models occur for approximately $2.0 < b_{out} < 2.5$ km s^{-1}. The inner turbulent velocity does not seem to have an effect on the fit of the models. The further addition of models between grid points would eliminate the triangular nature of the confidence level contours.

Table 4.14: NGC 7129 FIRS 2 $H_2^{18}O$ RATRAN models. Varying turbulent velocity. Seen plotted in Figures 4.16 - 4.18. FF = Free-fall towards central mass of $1.1M_\odot$.

Date/ID	Tested Parameter	X_{in}	X_{out}	b (km s^{-1})	vr (km s^{-1})	Figure
	b	1×10^{-6}	1×10^{-10}	0.5	-0.5	4.16
	b	1×10^{-6}	1×10^{-10}	1.0	-0.5	4.16
	b	1×10^{-6}	1×10^{-10}	1.5	-0.5	4.16
2017-12-18	b	1×10^{-6}	1×10^{-10}	2.0	-0.5	4.16
Model 9s	b	1×10^{-6}	1×10^{-10}	2.5	-0.5	4.16
	b	1×10^{-6}	1×10^{-10}	3.0	-0.5	4.16
	b	1×10^{-6}	1×10^{-10}	3.5	-0.5	4.16
	b	1×10^{-6}	1×10^{-10}	4.0	-0.5	4.16
	b	1×10^{-6}	1×10^{-12}	0.5	-0.5	4.17
	b	1×10^{-6}	1×10^{-12}	1.0	-0.5	4.17
	b	1×10^{-6}	1×10^{-12}	1.5	-0.5	4.17
2017-12-30	b	1×10^{-6}	1×10^{-12}	2.0	-0.5	4.17
Model 10s	b	1×10^{-6}	1×10^{-12}	2.5	-0.5	4.17
	b	1×10^{-6}	1×10^{-12}	3.0	-0.5	4.17
	b	1×10^{-6}	1×10^{-12}	3.5	-0.5	4.17
	b	1×10^{-6}	1×10^{-12}	4.0	-0.5	4.17
	b	1×10^{-6}	1×10^{-11}	0.5	-0.5	4.18
	b	1×10^{-6}	1×10^{-11}	1.0	-0.5	4.18
	b	1×10^{-6}	1×10^{-11}	1.5	-0.5	4.18
2017-12-31	b	1×10^{-6}	1×10^{-11}	2.0	-0.5	4.18
Model 10.2s	b	1×10^{-6}	1×10^{-11}	2.5	-0.5	4.18
	b	1×10^{-6}	1×10^{-11}	3.0	-0.5	4.18
	b	1×10^{-6}	1×10^{-11}	3.5	-0.5	4.18
	b	1×10^{-6}	1×10^{-11}	4.0	-0.5	4.18
	b, X_{in}	1×10^{-6}	5×10^{-11}	2.50	FF	4.19
2018-01-03	b, X_{in}	1×10^{-6}	5×10^{-11}	2.75	FF	4.19
O25,P25,Q25,R25	b, X_{in}	5×10^{-7}	5×10^{-11}	2.50	FF	4.19
	b, X_{in}	5×10^{-7}	5×10^{-11}	2.75	FF	4.19
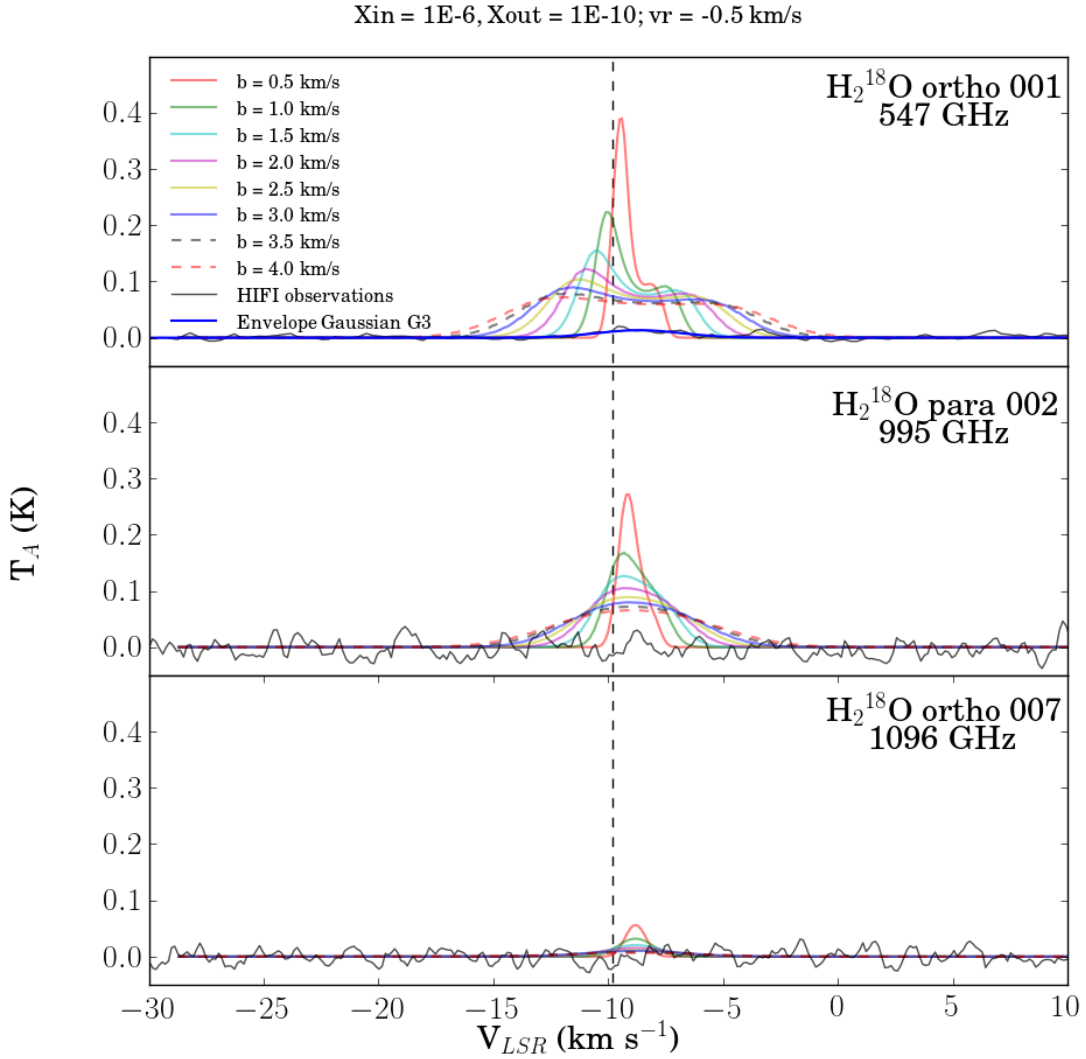
Figure 4.16: Radiative transfer models generated with RATRAN for $H_2^{18}O$, at 547 GHz, 995 GHz, and 1096 GHz. Outer abundance of $X_{out} = 1 \times 10^{-10}$, Inner abundance of X_{in} $= 1 \times 10^{-6}$, infall velocity of -0.5 km s^{-1}. Turbulent velocity at 0.5 (red), 1.0 (green), 1.5 (cyan), 2.0 (magenta), 2.5 (yellow), 3.0 (blue), 3.5 (black dashed), and 4.0 (red dashed) km s^{-1}. HIFI observations for each line seen in shaded black. Gaussian fit to the envelope contribution given in thick blue. Local V_{LSR} = -9.8 km s^{-1} (vertical black dashed).
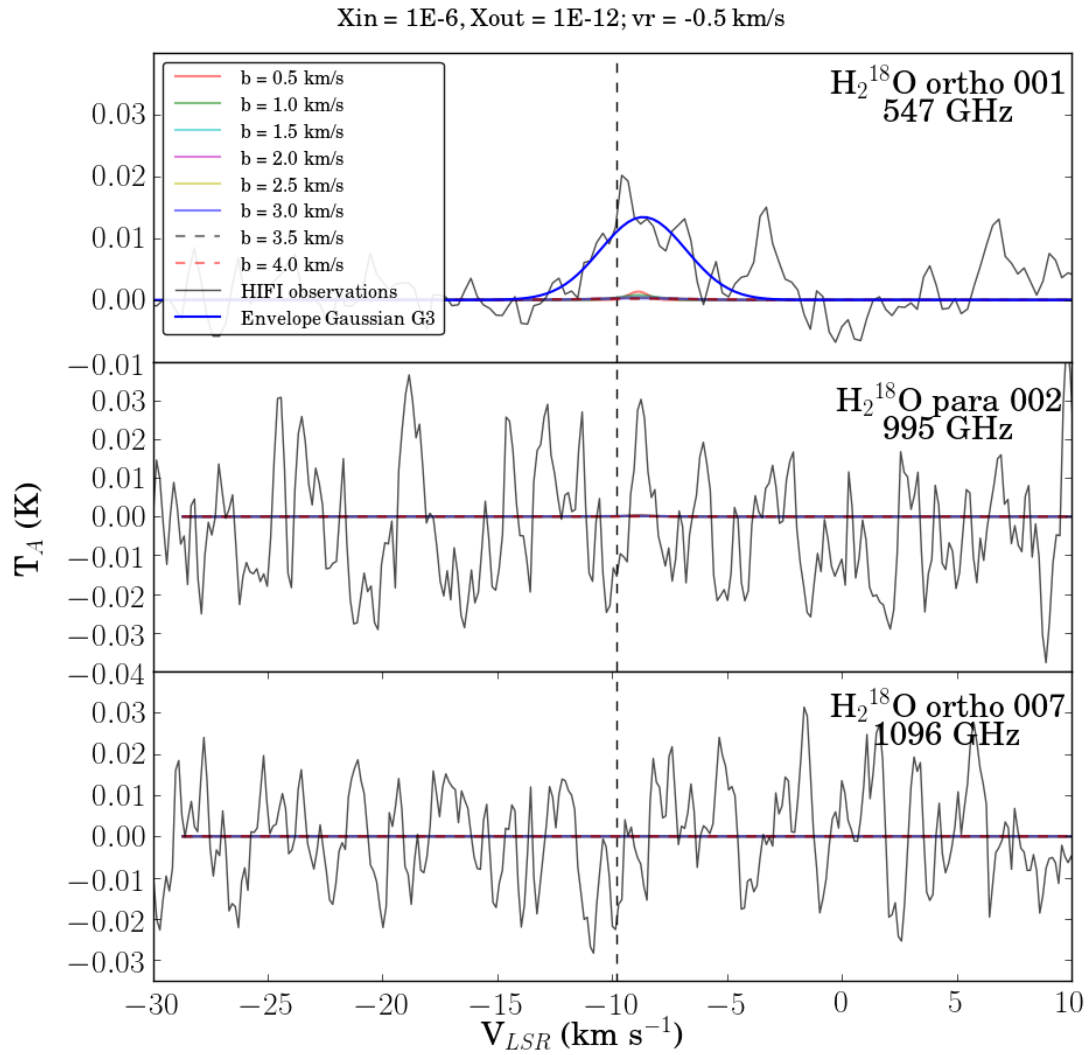
Figure 4.17: Same as Figure 4.16, but for outer abundance of $X_{out} = 1 \times 10^{-12}$. This outer abundance is much too small as it is not consistent with the Gaussian fit to the HIFI data. The non-detections in the excited lines are consistent with the data.
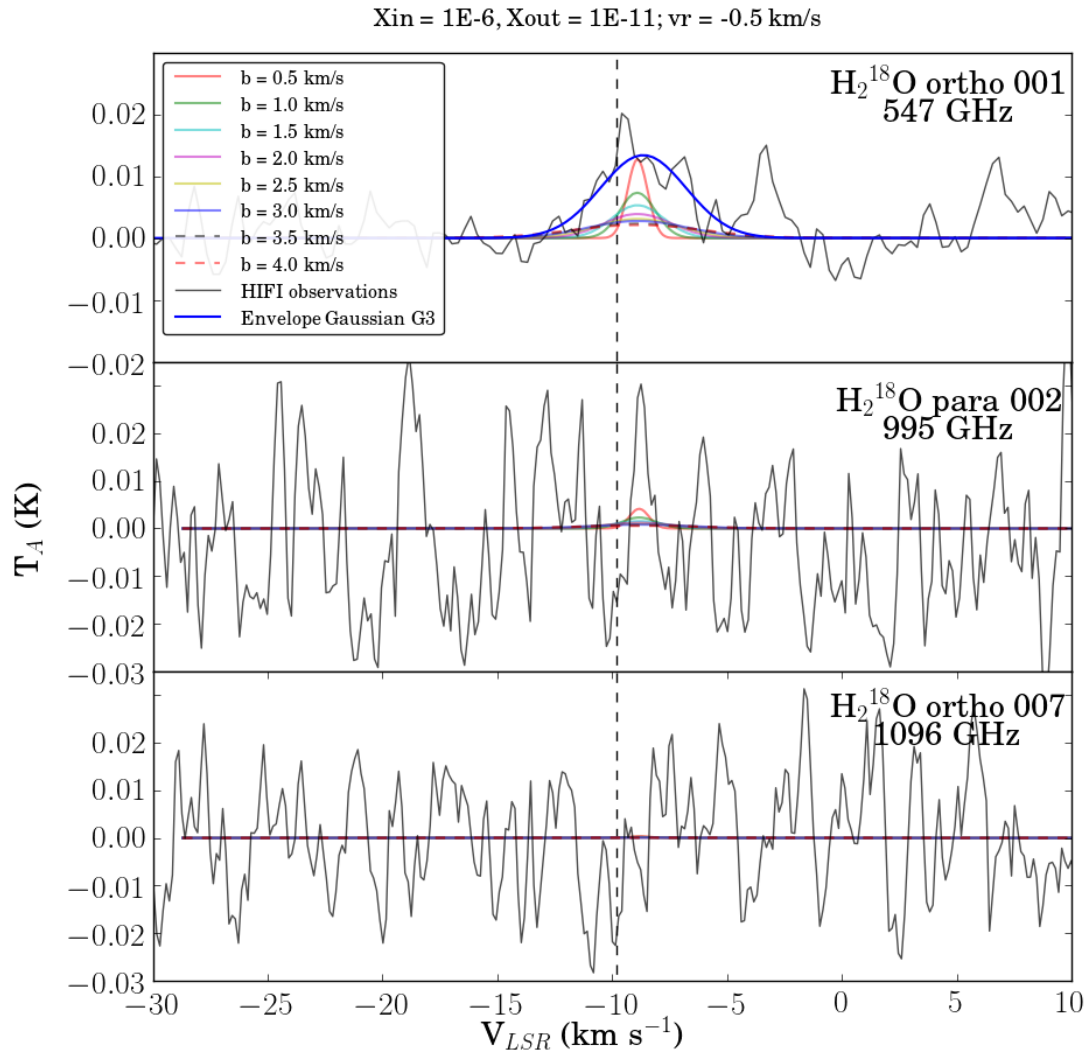
Figure 4.18: Same as Figure 4.16, but for outer abundance of $X_{out} = 1\times10^{-11}$. This outer abundance is more consistent with the Gaussian fit to the HIFI data. The slight to non-detections in the excited lines are consistent with the data.
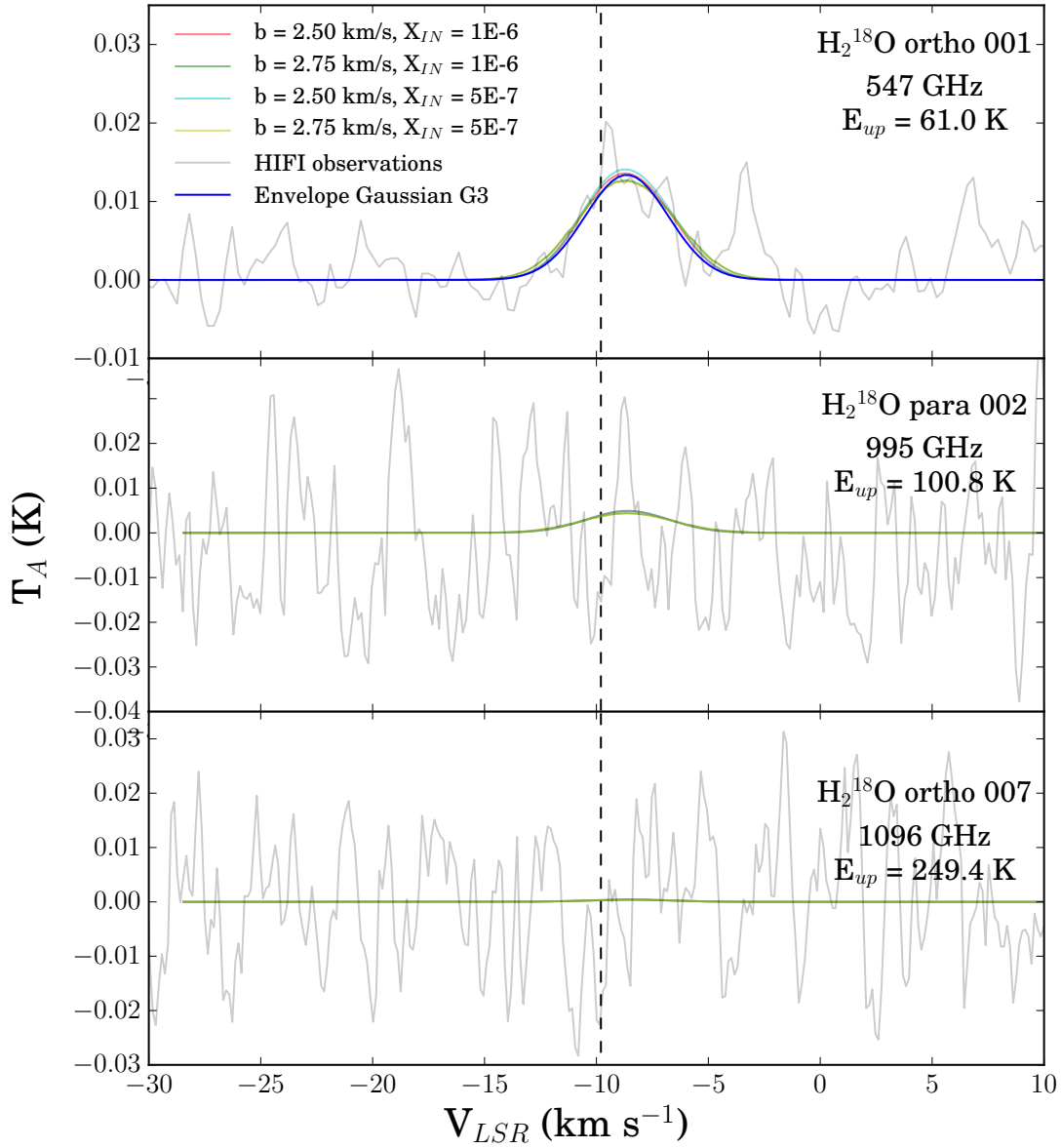
Figure 4.19: Considering the results from Figures 4.16 - 4.18. $X_{out} = 5 \times 10^{-11}$, vr = FF (1 $M_\odot$). $X_{in} = 1 \times 10^{-6}$ (red and green), and $X_{in} = 5 \times 10^{-7}$ (cyan and yellow). $b = 2.50$ km s^{-1} (red, cyan) and $b = 2.75$ km s^{-1} (green, yellow). All 4 radiative transfer models appear to fit the HIFI observational data quite well.

Table 4.15: Running a series of models comparing two parameters (b_{in} vs. b_{out}) for the purpose of analysing their spectral fits via chi-sq tests. Models labelled R1 - R81. Plotted in Figures 4.20 - 4.21. Models R26 - R81 added for a more complete picture. Turbulent velocity b units = km s^{-1}. $X_{in} = 1 \times 10^{-7}$, $X_{out} = 4.8 \times 10^{-11}$, vr = FF.

b_{in}	0.5	0.75	1.0	1.5	2.0	2.5	3.0	3.5	4.0
$b_{out} = 0.5$	R1	R26	R2	R27	R3	R28	R4	R29	R5
$b_{out} = 0.75$	R30	R31	R32	R33	R34	R35	R36	R37	R38
$b_{out} = 1.0$	R6	R39	R7	R40	R8	R41	R9	R42	R10
$b_{out} = 1.5$	R43	R44	R45	R46	R47	R48	R49	R50	R51
$b_{out} = 2.0$	R11	R52	R12	R53	R13	R54	R14	R55	R15
$b_{out} = 2.5$	R56	R57	R58	R59	R60	R61	R62	R63	R64
$b_{out} = 3.0$	R16	R65	R17	R66	R18	R67	R19	R68	R20
$b_{out} = 3.5$	R69	R70	R71	R72	R73	R74	R75	R76	R77
$b_{out} = 4.0$	R21	R78	R22	R79	R23	R80	R24	R81	R25

This information is plotted in a traditional manner in Figure 4.21. This version of the plotted data emphasizes the minimization of the chi-squared values for radiative transfer models that occur between approximately $2.0 < b_{out} < 2.5$ km s^{-1}. From these plots, we constrain the outer turbulent velocity between $2.0 < b_{out} < 2.5$ km s^{-1} for H$_2^{18}$O, with little effect contributed by the inner turbulent velocity.

In attempt to further constrain the outer turbulent velocity, grid models X1-X25 investigate the outer turbulent velocity and the inner abundance of H$_2^{18}$O. The idea behind this is that compared to an unconstrainable parameter, we should be able to put tighter constraints on b_{out}. The grid model parameters are tabulated in Table 4.16 and plotted in Figure 4.22 (colour plot) – 4.23 (traditional plot). For this grid of models, $X_{out} = 4.8 \times 10^{-11}$, $v_r = $ FF(1.1 M$_\odot$), and the outer $b = 2.0$ km s^{-1}. The 95% and 90% confidence levels are indicated on the colour plot, at $\chi^2 = 0.593$ and $\chi^2 = 0.632$, respectively. The colour plot indicates a well defined constraint; there is a clear minimum χ^2 value at ~ 2.25 km s^{-1}, at confidence greater than 95%. The inner abundance does not seem to have an effect on the models, as expected. This is confirmed by the traditional plot. This grid model constrains the outer turbulent velocity b ~ 2.25 km s^{-1} at confidence greater than 95%.
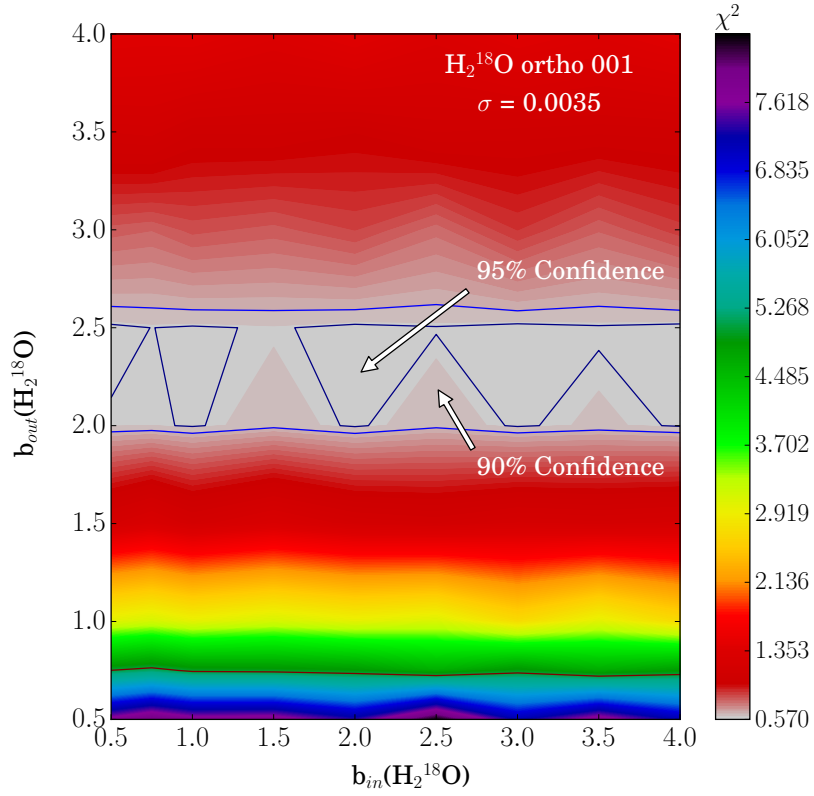
Figure 4.20: Models R1-R81: Comparing inner and outer b for ground state ortho (o001) $H_2^{18}O$. $X_{out} = 4.8 \times 10^{-11}$, X_{in} 1×10^{-7}, and vr = FF(1.1 $M_\odot$). The 95% and 90% confidence levels are indicated on the colour plot, at $\chi^2 = 0.593$ and $\chi^2 = 0.632$, respectively. The 95% confidence level indicates that the best fit radiative transfer models occur for approximately $2.0 < b_{out} < 2.5$ km s^{-1}.
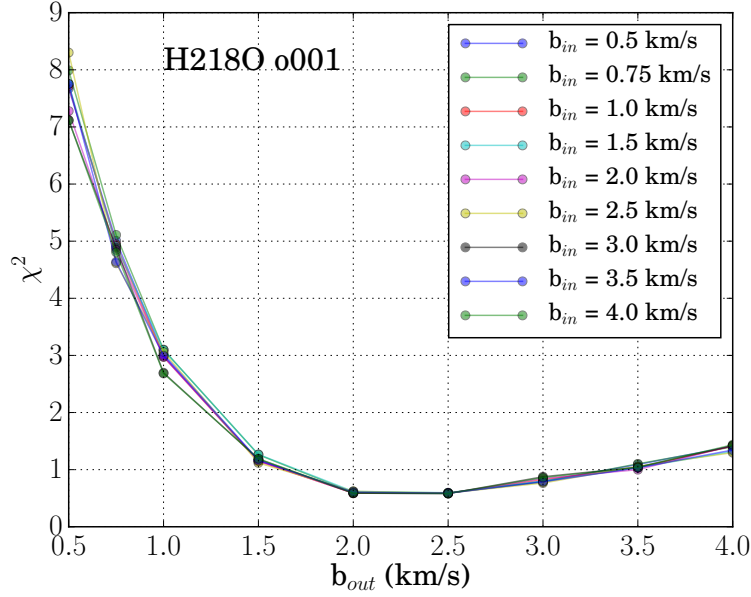
Figure 4.21: Comparing inner and outer turbulent velocity for ground state ortho (o001) $H_2^{18}O$. Same data presented as in Figure 4.20. The chi-squared values are minimized for radiative transfer models that occur between approximately $2.0 < b_{out} < 2.5$ km s^{-1}, as seen in the corresponding colour plot. The inner turbulent velocity does not seem to have an effect on the fit of the models. The addition of models between 2.0 and 2.5 km s^{-1} would be beneficial.

Table 4.16: Grid models comparing two parameters (b_{out} vs. X_{in}) for the purpose of analysing their spectral fits via chi-sq tests. Models labelled X1 - X24. Plotted in Figures 4.22 - 4.23. $X_{out} = 4.8 \times 10^{-11}$, $b = 2.0$ km s^{-1}, vr = FF.

	$b_{out} = 1.5$	$b_{out} = 1.75$	$b_{out} = 2.0$	$b_{out} = 2.25$	$b_{out} = 2.5$
$X_{in} = 10^{-8}$	X1	X2	X3	X4	X5
$X_{in} = 10^{-7}$	X6	X7	X8	X9	X10
$X_{in} = 10^{-6}$	X11	X12	X13	X14	X15
$X_{in} = 10^{-5}$	X16	X17	X18	X19	X20
$X_{in} = 10^{-4}$	X21	X22	X23	X24	X25
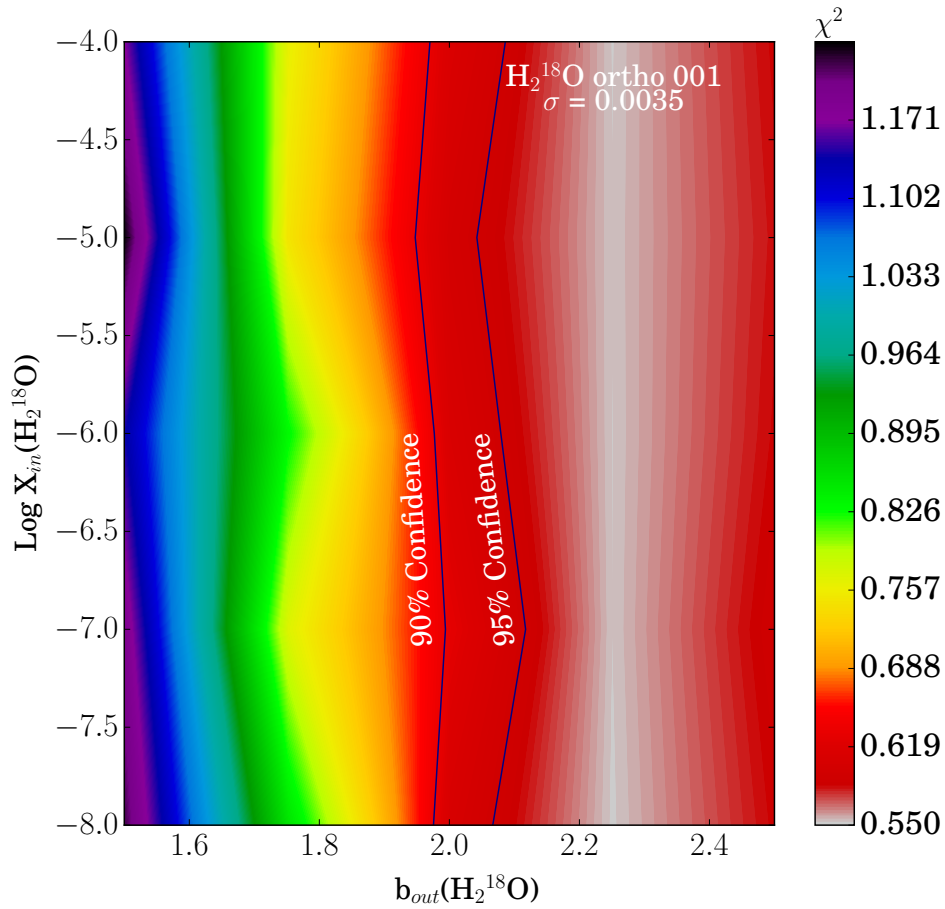
Figure 4.22: Chi-squared tests X1-X25. Comparing b_{out} and X_{in} for ground state ortho (o001) $H_2^{18}O$. $X_{out} = 4.8 \times 10^{-11}$, vr = FF (1.1 $M_\odot$), $b_{out} = 2.0$ km s^{-1}. The 95% and 90% confidence levels are indicated on the colour plot, at $\chi^2 = 0.593$ and $\chi^2 = 0.632$, respectively. This colour plot is well defined; there is a clear minimum χ^2 value ~ 2.25 km s^{-1}, at confidence greater than 95%.
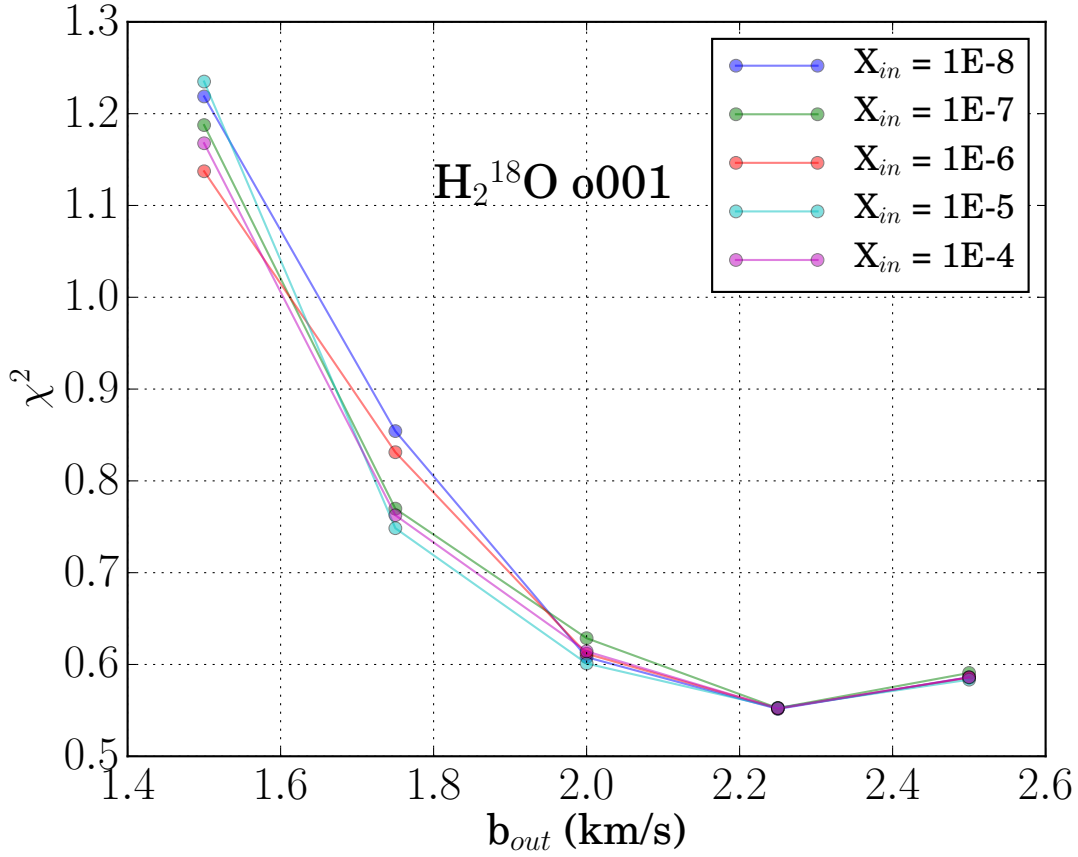
Figure 4.23: Comparing outer turbulent velocity and inner abundance for ground state ortho (o001) $H_2^{18}O$. Same as in Figure 4.22. The minimum χ^2 is well defined; there is a clear minimum χ^2 value ~ 2.25 km s^{-1}, at confidence greater than 95%, for an inner abundance range of $1 \times 10^{-8} - 1 \times 10^{-4}$.

These model grids investigate the best fit for the $H_2^{18}O$ Doppler broadening parameter, with a result $b_{out} = 2.25 \pm 0.25$ km s^{-1}. Applying this same fit to $H_2^{16}O$ yields RATRAN modelling results that are satisfactory for a majority of the lines, however; the $H_2^{16}O$ 3_{12}-3_{03} line would likely require a larger modelled turbulent velocity. Because we want to find a consistent model across the lines, we consider the effect of a larger inner turbulent velocity - 4.5 km s^{-1} instead of 2.25 km s^{-1}. From optical depth plots seen later, we know that the inner envelope must not contribute much to the RATRAN spectral line, if at all, so we expect minimal alterations to the produced spectral line. This is confirmed in Figure
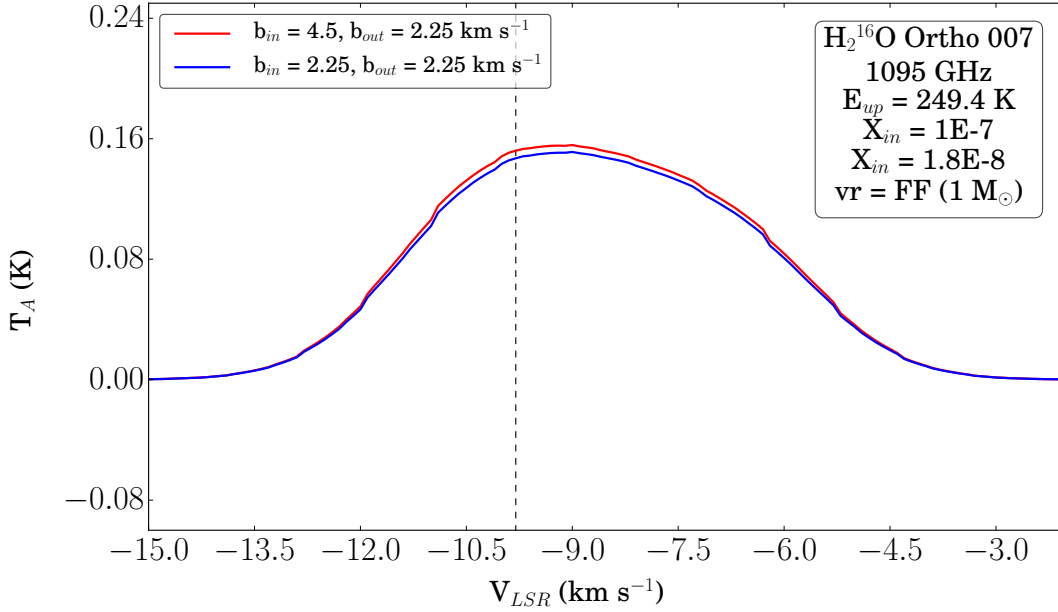
Figure 4.24: Doubling the Inner turbulent velocity b. The best fit model is plotted in blue, the increased inner turbulent velocity model is plotted in red. The inner abundance is held at $X_{in} = 1 \times 10^{-7}$, the outer abundance is held at $X_{out} = 1.8 \times 10^{-8}$, and the radial velocity is considered to be free-falling towards a $1.1 M_{\odot}$ central mass. The vertical dashed line indicates the v_{LSR} for NGC 7129 FIRS 2.

4.24; the best fit model is plotted in blue, the increased inner turbulent velocity model is plotted in red. The inner abundance is held at $X_{in} = 1 \times 10^{-7}$, the outer abundance is held at $X_{out} = 1.8 \times 10^{-8}$, and the radial velocity is considered to be free-falling towards a $1.1 M_{\odot}$ central mass.

Summary: Turbulent Velocity   Altering the turbulent velocity b in RATRAN adjusts the width of the resultant spectral line. For $H_2^{18}O$, it is determined at confidence greater than 95% that with a power law density of $\alpha = 1.5$, we expect an outer envelope best fit of $b_{out} = 2.25 \pm 0.25$ km s^{-1}. The turbulent velocity is expected to be the same for $H_2^{16}O$. The grid exercises presented in this section add to the notion that the inner envelope is not contributing to the RATRAN spectral lines.
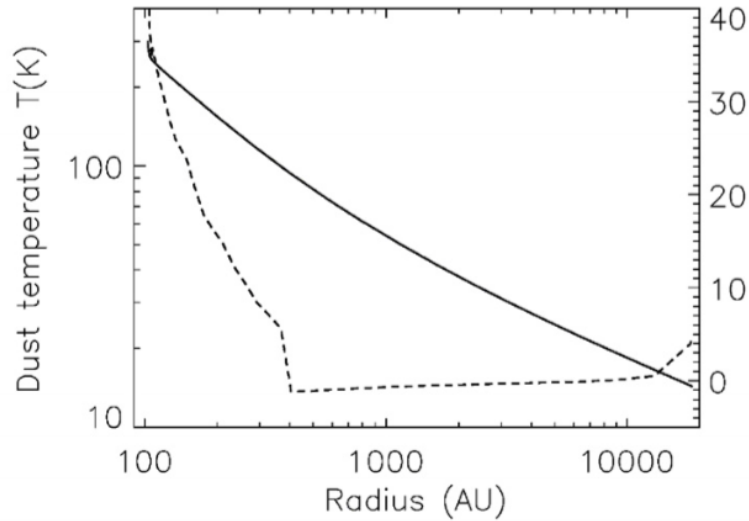
Figure 4.25: NGC 7129 FIRS 2 dust temperature profile from the Crimier et al. (2010) best-fit model. The dashed line represents the difference between the dust and gas temperature derived using $X(H_2O)in = 1 \times 10^{-5}$ and $X(H_2O)out = 1 \times 10^{-7}$ (scale on right axis). From Crimier et al. (2010), Figure A13a.

4.5.5 Gas and Dust Temperature

Although the main parameters varied in the 1D radiative transfer code RATRAN haven't yet included gas and dust temperature in this work (since they were derived by Crimier et al. (2010)), they *can* be altered. As mentioned in Crimier et al., it is possible that these temperatures aren't thermally coupled. These authors actually note for NGC 7129 FIRS 2, the difference between dust and gas temperature can reach a maximum of 40 K. They also note in the inner region of the envelope, the gas is colder than the dust in a small region just where the icy mantles are predicted to sublimate. See the dashed line in Figure 4.25, representing their derived dust to gas difference, corresponding to the right axis scale.

This thesis will briefly investigate the effects of increasing the gas temperature 10% higher than the dust temperature on the successfully modelled $H_2^{18}O$ molecular line, as well as decreasing the dust temperature by 10%. The effects of the temperature differences as determined by Crimier et al. (2010) (Figure 4.26) will also be investigated and compared to the thermally coupled $H_2^{18}O$ model already constrained. All of these temperature cases can be found in Figure 4.27.

For $H_2^{18}O$, the increase in gas temperature 10% above the dust temperature results in a molecular line intensity increase. Reproducing the Crimier et al. gas and dust temperature model doesn't have a large effect compared to the $T_d = T_g$ case - these are nearly identical. Lastly, the decrease in dust temperature 10% below the gas temperature results in a molecular line intensity decrease. This decrease is greater than the increase of the $1.10T_d$ model. The Crimier thermally decoupled model is in green, the equal temperature model is in cyan, the 10% gas temperature increase model is in red, and the 10% dust temperature decrease model is in yellow. In the latter figure, it is seen that the Crimier et al. model is just slightly more intense than the thermally coupled model for $H_2^{18}O$. The ratio of the 10% gas increase to the suggest Crimier et al. model is $T_A(10\%)/T_A(Crimier)$ $= 1.14$.
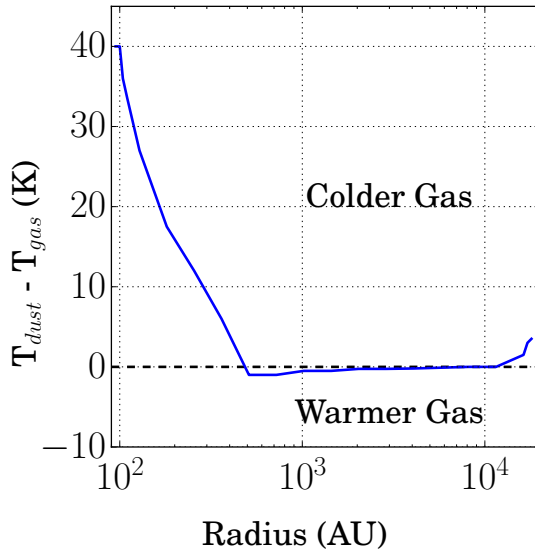
Figure 4.26: NGC 7129 FIRS 2: T_{dust} - T_{gas}. Values extracted from Figure 4.25, used to generate new RATRAN model.

From this short study, we can deduce that altering the gas temperature proportionally alters the peak antenna temperature. For this particular model, the outermost shells have the greatest effect on the lines due to the optical depth; thus, these shells are the only ones contributing to this temperature study. The 10% increase line still fits the HIFI observational data. That being said, if the gas temperature were to be increased by greater than 10%, the peak antenna temperature would increase further and no longer fit.
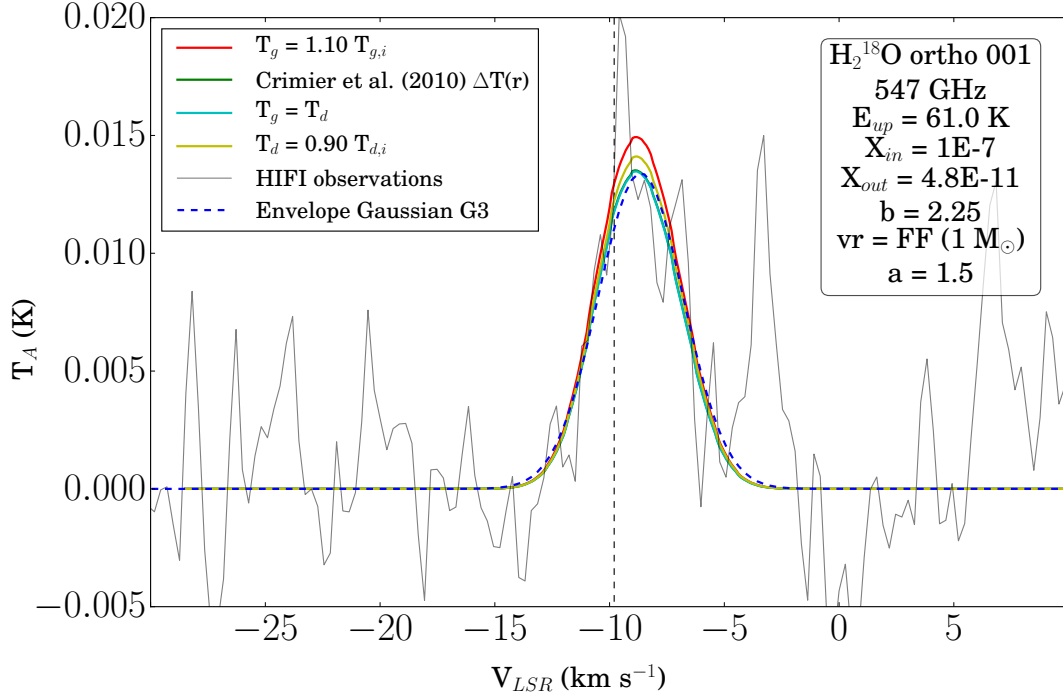
Figure 4.27: Results of varying gas temperature with respect to the dust temperature in RATRAN. All other variables are held constant: X_{in} ($H_2^{18}O$) = 1×10^{-7}, X_{out} ($H_2^{18}O$) = 4.8×10^{-11}, b = 2.25 km s^{-1}, and vr = free-fall towards $1M_\odot$ central mass. The 10% gas temperature increase = red, the Crimier et al. model = green, the thermally coupled model = yellow, and 10% dust temperature decrease. T_A(red, 10%)/ T_A(green, Crimier).

Summary: Gas and Dust Temperature   In summary, altering the gas temperature proportionally alters the peak antenna temperature (similar to the abundance and radial velocity).

4.5.6   Freeze-out Temperature

At a specific region within the envelope of a star formation region, water is expected to freeze out onto dust grains. This freeze-out region is included in RATRAN models by lowering the abundance after 100 K. This divides the envelope into two regions, 'inner' and 'outer'.

Table 4.17: Running a series of models comparing two parameters (X_{out} vs. T_{FO}) for the purpose of analysing their spectral fits via chi-sq tests. Models labelled W1 - W24. Plotted in Figures 4.28 - 4.29. X_{in} = 1E-7, b = 2.0 km s^{-1}, vr = FF. Parameters for models T1-T4 are also given in the bottom table segment.

X_{out} ($\times 10^{-11}$)	3	4	5	6	7	8
T_{FO} = 65.5	W1	W2	W3	W4	W5	W6
T_{FO} = 80.8	W7	W8	W9	W10	W11	W12
T_{FO} = 101.3	W13	W14	W15	W16	W17	W18
T_{FO} = 129.3	W19	W20	W21	W22	W23	W24
Date/ID	Tested Parameter	X_{in}	X_{out}	b (km s^{-1})	vr (km s^{-1})	Figure
	T_{FO} = 80.8 K	1×10^{-7}	4.8×10^{-11}	2.25	FF	4.30
2018/03/26	T_{FO} = 101.3 K	1×10^{-7}	4.8×10^{-11}	2.25	FF	4.30
T1-T4	T_{FO} = 129.3 K	1×10^{-7}	4.8×10^{-11}	2.25	FF	4.30
	T_{FO} = 65.5 K	1×10^{-7}	4.8×10^{-11}	2.25	FF	4.30

The model grid W1 - W24 is tabulated in Table 4.17 and investigates the best fit model with respect to outer envelope abundance and freeze-out radius for ground state ortho (o001) H$_2^{18}$O. It is assumed that water freezes out onto dust grains at $\sim$ 100 K; but what if it doesn't in NGC 7129 FIRS 2? For these models, freeze-out temperatures are varied (65.5, 80.8, 101.3, 129.3 K), and the outer envelope abundance is varied from $3 - 8 \times 10^{-11}$. The inner abundance is held constant at 1×10^{-7}, the infall velocity is taken to be in free-fall towards a central mass of 1.1 M$_\odot$, and the turbulent velocity is held constant at 2.0 km s^{-1} for both inner and outer envelope. Chi-squared values are calculated for the grid of models and presented in the colour plot in Figure 4.28. The 95% and 90% confidence levels are indicated on the colour plot, at $\chi^2 = 0.593$ and $\chi^2 = 0.632$, respectively. Both confidence level contours do not seem to be defined well enough; this colour plot would benefit from additional models. That being said, the region most requiring definition (between 85 – 110 K) falls between shells. In order to complete this picture, the density and temperature model would need to be increased from 22 shells. No constraints can be placed based on this information. This data is plotted in the traditional manner in Figure 4.29. From these, it is seen that the chi-squared values are minimized between outer abundances of $4 - 5 \times 10^{-11}$, although this depends on which freeze-out temperature is associated. As freeze-out temperature increases, the outer abundance at

which the chi-square is at a minimum increases. Again, this particular analysis would benefit from additional models and additional shells; no constraints can be placed on the freeze-out radius of NGC 7129 FIRS 2 by this particular analysis.
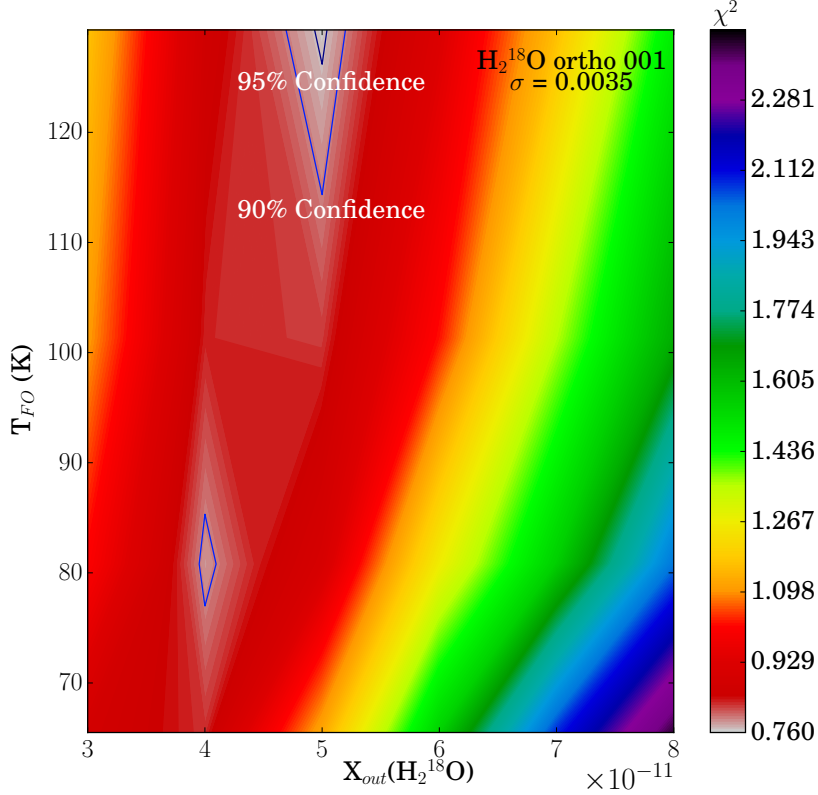
Figure 4.28: W1-W24: Comparing X_{out} and freeze-out temperature T_{FO} for ground state ortho (o001) $H_2^{18}O$. $X_{in} = 1 \times 10^{-7}$ 1.1 $M_\odot$, and the turbulent velocity is held constant at 2.0 km s^{-1} both inner and outer envelope. Freeze-out temperature = 65.5, 80.8, 101.3, 129.3 K. The 95% and 90% confidence levels are indicated on the colour plot, at $\chi^2 = 0.593$ and $\chi^2 = 0.632$, respectively.

To actually see what the spectral differences are when increasing or reducing the freeze-out temperature, and thus the region considered the "outer" envelope, a comparison of these temperatures is made in radiative transfer models T1-T4 for ortho (o001) $H_2^{18}O$ 547 GHz, described in Table 4.17 and plotted in Figure 4.30. These models hold constant inner abundance $X_{in} = 1 \times 10^{-7}$, outer abundance $X_{out} = 4.8 \times 10^{-11}$, $b = 2.25$ km s^{-1},

and free-fall infall velocity. Freeze-out temperature is increased from 65.5, 80.8, 101.3, and 129.3 K, effectively increasing the number of shells considered as outer envelope. An increase in freeze-out temperature results in a decrease of amplitude; this means an increase in outer-envelope region size decreases the emission contribution. This is consistent with an increase in the colder outer envelope increasing the absorption of hotter inner region molecules.
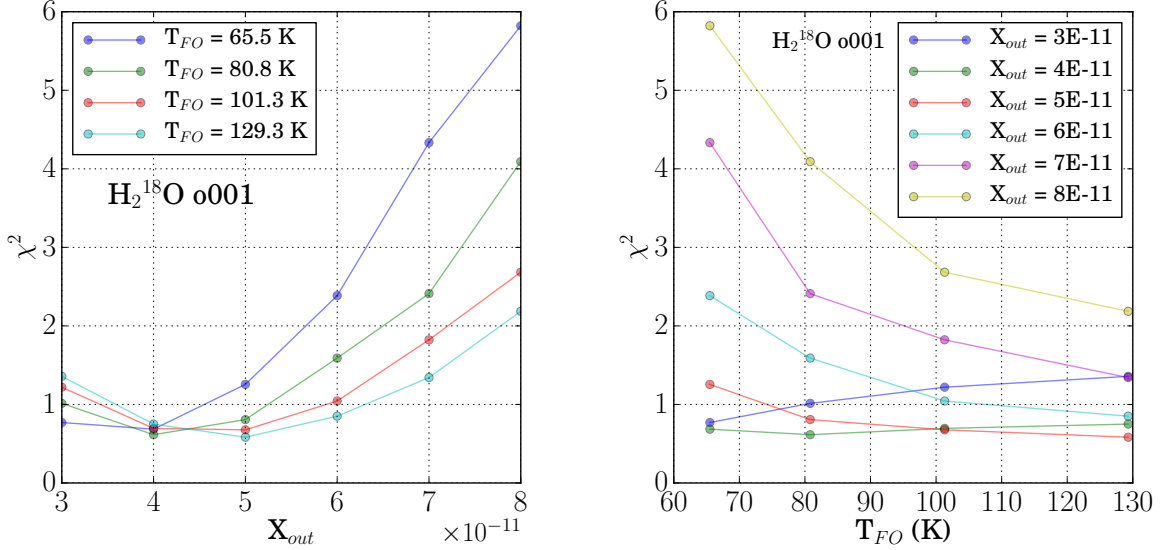
Figure 4.29: X_{out} vs. χ^2(left) and Freeze-out Temperature vs. χ^2 (right). Comparing outer abundance and freeze-out temperature for ground state ortho (o001) $H_2^{18}O$ 547 GHz. The chi-squared values are minimized between outer abundances of $4 - 5 \times 10^{-11}$, although this depends on which freeze-out temperature is associated. As freeze-out temperature increases, the outer abundance at which the chi-square is at a minimum increases. This analysis would benefit from additional models. That being said, the region most requiring definition (between $85 - 110$ K) falls between shells. In order to complete this picture, the density and temperature model would need to be increased from 22 shells.
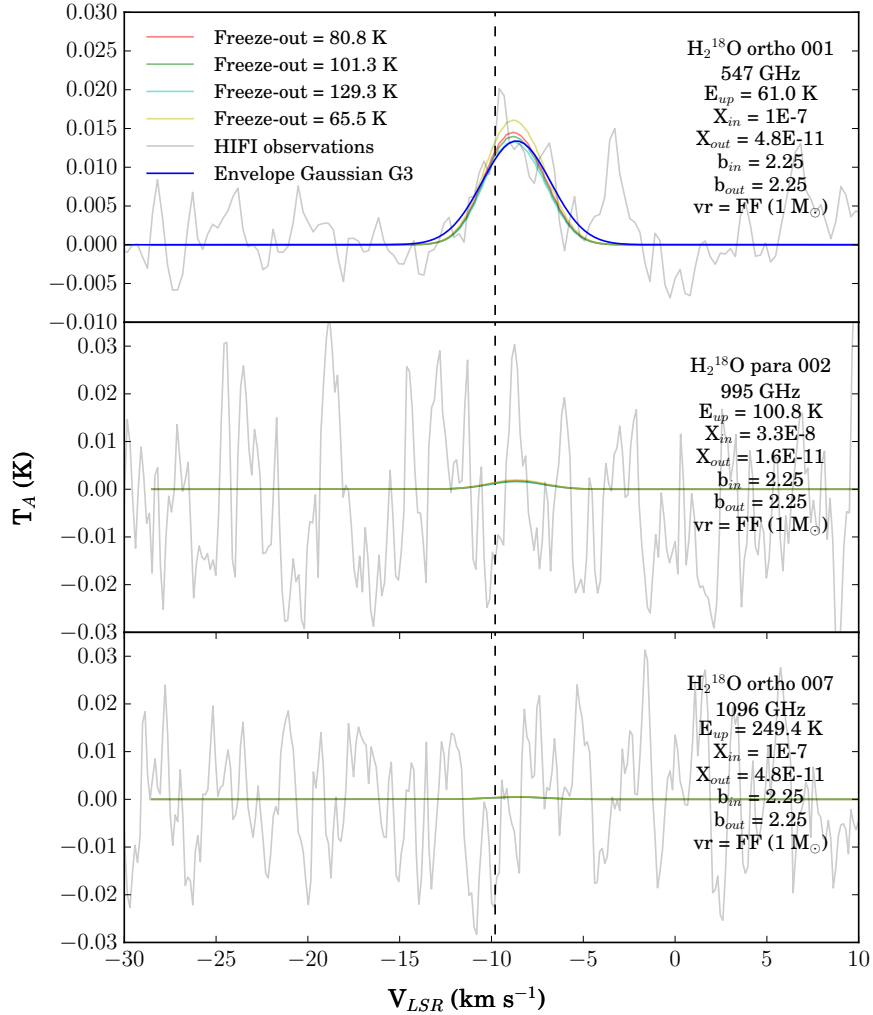
Figure 4.30: Varying the freeze-out temperature for radiative transfer models of ground state ortho (o001) $H_2^{18}O$ 547 GHz and excited states (p002, o007) 995 GHz, 1095 GHz respectively. Holding constant inner abundance $X_{in} = 1 \times 10^{-7}$, outer abundance $X_{out} = 4.8 \times 10^{-11}$, $b = 2.25$ km s^{-1}, and free-fall infall velocity. Freeze-out temperatures are increased from 65.5, 80.8, 101.3, and 129.3 K, effectively increasing the number of shells considered as "outer envelope". An increase in freeze-out temperature results in a decrease of amplitude; this means an increase in outer-envelope region size decreases the emission contribution.

Another way to investigate the effects of altering the freeze-out radius is by looking at the AMC output fractional populations. Figure 4.31 presents the fractional population as a function of RATRAN shell for each of the varied freeze-out temperatures mentioned (65.5, 80.8, 101.3, and 129.3 K) for the $H_2^{18}O$ 547 GHz line. Overall, the curves follow a similar trend throughout the inner envelope until their respective freeze-out temperatures, diverge slightly, then converge again in the extremities of the outer envelope.

Each of the curves in the ground state (panel 1 - top left) begin at $f_1 \sim 0.06$ (omitting the first 0-density shell), increase to $f_1 \sim 0.2$ at 65.5 K (shell 7), then increase to a steeper slope in what is considered the "outer envelope" for each of the models. Moving the freeze-out temperature inward causes the ground state fractional population to increase sooner. The first excited state (panel 2 - top center) curves begin at $f_2 \sim 0.065$ (again omitting the first 0-density shell), increase to $f_2 \sim 0.15$ at 65.5 K (shell 7), then undergo a turning point at their respective freeze-out temperatures. The curves then decrease to ~ 0.0 by shell 22. Moving the freeze-out radius inwards causes f_2 to decrease sooner. The next excited fractional population levels f_3 - f_6 exhibit the same behaviour as f_2, but vary in beginning population, diverging population, and RATRAN shell where $f_n \sim 0.0$. These are tabulated in Table 4.18.

Table 4.18: Trends in population f_n as freeze-out radius is altered. The second column outlines the beginning population level, the third column gives the population at 65.5 K (where curves begin to diverge), and the last column outlines when the curve reaches minimal population. At shell 7, f_4 is already beginning to diverge.

n	f_n (Shell 2)	f_n (Shell 7)	Shell ($f_n \sim 0.0$)
1	0.065	0.18	-
2	0.065	0.15	22
3	0.091	0.16	22
4	0.062	-	15
5	0.094	0.12	15
6	0.077	0.078	14
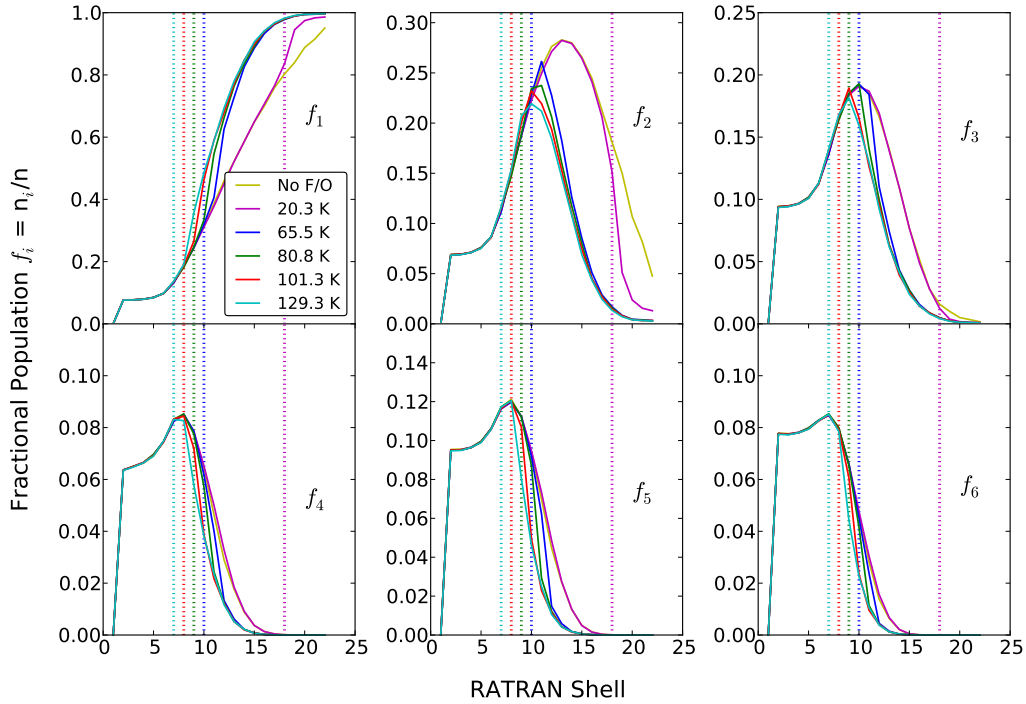
Figure 4.31: Population f_n trends with varying freeze-out temperature, shown as a function of RATRAN shell. Blue = 65.5 K (shell 7), green = 80.8 K (shell 8), red = 101.3 K (shell 9), and cyan = 129.3 K (shell 10). Panel 1 (top-left) = f_1, panel 2 (top-center) = f_2, panel 3 (top-right) = f_3, panel 4 (bottom-left) = f_4, panel 5 (bottom-center) = f_5, panel 6 (bottom-right) = f_6. Vertical dotted lines indicate the freeze-out location for each model in the same colour-scheme.

Summary: Effect of Freeze-out Temperature This RATRAN grid model exercise varied the location of the freeze-out radius within the envelope of NGC 7129 FIRS 2 for the $H_2^{18}O$ 547 GHz line. An increase in freeze-out temperature results in a decrease of amplitude of the modelled spectral line. In other words, an increase in outer-envelope region size decreases the emission contribution. This is consistent with an increase in the colder outer envelope increasing the absorption of hotter inner region molecules. Looking at the RATRAN output a little deeper, moving the freeze-out temperature inward causes the ground state fractional population f_1 to increase sooner and excited f_n to decrease sooner. Numerically, a 25% increase in the freeze-out temperature resulted in a 25% emission intensity reduction.

116

4.5.7 ncell: Number of Spherical Shells

As mentioned in §4.1, the precision of RATRAN spectral line models increases with the number of shells utilized, with the trade off being an increase in computation time. Three different cases will be conducted in this thesis to demonstrate this: 1.) 11 vs. 22 shells, 2.) 22 vs. 42 shells, and 3.) 22 vs. 62 shells.

For the first case, the Herpin et al. (2016) density and temperature model is used to demonstrate the effect of altering the number of shells on the resultant modelled spectral line. RATRAN is executed for models with 11 and 22 shells for all water lines listed in §4.4 ($H_2^{16}O$). As seen in Figure 4.32, increasing the number of shells exaggerates the absorption and emission features slightly.
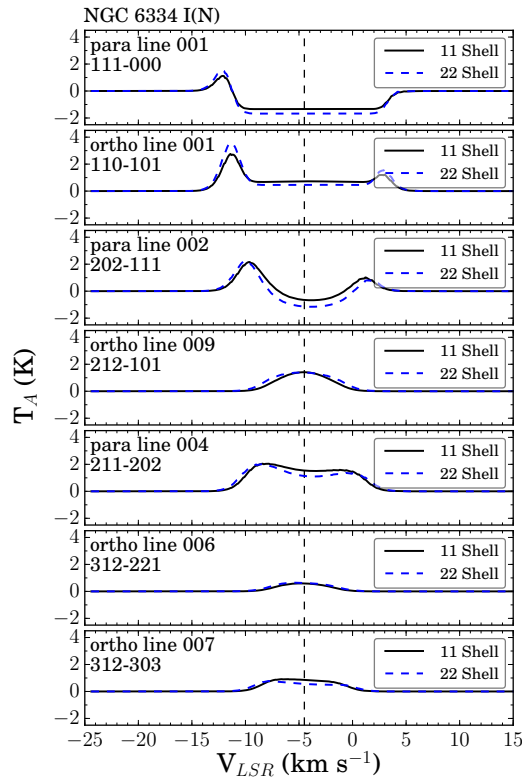
Figure 4.32: RATRAN: Determining effect of altering number of spherical shells from 11 (solid) to 22 (dashed). Using Herpin et al. (2016) model as an example.

117
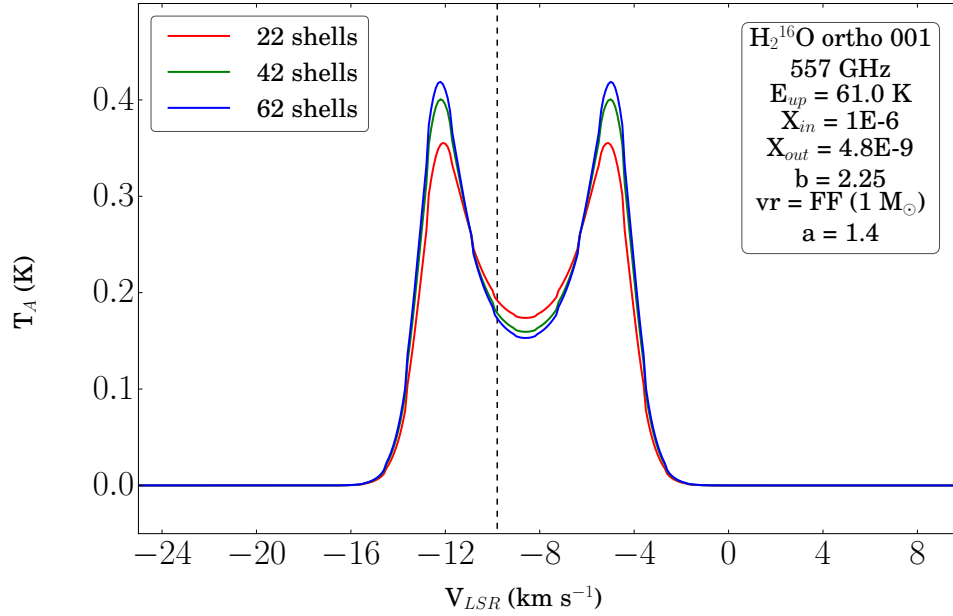
Figure 4.33: RATRAN: Determining effect of altering number of spherical shells from 22 (red) to 42 (green) and 62(blue) shells. Increasing number of shells exaggerates the emission and absorption features. Power law $\alpha = 1.4$, $X_{out} = 4.8 \times 10^{-9}$, $b = 2.25$ km s^{-1}, and $v_r = $ FF.

Comparing the 22 shell case to the 42 and 62 shell cases (Figure 4.33) for $H_2^{16}O$ 547 GHz, it is apparent that as the number of shells increases, the emission and absorption features intensify. In terms of computation time for this particular case, the 22 shell model took 15 minutes to run, the 42 shell model took 30 minutes, and the 62 shell model took approximately 1 hour.

Summary: Effect of Varying ncell   In the 11 shell vs. 22 shell comparison, the increase to 22 shells exaggerates the emission and absorption features slightly ($\lesssim 25\%$) for $H_2^{16}O$. The comparison between the 22 shell model and the 42 and 62 shell models exhibited the same behaviour, with intensity increases of $\lesssim 14\%$ and $\lesssim 20\%$, respectively. Here, this is simulated for $H_2^{18}O$ 547 GHz. Increasing from 42 to 62 shells sees an intensity increase of $\lesssim 5\%$. As the shell number increases, the intensity increase percentage as compared to the previously studied shell number decreases (i.e, 25%, 14%, 5%).

4.5.8 Ortho-to-Para Ratio

Recall from §1.4 that "ortho" refers to a hydrogen bearing species that exhibit aligned proton spins, while "para" refers to anti-parallel proton spins. In order to transition across the ortho-para ladders, a hydrogen nucleus must be exchanged. In colder gas ($T \lesssim 100$ K), the ortho-to-para conversions occur slowly through collisions with protons (Dalgarno, Black, & Weisheit, 1973; Flower & Watt, 1984), where the principle collider is molecular H_2. Note here that *ortho* and *para* are referring to molecular H_2 instead of water:

$$oH_2 + H^+ \rightleftharpoons pH_2 + H^+ \tag{4.10}$$

In warmer regions, reactive collisions with hydrogen atoms control the ortho-to-para conversion (Martin & Mandy, 1993; Tiné et al. 1997):

$$oH_2 + H \rightleftharpoons pH_2 + H \tag{4.11}$$
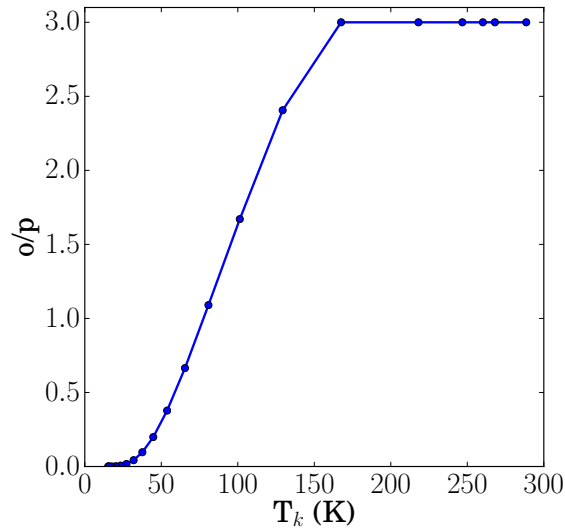
Figure 4.34: H_2 Ortho-to-para ratio as a function of temperature (LTE OPR_T). Values obtained from radiative transfer code RADEX. Markers indicate corresponding RATRAN shell.

Also note that the collision rates are different for all of these cases. When these reactions are fast enough, these transition collisions with H or H^+ drive the ortho-to para ratio to LTE (Sternberg & Neufeld, 1999). The LTE H_2 ortho-to-para ratio is plotted as a function of temperature in Figure 4.34; values were obtained from RADEX models executed for each RATRAN shell examined above (see next chapter). Markers on curve indicate each corresponding RATRAN shell.
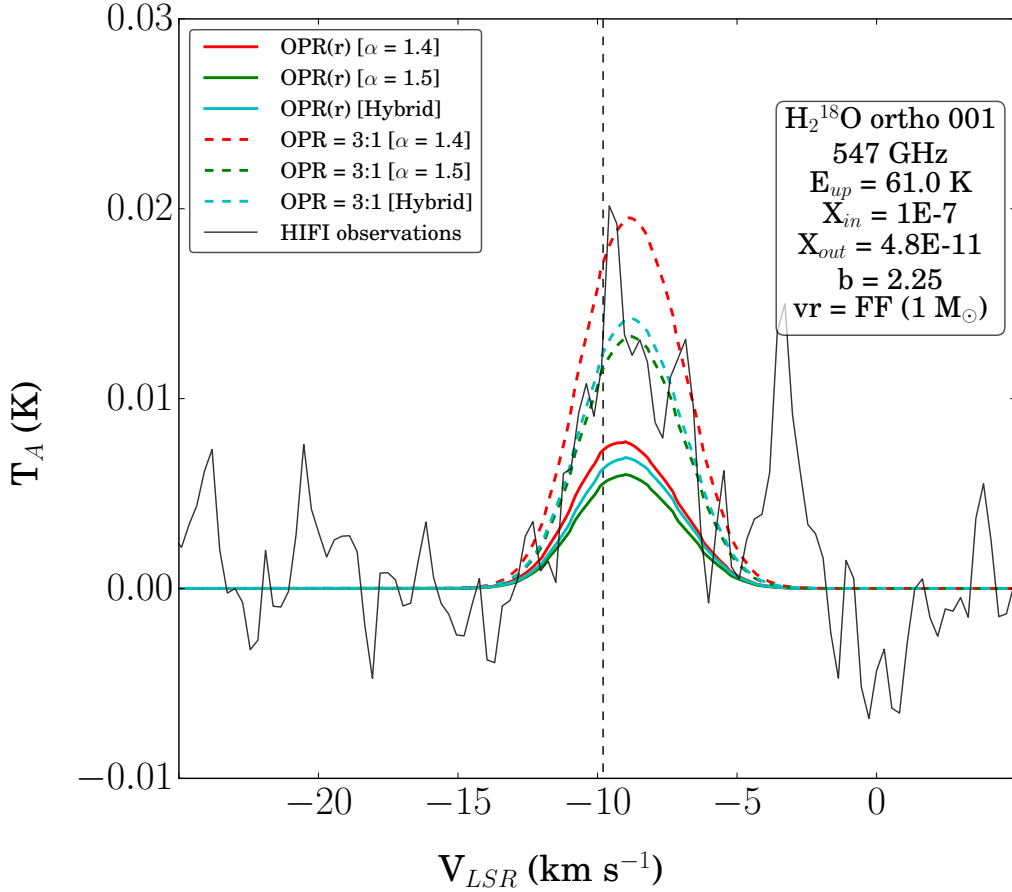
Figure 4.35: Varying the H_2 ortho-to-para ratio (OPR) with temperature for $H_2^{18}O$ ortho 1_{10}-1_{01}. Here, $\alpha = 1.4$ is plotted in red, $\alpha = 1.4$ is plotted in green, and the hybrid model is plotted in cyan. The varying LTE OPR is plotted as solid lines while the constant 3:1 ortho-to-para ratio is plotted as dashed lines. The varying LTE OPR produces an intensity approximately half of that for the constant 3:1 case.

A RATRAN $H_2^{18}O$ model using this varying ortho-to-para H_2 ratio, labelled as LTE OPR(T), is investigated and compared to a model using a constant ortho-to-para ratio of 3:1. In both models, $\alpha = (1.4, 1.5, \text{Hybrid})$, $b = 2.25 \text{ km s}^{-1}$, $v_r = \text{free-fall}$, $X_{in} = 1 \times 10^{-7}$, and $X_{out} = 4.8 \times 10^{-11}$ (Figure 4.35). In the figure, $\alpha = 1.4$ is plotted in red, $\alpha = 1.5$ is plotted in green, and the hybrid model is plotted in cyan. The varying LTE OPR(T) is plotted as solid lines while the constant 3:1 ortho-to-para ratio is plotted as dashed lines. From this plot, the varying LTE OPR(T) produces an intensity approximately half of that for the constant 3:1 case. For this molecule, $H_2^{18}O$, the majority of the emission originates from the outer envelope. At these temperatures, the LTE OPR(T) < 1.25, reaching values of $\sim 10^{-4}$ at the outer radius.
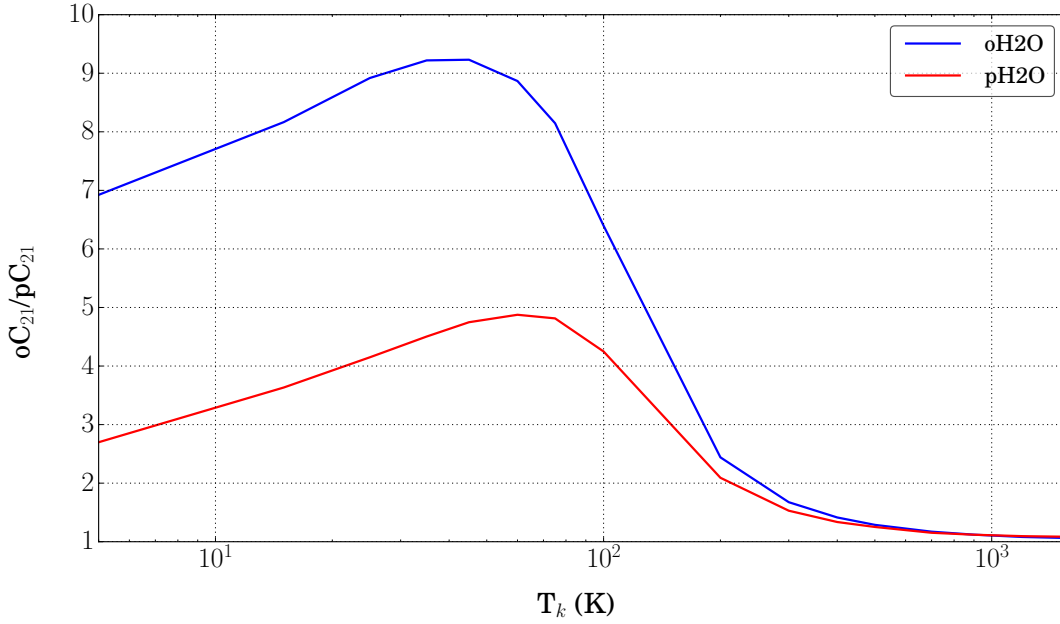
Figure 4.36: Comparing ortho and para water collision rates with ortho and para H_2 for the 2-1 transition (ortho 1_{10}-1_{01}, para 1_{11}-0_{00}). Collision rates with ortho-H_2 oC_{12} are seen to be stronger than para-H_2 collision rates pC_{12} for both ortho and para water. Ortho water collision rates appear to be stronger in general.

Because the total number of hydrogen atoms (which is used to deduce the water abundance) remains the same regardless of which OPR is used, the differences seen plotted are attributed to the change in collision rates with respect to H_2 density. At the temperatures mentioned, the ortho density is much less; because such a strong alteration is made in

intensity of the produced spectral lines, the ortho collision rates must be stronger than the para collision rates. The Daniel et al. (2011) ortho and para H_2collision rates for the ground state ortho water transition 2-1 (blue line) is compared to that of the ground state para water (red line) in Figure 4.36. This confirms that the ortho water collision rates are stronger than that for para water.

Summary: Ortho-to-Para Ratio Varying the ortho-to-para ratio (OPR) with temperature causes the line emission intensity to decrease for the $H_2^{18}O$ 547 GHz line (62.5% line intensity reduction). The outer envelope has such low temperatures that here, the OPR < 1.25, reaching a minimal value of $\sim 10^{-4}$ at the outermost edge.

4.5.9   Collision Rates

Collision Rate Evolution

As seen in Section §1.5 and Chapter §3, state-to-state collision rates are necessary to gain new insight into the role of water in star formation regions via radiative transfer calculations.

Tracing the study evolution of water collision rates begins with Green et al. (1993). Originally, scaled Green et al. H_2O-He quantum collision rates were used for H_2O-H_2 collisions and modelling molecular lines of water. Large differences were observed when these rates were used compared to updated collision rates; line fluxes have been seen to increase by a factor of ~ 10. (Faure et al. 2007). Phillips, Maluendes, and Green (1995) concluded that H2O-H_2 collisional cross-sections, especially ortho-H_2, cannot be adequately represented by the Green et al. water-helium collisions. One year later, Phillips et al. (1996), using the same rotational energies and wavefunctions for water as Green et al. (1993), obtained a rigid body 5D potential energy surface (PES) for the rotational excitations of H_2O-H_2. Using this, they computed rate coefficients for rotational de-excitation among the first 5 ortho and para levels of water with H_2 for T = 20 – 140 K. Dubernet et al. (2002) and Grosjean et al. (2003) extended these rate coefficients in temperature to T = 5 – 140 K. Shortly after, Faure et al. calculated a 9D PES. in 2005, used by Dubernet et al. (2009). Dubernet et al. (2006) used a newly determined 5D PES and extended or revised de-excitation collision rates for the lowest 10 rotational levels of ortho and para water collisions with ortho and para H_2 for a temperature range of T = 5 – 20 K. Faure et al. (2007) provided collisional rates for a temperature range of T = 20 – 2000 K, combining quantum calculations, the Dubernet et al. (2006) calculations, and scaled Green et al. (1993) calculations for the weakest rates.

Recalling the Faure et al. (2007) 9D PES, Dubernet et al. (2009) increased rate coefficients by a factor of 4 at T = 5 K and by 75% at T = 20 K. They showed that the 9D PES led to a significant re-evaluation of the collisional rates for H_2O-pH_2 at temperatures greater than 20 K. The H_2O-oH_2 collisional rates also seemed to be effected, but to a max difference of 40%. Most importantly, Dubernet et al. generated collision rates for 45 levels of oH_2O-pH_2. Comparing to Phillips et al. (1996), the new rates experience a total increase at T = 20 K of 185%. The impact of the 9D PES on both para and ortho H_2 is expected to become less significant at higher temperatures.

Finally, Daniel et al. (2010, 2011), using the 5D PES of Dubernet et al. (2006), calculated state-to-state rate coefficients for 20 levels of pH_2O, and completed the set with oH_2O-oH_2, respectively.

Collision Rates & RATRAN Modelling

Accurate state-to-state collision rates are necessary to gain new insight into the behaviour and role of water in star formation regions (Cernicharo & Crovisier, 2005) and are essential when describing energy exchange processes responsible for molecular line formation (Faure et al. 2007). Water's main collision partners include H, H_2, He, and e^-, but H_2 is the most abundant (H_2 is more abundant than He by a factor of 4-5; Phillips et al. 1994).

A numerical comparison is made in this work of the water collisional cross-sections deduced by Daniel et al. (2010, 2011), Dubernet et al. (2009), Phillips (1994), and Faure (2007). From Table 4.19, collision rates involving pH_2 as calculated by Phillips et al. (1994) are a factor of ~ 2 lower than that calculated by Dubernet et al. (2009) and Daniel et al. (2011). Collisions involving oH_2 are similar. See Daniel et al. (2012) for a more extensive collision rate comparison (they compare Daniel et al. (2010, 2011) with Green et al. (1993), Faure et al. (2007), and Dubernet et al. (2009)).

In short, Daniel et al. (2012) noted for oH_2O-oH_2 collisions, differences in line intensities are modest as long as the water abundance is greater than 10^{-6}. Main differences are found for n_{H_2} less than 10^7 and water abundance $\sim 10^{-8}$. For oH_2O-pH_2 collision rates, they noted a maximum difference occurs at high temperatures and low H_2 volume densities. Larger differences occur at abundances around 10^{-8}.

While carrying out the comparisons above, it was noted that larger differences are experienced at higher energies (Daniel et al. 2012; Faure et al. 2007). There was a common conclusion amongst the comparison sources: oH_2 collision rates are greater than that for pH_2, and population of high energy levels through collisions with oH_2 are favoured. In the absence of radiative pumping by dust photons, quantum and QCT sets relatively

Table 4.19: Comparing Water Cross-sections from Different Authors. Molecular data files obtained from BASECOL (Dubernet et al. 2013). D2011 = Daniel et al. (2011), D2006 = Dubernet et al. (2006), P1996 = Phillips et al. (1996), P1994 = Phillips et al. (1994), F2007 = Faure et al (2007), PES = potential energy surface,QCT = quasi-classical trajectory.

Transition	T (K)	D2011 [5D PES (D2006)]	P1996 [5D PES (P1994)]	F2007 [QCT]
oH_2O - oH_2				
2-1	20	2.884×10^{-10}	2.68×10^{-10}	2.9×10^{-10}
	40	3.098×10^{-10}	2.86×10^{-10}	-
	100	3.074×10^{-10}	2.21×10^{-10}	1.2×10^{-10}
oH_2O - pH_2				
2-1	20	3.35×10^{-11}	1.17×10^{-11}	3.4×10^{-11}
	40	3.35×10^{-11}	1.60×10^{-11}	-
	100	4.05×10^{-11}	2.44×10^{-11}	5.4×10^{-11}
pH_2O - oH_2				
2-1	20	1.198×10^{-10}	1.06×10^{-10}	1.2×10^{-10}
	40	1.295×10^{-10}	1.2×10^{-10}	-
	100	1.471×10^{-10}	1.41×10^{-10}	6.0×10^{-11}
pH_2O - pH_2				
2-1	20	3.05×10^{-11}	1.53×10^{-11}	3.0×10^{-11}
	40	2.79×10^{-11}	1.53×10^{-11}	-
	100	3.08×10^{-11}	1.88×10^{-11}	4.9×10^{-11}

agree to the same order of magnitude. Finally, while excitation by pH_2 is similar to He excitation (within factor of 1-3 larger), simply multiplying the Green et al. (1993) collision rates by a scaling factor isn't accurate enough.

This work carried out calculations using the combination of state-to-state rate coefficients as determined by Dubernet et al. (2006), Dubernet et al. (2009), Daniel et al. (2010), and Daniel et al. (2011).

To determine the sensitivity of RATRAN spectral modelling to the employed collision rates, the Daniel et al. (2011) collisions rates are altered slightly and their effect on the $H_2^{18}O$ ground state 547 GHz line observed. Two approaches were taken for this exercise: 1.) increasing the 2-1 collisional cross section C_{21} for T = 25.0 K by 10% and 2.) increasing C_{21} for all included T (from 0 – 1400 K) by 10%. The effects of this on the ortho $H_2^{18}O$ ground state (2-1) transition are given in Figure 4.37. Here, the first collisional dataset is labelled "fakedata.dat" (green) and the second is labelled "fakedata2.dat" (cyan). These are contrasted with the unaltered Daniel et al. collisional rates (red), the HIFI observations (faded black), and the fitted envelope Gaussian (blue). From this figure, it is clear that the first dataset alteration does not have a large effect on the spectral line; in fact, it has a spectral line intensity increase of a factor of 1.07. The second dataset on the other hand sees an intensity increase of a factor of 4.58. This is likely attributed to the higher temperatures being altered, and is consistent with the conclusion of Daniel et al. (2012) and Faure et al. (2007).

Summary: Collision Rate Coefficients

During the comparisons carried out above, it was noted that larger differences between the sets of collision rates are experienced at higher energies. Additionally, $o-H_2$ collision rates are greater than that for pH_2, and population of high energy levels through collisions with oH_2 are favoured. Increasing the collision rates by 10% increases the spectral line intensity up to a factor of ~ 4.58 for ortho ground state $H_2^{18}O$ (547 GHz).

In the past, Johnstone et al. (2010) modelled NGC 7129 FIRS 2 with RATRAN and scaled Green et al. (1993) H_2O-He collision rates. They deduce an $H_2^{16}O$ outer abundance of $X_{out} \sim 10^{-7}$. It will be seen later in §4.5.11 that this value is an order of magnitude smaller than that calculated in this thesis. That being said, stronger collision rates seem to require a lesser abundance in order for modelling results to be consistent with the observational data. Introducing a stronger collision rate increases the amount of collisions, and therefore increases the line intensity. This is consistent with the results of the 10% collision rate (2-1) increase mentioned above.
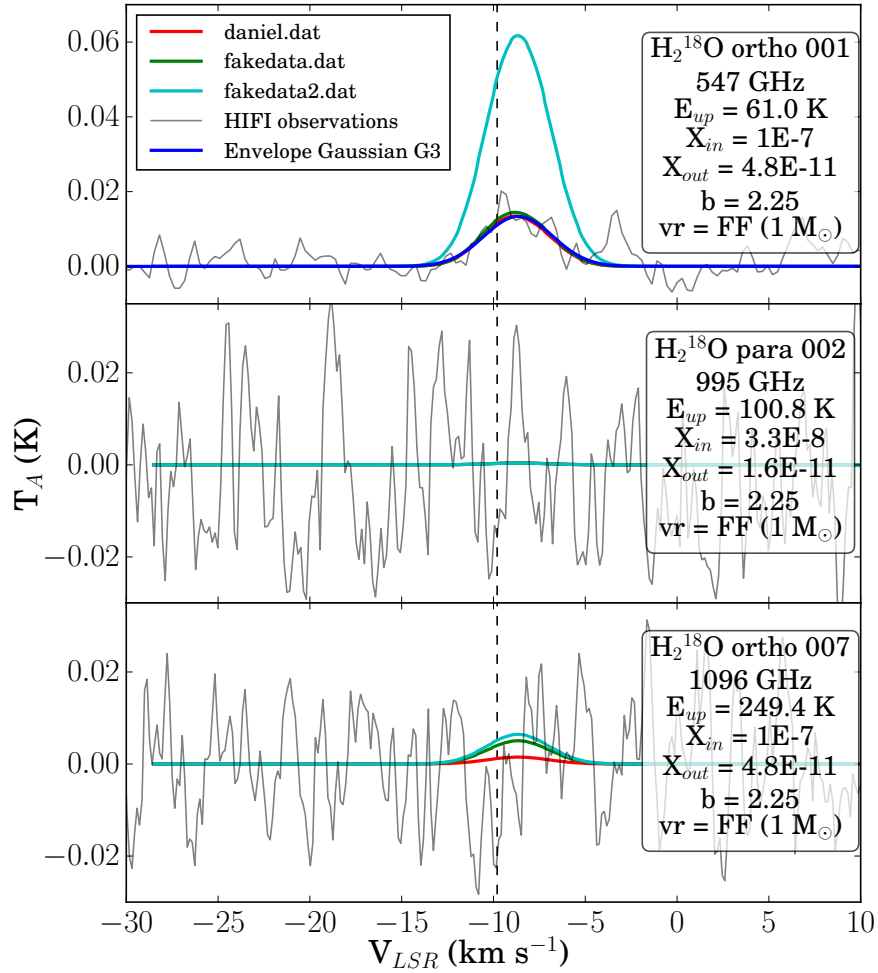
Figure 4.37: RATRAN: effects of altering collision rates. "fakedata.dat" = reduced 2-1 transition for T = 25.0 K ortho and para H_2-H_2O collision rate by a factor of 10. "fakedata2.dat" = reduced 2-1 transition for ortho and para H_2-H_2O collision rates by a factor of 10 for all included T (T = 0–1400 K).

While excitation by pH_2 is similar to He excitation (within factor of 1-3 larger), simply multiplying the Green et al. (1993) collision rates by a scaling factor isn't accurate enough. Excitation by oH_2 is significantly different (i.e, orders of magnitude larger than excitation by He), and non-negligible differences occur for pH_2 at temperatures greater than 60 K (Daniel et al. 2012). At this time, the Dubernet et al. (2006), Dubernet et al. (2009), Daniel et al. (2010), and Daniel et al. (2011) collision rates are the most accurate and up-to-date, and should be used instead of scaled He Green et al. (1993) rates.

4.5.10 Beamsize

A third program was written by Mike Fich to convert the SKY output brightness temperatures to antenna temperatures. SKY generates a .FITS file for each of the desired water lines, which are then convolved with HSO beamsizes to produce antenna temperatures. A baseline is then subtracted by taking the average of the first and last velocity channels, then subtracting this value from each of the velocity channels.

If the beamsize is incorrectly input for whichever reason, this has an effect on the spectral line. The following exercise determines how much of an effect a 10% beamsize variance has on the modelled results of the $H_2^{18}O$ 547 GHz line. The beamsizes and the corresponding baseline subtraction values are listed in Table 4.20. From this table, it is seen that as the beamsize is increased by 10%, the baseline decreases. No patterns are seen in the baseline decrease amount across transitions. In Figure 4.38, the quoted HIFI beamsize convolved result is plotted in green and the 10% increase beamsize convolved result is plotted in red. The HIPE Gaussian representing the envelope contribution is plotted in dashed blue against the HIFI observational data in faded solid black. From this figure, the 10% increase in beamsize reduces the intensity of the spectral line (by increasing the subtracted baseline) by $\sim 15\%$.

Table 4.20: The Roelfsema et al. (2012) beamsizes (θ) compared to a 10% beamsize increase (1.10 θ). The baselines are subtracted during convolution of RATRAN results.

Transition	θ	$T_{A,baseline}$	1.10 θ	$T_{A,baseline}$
o1_{10} - 1_{01}	38.718	0.0362	42.590	0.0233
p2_{02} - 1_{11}	21.318	0.1550	23.450	0.1262
o3_{12} - 3_{03}	19.354	0.1839	21.289	0.1051
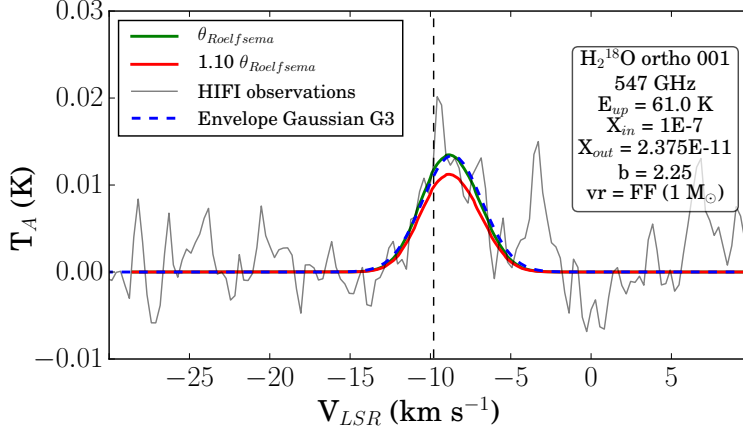
Figure 4.38: Determining the effect of convolving the brightness temperature with the incorrect beamsize. Green = HIFI water beamsize, red = 10% beamsize increase, dashed blue = HIPE envelope Gaussian, and faded black = HIFI observational data. Increasing beamsize decreases intensity.

4.5.11   RATRAN Physical Structure of NGC 7129 FIRS 2

This work's approach to modelling begins with fitting the $H_2^{18}O$ transition lines. Only the ground state ortho line is seen in emission, the p-2_{02}-1_{11} (p002) and o-3_{12}-3_{03} (o007) lines are non-detections. This is confirmed by the RATRAN models. The excited $H_2^{16}O$ lines p-2_{02}-1_{11} (p002) and o-3_{12}-3_{03} (o007) are then fit by applying a similar RATRAN model as that used for the $H_2^{18}O$ lines, while adjusting the abundance to obtain an optimal intensity fit. The deduced $H_2^{16}O$ fit parameters for these two excited lines are then applied to the remaining lines.

As seen in Sections 4.5.3 - 4.5.9, multiple input parameters are tested including the radial velocity, Doppler broadening parameter, water abundance with respect to H_2, dust and gas temperature, ortho-to-para ratio, and freeze-out temperature. While some parameters could not be constrained due to optical thickness in some of the lines (i.e, X_{in}, b_{in}, X_{ratio}), others are constrained very well.
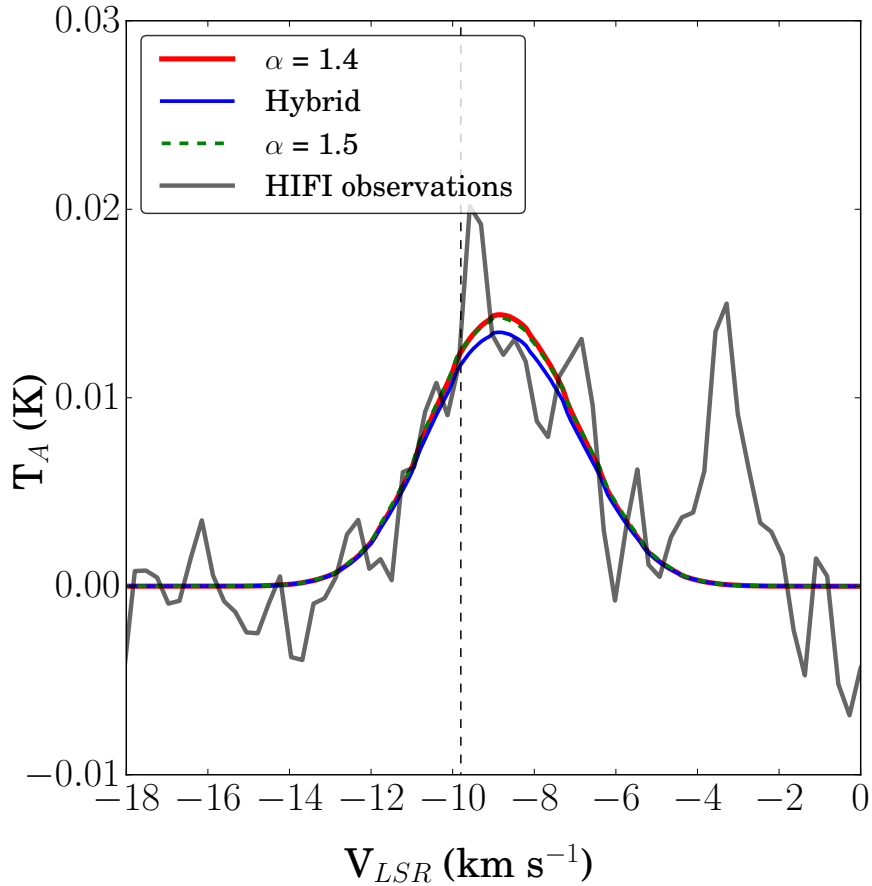
Figure 4.39: Fitting $H_2^{18}O$ 1_{10}-1_{01} for $\alpha = 1.4$ (red), 1.5 (dashed green) and hybrid (blue). HIFI observations plotted in faded black. $X_{out} = 3.5$, 4.8, and 5.2 $\times 10^{-11}$, respectively.

The RATRAN modelling results for each of the power laws studied ($\alpha = 1.4$, 1.5 and hybrid) are listed in Table 4.21 for a 3:1 ortho-to-para ratio (OPR) and Table 4.22 for an OPR that varies with temperature. The final columns of both tables list the calculated p-values, which give the significance of the reduced chi-squared. The null hypothesis is that the models are consistent with the HIFI observations; the alternative hypothesis is that they are not. For the perfect fit to astronomical observations, a reduced chi-square value of $\chi_R^2 \sim 1.0$ is desired; values less than this are considered an "over-fit" while values greater than this are considered an "under-fit" (Andrae, Schulze-Hartung,& Melchior, 2010). From these tables, we see that the RATRAN model fits for both isotopologues have p-values

much less than 0.05, indicating that the null hypothesis is rejected. The reduced chi-squared values indicate $H_2^{18}O$ is overfit, while the ground-state lines for $H_2^{16}O$ are underfit. The reduced chi-squared is closest to 1.0 for the excited-state $H_2^{16}O$ lines. For the purposes of this thesis, we are satisfied with the majority of the RATRAN model fit results; due to the rigorous and in-depth treatment of the model fit optimization, we expect that the goodness of fit has reached its maximum for these molecules. We are thus required to make final physical and chemical parameter assumptions for NGC 7129 FIRS 2 from these subpar fits.

Figure 4.39 presents the final RATRAN models for ground state $H_2^{18}O$ 1_{10}-1_{01} (o001). The model employing a power law of $\alpha = 1.4$ is shown in red, 1.5 is shown in dashed green, and the hybrid model is shown in blue, corresponding to outer abundances of X_{out} = 3.5, 5.2, and 4.8×10^{-11} respectively. Each has input parameters $b = 2.25$ km s^{-1}, $X_{in} = 1\times10^{-7}$ (arbitrary), and $v_r = $ FF. All three modelled spectral lines are fairly close together and have minimal reduced chi-square values between 0.54 and 0.57.

Final RATRAN model spectral lines for $H_2^{16}O$ o001, p002, and o007 are plotted in Figure 4.40. Here, the OPR = 3:1. The power law model $\alpha = 1.4$ is plotted in green, $\alpha = 1.5$ is plotted in dashed cyan, and the hybrid model is plotted in dashed magenta. The Gaussian subtracted $H_2^{16}O$ HIFI observations are plotted in red; this subtracted line is used to calculate the chi-square and reduced chi-square for $H_2^{16}O$. The corresponding $H_2^{18}O$ HIFI data is plotted in blue. The Gaussian attributed to the envelope is not subtracted from the HIFI data and is indicated on the plot with a dashed black line. Finally, the v_{LSR} is indicated by the vertical dashed line. Panel 1 depicts ground state ortho 1_{10}-1_{01} (o001), panel 2 depicts excited para 2_{02}-1_{11} (p002), and panel 3 depicts excited ortho 3_{12}-3_{03} (o007). As listed in Table 4.21, ortho-X_{out} = 1.5, 1.8, 2.2 $\times10^{-8}$ and para-X_{out} = 4.5, 4.9, 6.0 $\times10^{-9}$ for $\alpha = 1.4$, hybrid, and 1.5, respectively. This gives a respective OPR(H_2O) = 3.33:1, 3.66:1, and 3.66:1. While the fits for p002 and o007 are acceptable, the o001 fit is clearly not.

Table 4.21: RATRAN modelling final X_{out} results with OPR = 3:1. $(^L)$ = left-tail distribution. $b_{out} = 2.25$ km s^{-1}, v_r = FF.

Molecule	Line	Model	X_{out}	DoF	χ^2	χ^2_R	p
H$_2^{18}$O	o001	$\alpha = 1.4$	3.5($\pm$ 0.3)$\times 10^{-11}$		49.61	0.557	2.32$\times 10^{-4}$ ^{L}
		hybrid	4.8 ($\pm$ 0.3)$\times 10^{-11}$	89	51.18	0.575	4.38$\times 10^{-4}$ ^{L}
		$\alpha = 1.5$	5.2($\pm$ 0.3)$\times 10^{-11}$		48.76	0.548	1.61$\times 10^{-4}$ ^{L}
H$_2^{16}$O	o001	$\alpha = 1.4$	1.5 ($\pm$ 0.5)$\times 10^{-8}$		18217.03	82.43	0
		hybrid	1.8($\pm$ 0.4)$\times 10^{-8}$	221	11980.41	54.21	0
		$\alpha = 1.5$	2.2 ($\pm$ 0.6)$\times 10^{-8}$		11792.56	53.36	0
H$_2^{16}$O	p001	$\alpha = 1.4$	4.5 ($\pm$ 0.5)$\times 10^{-9}$		4120.32	9.28	0
		hybrid	4.9 ($\pm$ 0.3)$\times 10^{-9}$	444	4120.32	9.28	0
		$\alpha = 1.5$	6.0 ($\pm$ 0.4)$\times 10^{-9}$		3636.36	8.19	0
H$_2^{16}$O	p002	$\alpha = 1.4$	4.5 ($\pm$ 0.5)$\times 10^{-9}$		754.56	1.92	4.39$\times 10^{-25}$
		hybrid	4.9 ($\pm$ 0.3)$\times 10^{-9}$	393	742.77	1.89	7.46$\times 10^{-24}$
		$\alpha = 1.5$	6.0 ($\pm$ 0.6)$\times 10^{-9}$		805.65	2.05	1.21$\times 10^{-30}$
H$_2^{16}$O	p004	$\alpha = 1.4$	4.5 ($\pm$ 0.5)$\times 10^{-9}$		379.73	1.27	1.07$\times 10^{-3}$
		hybrid	4.9 ($\pm$ 0.3)$\times 10^{-9}$	299	379.73	1.27	1.07$\times 10^{-3}$
		$\alpha = 1.5$	6.0 ($\pm$ 0.4)$\times 10^{-9}$		346.84	1.16	2.95$\times 10^{-2}$
H$_2^{16}$O	o006	$\alpha = 1.4$	1.5 ($\pm$ 0.5)$\times 10^{-8}$		578.34	1.26	1.25$\times 10^{-4}$
		hybrid	1.8 ($\pm$ 0.4)$\times 10^{-8}$	459	578.34	1.26	1.25$\times 10^{-4}$
		$\alpha = 1.5$	2.2 ($\pm$ 0.6)$\times 10^{-8}$		569.16	1.24	3.35$\times 10^{-4}$
H$_2^{16}$O	o007	$\alpha = 1.4$	1.5 ($\pm$ 0.5)$\times 10^{-8}$		1031.32	2.36	5.26$\times 10^{-50}$
		hybrid	1.8 ($\pm$ 0.4)$\times 10^{-8}$	437	1009.47	2.31	2.82$\times 10^{-47}$
		$\alpha = 1.5$	2.2 ($\pm$ 0.6)$\times 10^{-8}$		965.77	2.21	5.94$\times 10^{-42}$
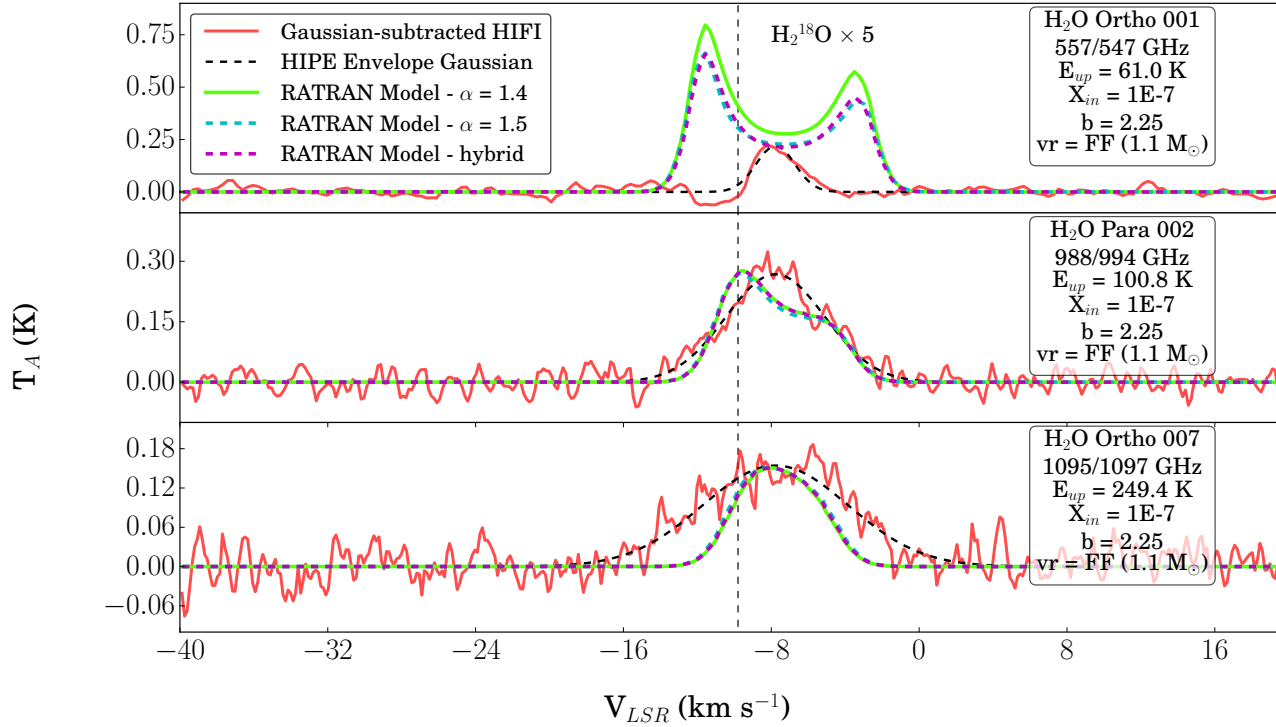
Figure 4.40: Final RATRAN model spectral lines for $H_2^{16}O$ o001, p002, and o007. Ortho-to-para ratio (OPR) = 3:1. Power law model $\alpha = 1.4$ is plotted in green, $\alpha = 1.5$ is plotted in dashed cyan, and the hybrid power law is plotted in dashed magenta. The Gaussian subtracted $H_2^{16}O$ HIFI observations are plotted in red and the corresponding $H_2^{18}O$ HIFI data is plotted in blue. The Gaussian attributed to the envelope is not subtracted from the HIFI data and is indicated on the plot with a dashed black line. The v_{LSR} is indicated by the vertical dashed line. Panel 1 depicts ground state ortho 1_{10}-1_{01} (o001), panel 2 depicts excited para 2_{02}-1_{11} (p002), and panel 3 depicts excited ortho 3_{12}-3_{03} (o007). As listed in Table 4.21, ortho-X_{out} = 1.5, 1.8, 2.2 $\times 10^{-8}$ and para-X_{out} = 4.5, 4.9, 6.0 $\times 10^{-9}$ for $\alpha = 1.4$, hybrid, and 1.5, respectively. This gives an OPR(H_2O) = 3.33:1, 3.66:1, and 3.66:1 respectively. While the fits for p002 and o007 are acceptable, the o001 fit is clearly not.
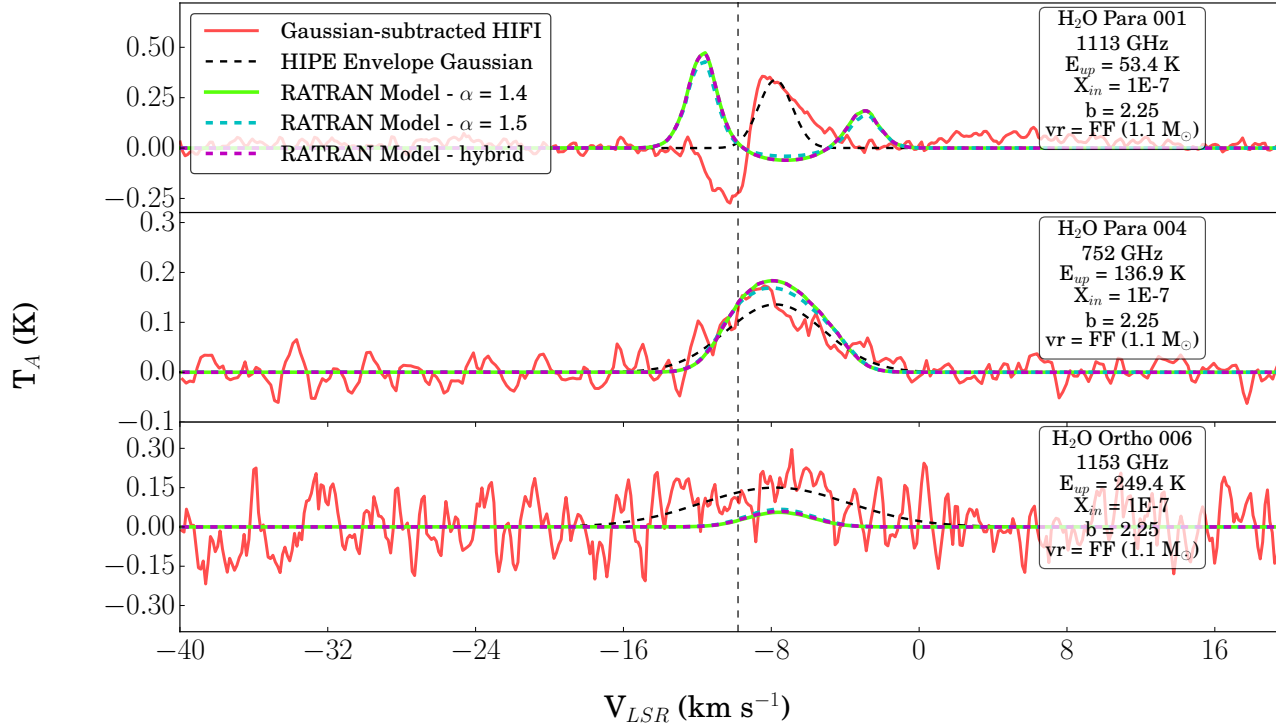
Figure 4.41: Final RATRAN model spectral lines for o007, p001, and p004. Same as Figure 4.39 except for the fact that these lines do not have corresponding $H_2^{18}O$ lines. Panel 1 depicts ground state para 1_{11}-0_{00} (p001), panel 2 depicts excited para 2_{12}-2_{02} (p004), and panel 3 depicts excited ortho 3_{12}-2_{21} (o007).

Final RATRAN model spectral lines for p001, p004, and o006 are plotted in Figure 4.41. These models have the same assumptions and plot attributes as the previous figure, except these lines do not have corresponding $H_2^{18}O$ lines. Panel 1 depicts ground state para 1_{11}-0_{00} (p001), panel 2 depicts excited para 2_{12}-2_{02} (p004), and panel 3 depicts excited ortho 3_{12}-2_{21} (o006). These lines were assumed to have the same abundances as the other ortho and para $H_2^{16}O$ lines. While the fits for p004 and o006 are acceptable with reasonably low chi-square values, the p001 line, similar to the o001 line, is not.

Considering an OPR that varies with temperature (LTE OPR$_T$, Figure 4.34), final RATRAN model spectral lines for $H_2^{16}O$ o001, p002, and o007 are plotted in Figure 4.42. The colour scheme and plot descriptions are the same as Figure 4.40. As listed in Table 4.22, ortho-X_{out} = 4.29, 5.14, 6.29 $\times 10^{-8}$ and para-X_{out} = 6.75, 7.35, 9.0 $\times 10^{-9}$ for α = 1.4, hybrid, and 1.5, respectively. This gives a respective OPR(H_2O) = 6.4:1, 7:1, and 7:1. Like the OPR$_{3:1}$ case, the fits for p002 and o007 are acceptable, while the o001 fit is not. The line shapes are all generally the same as the OPR$_{3:1}$ lines, except the o007 line in panel 3 shows more of a blue asymmetry. The main take-away is that with the varying OPR, the required abundances are larger. Compared to the OPR$_{3:1}$ case, the ortho outer abundances are increased by a factor of 2.86, while the para outer abundances are increased by a factor of 1.5. Taking the ratio of these two values yields

$$\frac{\text{ortho } (\text{OPR}_T/\text{OPR}_{3:1})}{\text{para } (\text{OPR}_T/\text{OPR}_{3:1})} = \frac{2.86}{1.5} = 1.91 \tag{4.12}$$

Final RATRAN model spectral lines for p001, p004, and o006 are plotted in Figure 4.43 for LTE OPR$_T$. This figure has the same colour scheme and description as that of Figure 4.41. While the fits for p004 and o006 are acceptable with reasonably low chi-square values, the ground state lines are still not reproduced. Different from the OPR$_{3:1}$ case, the o006 modelled line has an intensity comparable to that of the envelope Gaussian, resulting in a better χ_R^2. Overall, the LTE OPR$_T$ models have better χ_R^2 values, indicating that these are better fits. The water OPR is approximately doubled for the LTE OPR$_T$ case.

Table 4.23 estimates an abundance ratio via measurements for the o001 1_{10}-1_{01} abundance of both isotopologues, for both OPR models, and all power-law models. From this, we see an abundance ratio ranging from 411 ($\pm$ 104) (Hybrid) to 429($\pm$138) (α = 1.4) for the varying LTE OPR$_T$ case, and a range of 375 ($\pm$ 87) (Hybrid) to 428($\pm$147) (α = 1.4) for the OPR$_{3:1}$ case. For both OPR cases, the α = 1.4 power-law models possess uncertainty values that place the upper limit above the expected X_{ratio} = 550. The other power-law models yield abundance ratio results that fall just short of the expected value, even considering the upper uncertainty limit. With that being said, the $H_2^{16}O$ RATRAN models produced terrible fits for the ground state ortho line. Excited $H_2^{16}O$ lines would return

a better constraint on the abundance ratio; unfortunately, the only other corresponding $H_2^{18}O$ spectral lines obtained by HIFI in this dataset were seen to be non-detections.

Considering this, another approach is taken in attempt to constrain the abundance ratio. As seen in Figures 4.44 and 4.45, RATRAN models (Hybrid) are produced for p-2_{02}-1_{11} (p002) and o-3_{12}-3_{03} (o007), varying the outer abundance until the modelled line appears to be a flat line with respect to the corresponding HIFI observations (i.e, determining when the modelled line appears to produce a non-detection). For the former, a number of RATRAN models are run with outer abundance beginning at 9.0×10^{-10}. This is incrementally reduced until the RATRAN modelled line appears to have an intensity much less than that of the associated HIFI RMS noise σ. For $H_2^{18}O$ p-2_{02}-1_{11}, $\sigma = 0.016$ K; thus, any $X_{out} \lesssim 1 \times 10^{-10}$ would appear as a non-detection, according to this method of analysis. The modelled line appears completely flat at $X_{out} \lesssim 9 \times 10^{-12}$; this returns X_{ratio} = 544.4, within 1% of the expected value. The same method is applied to o-3_{12}-3_{03} (o007), beginning with an abundance estimate of $X_{out} = 6.0 \times 10^{-10}$, and incrementally reducing until the line appears to be a non-detection with respect to the RMS noise. The associated RMS noise for this line is also $\sigma = 0.016$ K. The outer abundance where this line appears completely flat is $\sim 3 \times 10^{-11}$. This returns $X_{ratio} = 600$, within 10% of the expected value.

It's possible that the above method of determining the abundance ratio allows for bias to slowly seep into the non-detection abundance determination process. As a second method, we begin with the expected ratio $X_{ratio} = 550$ and work backwards to determine the required outer abundance for p-2_{02}-1_{11} (p002) and o-3_{12}-3_{03} (o007) with respect to the best fit $H_2^{16}O$ outer abundances. Instead of computing the actual abundance ratio, we now test the expected abundance ratio. The spectral lines are not plotted before goodness of fit calculations so as to avoid any bias. The resultant abundance values are weak enough to be considered non-detections. The chi-square, reduced chi-square, and p-value are calculated for these fits and are found to be satisfactory. This analysis is located in Table 4.25.

Summary: NGC 7129 FIRS 2 RATRAN Model

Many learning points were acquired through this chapter's analysis. In summary, we learned that it is difficult to differentiate a free-fall infall velocity from a constant infall velocity for $H_2^{18}O$ without further information regarding the inner envelope (§4.5.3). The radial velocity analysis for $H_2^{16}O$ suggested a free-fall infall velocity is a better fit. Altering this parameter acts to increase or decrease the emission intensity T_A as well as alter the overall line-shape in the optically thick case. Also, changing the sign of the radial velocity from negative to positive mirrors the resultant spectral line about the envelope V_{LSR}. Ultimately, this parameter could not be constrained in this thesis, but it was assumed

to be in free-fall towards a central mass of $1.1M_\odot$. From Section §4.5.4, we learned that altering the Doppler broadening parameter b affects the width of the resultant spectral line; we constrained b_{out} to 2.25 ± 0.25 km s^{-1} for H$_2^{18}$O. This b value was applied to H$_2^{16}$O as well. The grid exercise presented in this section suggests the notion that the inner envelope is not contributing to the RATRAN spectral lines. Section §4.5.1 investigated the effects of altering the water abundance. It was determined that altering the abundance in turn alters the intensity T_A. The grid models presented in this section constrain the ortho ground state H$_2^{18}$O outer abundance between $4.8 \pm 0.3 \times 10^{-11}$ for the hybrid density and temperature model. The inner abundance was not constrained due to the thick optical depth.

In terms of indirect modelling parameters, from the abundance ratio study presented in Section §4.5.2, it was initially suggested that the abundance ratio of H$_2^{16}$O/H$_2^{18}$O was closer to a value of 100 as opposed to 550. That being said, these models use the ground state ortho lines of both isotopologues for this deduction, which proved to be poor spectral line reproductions for H$_2^{16}$O. (The models presented in Section §4.5.11 obtain a value closer to 550). From Section §4.5.5 we learned that altering the gas and dust temperatures have a significant effect on the resultant spectral line. Altering the gas temperature proportionally alters the peak antenna temperature. Moving the freeze-out radius (Section §4.5.6) inwards toward the protostar (i.e, increasing the freeze-out temperature) results in a decrease of spectral line intensity. In other words, increasing the size of the outer-envelope decreases the emission contribution. This is consistent with an increase in absorption by a larger outer envelope. In terms of the fractional state population, moving the freeze-out temperature inward causes the ground state population f_1 to increase to 1.0 sooner, causing excited f_n to decrease sooner. Increasing the number of cells (Section §4.5.7) results in an exaggeration of the absorption and emission features, and also increases the RATRAN model computational time.

Table 4.22: RATRAN modelling final outer abundance results. Varying LTE ortho-to-para ratio. $(^L)$ = left-tail distribution. $b_{out} = 2.25$ km s^{-1}, v_r = FF.

Molecule	Line	Model	X_{out}	DoF	χ^2	χ^2_R	p
$H_2^{18}O$	o001	$\alpha = 1.4$	$1.0(\pm 0.3)\times10^{-10}$		51.34	0.576	4.65×10^{-4} ^{L}
		hybrid	$1.25\ (\pm 0.3)\times10^{-10}$	89	50.67	0.569	3.58×10^{-4} ^{L}
		$\alpha = 1.5$	$1.46\ (\pm 0.3)\times10^{-10}$		54.98	0.618	1.73×10^{-2} ^{L}
$H_2^{16}O$	o001	$\alpha = 1.4$	$4.29\ (\pm 0.5)\times10^{-8}$		7396.30	33.47	0
		hybrid	$5.14\ (\pm 0.4)\times10^{-8}$	221	6752.86	30.56	0
		$\alpha = 1.5$	$6.29\ (\pm 0.6)\times10^{-8}$		5647.51	25.55	0
$H_2^{16}O$	p001	$\alpha = 1.4$	$6.75\ (\pm 0.5)\times10^{-9}$		3613.48	8.14	0
		hybrid	$7.35\ (\pm 0.3)\times10^{-9}$	444	3613.48	8.14	0
		$\alpha = 1.5$	$9.0\ (\pm 0.4)\times10^{-9}$		3108.54	7.00	0
$H_2^{16}O$	p002	$\alpha = 1.4$	$6.75\ (\pm 0.5)\times10^{-9}$		963.09	2.45	9.75×10^{-50}
		hybrid	$7.35\ (\pm 0.3)\times10^{-9}$	393	963.09	2.45	9.75×10^{-50}
		$\alpha = 1.5$	$9.0\ (\pm 0.4)\times10^{-9}$		1016.46	2.59	9.20×10^{-57}
$H_2^{16}O$	p004	$\alpha = 1.4$	$6.75\ (\pm 0.5)\times10^{-9}$		403.96	1.35	4.82×10^{-5}
		hybrid	$7.35\ (\pm 0.3)\times10^{-9}$	299	403.96	1.35	4.82×10^{-5}
		$\alpha = 1.5$	$9.0\ (\pm 0.4)\times10^{-9}$		356.32	1.19	1.27×10^{-2}
$H_2^{16}O$	o006	$\alpha = 1.4$	$4.29\ (\pm 0.5)\times10^{-8}$		524.79	1.14	1.80×10^{-2}
		hybrid	$5.14\ (\pm 0.4)\times10^{-8}$	459	515.76	1.12	3.42×10^{-2}
		$\alpha = 1.5$	$6.29\ (\pm 0.6)\times10^{-8}$		513.08	1.12	4.08×10^{-2}
$H_2^{16}O$	o007	$\alpha = 1.4$	$4.29\ (\pm 0.5)\times10^{-8}$		787.44	1.35	2.01×10^{-22}
		hybrid	$5.14\ (\pm 0.4)\times10^{-8}$	437	790.38	1.35	1.03×10^{-22}
		$\alpha = 1.5$	$6.29\ (\pm 0.6)\times10^{-8}$		763.70	1.19	3.83×10^{-20}
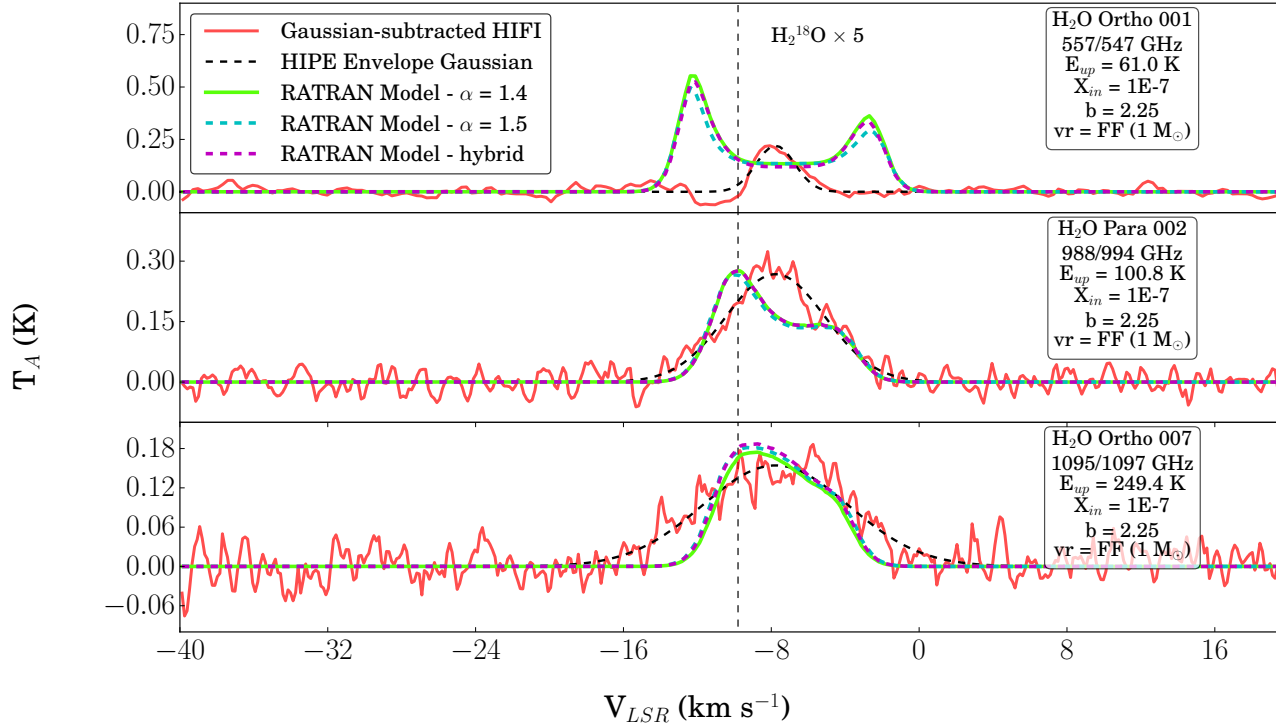
Figure 4.42: Final RATRAN model spectral lines for $H_2^{16}O$ o001, p002, and o007. Varying ortho-to-para ratio as a function of temperature LTE OPR (T). Same as Figure 4.40. As listed in Table 4.22, ortho-X_{out} = 4.29, 5.14, 6.29 $\times 10^{-8}$ and para-X_{out} = 6.75, 7.35, 9.0 $\times 10^{-9}$ for α = 1.4, hybrid, and 1.5, respectively. This gives an OPR(H_2O) = 6.36:1, 7:1, and 7:1 respectively. Like the OPR = 3:1 case, the p002 and o007 lines are acceptable, and the o001 fit is not. Overall similar line shape to the 3:1 case, although o007 shows a blue asymmetry in this case.
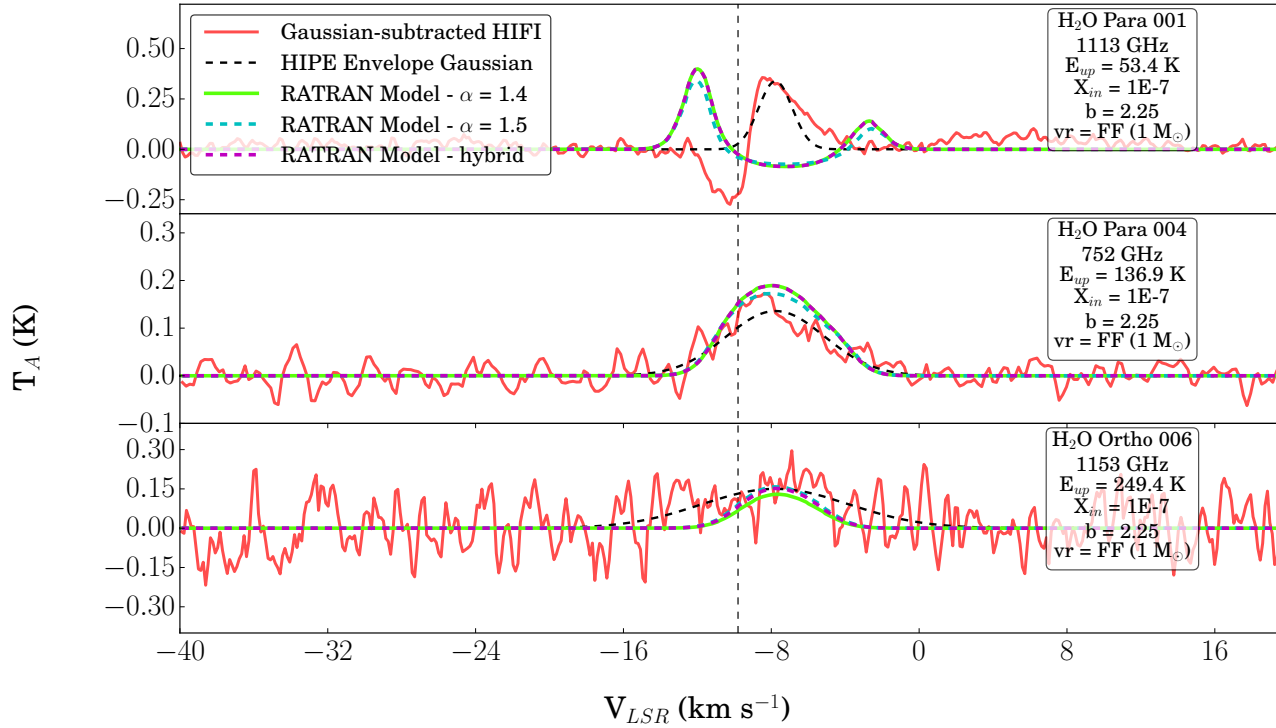
Figure 4.43: Final RATRAN model spectral lines for o007, p001, and p004 (OPR = LTE). Compared to Figure 4.41, the o006 line fits better. Overall similar line shape.

Table 4.23: Calculating the abundance ratio $X_{ratio} = X(H_2^{16}O)/X(H_2^{18}O)$ with o001 1_{10}-1_{01}

OPR	Power Law	Line	X_{out} ($H_2^{16}O$)	X_{out} ($H_2^{18}O$)	X_{ratio}
LTE	α=1.4	o001	4.29 ($\pm$0.5)$\times 10^{-8}$	1.00 ($\pm$0.3)$\times 10^{-10}$	429($\pm$138)
	Hybrid		5.14 ($\pm$0.4)$\times 10^{-8}$	1.25 ($\pm$0.3)$\times 10^{-10}$	411($\pm$104)
	α=1.5		6.29 ($\pm$0.6)$\times 10^{-8}$	1.46 ($\pm$0.3)$\times 10^{-10}$	431($\pm$98)
3:1	α=1.4	o001	1.5 ($\pm$0.5)$\times 10^{-8}$	3.5 ($\pm$0.3)$\times 10^{-11}$	428($\pm$147)
	Hybrid		1.8 ($\pm$0.4)$\times 10^{-8}$	4.8 ($\pm$0.3)$\times 10^{-11}$	375($\pm$87)
	α=1.5		2.2 ($\pm$0.6)$\times 10^{-8}$	5.2 ($\pm$0.3)$\times 10^{-11}$	423($\pm$118)

Section 4.5.9 proves that the radiative transfer code is very sensitive to the collision rates. Altering the collision rates for all temperatures of a single transition by 10% resulted in a $\sim 500\%$ spectral line intensity increase. Using the most up-to-date collision rates is vital for obtaining accurate spectral results with RATRAN. Employing an ortho to para ratio that varies with temperature (§4.5.8) resulted in a decrease in line intensity. Holding the water abundance constant between OPR models provides another collision rate comparison, this time between the ortho and para collision rates. Considering these spectral results with respect to those of the 3:1 OPR case, the varying LTE OPR_T models have better χ_R^2 values when the outer abundance is raised in order to obtain a best fit. This indicates that the OPR in the envelope of NGC 7129 FIRS 2 is not driven to LTE, as expected. Along with using the most up-to-date collision rates, ensuring the correct beamsizes are used during convolution is also vital to the success of the RATRAN model (§4.5.10). Using a larger beamsize results in a reduced line emission.

The various power-laws studied in this thesis produced RATRAN spectral results that were all very consistent (i.e, required abundances on the same order of magnitude). As expected, the hybrid density and temperature model fell between the pure $\alpha = 1.4$ and 1.5 models in terms of modelled intensity.

Considering all learning points of the above exercises, the $H_2^{16}O$ ortho and para ground state spectral lines were not able to be reproduced for any of the power-law models. Conversely, RATRAN modelling of the remaining water transitions produced satisfactory results. The $H_2^{18}O$ water lines also produced spectral results consistent with the HIFI observational data. H_2O abundance ratios ranged from $\sim 375 - 600$ depending on the method of determination; the OPR for water also varied depending on the density profile. These are listed in Table 4.24.

Table 4.24: H$_2$O Ortho to Para Ratio for all considered density profiles.

Model	OPR (H$_2$)	OPR (H$_2$O)
$\alpha = 1.4$	3:1	3.3 ± 1.2
Hybrid	3:1	3.7 ± 0.8
$\alpha = 1.5$	3:1	3.7 ± 1.0
$\alpha = 1.4$	LTE	6.4 ± 0.9
Hybrid	LTE	7.0 ± 0.6
$\alpha = 1.5$	LTE	7.0 ± 0.7
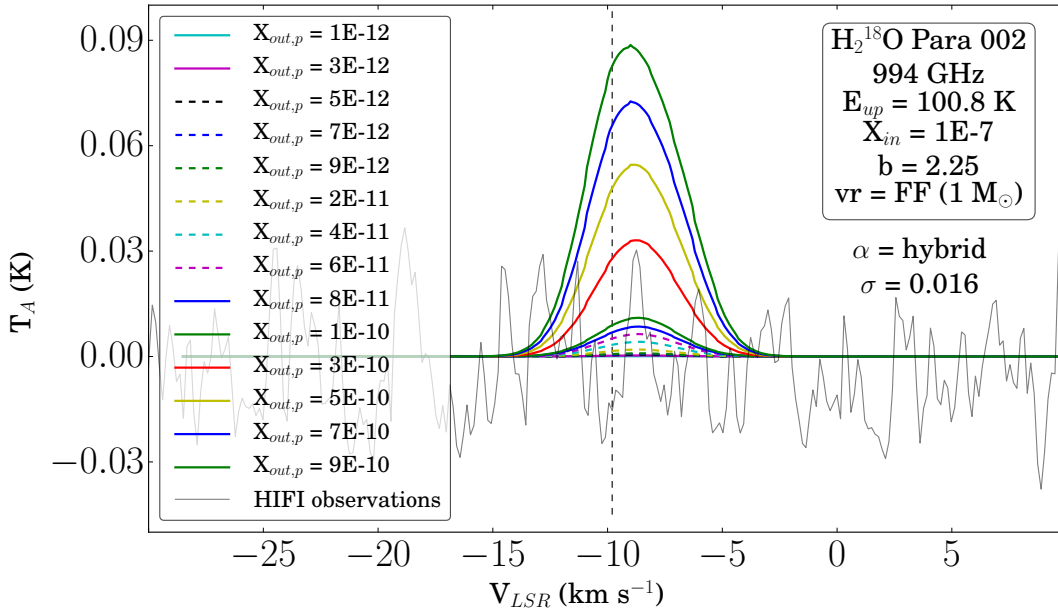
Figure 4.44: RATRAN: Placing upper limit on X$_{out}$ of H$_2^{18}$O p-2$_{02}$-1$_{11}$. Ranges in X$_{out}$ from 1×10^{-12} to 9×10^{-10}. The hybrid power-law and an OPR of 3:1 are assumed. Contrasted against HIFI observations (faded black). Vertical dashed line corresponds to v$_{LSR}$ = -9.8 km s^{-1}. Appears to be a flat modelled line around X$_{out} \lesssim 9.0\times10^{-12}$.
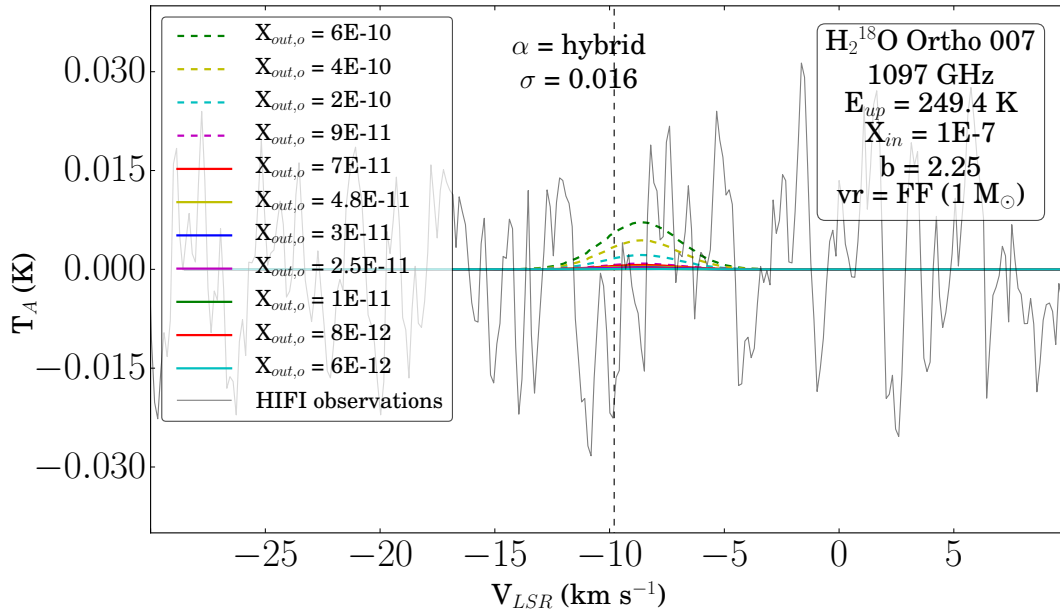
Figure 4.45: RATRAN: Placing upper limit on X_{out} of $H_2^{18}O$ o-3_{12}-3_{03}. Ranges in X_{out} from 6.0×10^{-12} to 6×10^{-10}. The hybrid power-law and an OPR of 3:1 are assumed. Contrasted against HIFI observations (faded black). Vertical dashed line corresponds to $v_{LSR} = -9.8$ km s^{-1}. Appears to be a flat modelled line around $X_{out} \lesssim 2.75 \times 10^{-11}$.

Table 4.25: Estimating $H_2^{18}O$ p002 and o007 X_{out} required for non-detection. $X_{ratio} = 550$, degrees of freedom = 89, velocity range = [-13.0, -4.0] km s^{-1}, $b_{out} = 2.25$ km s^{-1}, and v_r = FF. X_{out} ($H_2^{18}O$) = $X_{ratio} \times X_{out}$ ($H_2^{16}O$)

OPR	Power Law	Line	X_{out} ($H_2^{16}O$)	X_{out} ($H_2^{18}O$)	χ^2	χ_R^2	p
	$\alpha = 1.4$		$6.75(\pm0.5)\times10^{-9}$	$1.23(\pm0.9)\times10^{-11}$	74.753	0.840	0.14
LTE	Hybrid	p002	$7.35(\pm0.3)\times10^{-9}$	$1.34(\pm0.6)\times10^{-11}$	74.715	0.839	0.14
	$\alpha = 1.5$		$9.0(\pm0.4)\times10^{-9}$	$1.64(\pm0.1)\times10^{-11}$	74.759	0.840	0.14
	$\alpha = 1.4$		$4.29(\pm0.5)\times10^{-8}$	$7.80(\pm0.9)\times10^{-11}$	80.835	0.908	0.28
LTE	Hybrid	o007	$5.14(\pm0.4)\times10^{-8}$	$9.35(\pm0.7)\times10^{-11}$	80.824	0.908	0.28
	$\alpha = 1.5$		$6.29(\pm0.6)\times10^{-8}$	$1.14(\pm0.1)\times10^{-10}$	80.870	0.909	0.28
	$\alpha = 1.4$		$4.5(\pm0.5)\times10^{-9}$	$8.18(\pm0.9)\times10^{-12}$	74.667	0.839	0.14
3:1	Hybrid	p002	$4.9(\pm0.3)\times10^{-9}$	$8.91(\pm0.6)\times10^{-12}$	74.634	0.839	0.14
	$\alpha = 1.5$		$6.0(\pm0.4)\times10^{-9}$	$1.09(\pm0.1)\times10^{-11}$	74.676	0.839	0.14
	$\alpha = 1.4$		$1.5(\pm0.5)\times10^{-8}$	$2.73(\pm0.9)\times10^{-11}$	80.604	0.906	0.27
3:1	Hybrid	o007	$1.8(\pm0.4)\times10^{-8}$	$3.27(\pm0.7)\times10^{-11}$	80.612	0.906	0.27
	$\alpha = 1.5$		$2.2(\pm0.6)\times10^{-8}$	$4.00(\pm0.1)\times10^{-11}$	80.618	0.906	0.27

Chapter 5

RADEX Modelling

RADEX is a computer program, written originally by J. H. Black, that acts as a non-LTE excitation and radiative transfer code. See van Langevelde & van der Tak (2008) for the manual. The program considers collisional and radiative processes using the escape probability method, which then assumes an isothermal, homogeneous medium without large-scale velocity fields (van der Tak et al. 2007). The user can select from three geometries: uniform sphere, Large Velocity Gradient (LVG) (expanding sphere), or plane parallel slab, and can enter up to 7 collision partners. Assuming that the source fills the beam, RADEX calculates intensities of atomic and molecular lines, then outputs the background subtracted line intensity in terms of the radiation temperature T_R. This parameter can be directly compared to the observed antenna temperature corrected for the optical efficiency of the telescope (van der Tak et al. 2007). In the case that the source does not fill the beam, the user has to correct for beam dilution or ensure the source is resolved.

This code decouples the radiation from the molecular excitation, therefore the background radiation can be included. The main background radiation contributor is the Cosmic Microwave Background where $T_{CBR} = 2.725 \pm 0.001$ K. Internal radiation also plays a role in the chemistry of the interstellar medium (i.e re-absorption). At the frequencies used in this thesis (i.e., 557 GHz for ground state $H_2^{16}O$), the majority of the background contribution necessary for calculations is CMB radiation.

The purpose of modelling with RADEX is to further solidify confidence in the derived radiative transfer model. Code details are given in §5.1, limitations are given in §5.2, and RATRAN vs. RADEX comparison results can be found in §5.4. Input and output parameters are listed in Appendix B.

5.1 How does RADEX work?

RADEX uses the escape probability method for an isothermal, homogeneous medium. As explained in van der Tak et al. (2007), a first guess of the relative level populations is produced for an optically thin case. The only radiation taken into account for this estimation is the unshielded background radiation field. RADEX does not yet consider internally produced radiation. Solving for the level populations then allows the optical depth of each line to be derived, which in turn re-calculates the molecular excitation using the equations listed in §1.5 and §3.1. The new optical depth calculations treat the background radiation the same as the internally produced radiation. We can thus iteratively find a consistent solution for the level populations and the radiation. RADEX produces output and terminates once the optical depths of the lines with $\tau > 10^{-2}$ are stable between iterations.

The RADEX paper (van der Tak et al. 2007) describes the ways in which RADEX can be used to analyze molecular spectra. Most often, the modelled quantity is the velocity-integrated line intensity $\int T_A dv$. In an ideal case, the temperature and density are known from other observations and only the molecular column density needs to be varied to achieve an agreeing result. The limited number of free parameters makes RADEX very useful to rapidly analyze large datasets.

5.2 Limitations

RADEX does have a few drawbacks; only homogeneous mediums are considered, the program doesn't know anything about the geometry or velocity fields of the studied regions, doesn't know if the escape probability holds, cannot give flux or specific luminosity (only intensities), assumes the source fills the beam, and causes the user to blindly trust built in radiative and collisional transition rates. Self-absorbed lines cannot be modelled satisfactorily with RADEX as the excitation derived is assumed to be independent of velocity. RADEX can also only handle one molecule at a time, as such the effects of line overlap are not taken into account. Finally, some molecules undergo population inversion under conditions such as low density or a strong radiation field (masers); this would require non-local treatment of radiative transfer. RADEX is not capable of handling this.

On the plus side, RADEX can handle different molecule orientations (linear, symmetric-top and asymmetric-top molecules), and model up to seven different species. Additionally, RADEX includes background radiation.

5.3 How does RADEX apply?

In the context of this work, we are able to match the RADEX derived velocity integrated intensity ($\int T_A dv$), optical depth (τ), fractional populations (f_n or n_i), and the antenna temperature (T_A) with that of the observed spectra. Once these values are roughly equal, we are given an idea of what to expect for the column density. Additionally, other RADEX input and output can be compared with RATRAN models, such as the calculated optical depth, the observed antenna temperature, and the fractional population levels.

That being said, this is approached with caution. As mentioned in §5.1, self-absorbed lines cannot be modelled with RADEX to a high degree of satisfaction as the excitation derived is assumed to be independent of velocity. The strongest lines in this thesis exhibit self-absorption; RADEX is best-suited to simulating the expected column density for the outflow contribution, although an attempt will be made to simulate the spherical envelope.

5.4 Results

This section presents RADEX results and a comparison with RATRAN input and output parameters (hybrid power-law model, OPR = 3:1). Subsection 5.4.1 presents RADEX results modelled for the $H_2^{18}O$ foreground component at 0.6 km s^{-1}.

5.4.1 $H_2^{18}O$: Emission Components at 8.6 and 0.6 km s^{-1}

Emission Component at 0.6 km s^{-1}

In this subsection, RADEX results are compared to RATRAN model results for NGC 7129 FIRS 2 to obtain some sort of structural model for the foreground component seen in $H_2^{18}O$ 1_{10}-1_{01} spectra at 0.6 km s^{-1}.

To begin, a quick example of a RADEX model for $H_2^{18}O$ is calculated for a user defined line frequency range 540 – 2000 GHz, kinetic temperature $T_{kin} = 100$ K, n($H_2^{18}O$) = 10^{-4} cm^{-3}, T(CMB) = 2.73 K, N(H_2O) = 10^{14} cm^{-2}, and line width $\Delta V = 0.6$ km s^{-1}. A screenshot of the output for this model is seen in Figure 5.1. Listing the columns from first to last: quantum state transition (line), energy of the upper state (K), line frequency (GHz), wavelength (μm), excitation temperature (K), optical depth τ, antenna temperature (K), upper state population, lower state population, flux (K km s^{-1}), and flux (erg cm^{-2} s^{-1}). For the supplied frequency range, 29 transition lines are returned in 30 iterations.

The HIFI observational data, the fitted envelope Gaussian, and the deduced RATRAN model can be compared to these RADEX results via the velocity integrated line intensity $\int T_R dv = 1.0645\ T_R \Delta V$. The foreground component in the HIFI o001 $H_2^{18}O$ 547 GHz line has an observed integrated intensity of $\int T_A dv = 0.02$ K km s^{-1} (see HIFI observations, Figure 2.4). In this particular example, the source does not fill the beam and the radiation temperature (T_R) must be convolved to obtain antenna temperature; as mentioned in Table 3.6, this value is $A_{001} = 0.117$ for $H_2^{18}O$. Thus, the antenna temperature becomes $A_{o001} \times T_R(o001) = 0.117 \times 1.146$ K $= 0.13$ K. The antenna temperature produced by RADEX is an order of magnitude too large (0.013 K vs. 0.13 K), and the velocity integrated intensity equals 1.0645×0.13 K $\times 0.6$ km s$^{-1} = 0.09$ K km s^{-1}, also slightly too large (a factor of 4.5). These parameters can be brought into harmony with the observations by decreasing the molecular column density. This leads to a grid-like analysis to determine which column density will produce the desired velocity integrated intensity for both emission features seen in the $H_2^{18}O$ spectral line.

A total of 40 additional models are run in a grid-like manner for the 0.6 km s^{-1} emission feature ranging in column density from $10^{11} - 10^{14}$ cm^{-2} and a gas temperature from 10 – 100 K. Parallel plane slab geometry was selected for this grid model. It will be seen later (§5.4.2) that the differences between the geometries are minimal to none for the ground state ortho line. Gas vs. antenna temperature is plotted in Figure 5.2. For this emission feature $\int T_R dv = 0.02$ K km s^{-1}, yielding an expected $T_R = 0.031$ K. This is indicated on the plot with a black dotted line. The only column density that crosses the expected T_R line is the red N $= 10^{13}$ cm^{-2} line, at a temperature of approximately $T_{gas} \sim 45$ K. The cyan line, one order of magnitude higher, might also fit this model, but at a gas temperature $\lesssim$ 15 K. This data is plotted in a colour-plot manner in Figure 5.3, with T_k vs. Log ($N_{H_2^{18}O}$). Here, models with $\int T_R dv$ between 0.001 and 0.05 are shown in colour; models with velocity integrated intensity outside of these boundaries are indicated by the white regions. The desired velocity integrated intensity $\int T_R dv \sim 0.02$ is indicated on this plot by mint blue. In terms of a best fit region, we see a decreasing then plateauing trend with increasing temperature. This region is defined between column densities of 1.75×10^{12} and 10^{14}. The best fit of $\sim 10^{13}$ from the previous plot fits within these limits well, equalling $\int T_R dv = 0.02$ K km s^{-1} at $T_{gas} \sim 40$ K. Thus, the foreground cloud must be emitting around T_{gas} $= 40$-45 K, with a column density of $\sim 10^{13}$.

```
* Radex version       : 30nov2011
* Geometry            : Plane parallel slab
* Molecular data file : /home2/meconrad/RadexMasters/Radex/data/oh2o@daniel.dat
* T(kin)          [K]: 100.000
* Density of H2  [cm-3]: 1.000E+04
* Density of pH2 [cm-3]: 3.796E+03
* Density of oH2 [cm-3]: 6.204E+03
* T(background)   [K]:   2.730
* Column density [cm-2]: 1.000E+14
* Line width    [km/s]:   0.600
Calculation finished in   30 iterations
     LINE        E_UP     FREQ     WAVEL    T_EX      TAU        T_R       POP       POP       FLUX      FLUX
                 (K)     (GHz)    (um)     (K)                   (K)       UP        LOW     (K*km/s) (erg/cm2/s)
1_1_0  -- 1_0_1    61.0   556.9361  538.2888    8.379  3.089E+01  1.146E+00  3.948E-02  9.589E-01  7.321E-01  1.629E-06
2_1_2  -- 1_0_1   114.4  1669.9050  179.5267   11.630  3.219E+01  8.159E-02  1.625E-03  9.589E-01  5.211E-02  3.125E-06
2_2_1  -- 2_1_2   194.1  1661.0080  180.4883   10.850  1.819E-02  9.267E-04  1.047E-06  1.625E-03  5.919E-04  3.493E-08
3_0_3  -- 2_1_2   196.8  1716.7698  174.6259   12.079  3.806E-02  3.360E-03  2.482E-06  1.625E-03  2.146E-03  1.399E-07
3_1_2  -- 2_2_1   249.4  1153.1268  259.9822  126.919  1.494E-06  1.513E-04  9.481E-07  1.047E-06  9.664E-05  1.908E-09
3_1_2  -- 3_0_3   249.4  1097.3651  273.1930   54.725  3.211E-05  1.045E-03  9.481E-07  2.482E-06  6.676E-04  1.136E-08
3_2_1  -- 3_1_2   305.3  1162.9119  257.7946   16.180  2.242E-05  4.105E-05  3.012E-08  9.481E-07  2.622E-05  5.310E-10
4_1_4  -- 3_2_1   323.5   380.1974  788.5179 -567.243 -1.157E-09  6.669E-07  3.999E-08  3.012E-08  4.259E-07  3.015E-13
4_2_3  -- 3_3_0   432.2   448.0012  669.1778   47.020  5.522E-10  2.047E-08  9.695E-10  1.191E-09  1.308E-08  1.514E-14
4_3_2  -- 5_0_5   550.4  1713.8832  174.9200   52.784  1.076E-10  2.360E-09  3.443E-10  1.999E-09  1.507E-09  9.771E-14
5_2_3  -- 4_3_2   642.4  1918.4857  156.2652  113.864  6.201E-10  4.587E-08  1.875E-10  3.443E-10  2.930E-08  2.664E-12
5_3_2  -- 4_4_1   732.1   620.7012  482.9900   95.808  1.913E-12  1.562E-10  7.191E-12  8.030E-12  9.978E-11  3.073E-16
5_2_3  -- 5_1_4   642.4  1410.6182  212.5256   94.300  5.078E-09  3.274E-07  1.875E-10  3.843E-10  2.091E-07  7.559E-12
5_3_2  -- 5_2_3   732.1  1867.7487  160.5101   27.491  3.796E-09  1.357E-08  7.191E-12  1.875E-10  8.670E-09  7.275E-13
6_2_5  -- 5_3_2   795.5  1322.0650  226.7608   50.372  9.803E-12  2.464E-10  2.412E-12  7.191E-12  1.574E-10  4.684E-15
6_3_4  -- 5_4_1   933.7  1158.3241  258.8157   95.085  5.904E-13  4.132E-11  5.162E-13  7.838E-13  2.639E-11  5.282E-16
6_4_3  -- 5_5_0  1088.8   439.1509  682.6639  -29.270 -4.901E-15  2.006E-13  1.871E-14  7.705E-15  1.281E-13  1.398E-19
6_3_4  -- 7_0_7   933.7  1880.7526  159.4003   67.094  1.354E-13  4.302E-12  5.162E-13  2.287E-12  2.748E-12  2.354E-16
6_4_3  -- 7_1_6  1088.9  1574.2323  190.4372   59.751  5.911E-15  1.749E-13  1.871E-14  7.644E-14  1.117E-13  5.614E-18
7_4_3  -- 6_5_2  1339.8  1278.2661  234.5306 -225.591 -3.012E-16  5.721E-14  1.113E-15  7.350E-16  3.654E-14  9.829E-19
7_5_2  -- 6_6_1  1524.9   443.0184  676.7043  -17.374 -1.070E-17  0.000E+00  3.985E-17  1.016E-17  0.000E+00  0.000E+00
7_3_4  -- 7_2_5  1212.0  1797.1590  166.8147   41.716  9.068E-13  1.133E-11  4.917E-15  3.888E-14  7.234E-12  5.408E-16
7_2_5  -- 8_1_8  1125.7  1146.6215  261.4572  123.347  2.274E-15  2.173E-13  3.888E-14  6.883E-14  1.388E-13  2.695E-18
8_2_7  -- 7_3_4  1274.2  1296.4112  231.2480   50.806  2.893E-15  7.474E-14  1.638E-15  4.917E-15  4.774E-14  1.340E-18
8_4_5  -- 7_5_2  1615.4  1884.8882  159.0505   57.334  6.061E-17  2.613E-15  9.322E-18  3.985E-17  1.669E-15  1.439E-19
8_5_4  -- 7_6_1  1805.9  1168.3587  256.5928  -90.137 -8.048E-19  0.000E+00  1.980E-18  9.379E-19  0.000E+00  0.000E+00
8_4_5  -- 9_1_8  1615.4  1307.9635  229.2055   60.823  3.060E-18  0.000E+00  9.322E-18  2.924E-17  0.000E+00  0.000E+00
8_5_4  -- 9_2_7  1805.9  1596.2527  187.8102   67.557  5.166E-19  0.000E+00  1.980E-18  6.878E-18  0.000E+00  0.000E+00
10_2_9 -- 9_3_6  1861.3   321.2257  933.2767   14.716  1.042E-19  0.000E+00  2.203E-19  5.683E-19  0.000E+00  0.000E+00
```

Figure 5.1: Screenshot of example RADEX output at user defined line frequency range 540 – 2000 GHz, kinetic temperature $T_{kin} = 100$ K, n(H$_2^{18}$O) $= 10^{-4}$, T(CMB) $= 2.73$ K, N(H$_2$O) $= 10^{14}$, and line width ΔV $= 0.6$ km s^{-1}. The columns are listed in text. 29 transition lines were returned in 30 iterations. For ground state 547 GHz line (H$_2^{18}$O equivalent), the velocity integrated line intensity $\int T_R dv = 0.6876$. The observed o001 H$_2^{18}$O 547 GHz line has an observed integrated intensity of $\int T_A dv = 0.06$ K km s^{-1} (HIFI observations, Figure 2.4).
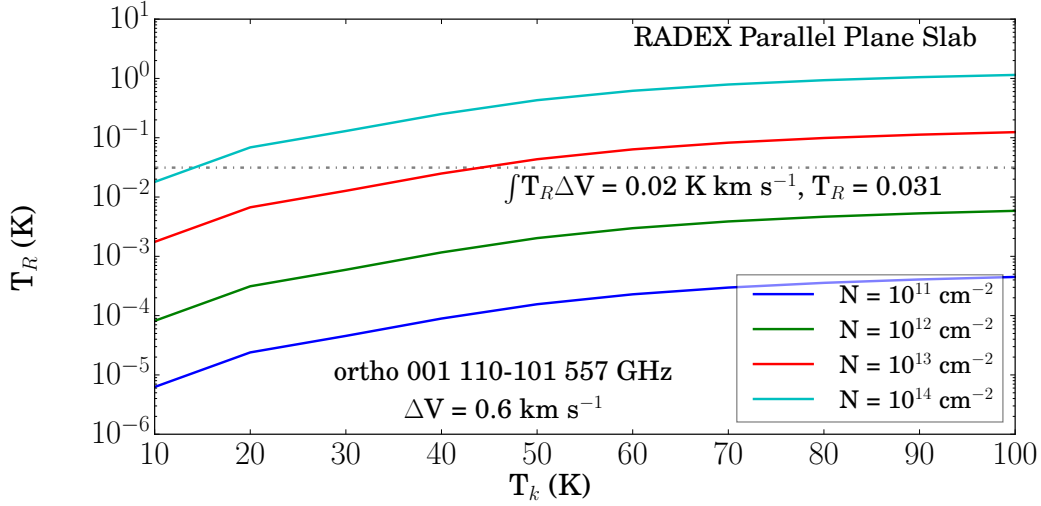
Figure 5.2: RADEX grid models for $H_2^{18}O$ 0.6 km s^{-1} component, using Parallel Plane Slab geometry. Gas vs. antenna temperature for varying column densities. $\int T_R dv = 0.02$ K km s^{-1}; for $\Delta V = 0.6$ km s^{-1}, the expected $T_R = 0.031$ for a Gaussian (black dotted line). The only N that crosses the expected T_R boundary is the red N $= 10^{13}$ cm^{-2} line. The cyan line might also fit this model, but at $T_{gas} < 15$ K.

Emission Component at 8.6 km s^{-1}

A grid of 80 RADEX models was generated for the main 1.9 km s^{-1} emission feature for column densities ranging from $10^{10} - 10^{17}$ cm^{-2} and for gas temperatures ranging from $10 - 100$ K. Parallel plane slab geometry was selected for this as well. Gas vs. antenna temperature is plotted in Figure 5.4; for this emission feature, $\int T_R dv = 0.06$ K km s^{-1}, yielding an expected $T_R = 0.0297$ K for a Gaussian. This is indicated on the plot with a black dotted line. The only column density that crosses the expected T_R line is the magenta N $= 10^{14}$ cm^{-2} line at a temperature of approximately $T_{gas} \sim 25$ K. This data is plotted in a colour-plot manner in Figure 5.5, with T_k vs. Log $(N_{H_2^{18}O})$. Here, models with $\int T_R \Delta V$ between 0.01 and 0.095 are shown in colour; models with velocity integrated intensity outside of these boundaries are indicated by the white regions. The desired velocity integrated intensity $\int T_R \Delta V \sim 0.06$ is indicated on this plot by lime green. In terms of a best fit region, we see a decreasing then plateauing trend with increasing temperature. This region is defined between column densities 10^{14} and 10^{16}, consistent with the findings of the previous plot. This is greater than the foreground component by a factor of 10^2.
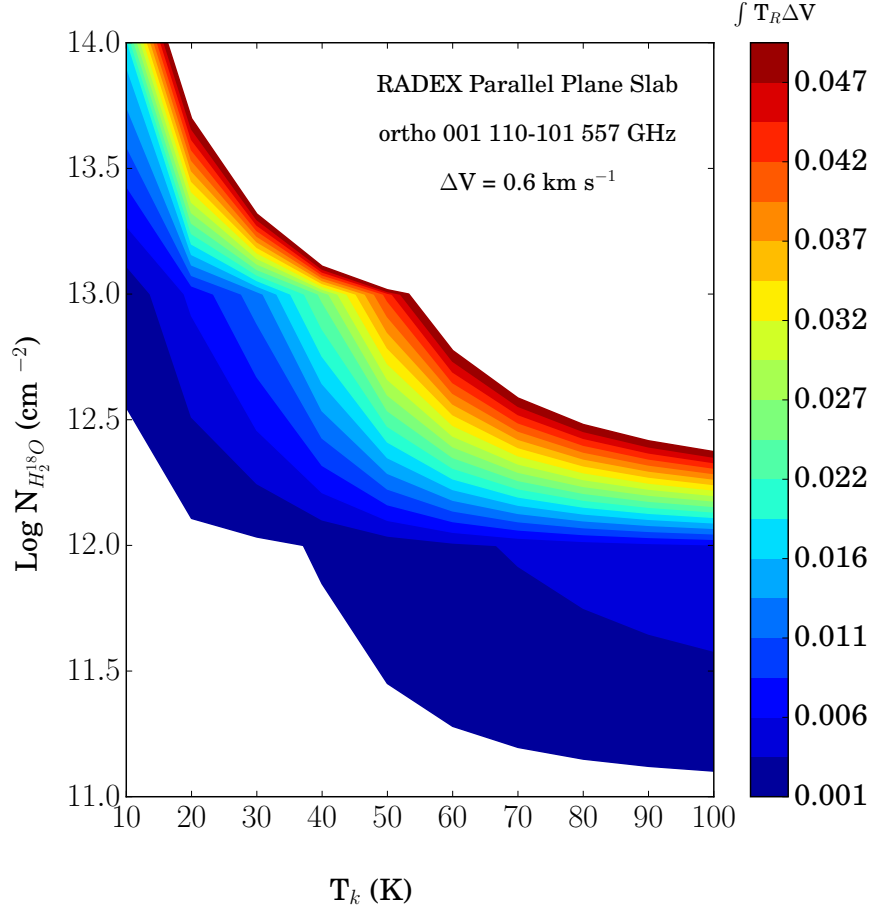
Figure 5.3: Colour plot depicting RADEX grid models for $H_2^{18}O$ 0.6 km s^{-1} foreground component. Ranging in column density N from $10^{11} - 10^{14}$, over gas temperature range of $10 - 100$ K. Models with $\int T_R \Delta V$ between 0.001 and 0.05 are shown in colour; models with velocity integrated intensity outside of these boundaries are indicated by the white regions. We see decreasing then plateauing trend with increasing temperature, similar to that in Figure 5.2. For the 0.6 km s^{-1} $H_2^{18}O$ emission feature, we are aiming for $\int T_R \Delta V \sim$ 0.02, indicated on this plot by mint blue. This region is defined between column densities of 1.75×10^{12} and 10^{14} for a parallel plane slab geometry. This is less than the NGC 7129 FIRS 2 component by a factor of 10^2.
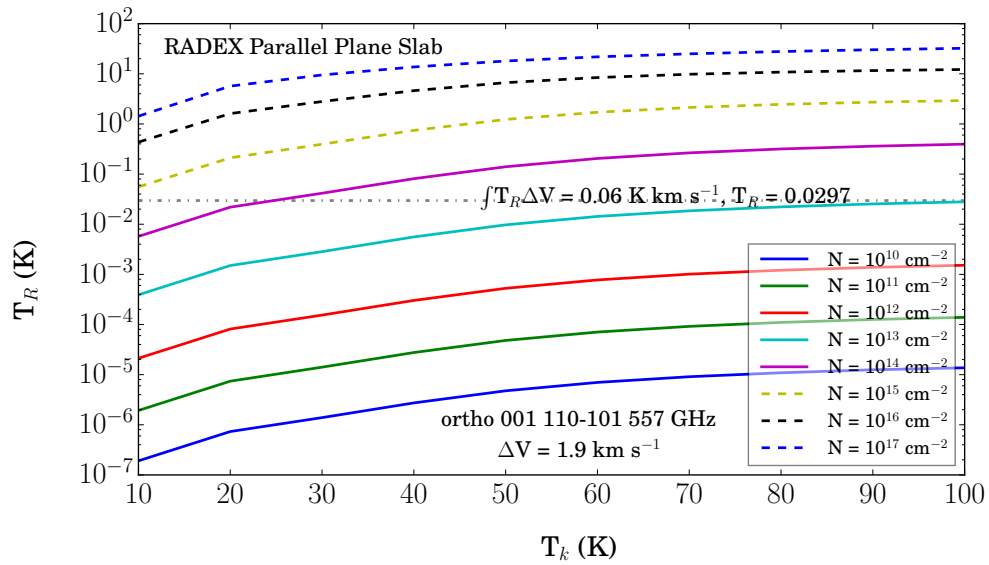
Figure 5.4: RADEX grid models for $H_2^{18}O$ 1.9 km s^{-1} component, using Parallel Plane Slab geometry. Plotting gas temperature vs. antenna temperature for varying column densities. The velocity integrated intensity $\int T_R dv = 0.06$ K km s^{-1}; for a $\Delta V = 1.9$ km s^{-1}, the expected $T_R = 0.0315$ for a Gaussian. This is indicated on the plot with a black dotted line. The only column densities that cross the expected T_R line is the magenta N = 10^{14} cm^{-2} line.
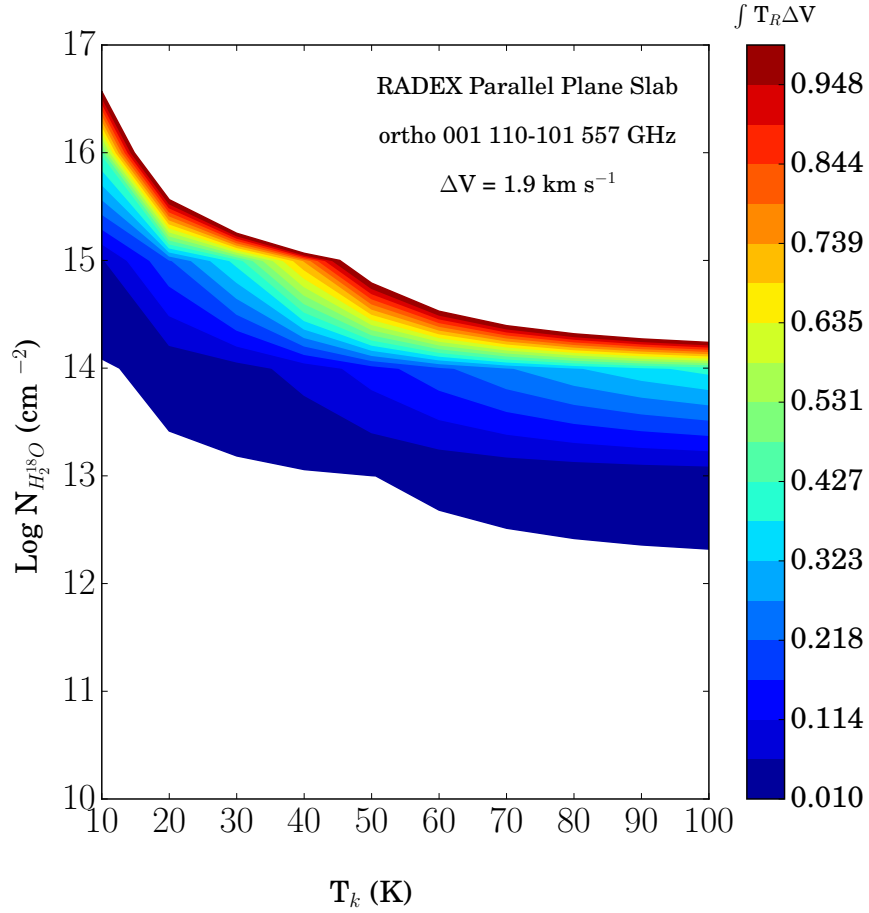
Figure 5.5: Colour plot depicting RADEX grid models for $H_2^{18}O$ 1.9 km s^{-1} component. Ranging in column density N from $10^{10} - 10^{17}$, over gas temperature range of $10 - 100$ K. Models with $\int T_R \Delta V$ between 0.01 and 0.095 are shown in colour; models with velocity integrated intensity outside of these boundaries are indicated by the white regions. We see decreasing then plateauing trend with increasing temperature. For the 1.9 km s^{-1} $H_2^{18}O$ emission feature, we are aiming for $\int T_R \Delta V \sim 0.06$, indicated on this plot by lime green. This region is defined between column densities of 2×10^{14} and 10^{16} for a parallel plane slab geometry.

5.4.2 RATRAN vs. RADEX

Table 5.1: RADEX Input Parameters: τ, N_ℓ, n_{H_2}- $H_2^{18}O$.

o001	$\tau = 1.0$	$\tau = 0.23$
o007	$\tau = 0.019$	$\tau = 7.21 \times 10^{-6}$
T_k (K)	69.76	25.0
$N(H_2^{18}O)$ (cm^{-2})	1.25×10^{13}	3.0×10^{12}
n_{H_2} (cm^{-3})	1.7×10^7	8.5×10^5

In order to compare RATRAN modelling results with RADEX results, we must first extract input variables that are consistent with both radiative transfer codes. This will be carried out for the ground state $H_2^{18}O$ line, o001 1_{10}-1_{01}, and an excited state $H_2^{18}O$ line, o007 3_{12}-3_{03}. The optical depth through the modelled NGC 7129 FIRS 2 molecular cloud is calculated with Equation 3.8. Optical depth figures can be found in Chapter 6. It is determined that $H_2^{18}O$ o007 reaches $\tau = 1.0$ at T = 80.79 K, and has $\tau \sim 7.2 \times 10^{-6}$ at 25.0 K. When o001 reaches $\tau = 1.0$ at 69.76 K, the optical depth of o007 reaches $\tau = 0.019$.

Column density and gas temperature per RATRAN Shell for $H_2^{18}O$ are plotted in Figure 5.6. The freeze-out radius is marked by a vertical black dashed line (shell 10). This plot was used to extract column density values for optical depths of $\tau = [1.0 \text{ (o001)}, 0.019 \text{ (o007)}]$ and $[0.23 \text{ (o001)}, \text{ and } 7.2 \times 10^{-6} \text{ (o007)}]$ corresponding to $T_k = 70$ and 25 K respectively. At 70 K, the column density of $H_2^{18}O$ is 1.25×10^{13} cm^{-2}, and at 25 K is 3.0×10^{12} cm^{-2}.

Lastly, the density of H_2 was determined at these temperatures (70, 25 K) with Figure 5.7, a plot of column density and H_2 density per RATRAN shell. Using the same method as above, the H_2 densities were determined to be $n_{H_2}(70 \text{ K}) = 1.7 \times 10^7$ cm^{-3} and $n_{H_2}(25 \text{ K}) = 8.5 \times 10^5$ cm^{-3}. See Table 5.1 for summary of all extracted values. In this figure, the n_{H_2} appears to plateau in the inner and outermost regions; this isn't actually occurring, the density profile is a power-law. This is simply a result of the shell spacing.

RADEX models for both o001 and o007 were produced for temperatures of 70 K and 25 K. The derived column and volume densities for a linewidth of 1.9 km s^{-1} and background temperature of 2.73 K will make up the RADEX input file. The RADEX results for the two models can be found in Table 5.2. All three geometries were considered and compared (uniform sphere, expanding sphere, and parallel plane slab). For both o001 and o007 lines, it is seen that with the progression through the three geometries as listed, the following parameters increase: iterations, T_{ex}, T_R (T_A), and n_u. The lower population n_l decreases slightly with each geometry. All three geometries use the same ortho to para ratio which
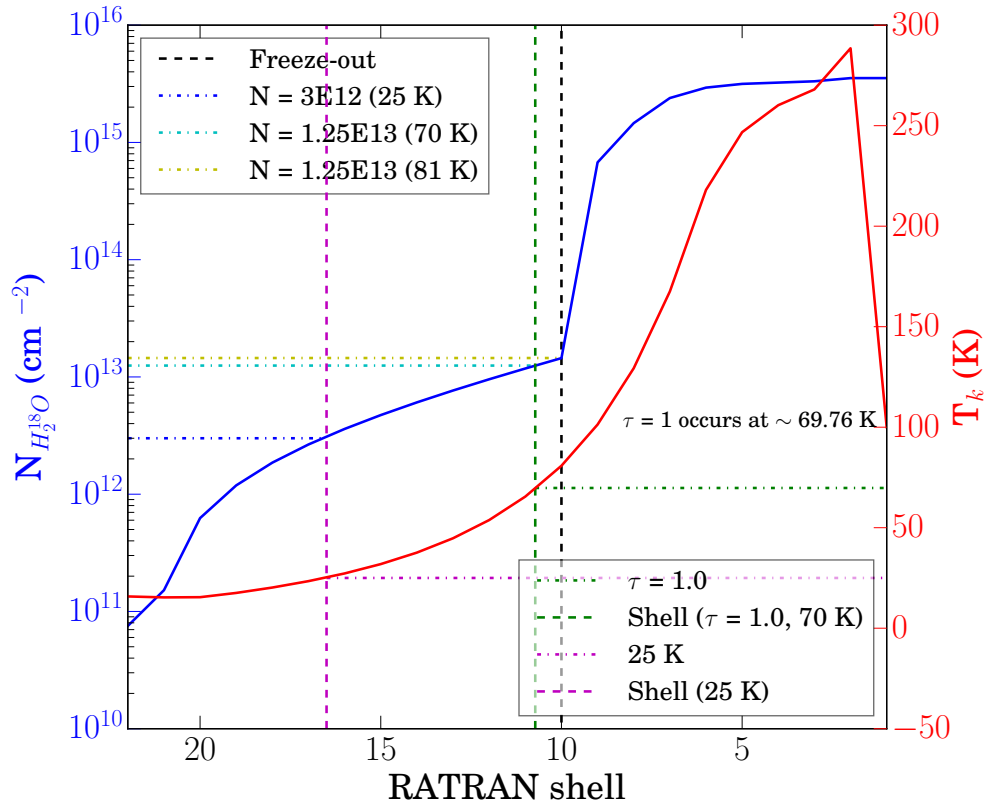
Figure 5.6: Column Density (blue) and Gas Temperature (red) per RATRAN Shell for $H_2^{18}O$. The freeze-out radius is marked by a black dashed line. This plot was used to extract values of N for optical depths of $\tau = 1.0$ (green dashed) and 0.23 (magenta dashed), corresponding to $T_k \sim 70$ (green dotted) and 25 K (magenta dotted) respectively, by drawing lines through the corresponding shells (vertical green and magenta dashed lines). It is seen at 70 K, the column density of $H_2^{18}O$ is 1.25×10^{13} cm^{-2} (cyan dotted), and at 25 K is 3.0×10^{12} cm^{-2} (blue dotted).
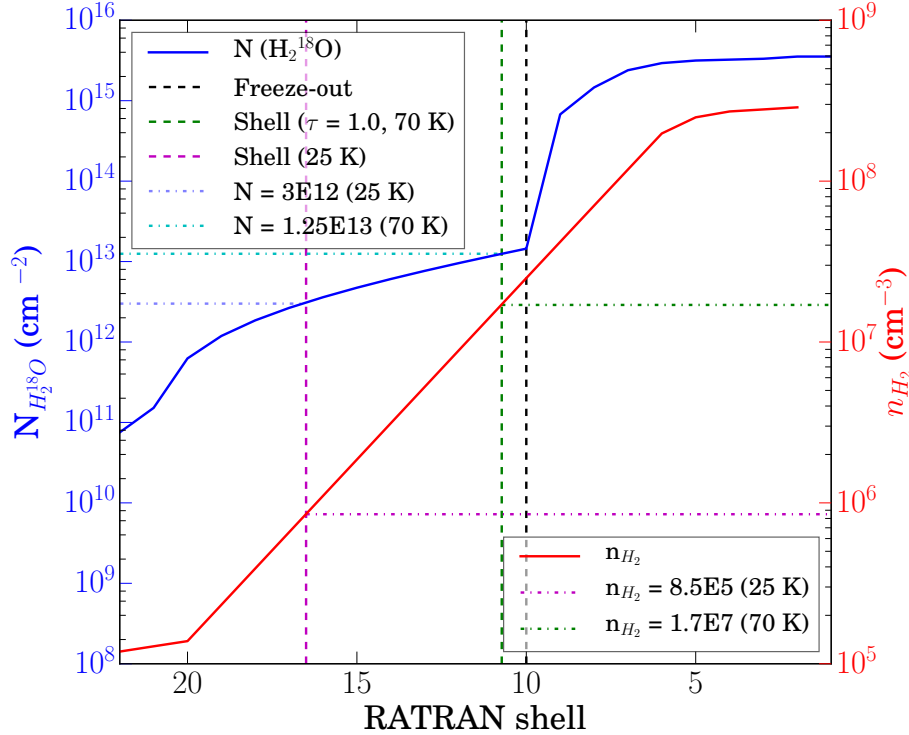
Figure 5.7: Column Density and H_2 Density per RATRAN Shell for $H_2^{18}O$. The freeze-out radius is marked by a black dashed line. This plot was used to extract values of n_{H_2} for optical depths of $\tau = 1.0$ (green dashed) and 0.23 (magenta dashed), corresponding to $T_k \sim$ 70 (green) and 25 K (magenta) respectively, by drawing lines through the corresponding shells (vertical green and magenta dashed lines). It is seen in Figure 5.6 at 70 K, the column density of $H_2^{18}O$ is 1.25×10^{13} cm^{-2} (cyan dashed), and at 25 K is 3.0×10^{12} cm^{-2} (blue dashed). Using the same vertical dashed lines, $n_{H_2}(70 \text{ K}) = 1.7 \times 10^7$ (horizontal green dotted) and $n_{H_2}(25 \text{ K}) = 8.5 \times 10^5$ (horizontal magenta dotted). See Table 5.1 below for summary of extracted values.

is determined by RADEX (see Figure 4.34). The o001 line uses o/p $= 9.786 \times 10^{-3}$ while the o007 line uses o/p $= 0.780$. The optical depth decreases for o001 with the progression in geometry, while increasing for o007.

Considering the T $= 25.0$ K case (as this is likely representative of the outer NGC 7129 FIRS 2 envelope), the uniform sphere geometry yields results that are the most consistent with the structural RATRAN model. The expected o001 τ is on the same order of magnitude as the RADEX values, but with a percentage difference of 37%. The same for o007 is not consistent with the expected value (much smaller than expected). From the HIFI observations, the expected antenna temperature for o001 $H_2^{18}O$ is $T_A = 0.012$ K (1.9 km s^{-1} feature). If $T_A = T_R$, the antenna temperature derived by RADEX for the T $= 25$ K case is on the same order of magnitude as that expected for o001, but it is doubled. If correcting for beam dilution and $T_A = AT_R$ where $A_{001} = 0.117$ and $A_{007} = 0.427$, the resultant T_A would be a factor of ~ 4 too large. For the excited o007 line, the antenna temperature returned by RADEX would be undetectable on the current HIFI observing scales. This is consistent with the data. As this is an ideal situation because the envelope of NGC 7129 FIRS 2 is not uniform, the results from RADEX as compared to RATRAN are considerably in agreement.

Comparing RATRAN and RADEX Population Levels n_i

Another method of verifying the validity of the RATRAN models is by comparing the population levels n_i output by AMC with that of RADEX. The population is compared for the uniform sphere geometry as well as the parallel plane slab geometry for ortho $H_2^{18}O$ and $H_2^{16}O$.

In Figure 5.8, the populations are compared for $H_2^{16}O$ using uniform sphere geometry. The ratio $R = n_{i,RAT}/n_{i,RAD}$ is plotted as a function of envelope shell; the boundary where the RATRAN and RADEX populations are equal occurs at $R = 1.0$. This is indicated by the horizontal black dashed line. The vertical red dashed line indicates the RATRAN freeze-out radius, the blue line indicates the n_1 population ratio, and the green line indicates the n_2 population ratio. The RATRAN population R_{n_2} becomes much greater (factor of $\lesssim$ 50) in the outer envelope. This is likely because RADEX employs the LTE OPR, while the RATRAN model used a constant 3:1 OPR. The RATRAN model also assumes a freeze-out radius (red dashed line) at $T_g = 100$ K; here the abundance drops, decreasing the RATRAN n_1 below the RADEX n_1. In addition to these suggestions, RADEX does not consider the region in a manner of nested spherical shells like RATRAN, it only considers the sphere as a single entity producing uniform emission.

Table 5.2: Comparing RADEX geometries (Uniform Sphere (US), Expanding Sphere (ES), and Parallel Plane Slab (PPS)) at 25.0 K. Modelling $H_2^{18}O$. Input: $N = 3 \times 10^{12}$, $n_{H_2} = 8.5 \times 10^5$, $\Delta V = 1.9$ km s^{-1}. Optical depth at 25.0 K is ~ 0.23 for o001 and 9.83×10^{-5} for o007, derived from RATRAN envelope model (5.6, 5.7, and 6.4). Antenna temperature ($T_A \sim AT_R$, where $A_{001} = 0.117$ and $A_{007} = 0.427$) for $H_2^{18}O$ is ~ 0.012 K.

Geometry	US		ES		PPS	
Line	o001	o007	o001	o007	o001	o007
State Transition	2-1	6-5	2-1	6-5	2-1	6-5
Frequency (GHz)	547	1095	547	1095	547	1095
$\tau = 0.23$, T $= 25$ K						
o/p ratio	9.786×10^{-3}					
Iterations	15	15	16	16	16	16
$T_{ex}(K)$	4.707	16.094	4.759	16.107	4.980	16.169
τ	3.16×10^{-1}	8.77×10^{-8}	3.16×10^{-1}	8.78×10^{-8}	3.15×10^{-1}	8.79×10^{-8}
T_R (K)	2.40×10^{-2}	1.82×10^{-7}	2.60×10^{-2}	1.83×10^{-7}	3.40×10^{-2}	1.85×10^{-7}
n_u	3.40×10^{-3}	1.74×10^{-8}	3.62×10^{-3}	4.60×10^{-7}	4.64×10^{-3}	1.78×10^{-8}
n_l	9.97×10^{-1}	4.60×10^{-7}	9.96×10^{-1}	4.60×10^{-7}	9.95×10^{-1}	4.61×10^{-7}
$\tau = 1.0$, T $= 70$ K						
o/p ratio	0.78012					
Iterations	24	24	25	25	27	27
$T_{ex}(K)$	22.484	60.364	23.513	61.778	27.073	61.967
τ	6.916×10^{-1}	7.984×10^{-4}	6.648×10^{-1}	8.012×10^{-4}	5.822×10^{-1}	9.237×10^{-4}
T_R (K)	5.844×10^{0}	3.018×10^{-2}	6.132×10^{0}	3.135×10^{-2}	7.004×10^{0}	3.630×10^{-2}
n_u	2.284×10^{-1}	6.938×10^{-4}	2.368×10^{-1}	7.207×10^{-4}	2.607×10^{-1}	8.346×10^{-4}
n_l	7.498×10^{-1}	1.660×10^{-3}	7.381×10^{-1}	1.690×10^{-3}	6.996×10^{-1}	1.952×10^{-3}
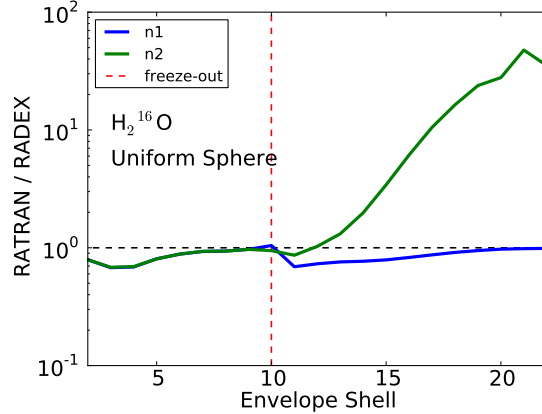
Figure 5.8: Comparing n_i of RATRAN and RADEX for $H_2^{16}O$ (uniform sphere geometry). $R = n_{i,RAT}/n_{i,RAD}$ vs. envelope shell. Values are equal at $R = 1.0$ (black dashed line). The freeze-out radius = red dashed line, n_1 ratio = blue line, and n_2 ratio = green line. The RATRAN population R_{n_2} becomes much greater (factor of $\lesssim 50$) in the outer envelope. The abundance X_{out} drops at the freeze-out radius, decreasing the RATRAN n_1 below the RADEX n_1

In terms of the goodness of fit between the population values of RATRAN and RADEX, the reduced chi-square $\chi_R^2(n_1) = 0.021$ and $\chi_R^2(n_2) = 0.028$.

In Figure 5.9, the populations are compared for $H_2^{18}O$ using uniform sphere geometry. The plotting attributes are the same as in Figure 5.8. The RATRAN population n_2 becomes much greater (factor of $\lesssim 100$) in the outer envelope, similar to the $H_2^{16}O$ version of this plot. Suggestions for this behaviour are the same as mentioned for $H_2^{16}O$ as the only difference between these isotopologues is the water abundance with respect to H_2. That being said, the ratio between RATRAN and RADEX populations has a larger deviation from $R = 1.0$ for $H_2^{18}O$ (i.e, $\lesssim 100$ vs. $\lesssim 50$). In terms of the goodness of fit between the population values of RATRAN and RADEX, the reduced chi-square $\chi_R^2(n_1) = 0.130$ and $\chi_R^2(n_2) = 0.108$. This is a factor of ~ 6 and 4 (respectively) times greater than that for the $H_2^{16}O$.

In Figure 5.10, the populations are compared for $H_2^{16}O$ using parallel plane slab geometry. The plotting attributes are the same as in Figure 5.8. The RATRAN population n_2 becomes much greater (factor of $\lesssim 30$) in the outer envelope, similar to the spherical geometry version of this plot. Suggestions for this behaviour are the same as mentioned. In terms of the goodness of fit between the population values of RATRAN and RADEX,

158
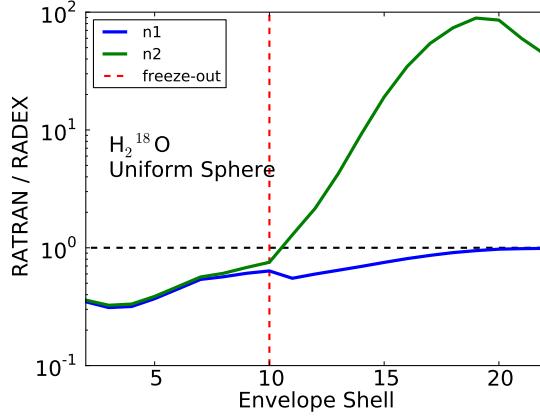
Figure 5.9: Comparing n_i of RATRAN and RADEX for $H_2^{18}O$ (uniform sphere geometry). Same as Figure 5.8. The RATRAN population R_{n_2} becomes much greater (factor of $\lesssim$ 100) in the outer envelope. The abundance X_{out} drops at the freeze-out radius, causing a slight decrease in R_{n_1} at this shell.

the reduced chi-square $\chi_R^2(n_1) = 0.0077$ and $\chi_R^2(n_2) = 0.0013$. This is a factor of ~ 2.5 and 2.0 (respectively) times less than that for the spherical geometry.

Lastly, in Figure 5.11, the populations are compared for $H_2^{18}O$ using parallel plane slab geometry. The plotting attributes are the same as in Figure 5.9. The RATRAN population n_2 becomes much greater (factor of $\lesssim$ 100) in the outer envelope, similar to the spherical geometry version of this plot. Suggestions for this behaviour are the same as mentioned. In terms of the goodness of fit between the population values of RATRAN and RADEX, the reduced chi-square $\chi_R^2(n_1) = 0.080$ and $\chi_R^2(n_2) = 0.075$. This is a factor of ~ 1.6 and 1.4 (respectively) times less than that for the spherical geometry.

All calculated chi-square and reduced chi-squares using the right-tail distribution method for the above RATRAN and RADEX population comparison are given in Table 5.3 for each of the geometries. The p-values are all equal to 1.0; thus, we fail to reject the null hypothesis that these values are consistent.
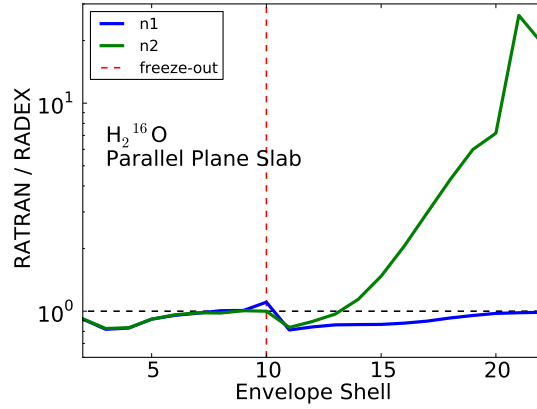
Figure 5.10: Same as Figure 5.8 but with parallel plane slab geometry. The RATRAN population n_2 becomes much greater (factor of < 30) in the outer envelope. The abundance X_{out} drops at the freeze-out radius, causing a slight decrease in R_{n_1} at this shell.
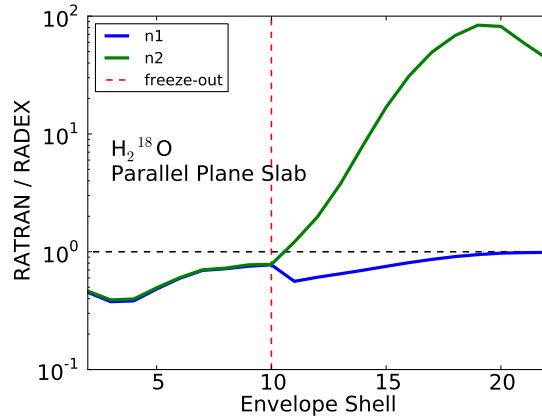
Figure 5.11: Comparing n_i of RATRAN and RADEX for $H_2^{18}O$ (parallel plane slab geometry). Same as Figure 5.9. The RATRAN population R_{n_2} becomes much greater (factor of $\lesssim 100$) in the outer envelope. The abundance X_{out} drops at the freeze-out radius, causing a slight decrease in R_{n_1} at this shell.

Table 5.3: RATRAN vs. RADEX: population χ^2 comparison

Isotopologue	Geometry	n_i	χ^2	χ^2_R	p
$H_2^{16}O$	US	n_1	0.446	0.021	1.0
		n_2	0.596	0.028	1.0
	PPS	n_1	0.142	0.0077	1.0
		n_2	0.267	0.013	1.0
$H_2^{18}O$	US	n_1	2.736	0.130	1.0
		n_2	2.270	0.108	1.0
	PPS	n_1	1.686	0.080	1.0
		n_2	1.582	0.075	1.0

Comparing RATRAN and RADEX Optical Depths τ

The optical depths calculated from the RATRAN AMC population levels are compared with RADEX output optical depths; these are calculated by RADEX using the same input parameters as that for RATRAN. Unfortunately, these values are not often consistent. For $H_2^{16}O$, the optical depth calculated from RATRAN parameters for both the uniform sphere (US) geometry (Figure 5.12) and parallel plane slab (PPS) geometry (5.14) are less than the RADEX optical depth by a factor of ~ 0.4. In both figures, the equality boundary is indicated by the black dashed line and the freeze-out radius is indicated by the red dashed line. Both geometry R_τ appear to experience drastic dips at the freeze-out radius on this scale; the PPS geometry also exhibits two peaks on either side of the freeze-out radius. It was determined that these were not a result of typos in the RADEX input file.

For $H_2^{18}O$, the optical depth calculated from RATRAN parameters for both the US geometry (Figure 5.12) and PPS geometry (5.14) are greater than the RADEX optical depth by a factor of ~ 12 - 50. Both geometry R_τ appear to experience drastic dips at the freeze-out radius on this scale (down to $R_\tau = 0.25$ and 0.4, respectively); both exhibit a second dip in the outer envelope ($\sim$ shell 16).

Table 5.4 gives the χ^2 and χ^2_R right tail distribution calculations for both uniform sphere and parallel plane slab geometries for both isotopologues. The p-values are so low that we reject the null hypothesis that these values are consistent.
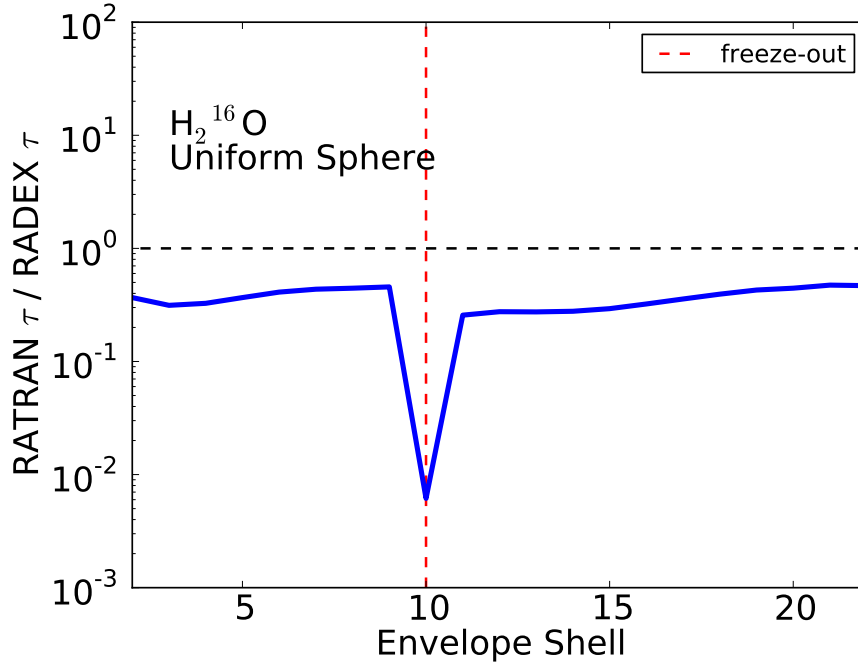
Figure 5.12: Comparing τ for $H_2^{16}O$, US geometry. R_τ vs. shell. Black dashed line: $R_\tau =$ 1.0, red dashed line: freeze-out radius, blue line: R_τ.

Table 5.4: RATRAN vs. RADEX optical depth χ^2 comparison

Isotopologue	Geometry	χ^2	χ_R^2	p
$H_2^{16}O$	US	43565.21	2074.53	0
	PPS	38203.77	1819.23	0
$H_2^{18}O$	US	460.82	21.94	2.2×10^{-84}
	PPS	464.40	22.11	4.0×10^{-85}

5.4.3   Summary: Validation of RATRAN Results with RADEX

1. **Emission component at 0.6 km s^{-1}:** The foreground cloud (if accurately modelled by a parallel plane slab), must emit around $T_{gas} = 40$–45 K, with a column density of $\sim 10^{13}$ to obtain a velocity integrated intensity ~ 0.02 K km s^{-1} (from HIFI observations).

162
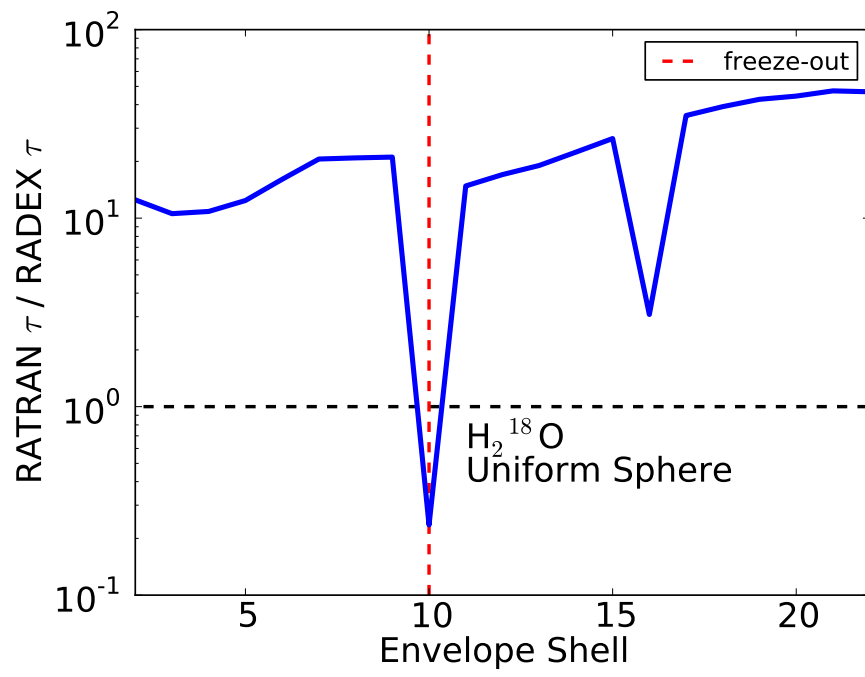
Figure 5.13: Comparing τ for $H_2^{18}O$, US geometry. Same as Figure 5.12
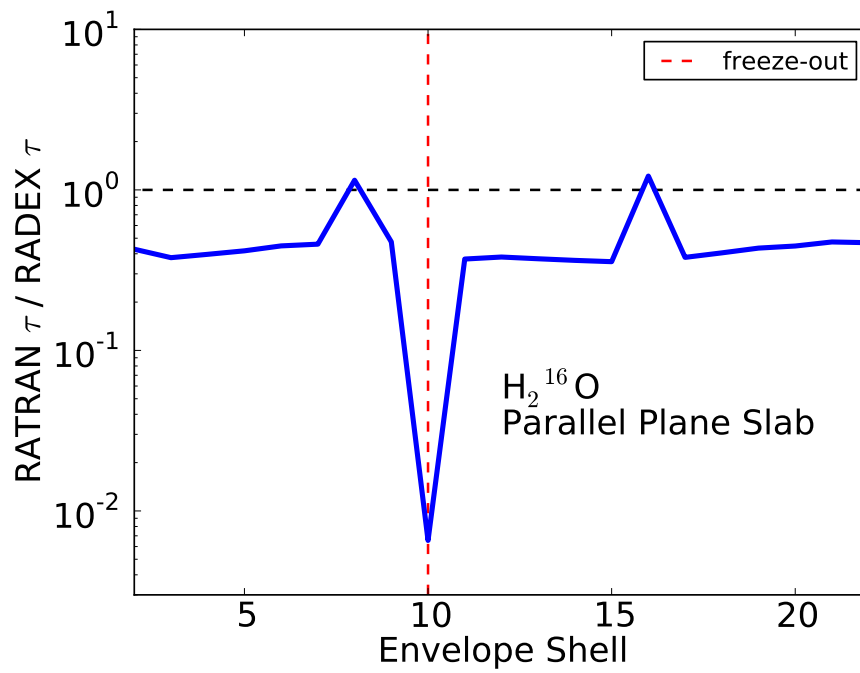
Figure 5.14: Comparing τ for $H_2^{16}O$, PPS geometry. R_τ vs. shell. Black dashed line: R_τ = 1.0, red dashed line: freeze-out radius, blue line: R_τ.

Figure 5.15: Comparing τ for $H_2^{16}O$, PPS geometry. Same as Figure 5.14

2. **Emission component at 8.6 km s^{-1}**: The NGC 7129 FIRS 2 envelope, if considered as a parallel plane slab, has a RADEX velocity integrated intensity $\int T_A dv \sim$ 0.06 K km s^{-1} for column densities of $10^{14} - 10^{16}$. This is consistent with the column densities seen in the RATRAN modelled outer envelope (Figure 5.6) and is greater than the foreground component by a factor of 10^2.

3. **Comparing geometries**: With progression through the RADEX geometries (US, ES, PPS), the following parameters increase: iterations, T_{ex}, T_R (T_A), and n_u. The lower population n$_l$ decreases slightly with each geometry. All three geometries use the same LTE ortho to para ratio. Lastly, the optical depth decreases for o001 with the progression in geometry, while increasing for o007.

4. **RADEX T = 25.0 K case**: This RADEX model is likely well representative of the outer NGC 7129 FIRS 2 envelope. Of the three RADEX geometries, the uniform sphere yields results that are the most consistent with the RATRAN model. The expected H$_2^{18}$O ground state line (o001) optical depth τ is on the same order of magnitude as the RADEX values, but with a percentage difference of 37%. The same for o007 is not consistent with the expected value (much smaller than expected). From the HIFI observations, the expected antenna temperature for o001 H$_2^{18}$O is T$_A$ = 0.012 K (1.9 km s^{-1} feature). If T$_A$ = T$_R$, the antenna temperature derived by RADEX is on the same order of magnitude, but it is doubled. If correcting for beam dilution with T$_A$ = AT$_R$ where A$_{001}$ = 0.117 and A$_{007}$ = 0.427, the resultant T$_A$ would be a factor of $\sim$ 4 too large. For the excited o007 line, the antenna temperature returned by RADEX would be undetectable on the current HIFI observing scales. This is consistent with the data. As this is an ideal situation because the envelope of NGC 7129 FIRS 2 is not uniform, the results from RADEX as compared to RATRAN are considerably in agreement.

5. **Comparing Population**: Comparing RATRAN and RADEX population results (while also comparing RADEX geometries US and PPS) for both isotopologues allows us to see that for H$_2^{16}$O, the population results of both codes are consistent until freeze-out occurs in RATRAN. At this point, the excited fractional population n_2 drastically increases for RATRAN while the ground state population n_1 is still fairly consistent. This observation is valid for both geometries. H$_2^{18}$O population results are less consistent, but still exhibit the same plotted effects as that of the H$_2^{16}$O. Of this exercise, the RADEX model that returned the best chi-square result is the H$_2^{16}$O parallel plane geometry, with a reduced chi-square of $\chi_R^2(n_1) = 0.0077$ and $\chi_R^2(n_2) = 0.013$. The null hypothesis (RADEX validates RATRAN results) fails to reject for the population comparison.

166

6. **Comparing Optical Depth**: For $H_2^{16}O$, the optical depth calculated from RATRAN parameters for both the uniform sphere (US) and parallel plane slab (PPS) geometry are less than the RADEX optical depth by a factor of ~ 0.4.

For $H_2^{18}O$, the optical depth calculated from RATRAN parameters for both the US and PPS geometry are greater than the RADEX optical depth by a factor of ~ 12 - 50. For both geometries, the RATRAN to RADEX ratio R_τ appears to experience drastic dips at the freeze-out radius on this scale (down to $R_\tau = 0.25$ and 0.4, respectively); both exhibit a second dip in the outer envelope ($\sim$ shell 16).

Differences in optical depth produced by the two radiative transfer codes are likely due to the use of a freeze-out temperature in the RATRAN models. Additionally, RADEX uses an LTE ortho to para ratio (OPR), while the RATRAN model used an OPR of 3:1. Statistically, the null hypothesis (RADEX validates RATRAN results) is rejected for the optical depth comparison.

Chapter 6

Discussion

This chapter will present a discussion on the HIFI observations obtained and their respective line profiles, P-Cygni and inverse P-Cygni profiles, Gaussian component fits, optical depth derivations, RATRAN sources of error, modelling results, and a comparison between mass regimes.

6.1 Observations

Molecular emission lines are very useful in the study of star formation. A total of 9 spectral water lines were observed for the IM YSO NGC 7129 FIRS 2, obtained under the WISH program. These can be found in Figure 2.1.

The strongest lines in our $H_2^{16}O$ HIFI spectral dataset are the ground state ortho and para lines, at 557 and 1113 GHz respectively, and the first excited para state at 988 GHz (para 002). The ground state lines exhibit blueshifted absorptions with respect to the V_{LSR}. This absorption feature does not appear in the higher state lines. The 752 GHz line (para 004) is similar in line shape to the 988 GHz, but reduced in intensity by a factor of 2.5. The 1153 GHz line is a noisier line compared to the rest of the dataset. All lines appear to exhibit line broadening. A wide outflow is present to some degree in all of the lines; this feature is strongest in the aforementioned lines, appearing centered at -19.7 km s^{-1}. Visually extracting this component, the ground state lines appear to have a P-Cygni profile. This will be discussed later.

The strongest line in the $H_2^{18}O$ HIFI spectral dataset is the ground state ortho 547 GHz line. The other observed spectral lines at 995 GHz (para 002) and 1096 GHz (ortho 007)

appeared as non-detections. The ground state ortho line also has a second emission line at $\sim$ -0.6 km s^{-1}, perhaps attributed to a foreground cloud.

The HIFI observation RMS noise calculated in this thesis is compared to Johnstone et al. (2010)'s calculations in Table 2.6. The values obtained in this work are slightly larger (i.e, 0.023 K vs. 0.020 K). The larger result is likely a result of a wider velocity range and updated beamsize; Johnstone et al. (2010) uses a velocity range of 1 km s^{-1} while this work uses a range from -60 to +60 km s^{-1} with respect to the V$_{LSR}$.

6.1.1   P-Cygni and Inverse P-Cygni Profiles

As mentioned in the Introduction, an informative classification of molecular line features in star formation regions is the P-Cygni (and inverse P-Cygni) profile. The qualitative difference can be seen in the cartoon in Figure 6.1, extracted from Kristensen et al. (2012).

Inverse P-Cygni profiles are usually found associated with Class 0 YSOs and are typically caused by a velocity and excitation gradient in gas falling towards the central core (Kristensen et al. 2012). As described in Kristensen et al., the narrow absorption feature is seen redshifted with respect to the narrow emission; this absorption feature takes place against both the outflow component and the continuum, indicating that the component is located between the outflow and the envelope edge. The line profile shape is dominated by the infall velocity $v_{inf}/\Delta v_{turb}$. If the entire envelope is in free-fall, the velocity approaches that in Equation 1.17. Of the LM YSOs these authors studied, NGC 1333 IRAS 4A (discussed in §6.4) shows an inverse P-Cygni profile, confirmed by both interferomic and single dish data of Di Francesco et al. (2001), Jørgensen et al. (2007), Altard et al. (2009), and Kristensen et al. (2010). They do not classify LM YSO NGC 1333 IRAS 2A (briefly studied in this work) as either P-Cygni or inverse P-Cygni.

Regular P-Cygni profiles on the other hand are usually attributed to Class I YSOs. These lines exhibit both absorption and emission features and assume a spherical envelope. The other structures of the star-forming region (i.e. outflow) are non-spherical in nature. The emission feature is due to a dense stellar wind near the YSO, while the blueshifted absorption feature is generated by radiation passing through the outflow. It has been suggested in Kristensen et al. (2012) that infall could persist while the outflow pushes specific regions to expand (i.e., infall reversal).

Bringing the focus back to NGC 7129 FIRS 2, the ground state ortho and para lines observed with Herschel HIFI show a distinct P-Cygni profile post-Gaussian subtraction (Figures 6.2 and 6.3). The outflows associated with NGC 7129 FIRS 2 are bipolar, unlike the spherically symmetric outflows of P-Cygni stars. The young stage of stellar evolution
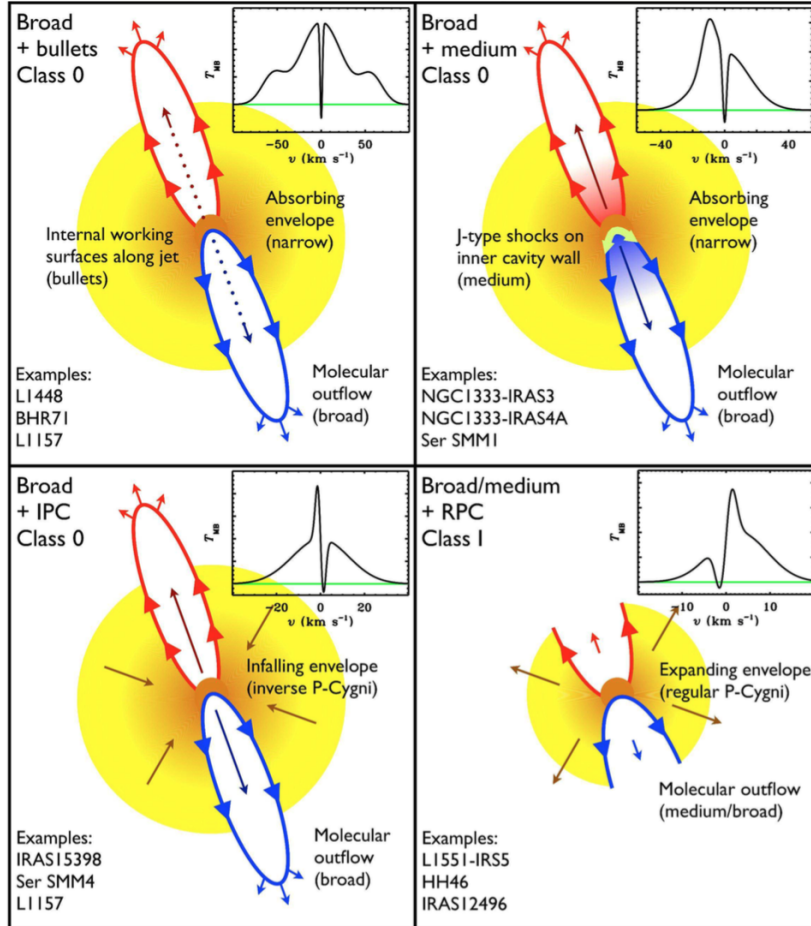
Figure 6.1: Cartoon showing the different dynamical and energetic components in protostars directly traced by water emission. Each panel shows a cartoon of a protostellar system with a sample spectrum and a number of specific examples of objects in this category. Note, the velocity scale of the inserted spectra change from the top left panel to bottom right. Inverse P-Cygni and regular P-Cygni profiles have been abbreviated IPC and RPC, respectively. The labels Class 0 and I refer to the Class where this type of profile is typically found. From Kristensen et al. (2012), Figure 10.

(Class 0) and the fact that the outflows are not directly aligned with the line of sight suggest NGC 7129 FIRS 2 is likely not expanding.
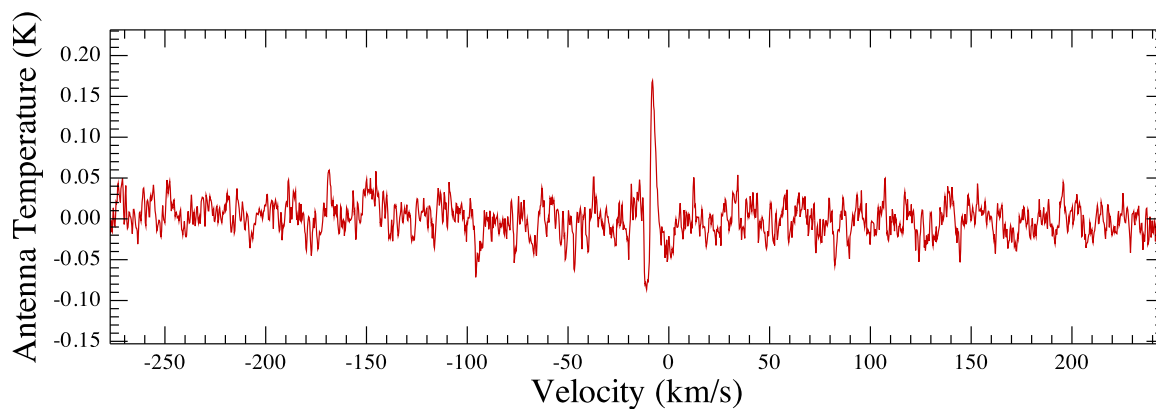
Figure 6.2: P-Cygni Profile of $H_2^{16}O$ 1_{10}-1_{01} o001. Residual of subtracting Gaussian G1 and G2. Image produced with HIPE
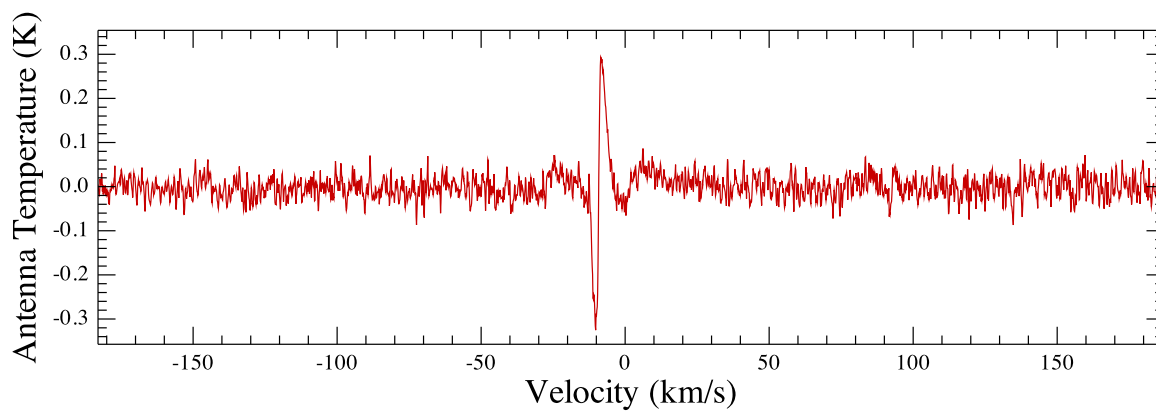
Figure 6.3: P-Cygni Profile of $H_2^{16}O$ 1_{11}-0_{00} p001. Same as Figure 6.2

171

6.2 Gaussian Decomposition of Observed Spectral Lines

Separating spectral lines into Gaussian components is useful for placing constraints on physical components of star formation regions (Kristensen et al. 2010; Johnstone et al. 2010). HIPE 15.0.0 was used to fit Gaussian profiles to the HIFI spectral dataset while minimizing the associated uncertainty. For the $H_2^{16}O$ spectral dataset, three Gaussians were placed at -19.7, -7.8, and -3.6 km s^{-1}; the second of which is expected to be the envelope component (see Table 2.4 and Figure 2.2). When subtracted from the spectral line, the residual is mostly within 3σ for each of the spectral lines.

For the $H_2^{18}O$ spectral dataset, two Gaussians were placed at -8.6 and -3.4 km s^{-1}; the former is expected to be the envelope component while the latter is expected to be a foreground component. When subtracted from the spectral line, the residual is mostly within 3σ for each of the spectral lines. The non-detection lines 995 GHz (p002) and 1095 GHz (o007) are also within 3σ without any subtraction.

An important point to note is that these fits do not absolutely have to be Gaussian; the spectral components could be another line shape altogether (i.e, Lorentzian). This was not investigated in this thesis but is an interesting thought that might be worth investigating in the future.

6.2.1 Other IM WISH Candidates

As mentioned, the IM-WISH candidates included more than just NGC 7129 FIRS 2. Observations for $H_2^{16}O$ and $H_2^{18}O$ (where applicable) were obtained from HIPE 15.0.0 for each of the following sources: NGC 2071 IR, Vela IRS 17, Vela IRS 19, AFGL 490, and L1641 S3MMS1. The details of these observations are listed in Table A.2 and A.3. The molecular emission lines are plotted in Figures A.1 - A.6. The Gaussian decompositions are listed in Tables A.4 - A.8 and plotted in Figures A.8 - A.15.

NGC 2071 IR

To elaborate, NGC 2071 IR is the only other IM candidate that has $H_2^{18}O$ observations. Like NGC 7129 FIRS 2, observations were obtained for the $H_2^{16}O$ 557 (o001), 1113 (p001), 988 (p002), 752 (p004), 1153 (o006) GHz lines, and the $H_2^{18}O$ 547 (o001), and 1096 (o007) GHz lines. As seen in Figure A.1, the ground state lines and the 988 GHz line are the strongest. The ground state lines exhibit a double blueshifted absorption feature. Wide components corresponding to the outflow are present in the 557, 1113, 988, and 752 GHz

172

lines. The emission seen in NGC 2071 IR is a lot stronger than that seen in NGC 7129 FIRS 2; the $H_2^{16}O$ ground state emission has an intensity of $\sim$ 2.0 K. Even the excited 1153 GHz line has a peak intensity of $\sim$ 2.5 K. The strongest line is the 988 GHz line, with an emission intensity of $\gtrsim$ 3.0 K. The highest excitation lines of this dataset appear very symmetrical about the V_{LSR} = 9.6 km s^{-1}; as such, these lines would likely be really straight-forward to model with RATRAN. The absorption feature seen in the ground state $H_2^{16}O$ lines is also observed in the $H_2^{18}O$ 547 GHz line. This ground state line has an emission intensity of roughly 0.075 K, greater than that of NGC 7129 FIRS 2 by a factor of 6.25. The absorption has an intensity of -0.05 K. The excited 1096 GHz line appears as though it might have a slight residual standing wave, and is also very noisy.

A total of five Gaussians were fit to the lines of both isotopologues (Table A.4). HIPE deduced the 1096 GHz line was also a non-detection for this source. The Gaussian $H_2^{16}O$ fits are as follows: very-broad emission at 11.6 km s^{-1}, broad emission at 10.6 km s^{-1}, medium emission at 11.6 km s^{-1}, narrow absorption at -9.2 km s^{-1}, and a narrow absorption at 4.2 km s^{-1}. The Gaussian $H_2^{18}O$ fits are as follows: broad emission at 10.6 km s^{-1}, narrow absorption at 11.6 km s^{-1}, medium emission at 11.6 km s^{-1}, narrow emission at -9.2 km s^{-1}, and a narrow absorption at -7.5 km s^{-1}.

The $H_2^{16}O$ residual fits (Figure A.7) show that the Gaussian fits aren't quite perfect; the residuals exceed 3σ in some places, indicating either some actual features (vs. noise) weren't properly fit with either a Gaussian profile, or not enough Gaussians were added during the HIPE optimization process. The $H_2^{18}O$ residuals are nicely encased by the 3σ level boundaries (Figure A.8).

RATRAN would likely produce a model fitting the medium and narrow components, as these appear to be associated with the envelope.

Vela IRS 17

Observations were obtained for the IM source Vela IRS 17 from HIPE 15.0.0; these include: $H_2^{16}O$ 557 (o001), 1113 (p001), 988 (p002), 752 (p004), 1153 (o006) GHz lines, and the $H_2^{18}O$ 547 (o001), and lines. The $H_2^{18}O$ line was thrown out after Gaussian fitting due to spurs in the data. As seen in Figure A.3, the ortho ground state line and the 988 GHz line are the strongest. The ground state lines exhibit an absorption feature at the V_{LSR} = 3.9 km s^{-1}. The emission seen in Vela IRS 17 is a more similar to NGC 7129 FIRS 2 than NGC 2071 IR; the $H_2^{16}O$ ground state emission has an intensity of $\sim$ 0.6 K. The excited 1153 GHz line is very noisy and appears to have a long standing wave. The highest excitation lines of this dataset appear very symmetrical about the V_{LSR}; as such, these lines would also likely be really straight-forward to model with RATRAN. From the observed para lines,

it also appears that the molecular spectra has a redshifted tail; i.e, the broad blueshifted emission has been absorbed.

A total of four Gaussians were fit to the lines of $H_2^{16}O$ (Table A.5: broad emission at 2.8 km s^{-1}, medium emission at 1.1 km s^{-1}, narrow emission at 1.5 km s^{-1}, and narrow emission at 6.5 km s^{-1}. The Gaussian $H_2^{18}O$ fit is as follows: Medium emission at 6.5 km s^{-1}. As seen in Figure A.9, the $H_2^{16}O$ residuals are nicely encased by the 3σ level boundaries. RATRAN would likely produce a molecular line that would fit the 6.5 km s^{-1} component; this component is likely associated with the envelope. The $H_2^{18}O$ Gaussian fit is plotted in Figure A.10. The residual for this line is also within 3σ, although this data was discarded after Gaussian fitting due to a spur further down the molecular line.

Vela IRS 19

Observations were obtained for the deeply embedded IM source Vela IRS 19 from HIPE 15.0.0; these include: $H_2^{16}O$ 557 (o001), 1113 (p001), 988 (p002), 752 (p004), 1153 (o006) GHz lines, and the $H_2^{18}O$ 547 (o001), and lines. This $H_2^{18}O$ 547 GHz and the $H_2^{16}O$ 1113 GHz lines were thrown out due to spurs in the data. As seen in Figure A.4, the excited para state 988 and 752 GHz lines are the strongest. The ground state lines do not exhibit absorption features, and are barely detected; the $H_2^{16}O$ ortho ground state emission has an intensity of ~ 0.15 K. The excited 1153 GHz line appears very noisy for this source as well. Because the lines are so weak, it is likely that the envelope is contributing to the majority of the emission, thus making it straight-forward to model with RATRAN. From the ground state lines and the observed excited para lines, this source also appears to have molecular spectra with a redshifted tail; i.e, the broad blueshifted emission has been absorbed.

A total of four Gaussians were fit to the lines of $H_2^{16}O$ (Table A.6; the Gaussian fit process for Vela IRS 19 was a little more difficult than the others due to the weak emission. Out of the four Gaussians, each transition fits a combination of 2-3 of these 4. The first component is located at 29.6 km s^{-1} (ground-state ortho only), second component is at 18.4 km s^{-1} (557, 988, 752 GHz), third component is at 11.9 km s^{-1} (excited para lines), and the fourth component is at 21.2 km s^{-1} (752 and 1153 GHz). As seen in Figure A.12, the $H_2^{16}O$ residuals are nicely encased by the 3σ level boundaries. RATRAN would likely produce a molecular line that would fit the 11.9 km s^{-1} components of the 988 and 752 GHz lines; this component is likely associated with the envelope.

Modelling Water in Vela IRS 17 & 19   Tisi (2013) derived a density profile power-law index of $\alpha = 1.35$ for Vela IRS 17 and $\alpha = 1.5$ for Vela IRS 19. The Gaussian components

fit to the Herschel HIFI observations (same as that seen here) by Tisi are given in Figures A.11 and A.13, respectively. The components for the most part are similar; Tisi optimized his total fit with three, as opposed to the four of this work. Different from Tisi, this work adds the 21.2 km s^{-1} component, fitting to the absorption in the 1153 GHz line. The envelopes of each were then modelled with RATRAN.

He deduced for both Vela IRS 17 and 19 that the 752 GHz line was the most useful in providing constraints on the inner and outer abundances of H$_2$O. Like this work, Tisi was also unable to constrain the inner abundance of H$_2$O. Ultimately, he suggested an outer envelope water abundance of 6×10^{-8} – 4×10^{-7}. This value is larger than that seen in this work for IM star formation by about a factor of $3 - 18$. After private communication with Tisi, this was determined to be the result of a difference in collision rates. Tisi (2013) employed a scaled version of the Green et al. (1993) H$_2$O-He collision rates, similar to Johnstone et al. (2010). As mentioned, it was determined that these collision rates cause non-negligible differences in the modelled line emission; the current H$_2$O-H$_2$ Daniel et al. (2011) collision rates are the most up-to-date.

AFGL 490

Observations were obtained for AFGL 490 with HIPE for the H$_2^{16}$O 557 (o001), 1113 (p001), 988 (p002), 752 (p004), 1153 (o006) GHz lines, and the H$_2^{18}$O 547 (o001) GHz line. The last line is thrown out due to bad data. As seen in Figure A.6, the ground state lines and the para excited lines 988 GHz and 752 GHz are the strongest. The ground state lines exhibit a redshifted absorption feature. The H$_2^{16}$O ground state emission has an intensity of ~ 0.2 K. The strongest line is the 988 GHz line, with an emission intensity of $\gtrsim 0.3$ K. The excited 1096 GHz line is also very noisy. Like the Vela IRS 17 and 19, the para 988 GHz line has a redshifted tail.

Like Vela IRS 19, A total of five Gaussians were fit to the H$_2^{16}$O lines (Table A.8). Out of the five Gaussians, each transition fits a combination of 3 of these 5 (the 1153 GHz line fits only 1). The first component is located at -10.7km s^{-1} (557, 1113, 988, 1153 GHz), second component is at -10.8 km s^{-1} (557 GHz), third component is at -11.2km s^{-1} (557, 1113, 752 GHz), the fourth component is at -13.1 km s^{-1} (988 and 752 GHz), and the fifth component is at -31.0 km s^{-1}. As seen in Figure A.15, the H$_2^{16}$O residuals are nicely encased by the 3σ level boundaries. RATRAN would likely produce a molecular line that would fit the -11.2 km s^{-1} and -13.1 km s^{-1} components of the 557, 988 and 752 GHz lines; these component is likely associated with the envelope.

175

L 1641 S3MMS1

Observations were obtained for L1641 S3MMS1 with HIPE for the $H_2^{16}O$ 557 (o001), 1113 (p001), 988 (p002), 752 (p004), 1153 (o006) GHz lines, and the $H_2^{18}O$ 547 (o001) GHz line. The last line is thrown out due to bad data. As seen in Figure A.5, all of the lines are quite strong relative to each other; the 1153 line while still noisy definitely shows emission. The ground state para line and the para excited line 988 GHz and ortho excited line 1153 GHz are the strongest. The ground state lines exhibit a both a blueshift, redshifted, and $V_L SR$ absorption feature. The $H_2^{16}O$ ground state emission has an intensity of ~ 0.1 K. T

A total of two Gaussians were fit to the $H_2^{16}O$ lines (Table A.7). The first component is located at 8.3 km s^{-1} and the second absorption component is at 5.5 km s^{-1}. As seen in Figure A.14, the $H_2^{16}O$ residuals are mostly encased by the 3σ level boundaries. In retrospect, the absorption Gaussians likely should have been divided into 3. RATRAN would likely produce a molecular line that would fit the 5.5 km s^{-1} components; this component is likely associated with the envelope.

6.3 Optical Depths

Optical depth calculations were used as a diagnostic in this work once it became obvious that the $H_2^{16}O$ 557 GHz RATRAN molecular line models were a result of a robustly complex structure. For Equation 3.8, repeated below, the Einstein coefficient A_{ul} and the statistical weight g are listed in the Daniel et al. (2011) molecular data file, the wavenumber $\tilde{\nu}$ is calculated from the line frequency, the column density N is calculated from the RATRAN model (i.e., each optical depth calculation is specific to each model), ΔV is the linewidth, and the populations f_l (lower state population) and f_u (upper state population) are obtainable from the AMC output file.

$$\tau = \frac{A_{ul}}{8\pi\tilde{\nu}^3} \frac{N}{1.0645\Delta V} \left(f_l \left(\frac{g_u}{g_l} \right) - f_u \right) \tag{6.1}$$

Each of the transition specific parameters are listed in Table 6.1. The optical depth calculation results can be found in Figures 6.4 - 6.9, corresponding to each of the water transitions discussed. All of these figures display a dashed line at $\tau = 1.0$, indicating the transition from optically thin (below) to optically thick (above). In Figure 6.4, the $H_2^{18}O$ o001 line is optically thick in a small region just inside the freeze-out radius. The optical depth reaches a maximum of $\tau = 9.02$. At this abundance, we expected to see only an outer envelope contribution; this plot confirms that expectation. The same line for $H_2^{16}O$ becomes optically

Table 6.1: NGC 7129 FIRS 2 $H_2^{16}O$ and $H_2^{18}O$ Optical Depth Calculation Parameters

Molecule	Transition	Line	ν (GHz)	$\tilde{\nu}$ (cm^{-1})	A_{ul} (cm^{-1})	g_l	g_u
	2-1	1_{10}-1_{01}	556.936	19	3.458×10^{-3}	9.0	9.0
	2-1	1_{11}-0_{00}	1113.343	37	1.842×10^{-2}	1.0	3.0
$H_2^{16}O$	3-2	2_{02}-1_{11}	987.927	33	5.835×10^{-3}	3.0	5.0
	4-3	2_{11}-2_{02}	752.033	25	7.062×10^{-3}	5.0	5.0
	6-4	3_{12}-2_{21}	1153.127	38	2.634×10^{-3}	15.0	21.0
	6-5	3_{12}-3_{03}	1097.365	37	1.648×10^{-2}	21.0	21.0
	2-1	1_{10}-$1_{01}{}^{a}$	547.676	18	3.458×10^{-3}	9.0	9.02
$H_2^{18}O$	3-2	2_{02}-$1_{11}{}^{a}$	994.675	33	5.835×10^{-3}	3.0	5.0
	6-5	3_{12}-$3_{03}{}^{a}$	1095.627	37	1.648×10^{-2}	21.0	21.0

thick almost immediately (within the last two shells), reaching a maximum of $\tau = 494.50$. This means RATRAN is only modelling the contribution from the two outermost shells for $H_2^{16}O$; any photons originating from the inner envelope would be absorbed before reaching the outer envelope. This is likely contributing to the large modelled self-absorptions in Figure 4.10. The $H_2^{16}O$ p001 line (Figure 6.5) also becomes optically thick quite quickly, reaching a maximum of $\tau = 493.53$.

The rest of the $H_2^{16}O$ lines (Figures 6.6 - 6.9) transition to optically thick either at freeze-out, or 2-4 shells outside of it. The exact transition shell is found in Table 6.2, along with the corresponding maximum optical depth. The other $H_2^{18}O$ lines transition to optically thick within the inner envelope (shells 7-9) (refer once again to Table 6.2). More details about the optical depth of each transition are given below.

The first excited para state for $H_2^{16}O$, p002 (Figure 6.6), becomes optically thick outside of the freeze-out zone at shell 14 and reaches a maximum of $\tau = 204.23$. Meanwhile, the same line for $H_2^{18}O$ is optically thin in the outer envelope, and inside of the freeze-out radius (shell 7) treads the $\tau = 1.0$ line. The maximum optical depth $H_2^{18}O$ reaches is $\tau = 1.23$.

This line would make an acceptable probe of the inner regions if it weren't so rare (it was found to be non-detected in this work). Referring back to Figure 4.10 for $H_2^{16}O$ now that we've considered optical depth, the RATRAN modelled line p002 is in the right ballpark in terms of antenna temperature and width, although it displays a slight blue-asymmetry. The peak antenna temperature falls short of the observations. This RATRAN modelled line is perhaps the only $H_2^{16}O$ line acceptable from this dataset.

The third excited para state, p004 (Figure 6.7) becomes optically thick at the 12th shell, just outside of the freeze-out radius, reaching a maximum optical depth at $\tau = 309.26$. This indicates the outer envelope is the only region contributing to the RATRAN spectral

Figure 6.4: NGC 7129 FIRS 2 RATRAN Modelling: Ortho 001 (1_{10}-1_{01}): Optical Depth plotted against RATRAN spherical shell. Dashed lines: red = $H_2^{18}O$ τ per shell, blue = $H_2^{16}O$ τ per shell, green = Freeze-out shell, black = τ = 1.0. Solid lines: red = $H_2^{18}O$ cumulative τ, blue = $H_2^{16}O$ cumulative τ. The $H_2^{18}O$ o001 line becomes optically thick just inside the freeze-out radius (shell 9-10). The same line for $H_2^{16}O$ becomes optically thick almost immediately (shell 20-21). Maximum Optical Depth: $H_2^{16}O$, τ_{max} = 494.50, $H_2^{18}O$, τ_{max} = 9.02.

Table 6.2: Transition to $\tau = 1.0$ for each water line. O = outer envelope, F/O = freeze-out radius, I = inner envelope.

Molecule	Line	Shell ($\tau = 1.0$)	Region	τ_{max}
$H_2^{16}O$	o001	20-21	O	494.50
	p001	20-21	O	493.53
	p002	14	O	204.23
	p004	12	O	309.26
	o006	9-10	F/O	61.71
	o007	10	F/O	341.60
$H_2^{18}O$	o001	9-10	F/O	9.02
	p002	7	I	1.23
	o007	9	I	4.16

model. Considering the RATRAN model for this line (Figure 4.10), the peak antenna temperature falls short but the linewidth looks acceptable.

The $H_2^{16}O$ ortho o006 line (Figure 6.8) also becomes optically thick at the freeze-out radius, reaching a maximum at $\tau = 61.71$. Considering the RATRAN model (Figure 4.10), this line barely shows up as detectable, indicating the peak antenna temperature needs to be greater. It is difficult to discern if the linewidth is acceptable.

Finally, the last ortho line, o007 (Figure 6.9), becomes optically thick for $H_2^{16}O$ at the freeze-out radius, reaching a maximum at $\tau = 341.60$. The $H_2^{18}O$ line becomes optically thick one shell inside the freeze-out radius (shell 9), and reaches a maximum at $\tau = 4.16$. The RATRAN model for $H_2^{18}O$ shows a non-detection, as expected at this abundance, while the $H_2^{16}O$ is very nearly in the right ball park, but needs to be wider and taller.

Summary: Optical Depth

In summary, the $H_2^{16}O$ optical depth for the ground state lines is optically thick almost immediately into the envelope, accounting for their lack of success with RATRAN modelling. Therefore, this transition is likely not an ideal probe of the innermost star formation region. This transition is likely better for modelling the NGC 7129 FIRS 2 outflow as it is thinner relative to the dense inner envelope.

Excited $H_2^{16}O$ lines and $H_2^{18}O$ lines are the most useful lines for modelling as they are optically thin until the freeze-out radius; this allows the majority of the outer envelope to be modelled. The $H_2^{18}O$ 995 GHz (p002) line is optically thin in the outer envelope, and
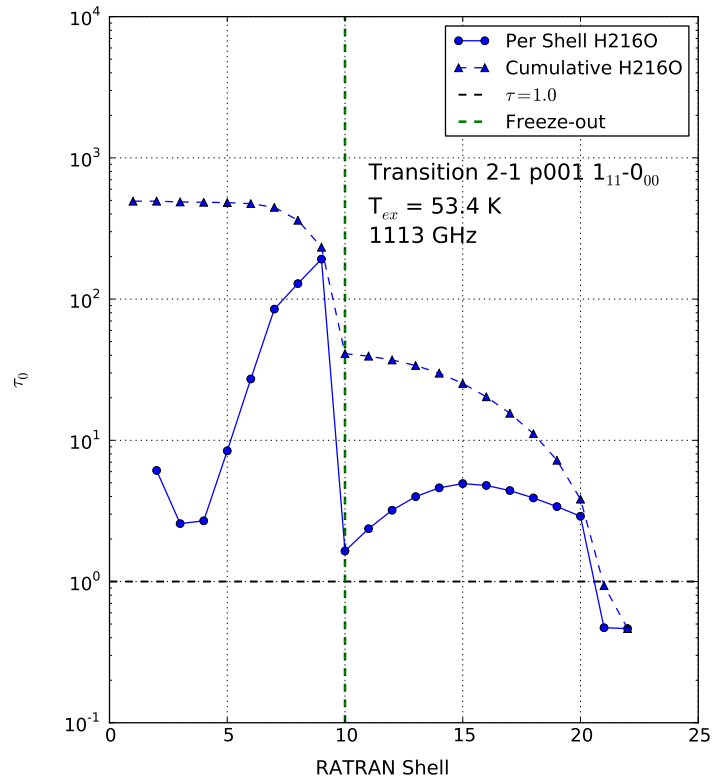
Figure 6.5: NGC 7129 FIRS 2 RATRAN Modelling: Para 001 (1_{11}-0_{00}): T_k vs RATRAN spherical shell. Dashed line indicates cumulative optical depth, from outside shell to inside shell. Solid line indicates optical depth per shell. $\tau = 1.0$ occurs just inside shell 21. $\tau_{max} = 493.53$.
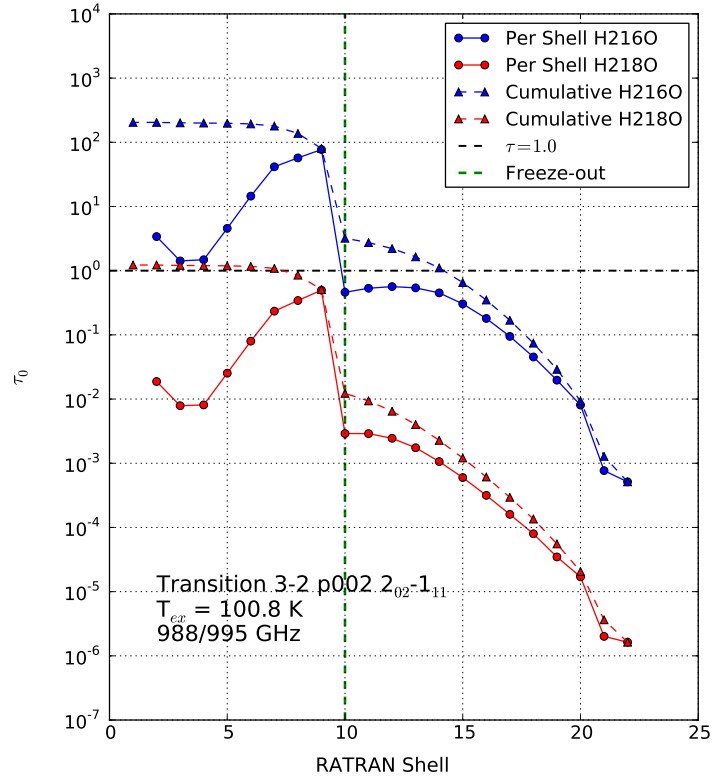
Figure 6.6: NGC 7129 FIRS 2 RATRAN Modelling: Para 002 (2_{02}-1_{11}): Optical Depth plotted against RATRAN spherical shell. Same as Figure 6.4. $H_2^{16}O$: $\tau = 1.0$ at shell 14, $\tau_{max} = 204.23$, $H_2^{18}O$: $\tau = 1.0$ at shell 7, $\tau_{max} = 1.23$.
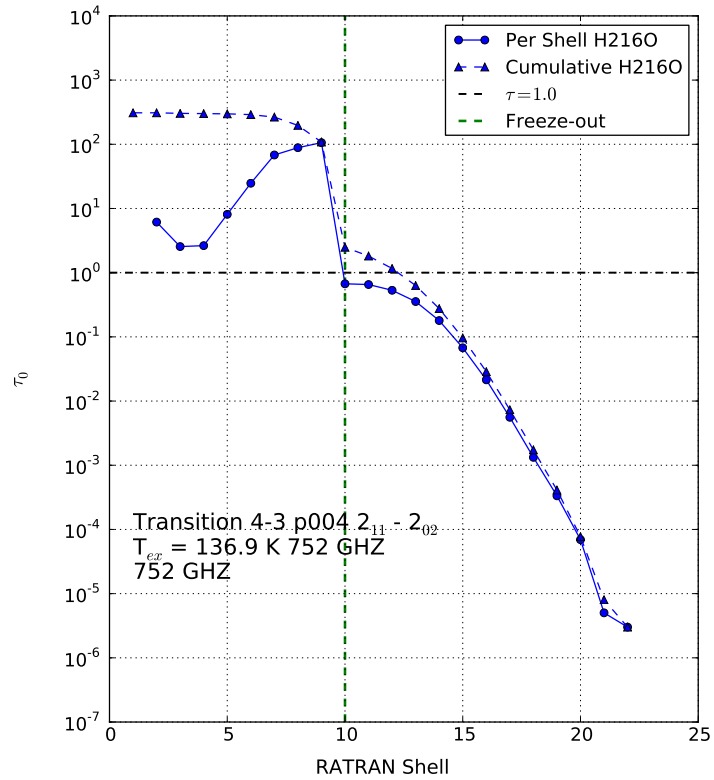
Figure 6.7: NGC 7129 FIRS 2 RATRAN Modelling: Para 004 (2_{11}-2_{02}): Optical Depth plotted against RATRAN spherical shell. Same as Figure 6.5. $\tau = 1.0$ at shell 12, $\tau_{max} = 309.26$.
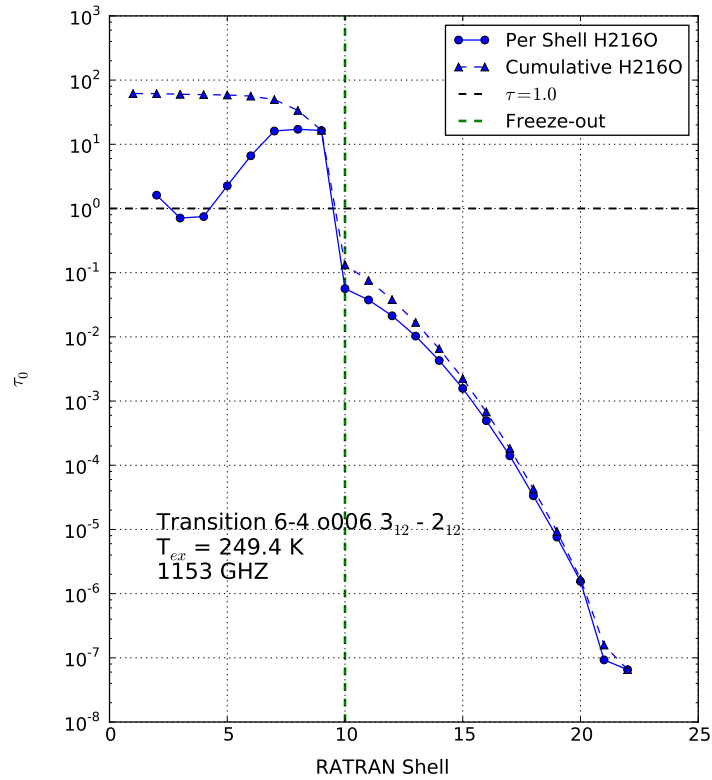
Figure 6.8: NGC 7129 FIRS 2 RATRAN Modelling: Ortho 006 (3_{12}-2_{12}): Optical Depth plotted against RATRAN spherical shell. Same as Figure 6.5. $\tau = 1.0$ at shell 9-10, $\tau_{max} = 61.71$.
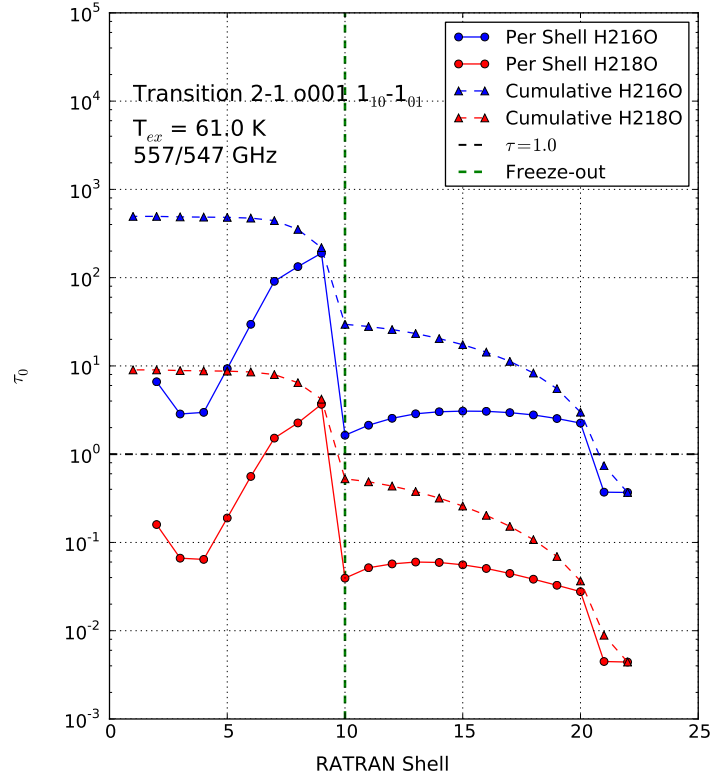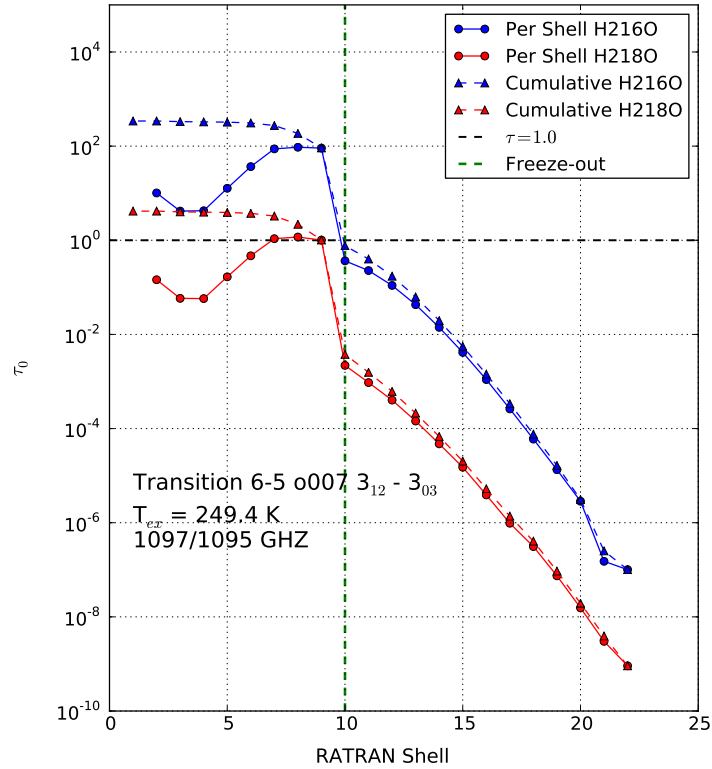
Figure 6.9: NGC 7129 FIRS 2 RATRAN Modelling: Ortho 007 (3_{12}-3_{03}): Optical Depth plotted against RATRAN spherical shell. Same as Figure 6.4. $H_2^{16}O$: $\tau = 1.0$ at shell 10, $\tau_{max} = 341.60$. $H_2^{18}O$: $\tau = 1.0$ at shell 9, $\tau_{max} = 4.16$.

reaches a modest maximum optical depth of $\tau = 1.23$. This transition was observed but not detected in this work; since this transition becomes optically thick around RATRAN shell 8, the photons that RATRAN is using to model with originate from shells 9-22. Here, for this line, as seen in Table E.1 in Appendix E, the beam dilution ranges from 1.47×10^{-3} – 1.84. The innermost, hotter regions have a greater effect of beam dilution due to their smaller angular diameter. Considering for example an expected brightness temperature T_B = 50 K, and we assume the average observed photon approaches from $\tau \lesssim 1.0$ (Shell 8), we would actually measure $T_A \sim 0.037$ K. Contrasting this value with the observations for this line in Figure 2.1b, this value is a little bit larger than the maximum intensity observed. The 995 GHz line could potentially be a decent probe into the innermost radii of star formation regions, assuming longer integration times were possible. As for the other $H_2^{18}O$ transitions, the optical depth calculations suggest the o007 might also be a decent inner envelope probe (with maximum $\tau = 4.16$, optically thick at shell ~ 9), although this line has a higher excitation temperature of $T_{ex} = 249.4$ K. This indicates a greater dependence on the inner environment compared to the p002 line. The optical depth calculations further suggest that RATRAN is successfully modelling spectral contribution from the majority of the outer envelope.

6.4   Modelling Results

RATRAN was used in attempt to reproduce the envelope Gaussian contributions; this in turn constrains physical and chemical parameters of the star formation environment.

In terms of sources of error, the HIFI spectral dataset clearly has varying level of associated noise. In addition to this, RATRAN assumes spherical symmetry and statistical equilibrium throughout the envelope. It also does not consider any external radiation. Additionally, while we assume RATRAN is modelling only the envelope component, it could be possible that it is also modelling an associated medium component (Tisi, 2013). If this were the case, the turbulent velocity would likely need to vary with radius. The effects of this were not presented in this thesis, but would be interesting to look into in the future.

To ensure the validity of the obtained RATRAN results, the models deduced by Herpin et al. (2016) were reproduced in this thesis. Upon the successful comparison of the Herpin et al. results with that of this work, we felt confident in moving forward with the RATRAN modelling of NGC 7129 FIRS 2. Once an acceptable model had been obtained, the radiative transfer code RADEX was employed to further validate the model parameters. This comparison resulted in a solidified confidence in the model parameters.

This thesis investigated the effects of altering the turbulent velocity, the water abundance with respect to H_2, the radial infall velocity, the abundance ratio, the H_2 ortho-to-para ratio (OPR), the density profile index, the convolved beamsize, the collision rates, and the freeze-out radius. Of these, constraints were placed on the turbulent velocity, $b = 2.25 \pm 0.25$ km s^{-1}, and the outer envelope $H_2^{18}O$ water abundance, X_{out} (Hybrid, OPR = 3:1) $= 4.8 \pm 0.3 \times 10^{-11}$. See Tables 4.21 and 4.22 for the results of the other density profiles and the varying LTE OPR. The inner envelope water abundance and turbulent velocity could not be constrained for either isotopologue, nor could the radial infall velocity. The abundance ratio was determined to be within 375 – 431 (considering all density profiles). When assuming an abundance ratio of 550 instead (and then dividing the $H_2^{16}O$ by this ratio), the resultant excited $H_2^{18}O$ lines would likely appear as non-detections, as observed. However, the returned $H_2^{18}O$ outer abundance values are less than the derived $H_2^{18}O$ water abundances (and less than the lower uncertainty limit). It was determined that the H_2 LTE OPR had minimal χ_R^2 values compared to the H_2 constant 3:1 OPR. The reduced chi-square χ_R^2 and p-values are not conclusive in terms of which density profile dominates; the "best" profile varies between isotopologues and molecular lines. It was also determined that increasing the beamsize decreases the produced molecular line, increasing the collision rates increases the molecular line, and increasing the freeze-out temperature decreases the spectral line. This last observation is consistent with that of Chavarría et al. (2010).

As mentioned in §4.5.9, Johnstone et al. (2010) modelled NGC 7129 FIRS 2 with RATRAN and scaled Green et al. (1993) H_2O-He collision rates. They deduce an $H_2^{16}O$ outer abundance of $X_{out} \sim 10^{-7}$, approximately an order of magnitude lower than that calculated in this thesis. That being said, stronger collision rates seem to require a lesser abundance in order for modelling results to be consistent with the observational data. Introducing a stronger collision rate increases the amount of collisions, and therefore increases the line intensity.

A comparison of one of the final NGC 7129 FIRS 2 RATRAN models is made in Table 6.3 to that of Kristensen et al. (2010) (NGC 1333 IRAS 2A, LM), Johnstone et al. (2010) (NGC 7129 FIRS 2, IM), Chavarría et al. (W3 IRS5, 2010) (HM), and Herpin et al. (NGC 6334 I(N)), 2016) (HM). All use RATRAN except for Kristensen et al., who uses the 3-dimensional radiative transfer code LIME (Brinch & Hogerheijde, 2010); an abundance jump at T = 100 K is also assumed across all compared works. The compared models range in density profile index between 1.2–1.5 (in no particular pattern) The turbulent velocities b are consistent between IM and HM sources, ranging from 2.0–2.5 km s^{-1}, while the LM source has $b = 0.8$ km s^{-1}. The $H_2^{16}O$ water abundances are all on the order of $X_{out} \sim 10^{-8}$, except for Johnstone et al. (2010) who computes a value an order of magnitude too large. This can likely be attributed to their use of scaled Green et al. (1993)

He collisional cross-sections. That being said, a smooth transition in outer envelope water abundance is seen across all three mass regimes. Lastly, the abundance ratio $H_2^{16}O/\ H_2^{18}O$ of this work is consistent with that derived by Herpin et al. (2016) (<431 vs. 437). These authors suggest that the abundance ratio varies with distance from the galactic center. Kristensen et al. does not mention their measurement for an abundance ratio between water isotopologues; the abundance ratios given in the other works are assumed to be 500-550. The HIFI observations for these sources can be found plotted in Figures 6.10 and 6.11.

Another comparison between these sources is given in van Dishoeck et al. (2011), the review paper of the WISH program. Figure 6.10 presents spectra of the lowest two p-H2O lines toward low-mass Class 0 NGC 1333 IRAS2A (Kristensen et al. 2010), intermediate-mass class 0 YSO NGC 7129 FIRS2 (Fich et al. 2010; Johnstone et al. 2010), and high-mass W3 IRS5 (Chavarría et al. 2010). The authors noted that the line profiles of NGC 7129 FIRS 2 are remarkably similar to those of the low-mass YSO NGC 1333 IRAS2A, showing both a broad component (FWHM $\sim$25 km s^{-1}) due to shocks along the outflow cavity and a medium-broad component (FWHM $\sim$6 km s^{-1}) associated with small-scale shocks in the inner dense envelope. The high-mass YSO line components are also similar their low- and intermediate-mass counterparts, but the profile of the ground-state line is clearly more complex. Many absorptions are present in the HM lines at various velocities; self-absorption and absorption of the cold envelope against the continuum are seen, as well as absorptions due to fore-ground clouds lying along the line of sight. Additionally, weak emission lines due to species other than H_2O are detected in line-rich sources.

A third comparison is made across the mass regimes in (Figure 6.11), swapping out W3 IRS5 for NGC 6334 I(N). All spectra were positioned such that they align with 0 km s^{-1}. The $H_2^{16}O$ observation for NGC 6334 I(N) shows evidence of absorption by a foreground cloud (-3.3 +) 10 km s^{-1} (see Emprechtinger et al. 2013 for more on this). From this figure, it is very clear that the particular sources chosen for LM and IM are very similar. In the top panel ($H_2^{16}O$), they both exhibit P-Cygni profiles, have relatively similar peak antenna temperatures, and have similar outflow components. The HM source is also similar, but doesn't exhibit the strong redshifted narrow emission associated with the envelope. The absorption is also symmetrical about the local V_{LSR} axis. Absorptions in both the LM and HM (but not IM) are saturated (i.e, dip below the continuum and flatten).

The modelled abundance was consistent across the mass regimes; the LM and IM spectral observations are consistent in terms of intensity (main effect of altering abundance), while the HM is approximately a factor of 10 stronger (and more complex). Numerically, the IM derived turbulent velocity (this work) is closer in value to that of the HM; the width of the narrow envelope component appears to be consistent between IM and HM,

187
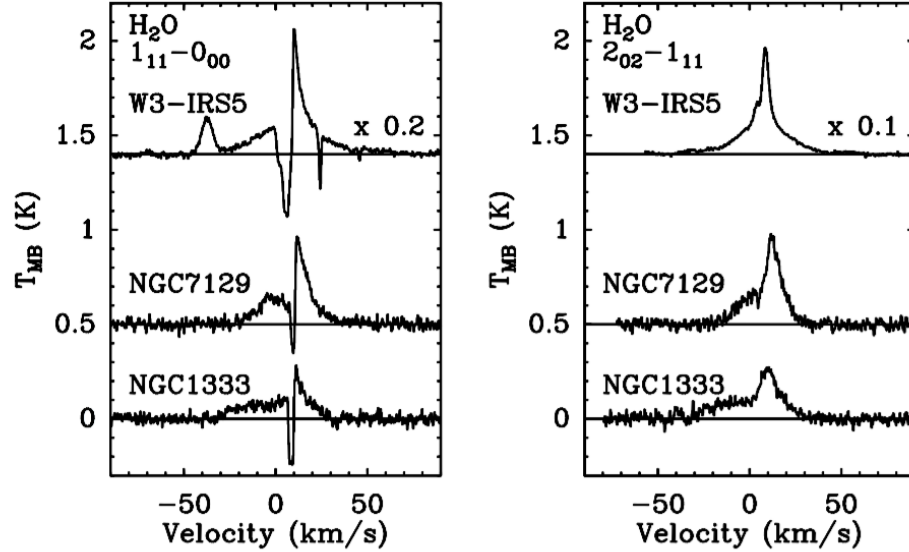
Figure 6.10: HIFI spectra of the p-H2O 1_{11}–0_{00} (p001) 1113 GHz (left) and 2_{02}–1_{11} (p002) 988 GHz (right) lines. From top to bottom: the high-mass YSO W3 IRS5 ($L = 1.5 \times 10^5$ $L_\odot$ and $d = 2.0$ kpc) (Chavarría et al. 2010), the intermediate-mass YSO NGC 7129 FIRS2 (430 $L_\odot$ and 1260 pc) (Johnstone et al. 2010), and the low-mass YSO NGC 1333 IRAS2A (20 $L_\odot$ and 235 pc) (Kristensen et al. 2010). All spectra have been shifted to a central velocity of 0 km s^{-1} . The red-shifted absorption features seen in the 1_{11}-0_{00} spectrum toward W3 IRS5 are due to water in foreground clouds, whereas the small emission line on the blue-shifted side can be ascribed to the SO$_2$ $13_{9,5}$–$12_{8,4}$ transition. Figure extracted from van Dishoeck et al. (2011).

while the width of that for the LM looks narrower. Thus, the numerical model results are consistent with what is observed with Herschel HIFI.

This thesis, alongside the WISH-IM team, has placed constraints on the outer abundance, turbulent velocity, abundance ratio, and water ortho-to-para ratio for the first time. From the above, intermediate-mass star formation has a similar turbulent velocity to its high-mass counterpart, but smoothly connects the outer envelope abundance across mass regimes.

Table 6.3: Comparing derived envelope parameters for HM, IM, LM YSOs. K(2010) = Kristensen et al. (2010), J(2010) = Johnstone et al. (2010), C(2010) = Chavarría et al. (2010), H(2016) = Herpin et al. (2016). (^{a}) = Assumed. To compare $H_2^{16}O$ X_{out} across mass regimes, take the sum of the ortho and para components.

	LM	**IM**		**HM**	
Author	K(2010)	This Work	J(2010)	C(2010)	H(2016)
Source	NGC 1333 IRAS 2A	NGC 7129 FIRS 2		W3 IRS5	NGC 6334 I(N)
Code	LIME	RATRAN	RATRAN	RATRAN	RATRAN
α	1.5	1.4	1.4	1.2	1.3
v_r	Infalling	Infalling	Infalling	Expanding	Infalling
T_{FO}	100 K	100 K	100 K	100-150 K	90-110 K
X_{ratio}	-	375-431	550^a	500^a	437
b (km s^{-1})	0.8	2.25	2.0	2.0	2.5
$H_2^{16}O$ X_{out}	$\sim 10^{-8}$	ortho: $1.5\pm0.5 \times 10^{-8}$ para: $4.5\pm0.5 \times 10^{-9}$ SUM: $1.95\pm0.5 \times 10^{-8}$	ortho: 3.0×10^{-7} para: 3.0×10^{-8} SUM: 3.3×10^{-7}	$\sim 10^{-10}$ - 10^{-8}	2.3×10^{-8}
$H_2^{18}O$ X_{out}	-	ortho: $3.5\pm0.3\times10^{-11}$	ortho: $3\pm1\times10^{-10}$	$\sim 10^{-13}$ - 10^{-11}	5.3×10^{-11}
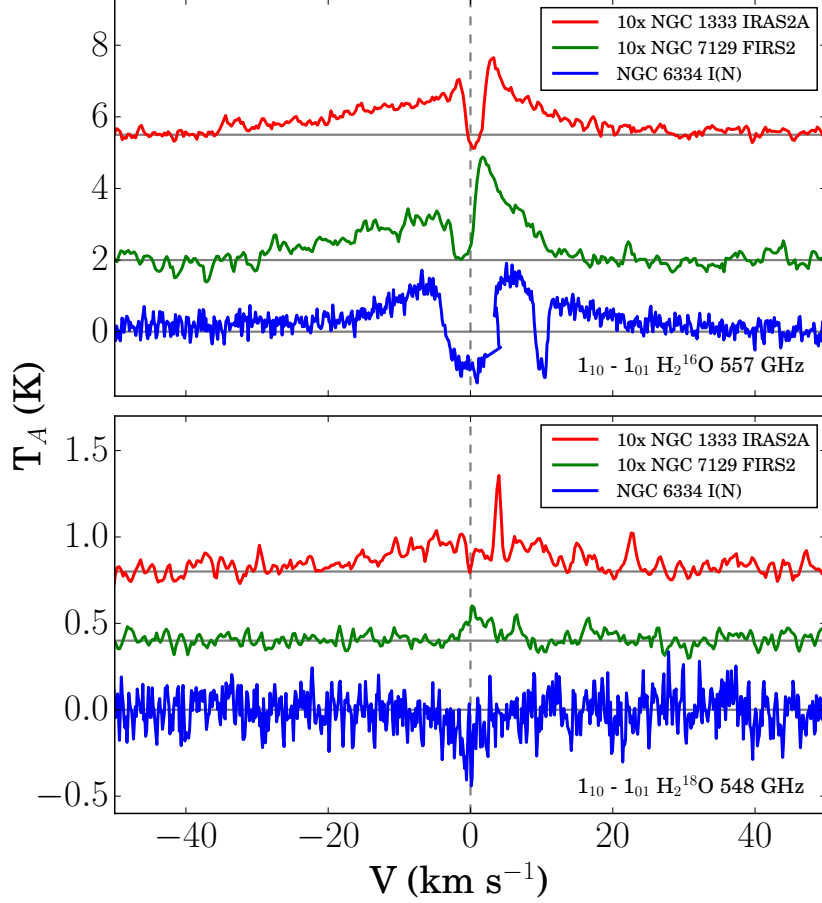
Figure 6.11: Comparing $H_2^{16}O$ and $H_2^{18}O$ spectra of 3 different sources observed with HIFI: a high-mass YSO NGC 6334 I(N) (L_{bol} = 1900 $L_\odot$, d = 1700 pc, v_{LSR} = -3.3 km s^{-1}) (Sandell 2000; Neckel 1978), an intermediate-mass YSO NGC 7129 FIRS 2 (L_{bol}= 430 $L_\odot$, d = 1260 pc, v_{LSR} = -9.8 km s^1; Shevchenko & Yakubov, 1989; Johnstone et al. 2010), and a low-mass YSO NGC 1333 IRAS 2A (L_{bol}= 20 $L_\odot$, d = 235 pc, v_{LSR} = +7.5 km s^{-1}) (Hirota et al. 2008; Kristensen et al. 2010). All spectra were positioned such that they align with 0 km s^{-1}. The $H_2^{16}O$ observation for NGC 6334 I(N) shows evidence of absorption by a foreground cloud (-3.3 +) 10 km s^{-1} (see Emprechtinger et al. 2013 for more on this.)

Chapter 7

Conclusions

The processes of high-mass star formation are still not well understood. Intermediate-mass star formation offers more opportunities for study as these YSOs are closer and available in greater number. It is expected that intermediate-mass YSO observations are the key to understanding the conditions required for high-mass star formation.

This thesis analysed Herschel HIFI spectroscopy of water ($H_2^{18}O$ and $H_2^{16}O$) in the vicinity of NGC 7129 FIRS 2. This appears to be one of the first thorough studies of the role of $H_2^{18}O$ in intermediate-mass star formation regions. The Herschel Interactive Processing Environment (HIPE) 15.0.0 was used acquire observations and to remove baselines and standing waves. This program was also used to decompose the observations into Gaussians. The line emission from the former isotopologue appears to be produced from two sources, and three sources for the latter. The spectral lines were decomposed into their respective components: [-8.6 $\pm$ 0.21 km s^{-1}(narrow) and -3.4 $\pm$ 0.1 km s^{-1}(narrow foreground)], and [-19.7 km s^{-1}(broad), -7.8 km s^{-1}(narrow), and -3.6 km s^{-1}(medium)].

This HIPE process was also conducted for other IM-candidates of the WISH program: NGC 2071 IR, Vela IRS 17, Vela IRS 19, AFGL 490, and L1641 S3MMS1. Of these, only NGC 2071 IR has usable $H_2^{18}O$ HIFI detections. Because of this, and because of time constraints, NGC 7129 FIRS 2 was selected as the main focus of this thesis.

With RATRAN modelling (with the most up-to-date RATRAN version), the following constraints were placed for a power-law density model of $\alpha = 1.4$, assuming a molecular H_2 ortho-to-para ratio of 3:1, an abundance jump at 100 K, and a free-falling infall velocity toward a central mass of $1.1 M_\odot$:

- ortho-$H_2^{18}O$ Outer Abundance $X_{out} = 3.5 \pm 0.3 \times 10^{-11}$

- ortho-$H_2^{16}O$ Outer Abundance $X_{out} = 1.5 \pm 0.5 \times 10^{-8}$

- para-$H_2^{16}O$ Outer Abundance $X_{out} = 4.5 \pm 0.5 \times 10^{-9}$

- Total $H_2^{16}O$ Outer Abundance $X_{out} = 1.95 \pm 0.5 \times 10^{-8}$

- Turbulent Velocity $b = 2.25 \pm 0.25$ km s^{-1}

- Infall Velocity = Free-Fall towards $1.1 M_\odot$, or constant $v_{inf} = $ -0.5 km s^{-1}

- H_2O Ortho-to-Para Ratio $\sim 3.3 \pm 1.2{:}1$

- Abundance Ratio [$H_2^{16}O/H_2^{18}O$] ~ 428 ($\pm$ 147)

The parameters that could not be constrained by this analysis are listed below:

- Inner Abundance

- Inner Turbulent Velocity

- $H_2^{18}O$ Excited Line Abundance Limits

The derivation of the above star forming environment parameters was also conducted for a density profile power law index of $\alpha = 1.5$, and a hybrid of the $\alpha = 1.4$ and 1.5 profiles. There wasn't a consistent trend in terms of which profile offered the best model. It was noticed that the radiative transfer code is highly sensitive to changes in the collision rates. Increasing the Daniel et al. (2011) 2–1 transition collision rates for T = 0 – 1400 K by 10% resulted in the $H_2^{18}O$ 547 GHz line intensity increasing by a factor of 4.58. This helps explain the difference in outer abundance measured in this work as compared to Johnstone et al (2010). They used the Green et al. (1993) H_2O-He collision rates scaled by a factor of 1.348 for a first order approximation for H_2O-H_2 collisions. With these rates, they deduced an $H_2^{16}O$ total outer abundance of $X_{out} = 3.3 \times 10^{-7}$, approximately an order of magnitude too large. By updating the collision rates in this work, a lower abundance was required to model line emission consistent with that of the HIFI data. This lower abundance proved to be more consistent with that of the low and high-mass WISH teams. Additionally, Johnstone et al. were also unable to place constraints on the inner envelope. This inability to constrain the inner region is supported by the optical depth analysis of both isotopologues which used the population output from RATRAN AMC to calculate

the expected optical depth at each shell. From this, it was determined that $H_2^{16}O$ is too optically thick to probe the inner star formation region and $H_2^{18}O$ becomes optically thick at, or just inside, the freeze-out radius.

The effects of altering the convolving beamsize were also investigated. Increasing the convolving beamsize by 10% resulted in decrease of line intensity (for $H_2^{18}O$ 547 GHz) by 15%. Moving the freeze-out temperature higher (i.e, 129 K vs. 100 K) resulted in a reduction of spectral line emission. A 25% increase in freeze-out temperature resulted in a $\sim 25\%$ line intensity reduction. The number of shells used to divide the envelope was varied (using $H_2^{18}O$ 547 GHz as an example). From this, the increase in shell number resulted in an increase in emission or absorption feature intensity. Increasing in shell number from 22 to 42 resulted in an emission intensity increase of a factor of 1.11; increasing from 22 to 62 resulted in an emission intensity increase of a factor of 1.18. However, the larger the number of shells, the larger the computational time required to run the model. Lastly, two different H_2 ortho-to-para ratios (OPR) were investigated: a constant 3:1 OPR and a varying with temperature (LTE) OPR. Because the LTE OPR varies with temperature (equalling 3 at higher temperatures, <1 at colder temperatures), the cold outer envelope had a much lower OPR than the inner envelope. Reducing the OPR(H_2) reduced the collision rates, resulting in a decrease in line intensity (approximately 62.5% for $H_2^{18}O$ 547 GHz).

In short, only the outer envelope was modelled with RATRAN; this was supported by the optical depth analysis of both isotopologues. This analysis showed the spectral lines with the highest potential for successfully probing the star formation region are the excited $H_2^{18}O$ lines, or the para-$H_2^{16}O$ excited 988 GHz line (2_{12}-1_{11}). The latter spectral line is less dependent on the inner hot regions for emission (E_{up} = 100.8 K) while the surrounding envelope isn't hot enough to absorb or emit at this frequency. This optical depth analysis proved to be a really useful tool in the modelling process.

The deduced outer $H_2^{16}O$ abundance of $\sim 10^{-8}$ is consistent with numerical results of the LM and HM WISH teams. The deduced turbulent velocity is more consistent with that of the HM team. The derived abundance ratio of < 431 is consistent with the ratio ~ 437 derived by Herpin et al. (2016). In terms of the spectral lines, the IM $H_2^{16}O$ appears similar to both its LM and HM counterparts, but more closely resembles that of the LM. The $H_2^{18}O$ IM line also resembles the LM spectral line more than the HM.

The intermediate-mass star formation study presented in this thesis indicates smooth transitions across physical and chemical parameters between mass regimes.

Chapter 8

Future Work

While I'd like to be able to say I accomplished everything I set out to complete, there are some ideas that could be expanded in the future in terms of new observations and new modelling exercises. These ideas for future work are listed below.

Observations:

- Investigate NGC 7129 FIRS 2 with other low abundance molecules such as $C^{18}O$, $^{13}C^{18}O$, etc. These are rare molecular lines but will likely be able to probe deeper into the cloud, similar to $H_2^{18}O$.

- Acquire additional observations of 988 GHz line (para-002, 2_{12}-1_{11}), as mentioned, this $H_2^{16}O$ line has a lesser dependence on the inner envelope and is less likely to be absorbed or emitted in the colder outer envelope. It was shown in this thesis to have a maximum optical depth of $\tau = 1.23$ near the freeze-out radius. This line is likely a decent probe of star formation regions.

- Attempt to observe $H_2^{18}O$ in the other 5 IM YSO candidates: NGC 2071 IR, Vela IRS 17, Vela IRS 19, AFGL 490, and L 1641 S3MMS1.

- It was mentioned in Chapter 6 that while this thesis fits Gaussians to the Herschel HIFI observations, other line shapes might perhaps fit better (i.e, Lorentzian). This was not investigated in this work, but is a worthwhile exercise to complete in the future.

- Obtain observations of water in NGC 7129 FIRS at higher T_{ex}, perhaps ~ 3400 K. At this temperature, it's unlikely this line would be absorbed by the outer envelope.

Modelling:

- Model other low abundance molecules such as $C^{18}O$, $^{13}C^{18}O$, etc. with same RA-TRAN model presented in this thesis.

- Model the suggested additional observations of 988 GHz line (para-002, 2_{12}-1_{11}).

- Model $H_2^{18}O$ and $H_2^{16}O$ for the other 5 IM YSO candidates: NGC 2071 IR, Vela IRS 17, Vela IRS 19, AFGL 490, and L 1641 S3MMS1.

- Remodel NGC 7129 FIRS 2 $H_2^{18}O$ 557 GHz line secondary emission feature at -3.6 km s^{-1} with RATRAN (assuming spherical symmetry) to rule out YSO multiplicity within the vicinity of FIRS 2 (in addition to FIRS 1). Add to the RATRAN model of this work and consider results.

- Repeat the $H_2^{18}O$ and $H_2^{16}O$ models of this work with LIME, the 3-dimensional radiative transfer code.

- Model NGC 7129 FIRS 2 outflows with RADEX.

- Conduct more modelling to investigate OPR as a function of temperature. Perhaps try this with other H218O lines - i.e, higher excitation lines. This exercise further explores the collision rates.

- Investigate the effects of altering the turbulent velocity with radius. Tisi (2013) suggested the medium component may also be modelled with RATRAN; if this is the case, the turbulent velocity must be varied with radius.

References

[1] Adams F. C., Shu F. H., 1986. *Infrared spectra of rotating protostars.* ApJ, 308(Sept.), 836

[2] Adams F. C., Lada C. J., Shu F. H., 1987. *Spectral evolution of young stellar objects.* ApJ, 312(Jan.), 788

[3] Andrae, R., Schulze-Hartung, T., & Melchior, P. 2010. *"The Dos and Don'ts of Reduced Chi Squared".* arXiv:1012.3754

[4] Atkinson, R., Baulch, D., Cox, R., Crowley, J., Hampson, R., & Hynes, R. 2004. *Evaluated kinetic and photochemical data for atmospheric chemistry: Volume I gas phase reactions of O_x, HO_x, NO_x and SO_x species.* Atmos. Chem. Phys., 4, 1461

[5] Attard, M., Houde, M., Novak, G., Li, H.-B, Vaillancourt, J. E., Dowell, C. D., Davidson, J., Shinnaga, H, 2009. *Magnetic Fields and Infall Motions in NGC 1333 IRAS 4.* ApJ, 702, 1584

[6] Beals, C. S., 1953, *The Spectra of the P Cygni Stars*, Publications of the Dominion Astrophysical Observatory Victoria, 9, 1

[7] Bechis, K. P., Harvey, P. M., Campbell, M. F., Hoffman, W. F., 1978. *Star formation in the NGC 7129 region - A CO molecular-line and far-infrared continuum study.* ApJ, 226 (Dec.), 439

[8] Blitz L., 1978. *A Study of the Molecular Complexes Accompanying Mon OB1, Mon OB2 and CMa OB1.* PhD thesis. Columbia Univ., New York, N.Y.

[9] Blitz L., Thaddeus P., 1980. *Giant molecular complexes and OB associations. I - The Rosette molecular complex.* ApJ, 241(Oct.), 676

[10] Bodenheimer P. H., 2011. *Principles of Star Formation.* doi:10.1007/978-3-642-15063-0.

[11] Bonnell I. A., Dobbs C. L., Robitaille T. P., Pringle J. E., 2006. *Spiral shocks, triggering of star formation and the velocity dispersion in giant molecular clouds.* MNRAS, 365(Jan.), 37

[12] Boss A. P., Ipatov S. I., Keiser S. A., Myhill E. A., Vanhala H. A. T., 2008. *Simultaneous Triggered Collapse of the Presolar Dense Cloud Core and Injection of Short-Lived Radioisotopes by a Supernova Shock Wave.* ApJ, 686(Oct.), L119

[13] Boss A. P., Keiser S. A., Ipatov S. I., Myhill E. A., Vanhala H. A. T., 2010. *Triggering Collapse of the Presolar Dense Cloud Core and Injecting Short-lived Radioisotopes with a Shock Wave. I. Varied Shock Speeds.* ApJ, 708(Jan.), 1268

[14] Brinch, C., & Hogerheijde, M. R. 2010. *LIME - a flexible, non-LTE line excitation and radiation transfer method for millimeter and far-infrared wavelengths.* A&A, 523(Nov.), A25

[15] Burton W. B., 1976. *The morphology of hydrogen and of other tracers in the Galaxy.* ARA&A, 14, 275

[16] Carroll, Bradley., & Ostlie, Dale. 2007. *An Introduction to Modern Astrophysics.* Pearson Assidon-Wesley.

[17] Cernicharo, J., & Crovisier, J. 2005. *Water in Space: The Water World of ISO.* Space Sc. Rev., 119(Aug.), 29

[18] Charnley, S. B. 1997. *Sulfuretted Molecules in Hot Cores.* ApJ, 481(May), 396

[19] Chavarría, L., Herpin, F., Jacq, T., Braine, J., Bontemps, S., Baudry, A., Marseille, M., van der Tak, F., Pietropaoli, B., Wyrowski, F., Shipman, R., Frieswijk, W., van Dishoeck, E. F., Cernicharo, J., Bachiller, R., Benedettini, M., Benz, A. O., Bergin, E., Bjerkeli, P., Blake, G. A., Bruderer, S., Caselli, P., Codella, C., Daniel, F., di Giorgio, A. M., Dominik, C., Doty, S. D., Encre- naz, P., Fich, M., Fuente, A., Giannini, T., Goicoechea, J. R., de Graauw, T., Hartogh, P., Helmich, F., Herczeg, G. J., Hogerheijde, M. R., Johnstone, D., JØrgensen, J. K., Kristensen, L. E., Larsson, B., Lis, D., Liseau, R., McCoey, C., Melnick, G., Nisini, B., Olberg, M., Parise, B., Pearson, J. C., Plume, R., Risacher, C., Santiago-Garc a, J., Saraceno, P., Stutzki, J., Szczerba, R., Tafalla, M., Tielens, A., van Kempen, T. A., Visser, R., Wampfler, S. F., Willem, J., & Yıldız, U. A. 2010. Water in massive star-forming regions: HIFI observations of W3 IRS5. AAP, 521(Oct.), L37.

[20] Cheung, A. C., Rank, D. M., & Townes, C. H. 1969. *Detection of Water in Interstellar Regions by its Microwave Radiation.* Nature, 221(Feb.), 626

[21] Christie, D., Wu, B., Tan, J. C., 2017. *GMC Collisions as Triggers of Star Formation. IV. The Role of Ambipolar Diffusion.* ApJ, 848(Oct.), 50

[22] Crimier, N., Ceccarelli, C., Alonso-Albi, T., Fuente, A., Caselli, P., Johnstone, D., Kahane, C., Lefloch, B., Maret, S., Plume, R., Rizzo, J. R., Tafalla, M., van Dishoeck, E., & Wyrowski, F. 2010. *Physical structure of the envelopes of intermediate-mass protostars.* Astronomy and Astrophysics, 516(June), A102.

[23] Dale J. E., Bonnell I. A., 2012. *Ionization-induced star formation - III. Effects of external triggering on the initial mass function in clusters.* MNRAS, 422(May), 1352

[24] Dalgarno, A., Black, J., & Weisheit, J. C., 1973. *Ortho-para transitions in H_2 and the fractionation of HD.* ApJ, 14, L77.

[25] Damgaard P. H., Hjorth P. G., Thejll P. A., 1992. *A Note on Positivity of Equilibrium Populations in Radiative Transfer Theory.* AA, 254(Feb.), 422

[26] Daniel, F., Dubernet, M., Pacaud, F., & Grosjean, A. 2010. *Rotational excitation of 20 levels of para-H2O by ortho-H2 (j2 = 1, 3, 5, 7) at high temperature.* A&A, 517, A13

[27] Daniel, F., Dubernet, M.-L., and Grosjean A., 2011. *Rotational excitation of 45 levels of ortho/para-H2O by excited ortho/para-H2 from 5 K to 1500 K: state-to-state, effective, and thermalized rate coefficients.* A&A 536(Oct.), A76

[28] Daniel F., Goicoechea J. R., Cernicharo J., Dubernet M. L., Faure A., 2012. *Influence of collisional rate coefficients on water vapour excitation.* A&A, 547(Nov.), A81

[29] Daniel, F., Cernicharo, J., 2013. *Non-local radiative transfer in strongly inverted masers.* A&A, 553, A70.

[30] de Graauw, T., Helmich, F. P., Phillips, T. G., Stutzki, J., Caux, E., Whyborn, N. D., Dieleman, P., Roelfsema, P. R., Aarts, H., Assendorp, R., Bachiller, R., Baechtold, W., Barcia, A., Beintema, D. A., Belitsky, V., Benz, A. O., Bieber, R., Boogert, A., Borys, C., Bumble, B., Caïs, P., Caris, M., CerulliIrelli, P., Chattopadhyay, G., Cherednichenko, S., Ciechanowicz, M., Coeur-Joly, O., Comito, C., Cros, A., de Jonge, A., de Lange, G., Delforges, B., Delorme, Y., den Boggende, T., Desbat, J.-M., Diez-González, C., di Giorgio, A. M., Dubbeldam, L., Edwards, K., Eggens, M., Erickson, N., Evers, J., Fich, M., Finn, T., Franke, B., Gaier, T., Gal, C., Gao, J. R., Gallego, J.D., Gauffre, S., Gill, J. J., Glenz, S., Golstein, H., Goulooze, H., Gunsing, T., Güsten, R., Hartogh, P., Hatch, W. A., Higgins, R., Honingh, E. C., Huisman, R., Jackson, B. D., Jacobs, H., Jacobs, K., Jarchow, C., Javadi, H., Jellema, W., Justen, M., Karpov, A., Kasemann, C.,

Kawamura, J., Keizer, G., Kester, D., Klapwijk, T. M., Klein, T., Kollberg, E., Kooi, J., Kooiman, P. P., Kopf, B., Krause, M., Krieg, J.-M., Kramer, C., Kruizenga, B., Kuhn, T., Laauwen, W., Lai, R., Larsson, B., Leduc, H. G., Leinz, C., Lin, R. H., Liseau, R., Liu, G. S., Loose, A., López-Fernandez, I., Lord, S., Luinge, W., Marston, A., Martín-Pintado, J., Maestrini, A., Maiwald, F. W., McCoey, C., Mehdi, I., Megej, A., Melchior, M., Meinsma, L., Merkel, H., Michalska, M., Monstein, C., Moratschke, D., Morris, P., Muller, H., Murphy, J. A., Naber, A., Natale, E., Nowosielski, W., Nuzzolo, F., Olberg, M., Olbrich, M., Orfei, R., Orleanski, P., Ossenkopf, V., Peacock, T., Pearson, J. C., Peron, I., Phillip-May, S., Piazzo, L., Planesas, P., Rataj, M., Ravera, L., Risacher, C., Salez, M., Samoska, L. A., Saraceno, P., Schieder, R., Schlecht, E., Schlöder, F., Schmülling, F., Schultz, M., Schuster, K., Siebertz, O., Smit, H., Szczerba, R., Shipman, R., Steinmetz, E., Stern, J. A., Stokroos, M., Teipen, R., Teyssier, D., Tils, T., Trappe, N., van Baaren, C., van Leeuwen, B.-J., van de Stadt, H., Visser, H., Wildeman, K. J., Wafelbakker, C. K., Ward, J. S., Wesselius, P., Wild, W., Wulff, S., Wunsch, H. J., Tielens, X., Zaal, P., Zirath, H., Zmuidzinas, J., & Zwart, F. 2010. The Herschel-Heterodyne Instrument for the Far-Infrared (HIFI). Astronomy and Astrophysics, 518(July), L6.

[31] Dubernet, M., Grosjean, A., Daniel, F., et al. 2006a, in Ro-vibrational Collisional Excitation Database: BASECOL http://basecol.obspm.fr (Japan: Journal of Plasma and Fusion Research Series, series 7)

[32] Dubernet, M.-L., Daniel, F., Grosjean, A., Valiron, P., Wernli, M., Wiesenfeld, L., Rist, C., Noga, J., Tennyson, J., 2006b. *Influence of a new potential energy surface on the rotational (de)excitation of H2O by H2 at low temperature.* A&A, 460 (Dec.), 323

[33] Dubernet, M.-L., Daniel, F., Grosjean, A., & Lin, C. Y. 2009. *Rotational excitation of ortho-H2O by para-H2 (j2 = 0, 2, 4, 6, 8) at high temperature.* A&A, 497 (Apr.), 911

[34] Dubernet, M.-L.; Alexander, M. H.; Ba, Y. A.; Balakrishnan, N.; Balana, C.; Ceccarelli, C.; Cernicharo, J.; Daniel, F.; Dayou, F.; Doronin, M.; Dumouchel, F.; Faure, A.; Feautrier, N.; Flower, D. R.; Grosjean, A.; Halvick, P.; Kos, J.; Lique, F.; McBane, G. C.; Marinakis, S.; Moreau, N.; Moszynski, R.; Neufeld, D. A.; Roueff, E.; Schilke, P.; Spielfiedel, A.; Stancil, P. C.; Stoecklin, T.; Tennyson, J.; Yang, B.; Vasserot, A.-M.; Wiesenfeld, L., 2013. *BASECOL2012: A collisional database repository and web service within the Virtual Atomic and Molecular Data Centre (VAMDC).* A&A, 553(May), A50.

[35] Eiroa, C., Palacios, J., & Casali, M. M. 1998. *NGC 7129 FIRS 2: an intermediate-mass counterpart of Class 0 objects.* A&A, 335(July), 243

[36] Elitzur, M., & Watson, W. D. 1978. *Formation of molecular CH+ in interstellar shocks.* ApJ, 222(June), L141

[37] Emprechtinger, M., Lis, D. C., Rolffs, R., Schilke, P., Monje,R. R., Comito, C., Ceccarelli, C., Neufeld, D. A., and van der Tak, F. F. S., 2013. *THE ABUNDANCE, ORTHO/PARA RATIO, AND DEUTERATION OF WATER IN THE HIGH-MASS STAR-FORMING REGION NGC 6334 I.* ApJ, 765 (Feb.), 1

[38] Evans N. J., 1978, In Protostars and Planets. ed. T Gehrels. p.152. Tuscon: Univ. Ariz. Press

[39] Faure, A., Crimier, N., Ceccarelli, C., Valiron, P., Wiesenfeld, L., Dubernet, M. L., 2007. *Quasi-classical rate coefficient calculations for the rotational (de)excitation of H2O by H2.* A&A, 472 (Sept.), 1029

[40] Flower, D. R., & Watt, G. D., 1984. *On the ortho-H_2/para-H_2 ratio in molecular clouds.* MNRAS, 209(July), 25

[41] Fich, M.; Johnstone, D.; van Kempen, T. A.; McCoey, C.; Fuente, A.; Caselli, P.; Kristensen, L. E.; Plume, R.; Cernicharo, J.; Herczeg, G. J.; van Dishoeck, E. F.; Wampfler, S.; Gaufre, P.; Gill, J. J.; Javadi, H.; Justen, M.; Laauwen, W.; Luinge, W.; Ossenkopf, V.; Pearson, J.; Bachiller, R.; Baudry, A.; Benedettini, M.; Bergin, E.; Benz, A. O.; Bjerkeli, P.; Blake, G.; Bontemps, S.; Braine, J.; Bruderer, S.; Codella, C.; Daniel, F.; di Giorgio, A. M.; Dominik, C.; Doty, S. D.; Encrenaz, P.; Giannini, T.; Goicoechea, J. R.; de Graauw, Th.; Helmich, F.; Herpin, F.; Hogerheijde, M. R.; Jacq, T.; Jørgensen, J. K.; Larsson, B.; Lis, D.; Liseau, R.; Marseille, M.; Melnick, G.; Nisini, B.; Olberg, M.; Parise, B.; Risacher, C.; Santiago, J.; Saraceno, P.; Shipman, R.; Tafalla, M.; van der Tak, F.; Visser, R.; Wyrowski, F.; Yıldız, U. A., 2010. *Herschel-PACS spectroscopy of the intermediate mass protostar NGC 7129 FIRS 2.* A&A, 518(July), L86

[42] Fraser, H. J., Collings, M. P., McCoustra, M. R. S., & Williams, D. A. 2001. *Thermal desorption of water ice in the interstellar medium.* MNRAS, 327, (Nov.) 1165

[43] Fuente, A., Neri, R., Martin-Pintado, J., Bachiller, R., Rodríguez-Franco, A., Palla, F., 2001. *Disks and outflows around intermediate-mass stars and protostars.* A&A, 366 (Feb.), 873

[44] Fuente, A., Neri, R., & Caselli, P. 2005. *Detection of a hot core in the intermediate-mass Class 0 protostar NGC 7129-FIRS 2.* A&A, 444(Dec.), 481

[45] Fuente A., Ceccarelli C., Neri R., Alonso-Albi T., Caselli P., Johnstone D., van Dishoeck E. F., Wyrowski F., 2007. *Protostellar clusters in intermediate mass (IM) star forming regions.* A&A, 468(June), L37

[46] Fuente, A., Caselli, P., McCoey, C., Cernicharo, J., Johnstone, D., Fich, M., van Kempen, T., van Dishoeck, E., Yıldız, U., Visser, R., Kristensen, L., Alonso-Albi, T., Herpin, F., & Tisi, S. 2012. *The abundance of C18O and HDO in the envelope and hot core of the intermediate mass protostar NGC 7129 FIRS 2.* Astronomy and Astrophysics, 540(Apr.), A75.

[47] Fuente, A., Cernicharo, J., Caselli, P., McCoey, C., Johnstone, D., Fich, M., van Kempen, T., Palau, Aina; Yıldız, U. A.; Tercero, B.; López, A. 2014. *The hot core towards the intermediate-mass protostar NGC 7129 FIRS 2. Chemical similarities with Orion KL.* A&A, 568 (July.), A65

[48] Giannini, T., Massi, F., Podio, L., Lorenzetti, D., Nisini, B., Caratti o Garatti, A., Liseau, R., Lo Curto, G., & Vitali, F. 2005. *Star formation in the Vela Molecular Clouds: A new protostar powering a bipolar jet.* Astronomy and Astrophysics, 433(Apr.), 941954.

[49] Gomez M., Hartmann L., Kenyon S. J., Hewett R., 1993. *On the spatial distribution of pre-main-sequence stars in Taurus.* AJ, 105(May), 1927

[50] Gondhalekar, P. M., and Wilson, R. 1975. *The interstellar radiation field between 912 A and 2740 A.* A&A, 38 (Feb.), 329.

[51] Green, S., Maluendes, S., & McLean, A. D., 1993. *Improved collisional excitation rates for interstellar water.* ApJS, 85 (Mar.), 181

[52] Griffin, M. J.; Abergel, A.; Abreu, A.; Ade, P. A. R.; André, P.; Augueres, J.-L.; Babbedge, T.; Bae, Y.; Baillie, T.; Baluteau, J.-P.; Barlow, M. J.; Bendo, G.; Benielli, D.; Bock, J. J.; Bonhomme, P.; Brisbin, D.; Brockley-Blatt, C.; Caldwell, M.; Cara, C.; Castro-Rodriguez, N.; Cerulli, R.; Chanial, P.; Chen, S.; Clark, E.; Clements, D. L.; Clerc, L.; Coker, J.; Communal, D.; Conversi, L.; Cox, P.; Crumb, D.; Cunningham, C.; Daly, F.; Davis, G. R.; de Antoni, P.; Delderfield, J.; Devin, N.; di Giorgio, A.; Didschuns, I.; Dohlen, K.; Donati, M.; Dowell, A.; Dowell, C. D.; Duband, L.; Dumaye, L.; Emery, R. J.; Ferlet, M.; Ferrand, D.; Fontignie, J.; Fox, M.; Franceschini, A.; Frerking, M.; Fulton, T.; Garcia, J.; Gastaud, R.; Gear, W. K.; Glenn, J.; Goizel, A.; Griffin, D. K.; Grundy, T.; Guest, S.; Guillemet, L.; Hargrave, P. C.; Harwit, M.; Hastings, P.; Hatziminaoglou, E.; Herman, M.; Hinde, B.; Hristov, V.; Huang, M.; Imhof, P.; Isaak, K. J.; Israelsson, U.; Ivison, R. J.; Jennings, D.; Kiernan, B.; King, K. J.; Lange, A. E.; Latter, W.; Laurent, G.; Laurent, P.; Leeks, S. J.; Lellouch, E.; Levenson, L.; Li, B.; Li, J.; Lilienthal, J.; Lim, T.; Liu, S. J.; Lu, N.; Madden, S.; Mainetti, G.; Marliani, P.; McKay, D.; Mercier, K.; Molinari, S.; Morris, H.; Moseley, H.; Mulder, J.; Mur, M.; Naylor, D. A.; Nguyen, H.; O'Halloran, B.; Oliver, S.; Olofsson, G.; Olofsson, H.-G.; Orfei,

R.; Page, M. J.; Pain, I.; Panuzzo, P.; Papageorgiou, A.; Parks, G.; Parr-Burman, P.; Pearce, A.; Pearson, C.; Pérez-Fournon, I.; Pinsard, F.; Pisano, G.; Podosek, J.; Pohlen, M.; Polehampton, E. T.; Pouliquen, D.; Rigopoulou, D.; Rizzo, D.; Roseboom, I. G.; Roussel, H.; Rowan-Robinson, M.; Rownd, B.; Saraceno, P.; Sauvage, M.; Savage, R.; Savini, G.; Sawyer, E.; Scharmberg, C.; Schmitt, D.; Schneider, N.; Schulz, B.; Schwartz, A.; Shafer, R.; Shupe, D. L.; Sibthorpe, B.; Sidher, S.; Smith, A.; Smith, A. J.; Smith, D.; Spencer, L.; Stobie, B.; Sudiwala, R.; Sukhatme, K.; Surace, C.; Stevens, J. A.; Swinyard, B. M.; Trichas, M.; Tourette, T.; Triou, H.; Tseng, S.; Tucker, C.; Turner, A.; Vaccari, M.; Valtchanov, I.; Vigroux, L.; Virique, E.; Voellmer, G.; Walker, H.; Ward, R.; Waskett, T.; Weilert, M.; Wesson, R.; White, G. J.; Whitehouse, N.; Wilson, C. D.; Winter, B.; Woodcraft, A. L.; Wright, G. S.; Xu, C. K.; Zavagno, A.; Zemcov, M.; Zhang, L.; Zonca, E., 2010. *The Herschel-SPIRE instrument and its in-flight performance.* A&A 518 (July), L3

[53] Gritschneder M., Naab T., Walch S., Burkert A., Heitsch F., 2009. *Driving Turbulence and Triggering Star Formation by Ionizing Radiation.* ApJL, 694(Mar.), L26

[54] Gritschneder M., Lin D. N. C., Murray S. D., Yin Q.Z., Gong M. N., 2012. *The Supernova Triggered Formation and Enrichment of Our Solar System.* ApJ, 745(Jan.), 22

[55] Grosjean, A., Dubernet, M. L., & Ceccarelli, C. 2003. Collisional excitation rates of H2O with H2. II. Rotational excitation with ortho-H2 at very low temperature and application to cold molecular clouds. A&A, 408 (Sept.), 1197

[56] Habing, H. J. 1968. *The interstellar radiation density between 912 A and 2400 A.* Bull. Astr. Inst. Netherlands, 19 (Jan.), 421

[57] Hartigan P., Lada C. J., 1985. *CCD images of suspected Herbig-Haro objects.* ApJS, 59 (Nov.), 383

[58] Harvey P.M., Wilking B.A., Joy M. 1984. *Infrared observations of dust cloud structure in young R associations : NGC 1333, S 68 and NGC 7129.* ApJ 278 (Mar.), 156

[59] Hatchell, J., & van der Tak, F. F. S. 2003. *The physical structure of high-mass star-forming cores.* A&A, 409 (Oct.), 589

[60] Herpin, F.; Chavarría, L.; Jacq, T.; Braine, J.; van der Tak, F.; Wyrowski, F.; van Dishoeck, E. F.; Baudry, A.; Bontemps, S.; Kristensen, L.; Schmalzl, M.; Mata, J., 2016. *Herschel-HIFI view of mid-IR quiet massive protostellar objects.* A&A, 587(Mar.), A139

[61] Hillenbrand L. A., Hartmann L. W., 1998. *A Preliminary Study of the Orion Nebula Cluster Structure and Dynamics.* ApJ, 492(Jan.), 540

[62] Hillier, Michael. 2008. *Modelling Water Emission from Intermediate Mass Star Formation Regions.* M.Sc. thesis, University of Waterloo, Waterloo, ON., Canada.

[63] Tomoya Hirota, Takeshi Bushimata, Yoon Kyung Choi, Mareki Honma, Hiroshi Imai, Kenzaburo Iwadate, Takaaki Jike, Osamu Kameya, Ryuichi Kamohara, Yukitoshi Kan-Ya, Noriyuki Kawaguchi, Masachika Kijima, Hideyuki Kobayashi, Seisuke Kuji, Tomoharu Kurayama, Seiji Manabe, Takeshi Miyaji, Takumi Nagayama, Akiharu Nakagawa, Chung Sik Oh, Toshihiro Omodaka, Tomoaki Oyama, Satoshi Sakai, Tetsuo Sasao, Katsuhisa Sato, Katsunori M. Shibata, Yoshiaki Tamura, Kazuyoshi Yamashita, 2008. *Astrometry of H2O Masers in Nearby Star-Forming Regions with VERA II SVS 13 in NGC 1333*, PASJ, 60:1 (Feb.), 37

[64] Hogerheijde, M. R., & van der Tak, F. F. S. 2000. *An accelerated Monte Carlo method to solve two-dimensional radiative transfer and molecular excitation. With applications to axisymmetric models of star formation.* Astronomy and Astrophysics, 362(Oct.), 697710.

[65] Johnstone, D., Fich, M., Mitchell, G. F., & Moriarty-Schieven, G. 2001. *Large Area Mapping at 850 Microns. III. Analysis of the Clump Distribution in the Orion B Molecular Cloud.* ApJ, 559 (Sept.), 307

[66] Johnstone, D., Fich, M., McCoey, C., van Kempen, T. A., Fuente, A., Kris- tensen, L. E., Cernicharo, J., Caselli, P., Visser, R., Plume, R., Herczeg, G. J., van Dishoeck, E. F., Wampfler, S., Bachiller, R., Baudry, A., Benedettini, M., Bergin, E., Benz, A. O., Bjerkeli, P., Blake, G., Bontemps, S., Braine, J., Bruderer, S., Codella, C., Daniel, F., di Giorgio, A. M., Dominik, C., Doty, S. D., Encrenaz, P., Giannini, T., Goicoechea, J. R., de Graauw, T., Helmich, F., Herpin, F., Hogerheijde, M. R., Jacq, T., Jørgensen, J. K., Larsson, B., Lis, D., Liseau, R., Marseille, M., Melnick, G., Neufeld, D., Nisini, B., Olberg, M., Parise, B., Pearson, J., Risacher, C., Santiago-García, J., Saraceno, P., Shipman, R., Tafalla, M., van der Tak, F., Wyrowski, F., Yıldız, U. A., Caux, E., Honingh, N., Jellema, W., Schieder, R., Teyssier, D., & Whyborn, N. 2010. *Herschel/HIFI spectroscopy of the intermediate mass protostar NGC 7129 FIRS 2.* Astronomy and Astrophysics, 521(Oct.), L41.

[67] Jørgensen, J. K., Schöier, F. L., & van Dishoeck, E. F. 2002. *Physical structure and CO abundance of low-mass protostellar envelopes.* A&A, 389 (Sept.), 908

[68] Jørgensen, J. K., Bourke, T. L., Myers, P. C., Di Francesco, J., van Dishoeck, E. F., Lee, C.-F, Ohashi, N., Schöier, F. L., Takakuwa, S., Wilner, D. J., Zhang, Q., 2007. *PROSAC: A Submillimeter Array Survey of Low-Mass Protostars. I. Overview of Program: Envelopes, Disks, Outflows, and Hot Cores.* ApJ, 659(Apr.), 479

[69] Kristensen, L. E., Visser, R., van Dishoeck, E. F., Yıldız, U. A., Doty, S. D., Herczeg, G. J., Liu, F. C., Parise, B., Jørgensen, J. K., van Kempen, T. A., Brinch, C., Wampfler, S. F., Bruderer, S., Benz, A. O., Hogerheijde, M. R., Deul, E., Bachiller, R., Baudry, A., Benedettini, M., Bergin, E. A., Bjerkeli, P., Blake, G. A., Bontemps, S., Braine, J., Caselli, P., Cernicharo, J., Codella, C., Daniel, F., de Graauw, T., di Giorgio, A. M., Dominik, C., Encrenaz, P., Fich, M., Fuente, A., Giannini, T., Goicoechea, J. R., Helmich, F., Herpin, F., Jacq, T., Johnstone, D., Kaufman, M. J., Larsson, B., Lis, D., Liseau, R., Marseille, M., McCoey, C., Melnick, G., Neufeld, D., Nisini, B., Olberg, M., Pearson, J. C., Plume, R., Risacher, C., Santiago-García, J., Saraceno, P., Shipman, R., Tafalla, M., Tielens, A. G. G. M., van der Tak, F., Wyrowski, F., Beintema, D., de Jonge, A., Dieleman, P., Ossenkopf, V., Roelfsema, P., Stutzki, J., & Whyborn, N. 2010a. *Water in low-mass star-forming regions with Herschel . HIFI spectroscopy of NGC 1333*. AAP, 521(Oct.), L30.

[70] Kristensen, L. E.; van Dishoeck, E. F.; Bergin, E. A.; Visser, R.; Yldz, U. A.; San Jose-Garcia, I.; Jrgensen, J. K.; Herczeg, G. J.; Johnstone, D.; Wampfler, S. F.; Benz, A. O.; Bruderer, S.; Cabrit, S.; Caselli, P.; Doty, S. D.; Harsono, D.; Herpin, F.; Hogerheijde, M. R.; Karska, A.; van Kempen, T. A.; Liseau, R.; Nisini, B.; Tafalla, M.; van der Tak, F.; Wyrowski, F., 2012. *Water in star-forming regions with Herschel (WISH). II. Evolution of 557 GHz 1_{10}-1_{01} emission in low-mass protostars.* A&A 542, A8

[71] Liseau, R., Lorenzetti, D., Nisini, B., Spinoglio, L., & Moneti, A. 1992. *Star formation in the VELA molecular clouds. I - The IRAS-bright Class I sources.* Astronomy and Astrophysics, 265(Nov.), 577596.

[72] Mannings, V., & Sargent, A. I. 1997. *A High-Resolution Study of Gas and Dust around Young Intermediate-Mass Stars: Evidence for Circumstellar Disks in Herbig Ae Systems.* ApJ, 490 (Dec.), 792

[73] Mannings, V., & Sargent, A. I. 2000. *High-Resolution Studies of Gas and Dust around Young Intermediate-Mass Stars. II. Observations of an Additional Sample of Herbig AE System*s. ApJ, 529 (Jan.), 391

[74] Martin, P. G., & Mandy, M. E., 1993. *Collisional excitation of H_2 molecules by H atoms.* ApJS, 86(May), 199

[75] Melnick, G. J. 2009, in ASP Conf. Ser. 417, Submillimeter Astrophysics and Technology: A Symposium Honoring Thomas G. Phillips (San Francisco: ASP), 59

[76] Miranda L.F., Eiroa C., Gómez de Castro A.I. 1993. *New Herbig-Haro Objects and Pre-Main Sequence Stars in the Star Formation Region NGC7129.* A&A 271 (Apr.), 564

[77] Mouschovias, T., Spitzer, L., 1976. "Note on the Collapse of Magnetic Interstellar Clouds". ApJ, 210(Dec.), 326

[78] Mozurkewich, D., Schwartz, P. R., & Smith, H. A. 1986. *Luminosities of sources associated with molecular outflows.* ApJ, 311(Dec.), 371

[79] Mueller, K. E., Shirley, Y. L., Evans, II, N. J., & Jacobson, H. R. 2002. *The Physical Conditions for Massive Star Formation: Dust Continuum Maps and Modeling.* ApJS, 143(Dec.), 469

[80] Myers P. C., Fuller G. A., Mathieu R. D., Beichman C. A., Benson P. J., Schild R. E., Emerson J. P., 1987. *Near-infrared and optical observations of IRAS sources in and near dense cores.* ApJ, 319(Aug.), 340

[81] Neckel, T. 1978, A&A, 69, 51

[82] Neri, R.; Fuente, A.; Ceccarelli, C.; Caselli, P.; Johnstone, D.; van Dishoeck, E. F.; Wyrowski, F.; Tafalla, M.; Lefloch, B.; Plume, R., 2007. *The IC1396N proto-cluster at a scale of 250 AU.* A&A, 468(June), L33

[83] Neufeld D. A., Kaufman M. J., 1993. *Radiative Cooling of Warm Molecular Gas.* ApJ, 418(Nov.), 263

[84] Neufeld, D. A., Lepp, S., & Melnick, G. J. 1995. *Thermal Balance in Dense Molecular Clouds: Radiative Cooling Rates and Emission-Line Luminosities.* ApJ, 100(Sept.), 132

[85] Ossenkopf, V., & Henning, T. 1994. *Dust opacities for protostellar cores.* A&A, 291(Nov.), 943959.

[86] Ott, S., 2010. *The Herschel Data Processing System HIPE and Pipelines Up and Running Since the Start of the Mission*, in ASP Conf. Ser. 434, Astronomical Data Analysis Software and Systems XIX, ed. Y. Mizumoto, K.-I. Morita, & M. Ohishi (San Francisco: ASP), 139

[87] Phillips, T. R., Maluendes, S., McLean, A. D., & Green, S. 1994. *Anisotropic rigid rotor potential energy function for H2O-H2.* J. Chem. Phys.,101 (Oct.), 5824

[88] Phillips, T. R., Maluendes, S., & Green, S. 1996. *Collisional Excitation of H 2O by H 2 Molecules.* ApJS, 107 (Nov.), 467

[89] Pilbratt, G. L., Riedinger, J. R., Passvogel, T., Crone, G., Doyle, D., Gageur, U., Heras, A. M., Jewell, C., Metcalfe, L., Ott, S., & Schmidt, M. 2010. *Herschel Space Observatory. An ESA facility for far-infrared and submillimetre astronomy.* Astronomy and Astrophysics, 518(July), L1.

[90] Pinsonneault, M. H., & Delahaye, F. 2009. *The Solar Heavy Element Abundances. II. Constraints from Stellar Atmospheres.* ApJ, 704(Oct.), 11741188.

[91] Poglitsch, A.; Waelkens, C.; Geis, N.; Feuchtgruber, H.; Vandenbussche, B.; Rodriguez, L.; Krause, O.; Renotte, E.; van Hoof, C.; Saraceno, P.; Cepa, J.; Kerschbaum, F.; Agnse, P.; Ali, B.; Altieri, B.; Andreani, P.; Augueres, J.-L.; Balog, Z.; Barl, L.; Bauer, O. H.; Belbachir, N.; Benedettini, M.; Billot, N.; Boulade, O.; Bischof, H.; Blommaert, J.; Callut, E.; Cara, C.; Cerulli, R.; Cesarsky, D.; Contursi, A.; Creten, Y.; De Meester, W.; Doublier, V.; Doumayrou, E.; Duband, L.; Exter, K.; Genzel, R.; Gillis, J.-M.; Grzinger, U.; Henning, T.; Herreros, J.; Huygen, R.; Inguscio, M.; Jakob, G.; Jamar, C.; Jean, C.; de Jong, J.; Katterloher, R.; Kiss, C.; Klaas, U.; Lemke, D.; Lutz, D.; Madden, S.; Marquet, B.; Martignac, J.; Mazy, A.; Merken, P.; Montfort, F.; Morbidelli, L.; Mller, T.; Nielbock, M.; Okumura, K.; Orfei, R.; Ottensamer, R.; Pezzuto, S.; Popesso, P.; Putzeys, J.; Regibo, S.; Reveret, V.; Royer, P.; Sauvage, M.; Schreiber, J.; Stegmaier, J.; Schmitt, D.; Schubert, J.; Sturm, E.; Thiel, M.; Tofani, G.; Vavrek, R.; Wetzstein, M.; Wieprecht, E.; Wiezorrek, E., 2010. *The Photodetector Array Camera and Spectrometer (PACS) on the Herschel Space Observatory.* A&A, 518(July), L2

[92] Pontoppidan, K. M., van Dishoeck, E. F., & Dartois, E. 2004. *Mapping ices in protostellar environments on 1000 AU scales. Methanol-rich ice in the envelope of Serpens SMM 4.* A&A, 426(Nov.), 925

[93] Roelfsema, P. R.; Helmich, F. P.; Teyssier, D.; Ossenkopf, V.; Morris, P.; Olberg, M.; Shipman, R.; Risacher, C.; Akyilmaz, M.; Assendorp, R.; Avruch, I. M.; Beintema, D.; Biver, N.; Boogert, A.; Borys, C.; Braine, J.; Caris, M.; Caux, E.; Cernicharo, J.; Coeur-Joly, O.; Comito, C.; de Lange, G.; Delforge, B.; Dieleman, P.; Dubbeldam, L.; de Graauw, Th.; Edwards, K.; Fich, M.; Flederus, F.; Gal, C.; di Giorgio, A.; Herpin, F.; Higgins, D. R.; Hoac, A.; Huisman, R.; Jarchow, C.; Jellema, W.; de Jonge, A.; Kester, D.; Klein, T.; Kooi, J.; Kramer, C.; Laauwen, W.; Larsson, B.; Leinz, C.; Lord, S.; Lorenzani, A.; Luinge, W.; Marston, A.; Martín-Pintado, J.; McCoey, C.; Melchior, M.; Michalska, M.; Moreno, R.; Müller, H.; Nowosielski, W.; Okada, Y.; Orleański, P.; Phillips, T. G.; Pearson, J.; Rabois, D.; Ravera, L.; Rector, J.; Rengel, M.; Sagawa, H.; Salomons, W.; Sánchez-Suárez, E.; Schieder, R.; Schlöder, F.; Schmülling, F.; Soldati, M.; Stutzki, J.; Thomas, B.; Tielens, A. G. G. M.; Vastel, C.; Wildeman, K.; Xie, Q.; Xilouris, M.; Wafelbakker, C.; Whyborn, N.; Zaal, P.; Bell, T.; Bjerkeli, P.; De Beck,

E.; Cavalié, T.; Crockett, N. R.; Hily-Blant, P.; Kama, M.; Kaminski, T.; Leflóch, B.; Lombaert, R.; de Luca, M.; Makai, Z.; Marseille, M.; Nagy, Z.; Pacheco, S.; van der Wiel, M. H. D.; Wang, S.; Yıldız, U., 2012. *In-orbit performance of Herschel-HIFI.* A&A, 537(Jan.), A17

[94] Rowan-Robinson M., 1979. *Clouds of dust and molecules in the Galaxy.* ApJ, 234(Nov.), 111

[95] Sandell, G. 2000. *(Sub)mm continuum mapping of NGC 6334 I & I(N). A cobweb of filaments and protostars.* A&A, 358(June), 242

[96] Sargent A. I., 1977. *Molecular clouds and star formation. I - Observations of the Cepheus OB3 molecular cloud.* ApJ, 218(Dec.), 736

[97] Schreyer, K., Henning, T., van der Tak, F. F. S., Boonman, A. M. S., & van Dishoeck, E. F. 2002, A&A, 394, 561

[98] Shevchenko, V. S., & Yakubov, S. D. 1989. *Compact Star-Formation Regions Associated with the Herbig Ae-Stars / Be-Stars LK-H-ALPHA:198 and LK-H-ALPHA:234.* Soviet Astron., 33(Aug.), 370

[99] Shirley, Y. L., Evans, II, N. J., & Rawlings, J. M. C. 2002. *Tracing the Mass during Low-Mass Star Formation. III. Models of the Submillimeter Dust Continuum Emission from Class 0 Protostars.* ApJ, 575 (Aug.), 337

[100] Shu F. H., Adams F. C., Lizano S., 1987. *Star formation in molecular clouds - Observation and theory.* ARA&A, 25, 23

[101] Slawson, R. W., & Reed, B. C. 1988. *The stellar distribution at (l,b) = (268,0) in Vela. I - The OB associations.* AJ, 96(Sept.), 988

[102] Snell, R. L., Scoville, N. Z., Sanders, D. B., & Erickson, N. R. 1984. *High-velocity molecular jets.* ApJ, 284(Sept.), 176

[103] Solomon P. M., Sanders D. B., Scoville N. Z., 1979, in Burton W. B., ed., IAU Symposium Vol. 84, *The Large-Scale Characteristics of the Galaxy.* 3552

[104] Spitzer, L. 1978. *Physical processes in the interstellar medium.* New York, NY. Wiley - Interscience.

[105] Stahler S. W., Palla F., 2005. *The Formation of Stars.* Wiley-VCH.

[106] Stanke, T., McCaughrean, M. J., & Zinnecker, H. 2000. *Giant protostellar outflows revealed by infrared imaging.* A&A, 355(Mar.), 639

[107] Sternberg, A. & Neufeld, D. A.. 1999. *The Ratio of Ortho- to Para-H_2 in Photodissociation Regions.* ApJ, 516(May), 371

[108] Straižys, V., Maskoliūnas, M., Boyle, R. P., Prada Moroni, P. G., Tognelli, E., Zdanavičius, K., Zdanavičius, J., Laugalys, V., and Kazlauskas, A., 2014. *The distance to the young cluster NGC 7129 and its age.* MNRAS, 438 (Jan.), 1848

[109] Takahashi, T., Silk, J., & Hollenbach, D. J. 1983. *H2O heating in molecular clouds - Line transfer and thermal balance in a warm dusty medium.* ApJ, 275(Dec.), 145

[110] Takahira K., Tasker E. J., Habe A., 2014. *Do Cloud-Cloud Collisions Trigger High-mass Star Formation? I. Small Cloud Collisions.* ApJ, 792(Sept.), 63

[111] Testi L., Sargent A. I., 1998. *Star Formation in Clusters: A Survey of Compact Millimeter-Wave Sources in the Serpens Core.* ApJ, 508(Nov.), L91

[112] Testi L., Palla F., Natta A., 1999. *The onset of cluster formation around Herbig Ae/Be stars.* A&A, 342(Feb.), 515

[113] Tielens, Alexander G G. 2005. *The Physics and Chemistry of the Interstellar Medium.* University University Press, Cambridge.

[114] Tiné, S., Lepp, S., Gredel, R., & Dalgarno, A., 1997. *Infrared response of H_2 to x-rays in dense clouds.* ApJ, 481, 282.

[115] Samuel Tisi (2013). *A Herschel/HIFI study of Water in Two Intermediate-Mass Star Forming Regions: Vela IRS 17 and Vela IRS 19.* UWSpace.

[116] Van der Tak, F. F. S., van Dishoeck, E. F., Evans, II, N. J., & Blake, G. A. 2000. *Structure and Evolution of the Envelopes of Deeply Embedded Massive Young Stars.* ApJ, 537(July), 283

[117] van der Tak, F., Walmsley, M., Herpin, F., & Ceccarelli, C. 2005. "*A dust and water disk in AFGL 2591*". Page 312P of: IAU Symposium. IAU Symposium, vol. 235.

[118] van der Tak, F. F. S.; Chavarra, L.; Herpin, F.; Wyrowski, F.; Walmsley, C. M.; van Dishoeck, E. F.; Benz, A. O.; Bergin, E. A.; Caselli, P.; Hogerheijde, M. R.; Johnstone, D.; Kristensen, L. E.; Liseau, R.; Nisini, B.; Tafalla, M., 2013. *Water in star-forming regions with Herschel (WISH). IV. A survey of low-J H2O line profiles toward high-mass protostars.* A&A, 554(June), A83

[119] van der Tak, F. F. S., Black, J. H., Schöer, F. L., Jansen, D. J., and van Dishoeck, E. F. 2007. *A computer program for fast non-LTE analysis of interstellar line spectra:With diagnostic plots to interpret observed line intensity ratios.* A&A, 468(June), 2

[120] van Dishoeck, E. F., Kristensen, L. E., Benz, A. O., Bergin, E. A., Caselli, P., Cernicharo, J., Herpin, F., Hogerheijde, M. R., Johnstone, D., Liseau, R., Nisini, B., Shipman, R., Tafalla, M., van der Tak, F., Wyrowski, F., Aikawa, Y., Bachiller, R., Baudry, A., Benedettini, M., Bjerkeli, P., Blake, G. A., Bontemps, S., Braine, J., Brinch, C., Bruderer, S., Chavarría, L., Codella, C., Daniel, F., de Graauw, T., Deul, E., di Giorgio, A. M., Dominik, C., Doty, S. D., Dubernet, M. L., Encrenaz, P., Feuchtgruber, H., Fich, M., Frieswijk, W., Fuente, A., Giannini, T., Goicoechea, J. R., Helmich, F. P., Herczeg, G. J., Jacq, T., JØrgensen, J. K., Karska, A., Kaufman, M. J., Keto, E., Larsson, B., Lefloch, B., Lis, D., Marseille, M., McCoey, C., Melnick, G., Neufeld, D., Olberg, M., Pagani, L., Paníc, O., Parise, B., Pearson, J. C., Plume, R., Risacher, C., Salter, D., Santiago-García, J., Saraceno, P., Stäuber, P., van Kempen, T. A., Visser, R., Viti, S., Walmsley, M., Wampfler, S. F., & Yıldız, U. A. 2011. *Water in Star-forming Regions with the Herschel Space Observatory (WISH). I. Overview of Key Program and First Results.* PASP, 123(Feb.), 138170.

[121] van Langevelde, H. J. & van der Tak, F. *Radiation Bookkeeping: a guide to astronomical molecular spectroscopy and radiative transfer problems with an emphasis on RADEX*, (Dec) 2008. http://var.sron.nl/radex/radex_manual.pdf

[122] Vanhala H. A. T., Cameron A. G. W., 1998. *Numerical Simulations of Triggered Star Formation. I. Collapse of Dense Molecular Cloud Cores.* ApJ, 508(Nov.), 291

[123] Whittet, D. C. B., Bode, M. F., Longmore, A. J., Adamson, A. J., McFadzean, A. D., Aitken, D. K., & Roche, P. F. 1988. *Infrared spectroscopy of dust in the Taurus dark clouds - Ice and silicates.* MNRAS, 233(July), 321

[124] Williams, S. J., Fuller, G. A., & Sridharan, T. K., 2005. *The circumstellar environments of high-mass protostellar objects. II. Dust continuum models.* A&A, 434 (Apr.), 257

[125] Wilson, B. A., Dame, T. M., Masheder, M. R. W., & Thaddeus, P. 2005. *A uniform CO survey of the molecular clouds in Orion and Monoceros.* A&A, 430(Feb.), 523

[126] Zhou T., Huang C. X., Lin D. N. C., Gritschneder M., Lau H., 2015. *On the IMF in a Triggered Star Formation Context.* ApJ, 808(July), 10

[127] Zuckerman B., Palmer P., 1974. *Radio radiation from interstellar molecules.* ARA&A, 12, 279

Appendix A

Other WISH IM Candidates

This appendix outlines the other 5 intermediate mass WISH candidates: NGC 2071 IR, Vela IRS 17, Vela IRS 19, AFGL 490, and L 1641 S3MMS 1. The source properties in Table 2.2 are reiterated below in Table A.1 for convenience. Tables A.2 and A.3 summarize the water observations for each of the 5 sources. The Herschel HIFI molecular line emission ($H_2^{16}O$ and $H_2^{18}O$ where applicable) is plotted in Figures A.1 - A.6. The Gaussian fits to each of these water transitions are outlined in Tables A.4 - A.8 respectively. These Gaussian fits are plotted against the Hershel HIFI water observations in Figures A.7 - A.14.

Table A.1: Properties of other WISH IM YSOs

Source	RA (J2000) (h m s)	dec (J2000) ($'$ $''$ $°$)	D (pc)	L_{bol} ($L_\odot$)	V_{LSR} (km s^{-1})	M_{env} ($M_\odot$)	References
NGC 2071 IR	05 47 04.4	+00 21 49	422	520	9.6	30	64, 124
Vela IRS 17	08 46 34.7	-43 54 30.5	700	715	3.9	6.4	47, 70, 100
Vela IRS 19	08 48 48.5	-43 32 29.0	700	776	12.2	3.5	70, 100
L1641 S3MMS1	05 39 55.9	-07 30 28.0	465	70	5.3	20.9	105, 124
AFGL 490	03 27 38.4	+58 47 04.0	1000	2000	-13.5	45	77,101

Table A.2: Summary of water observations for other IM WISH candidates.

Object	Transition	Rest ν (GHz)	Band	Integration (s)	Resolution (MHz)	Date	θ_{beam} ('')
NGC 2071 IR	o-H$_2^{16}$O 1_{10}-1_{01}	556.936	1a	405	1.022	28-09-10	38.074
	o-H$_2^{16}$O 1_{10}-1_{01}	556.936	1a	405	1.022	31-08-10	38.074
	p-H$_2^{16}$O 1_{11}-0_{00}	1113.343	4b	2431	1.135	17-04-10	19.046
	p-H$_2^{16}$O 2_{02}-1_{11}	987.927	4a	1271	1.022	13-09-10	21.464
	p-H$_2^{16}$O 2_{11}-2_{02}	752.033	2b	922	1.139	13-04-10	28.197
	o-H$_2^{16}$O 3_{12}-2_{21}	1153.127	5a	598	1.020	01-10-10	18.389
	o-H$_2^{18}$O 1_{10}-1_{01}	547.676	1a	3599	1.139	11-04-10	38.718
	o-H$_2^{18}$O 3_{12}-3_{03}	1095.627	4b	6495	1.119	25-08-11	19.354
Vela IRS 17	o-H$_2^{16}$O 1_{10}-1_{01}	556.936	1a	405	1.022	15-06-10	38.074
	o-H$_2^{16}$O 1_{10}-1_{01}	556.936	1a	405	1.022	03-12-10	38.074
	p-H$_2^{16}$O 1_{11}-0_{00}	1113.343	4b	2431	1.135	09-06-10	19.046
	p-H$_2^{16}$O 2_{02}-1_{11}	987.927	4a	1271	1.022	08-06-10	21.464
	p-H$_2^{16}$O 2_{11}-2_{02}	752.033	2b	922	1.139	17-07-10	28.197
	o-H$_2^{16}$O 3_{12}-2_{21}	1153.127	5a	598	1.020	15-06-10	18.389
	o-H$_2^{18}$O 1_{10}-1_{01}	547.676	1a	3599	1.139	15-06-10	38.718

Table A.3: Continued Summary of water observations for other IM WISH candidates.

Object	Transition	Rest ν (GHz)	Band	Integration (s)	Resolution (MHz)	Date	θ_{beam} ('')
Vela IRS 19	o-H$_2^{16}$O 1_{10}-1_{01}	556.936	1a	405	1.022	15-06-10	38.074
	o-H$_2^{16}$O 1_{10}-1_{01}	556.936	1a	405	1.022	03-12-10	38.074
	p-H$_2^{16}$O 1_{11}-0_{00}	1113.343	4b	2431	1.135	09-06-10	19.046
	p-H$_2^{16}$O 2_{02}-1_{11}	987.927	4a	1271	1.022	08-06-10	21.464
	p-H$_2^{16}$O 2_{11}-2_{02}	752.033	2b	922	1.139	17-07-10	28.197
	o-H$_2^{16}$O 3_{12}-2_{21}	1153.127	5a	598	1.020	15-06-10	18.389
	o-H$_2^{18}$O 1_{10}-1_{01}	547.676	1a	3599	1.139	15-06-10	38.718
L1641	o-H$_2^{16}$O 1_{10}-1_{01}	556.936	1a	405	1.022	31-08-10	38.074
S3MMS1	o-H$_2^{16}$O 1_{10}-1_{01}	556.936	1a	405	1.022	28-09-10	38.074
	p-H$_2^{16}$O 1_{11}-0_{00}	1113.343	4b	2431	1.135	30-09-10	19.046
	p-H$_2^{16}$O 2_{02}-1_{11}	987.927	4a	1271	1.022	14-09-10	21.464
	p-H$_2^{16}$O 2_{11}-2_{02}	752.033	2b	922	1.139	19-08-10	28.197
	o-H$_2^{16}$O 3_{12}-2_{21}	1153.127	5a	598	1.020	20-08-10	18.389
	o-H$_2^{18}$O 1_{10}-1_{01}	547.676	1a	3599	1.139	31-08-10	38.718
AFGL 490	o-H$_2^{16}$O 1_{10}-1_{01}	556.936	1a	405	1.022	16-02-10	38.074
	o-H$_2^{16}$O 1_{10}-1_{01}	556.936	1a	405	1.022	02-04-10	38.074
	p-H$_2^{16}$O 1_{11}-0_{00}	1113.343	4b	2431	1.135	01-04-10	19.046
	p-H$_2^{16}$O 2_{02}-1_{11}	987.927	4a	1271	1.022	14-09-10	21.464
	p-H$_2^{16}$O 2_{11}-2_{02}	752.033	2b	922	1.139	01-04-10	28.197
	o-H$_2^{16}$O 3_{12}-2_{21}	1153.127	5a	598	1.020	01-04-10	18.389
	o-H$_2^{18}$O 1_{10}-1_{01}	547.676	1a	3599	1.139	16-02-10	38.718
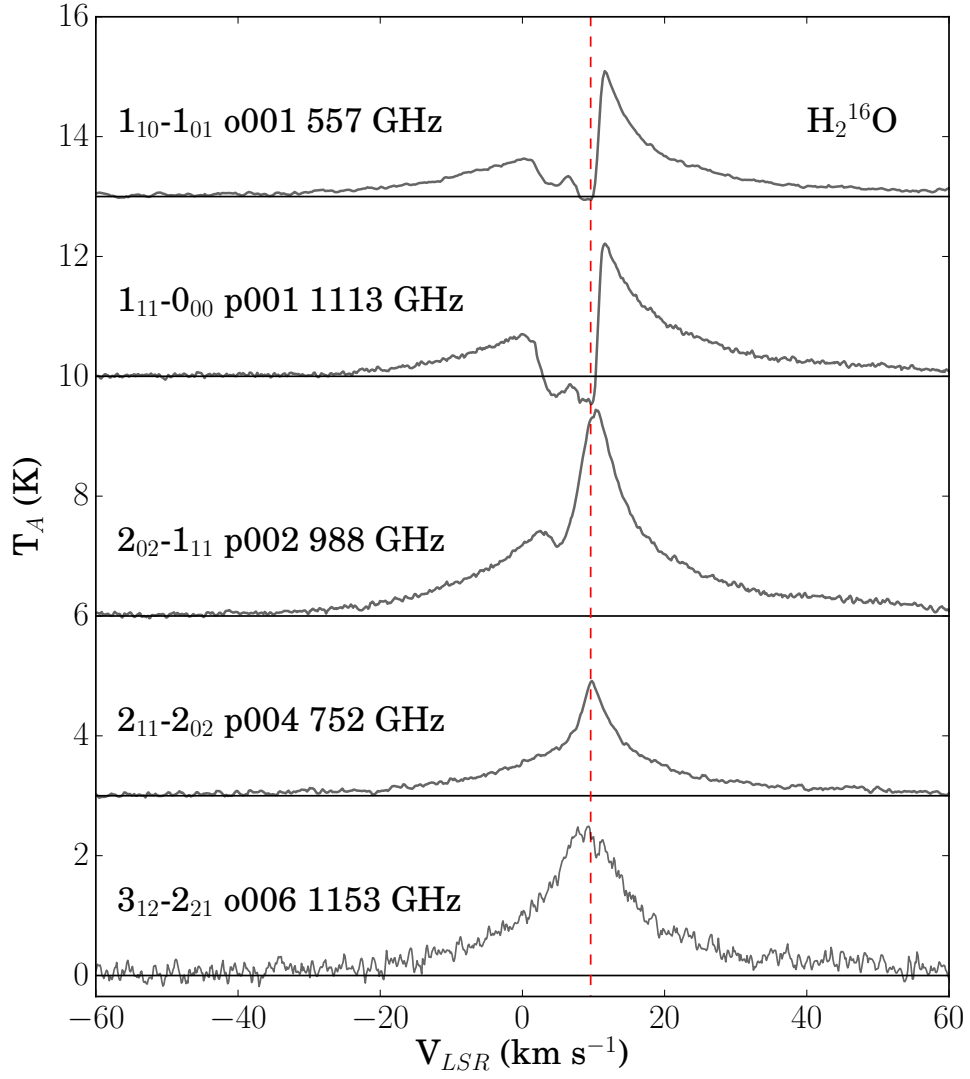
Figure A.1: NGC 2071 IR $H_2^{16}O$ observations. System V_{LSR} located at $+9.6$ km s^{-1} (red dashed line). Double absorption feature present in ground state lines, blueshifted absorption present still in $H_2^{16}O$ 988 GHz line. Wide wings indicative of strong outflows. Blueshifted absorption feature also present in $H_2^{18}O$ ground state line. $H_2^{16}O$ ground state emission peak ~ 2.0 K
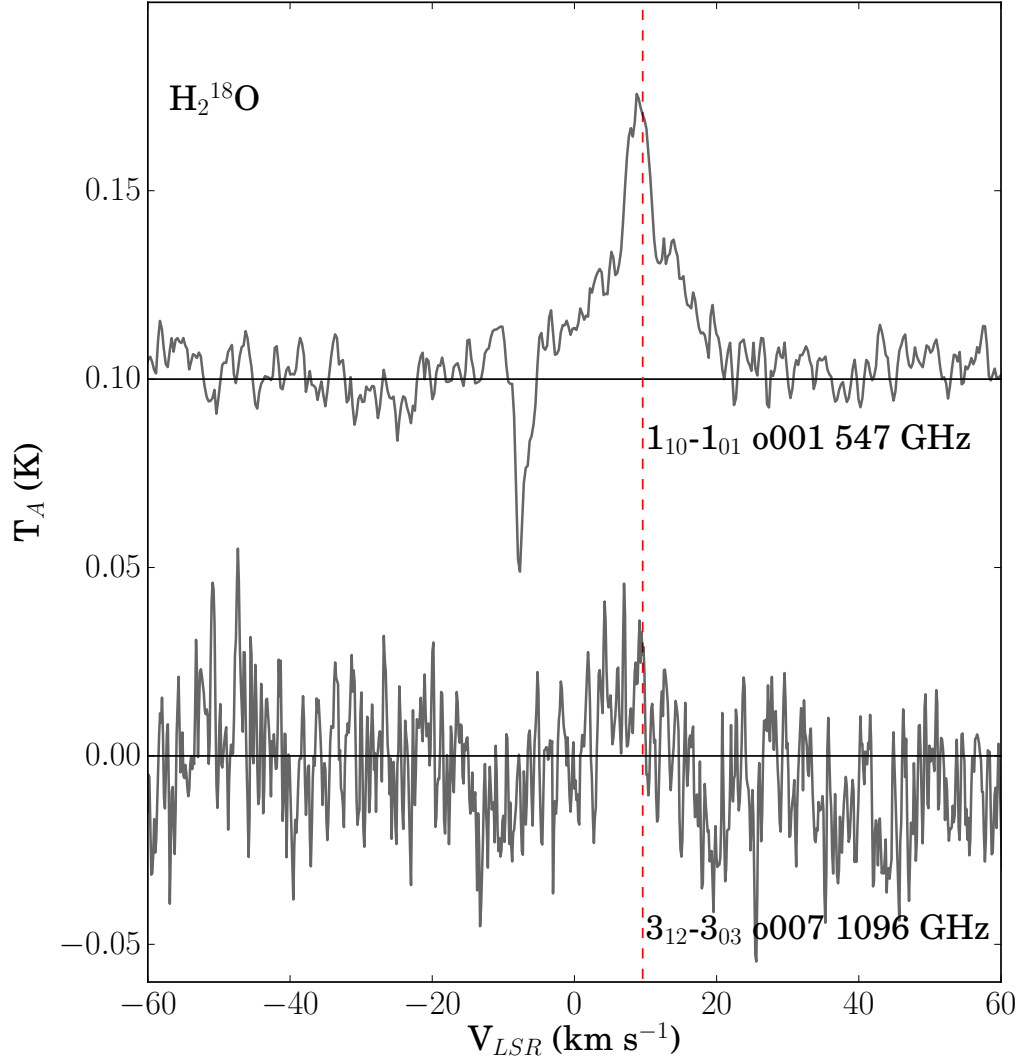
Figure A.2: NGC 2071 IR $H_2^{18}O$ observations. System V_{LSR} located at +9.6 km s^{-1} (red dashed line). Standing wave seems to be present in 1096 GHz line. $H_2^{18}O$ ground state emission peak ~ 0.075 K.
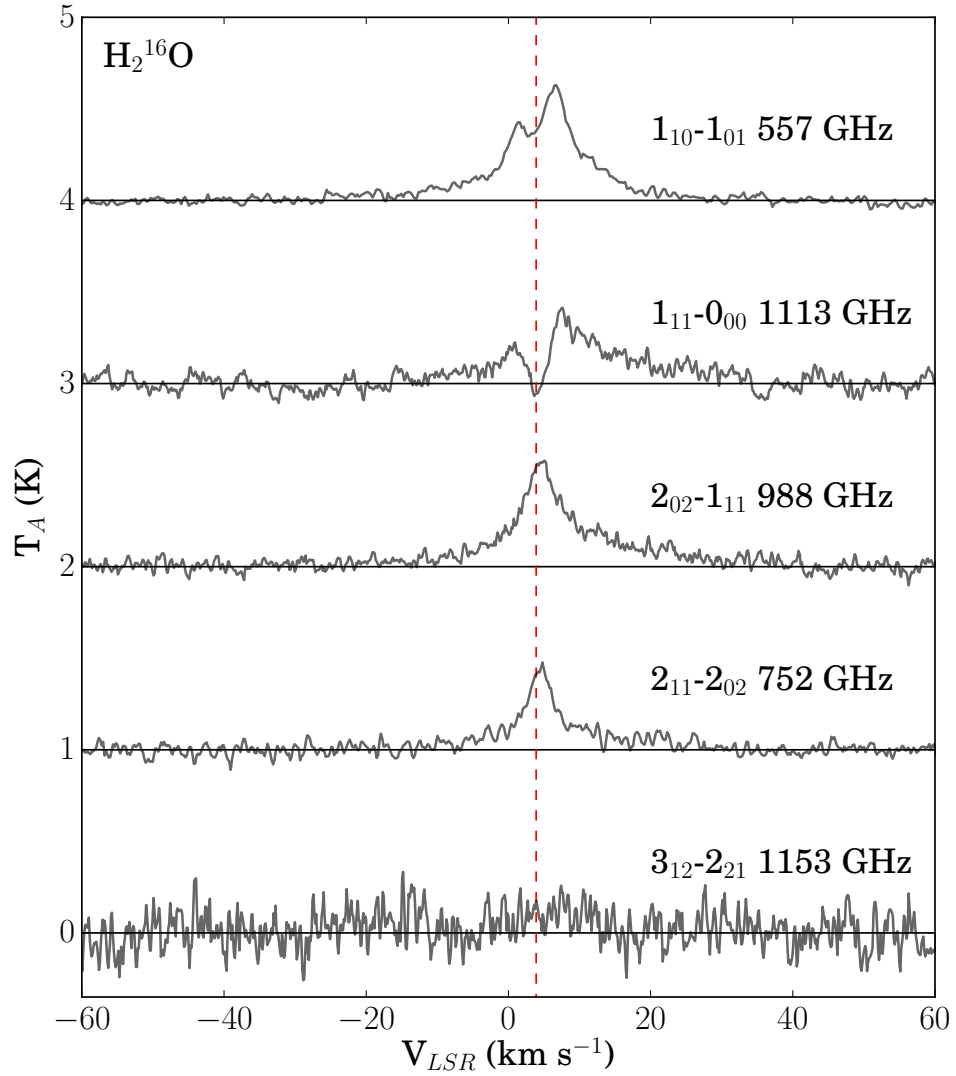
Figure A.3: Vela IRS 17 Observations. System V_{LSR} located at $+3.9$ km s^{-1} (red dashed line). Absorption feature present in ground state lines, resembling P-Cygni profiles. Wide wings indicative of strong outflows. $H_2^{16}O$ ground state emission peak ~ 0.55 K.
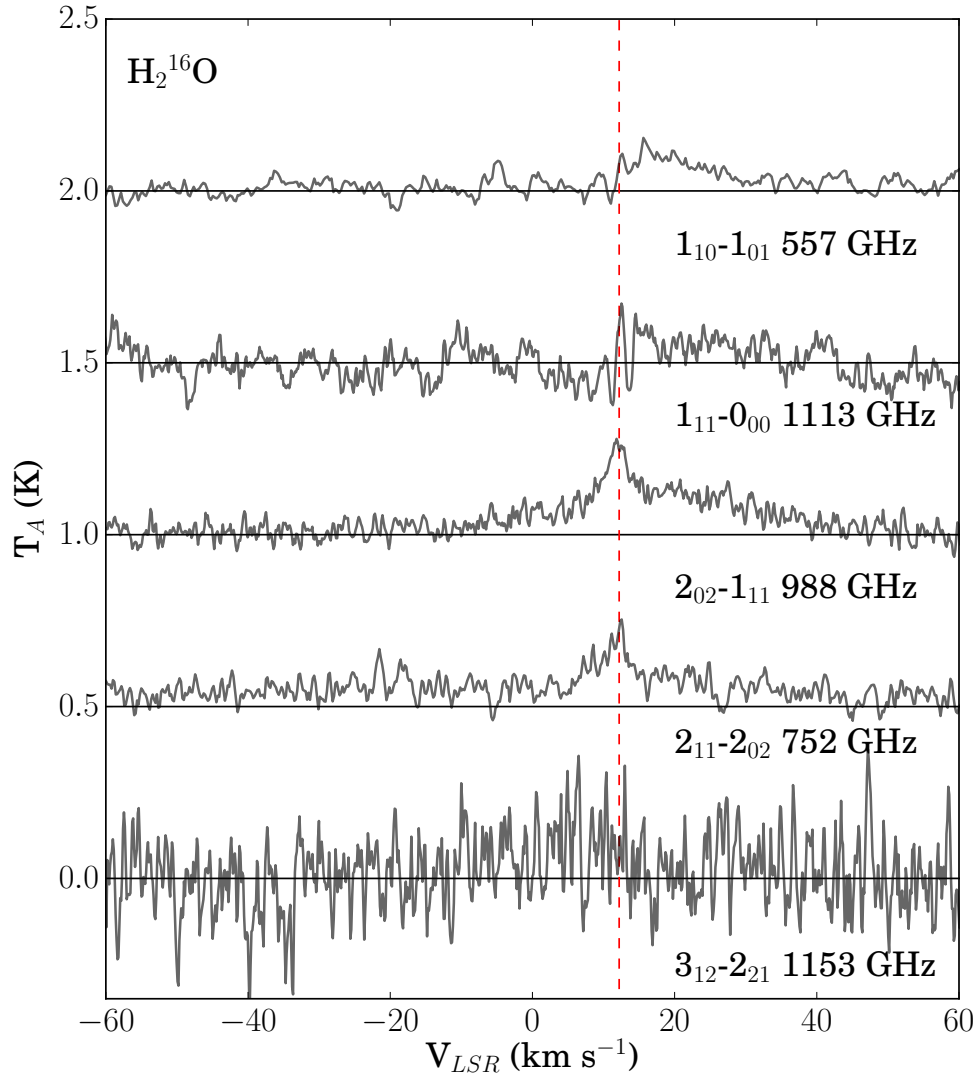
Figure A.4: Vela IRS 19 $H_2^{16}O$ Observations. System V_{LSR} located at $+12.2$ km s^{-1} (red dashed line). $H_2^{16}O$ ground state emission peak ~ 0.2 K. Lack of structure seen in ground state lines, emission redshifted. Higher transition lines p002 and p004 (988 GHz and 752 GHz respectively) approximately doubled in antenna temperature.
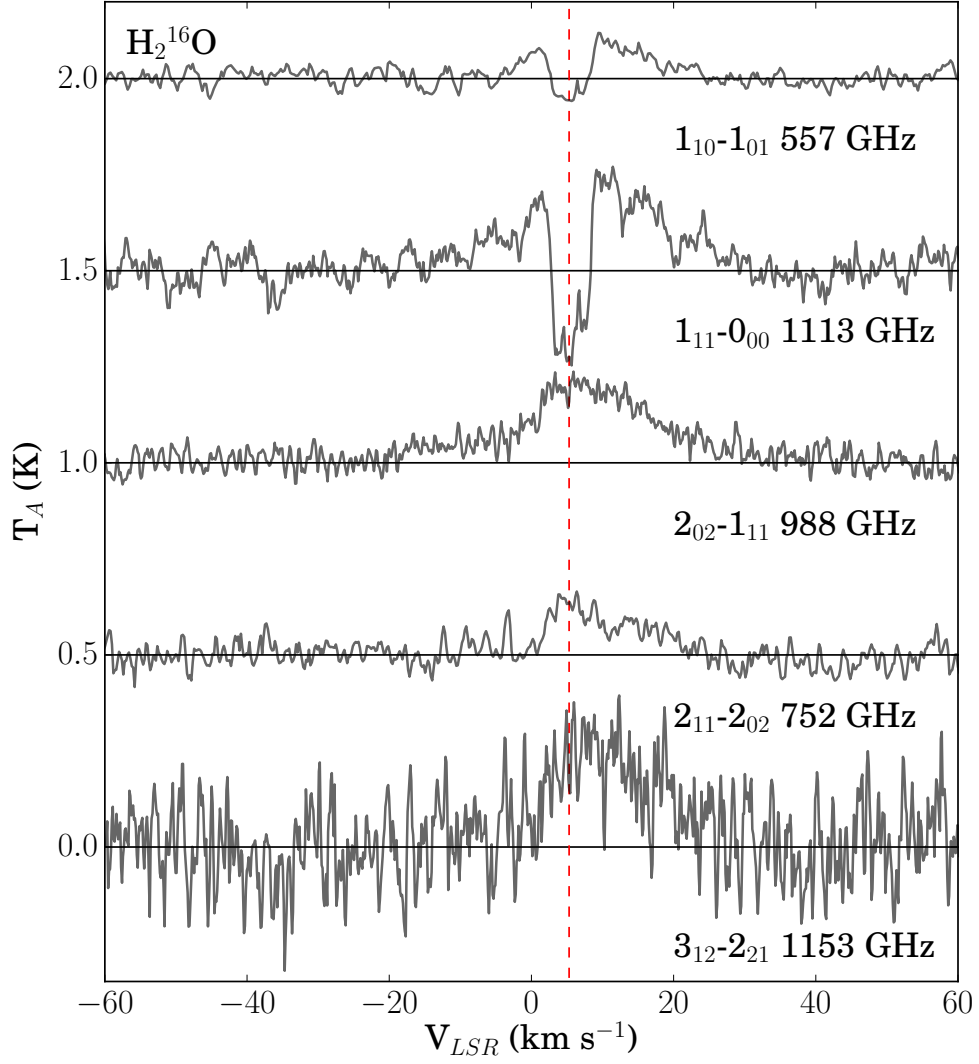
Figure A.5: L1641 $H_2^{16}O$ Observations. System V_{LSR} located at $+5.3$ km s^{-1} (red dashed line). o-$H_2^{16}O$ ground state emission peak ~ 0.25 K. Multiple absorption features seen to the red and blue of the system V_{LSR}. Absorption features not present in higher state lines. Strong 1153 GHz line compared to other IM WISH candidates, potentially indicating hotter central source.
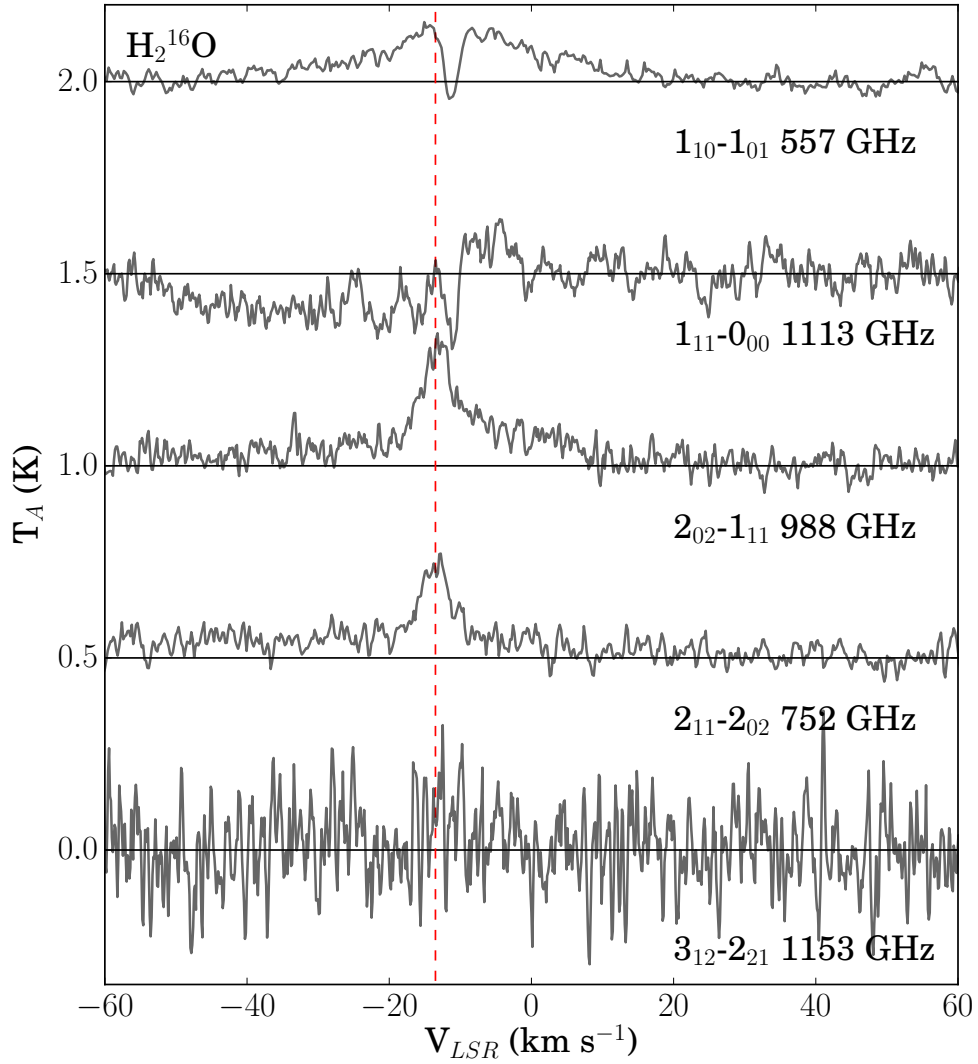
Figure A.6: AFGL 490 $H_2^{16}O$ Observations. System V_{LSR} located at -13.5 km s^{-1} (red dashed line). o-$H_2^{16}O$ ground state emission peak ~ 0.25 K. Absorption features seen in ortho ground state line, but not present in higher state lines. The blueshifted segment of the para ground state spectra seems to have a baseline or instrument issue as this broad absorption is not present in any other lines.

Table A.4: Spectral Fits to Water Data: NGC 2071 IR

Transition	σ_{RMS}	ID	Colour	Component	Position (km/s)	Width (km/s)	Amplitude (K)	$\int T_A dv$ (K)	FWHM (km/s)
o-H$_2^{16}$O 1_{10}-1_{01}	0.06	G1	Green	Broad	10.6	12.3 $\pm$ 0.2	0.8 $\pm$ 0.01	24.2 $\pm$ 0.3	29.07
		G2	Red	Very-Broad	11.6	50.3 $\pm$ 1.9	0.1 $\pm$ 0.006	15.2 $\pm$ 0.91	118.5
		G3	Cyan	Medium	11.6	2.2 $\pm$ 0.04	1.2 $\pm$ 0.02	6.6 $\pm$ 0.11	5.115
		G4	Magenta	Narrow	9.2	1.3 $\pm$ 0.02	-1.7 $\pm$ 0.02	-5.8 $\pm$ 0.07	3.158
		G5	Yellow	Narrow	4.2	1.8 $\pm$ 0.06	-0.7 $\pm$ 0.02	-2.9 $\pm$ 0.08	4.137
p-H$_2^{16}$O 1_{11}-0_{00}	0.07	G1	Green	Medium	10.6	5.7 $\pm$ 0.09	1.3 $\pm$ 0.02	18.1 $\pm$0.28	13.52
		G2	Red	Broad	11.6	19.7 $\pm$ 0.2	0.6 $\pm$ 0.01	31.6 $\pm$0.53	46.37
		G3	Cyan	Narrow	11.6	0.8 $\pm$ 0.01	1.7 $\pm$ 0.02	3.4 $\pm$0.04	1.909
		G4	Magenta	Medium	9.2	2.1 $\pm$ 0.02	-2.4 $\pm$ 0.02	-12.9 $\pm$0.11	5.044
		G5	Yellow	Narrow	4.2	1.7 $\pm$ 0.02	-1.5 $\pm$ 0.01	-6.2 $\pm$ 0.04	3.895
p-H$_2^{16}$O 2_{02}-1_{11}	0.07	G1	Green	Broad	10.6	10.8 $\pm$ 0.2	1.1 $\pm$ 0.02	29.1 $\pm$0.53	25.37
		G2	Red	Broad	11.6	28.8 $\pm$ 0.7	0.4 $\pm$ 0.02	30.2 $\pm$1.51	67.90
		G3	Cyan	Narrow	11.6	1.9 $\pm$ 0.04	1.4 $\pm$ 0.02	6.6 $\pm$0.09	4.347
		G4	Magenta	Narrow	9.2	1.2 $\pm$ 0.03	1.0 $\pm$ 0.02	3.1 $\pm$0.06	2.861
p-H$_2^{16}$O 2_{11}-2_{02}	0.06	G1	Green	Medium	10.6	2.3 $\pm$ 0.04	1.0 $\pm$ 0.02	5.6 $\pm$0.11	5.455
		G2	Red	Very-Broad	11.6	30.4 $\pm$ 1.1	0.2 $\pm$ 0.01	14.1 $\pm$0.71	71.68
		G3	Cyan	Broad	11.6	10.5 $\pm$ 0.3	0.5 $\pm$ 0.01	14.2 $\pm$0.28	24.76
o-H$_2^{16}$O 3_{12}-2_{21}	0.1	G1	Green	Broad	10.6	8.5 $\pm$ 0.7	0.6 $\pm$ 0.06	13.2 $\pm$1.32	19.95
		G2	Red	Broad	11.6	26.9 $\pm$ 1.0	0.4 $\pm$ 0.03	27.8 $\pm$2.09	63.33
		G4	Magenta	Medium	9.2	3.4 $\pm$ 0.2	1.1 $\pm$ 0.07	9.4 $\pm$0.60	8.115
		G5	Yellow	Medium-Broad	4.2	8.2 $\pm$ 0.6	0.3 $\pm$ 0.03	6.5 $\pm$0.65	19.30
o-H$_2^{18}$O 1_{10}-1_{01}	0.006	G1	Green	Broad	10.6	9.0 $\pm$ 0.8	0.02 $\pm$ 0.003	0.4 $\pm$0.06	21.29
		G2	Red	Narrow	11.6	1.1 $\pm$ 0.5	-0.03 $\pm$ 0.03	-0.9 $\pm$0.90	2.674
		G3	Cyan	Medium	11.6	2.1 $\pm$ 1.0	0.02 $\pm$ 0.003	0.1 $\pm$0.02	5.009
		G4	Magenta	Narrow	9.2	1.9 $\pm$ 0.2	0.04 $\pm$ 0.003	0.2 $\pm$0.03	4.516
		G7	Blue	Narrow	-7.5	0.8 $\pm$ 0.06	-0.05 $\pm$ 0.003	-0.1 $\pm$0.006	1.890
o-H$_2^{18}$O 3_{12}-3_{03}	0.02	-	-	-	-	-	-	-	-

Table A.5: Spectral Fits to Water Data: Vela IRS 17

Transition	σ_{RMS}	ID	Colour	Component	Position (km/s)	Width (km/s)	Amplitude (K)	$\int T_A dv$ (K)	FWHM (km/s)
o-H$_2^{16}$O 1_{10}-1_{01}	0.02	G1	Red	Narrow	6.5 ± 0.08	1.6 ± 0.1	0.5 ± 0.04	2.0 ± 0.16	3.893
		G2	Green	Broad	2.8 ± 0.5	17.5 ± 0.5	0.1 ± 0.005	5.3 ± 0.27	41.25
		G3	Yellow	Narrow	1.5 ± 0.1	1.8 ± 0.1	0.3 ± 0.009	1.4 ± 0.04	4.245
		G4	Cyan	Medium	1.1 ± 0.7	2.7 ± 0.5	0.1 ± 0.01	9.1 ± 0.91	6.254
p-H$_2^{16}$O 1_{11}-0_{00}	0.04	G1	Red	Medium	6.5	2.8 ± 0.2	0.2 ± 0.02	1.6 ± 0.16	6.494
		G3	Yellow	Narrow	1.5	1.7 ± 0.4	0.07 ± 0.02	0.3 ± 0.09	3.907
		G4	Cyan	Broad	1.1	11.2 ± 0.4	0.2 ± 0.007	2.7 ± 0.1	26.47
		G5	Magenta	Narrow	4.2 ± 0.08	1.4 ± 0.1	-0.4 ± 0.02	-1.3 ± 0.07	3.249
p-H$_2^{16}$O 2_{02}-1_{11}	0.03	G1	Red	Medium	6.5	3.9 ± 0.3	0.2 ± 0.02	1.5 ± 0.15	9.140
		G3	Yellow	Medium	1.5	4.8 ± 0.8	0.06 ± 0.01	0.7 ± 0.12	11.22
		G4	Cyan	Broad	1.1	13.9 ± 0.6	0.01 ± 0.007	4.2 ± 2.94	32.80
		G5	Magenta	Narrow	4.2	1.6 ± 0.1	0.3 ± 0.02	1.1 ± 0.07	3.786
p-H$_2^{16}$O 2_{11}-2_{02}	0.03	G1	Red	Medium	6.5	2.5 ± 0.4	0.07 ± 0.01	0.4 ± 0.06	5.883
		G3	Yellow	Medium	1.5	5.7 ± 0.7	0.06 ± 0.007	0.9 ± 0.11	13.35
		G4	Cyan	Broad	1.1	10.2 ± 0.7	0.07 ± 0.005	2.0 ± 0.14	25.45
		G5	Magenta	Narrow	4.2	1.4 ± 0.07	0.3 ± 0.01	1.0 ± 0.03	3.341
o-H$_2^{16}$O 3_{12}-2_{21}	0.09	G1	Red	Medium	6.5	5.0 ± 0.7	0.1 ± 0.02	1.5 ± 0.30	11.68
o-H$_2^{18}$O 1_{10}-1_{01}	0.008	G4	Cyan	Medium	1.1	3.1 ± 1.1	0.01 ± 0.003	0.08 ± 0.02	7.342

Table A.6: Spectral Fits to Water Data: Vela IRS 19

Transition	σ_{RMS}	ID	Colour	Component	Position (km/s)	Width (km/s)	Amplitude (K)	$\int T_A dv$ (K)	FWHM (km/s)
o-H$_2^{16}$O 1_{10}-1_{01}	0.02	G1	Red	Very-Broad	29.6 ± 2.6	30.0 ± 2.6	0.03 ± 0.002	2.0 ± 0.13	70.70
		G2	Green	Medium	18.4 ± 0.3	42.4 ± 0.3	0.09 ± 0.005	0.9 ± 0.05	9.97
p-H$_2^{16}$O 2_{02}-1_{11}	0.02	G2	Green	Broad	18.4	14.5 ± 0.4	0.1 ± 0.003	4.3 ± 0.13	34.19
		G3	Yellow	Narrow	11.9 ± 0.1	1.5 ± 0.1	0.2 ± 0.009	0.6 ± 0.03	3.515
p-H$_2^{16}$O 2_{11}-2_{02}	0.03	G2	Green	Very-Broad	18.4	81.7 ± 4.0	0.03 ± 0.001	6.2 ± 0.21	192.5
		G3	Yellow	Medium	11.9	3.0 ± 0.2	0.1 ± 0.007	1.0 ± 0.07	7.17
		G4	Cyan	Medium	21.2 ± 0.6	2.5 ± 0.6	0.04 ± 0.007	0.3 ± 0.05	5.862
o-H$_2^{16}$O 3_{12}-2_{21}	0.1	G3	Yellow	Broad	11.9	15.8 ± 1.8	0.09 ± 0.01	3.7 ± 0.41	37.31
		G4	Cyan	Medium	21.2	3.5 ± 1.0	-0.08 ± 0.02	-0.7 ± 0.18	8.180

Table A.7: Spectral Fits to Water Data: L1641 S3MMS1

Transition	σ_{RMS}	ID	Colour	Component	Position (km/s)	Width (km/s)	Amplitude (K)	$\int T_A dv$ (K)	FWHM
o-H$_2^{16}$O 1_{10}-1_{01}	0.019	G1	Red	Medium	8.3 ± 0.4	7.0 ± 0.4	0.1 ± 0.009	1.8 ± 0.16	16.48
		G2	Green	Narrow	5.5 ± 0.1	2.1 ± 0.2	-0.2 ± 0.01	0.8 ± 0.04	4.827
p-H$_2^{16}$O 1_{11}-0_{00}	0.04	G1	Red	Broad	8.3	9.1 ± 0.3	0.2 ± 0.009	5.3 ± 0.24	21.53
		G2	Green	Narrow	5.5	2.0 ± 0.07	-0.5 ± 0.01	2.3 ± 0.05	4.646
p-H$_2^{16}$O 2_{02}-1_{11}	0.03	G1	Red	Broad	8.3	11.0 ± 0.4	0.2 ± 0.008	4.4 ± 0.17	25.96
		G2	Red	Medium	5.5	3.2 ± 0.8	0.04 ± 0.009	0.3 ± 0.07	7.579
p-H$_2^{16}$O 2_{11}-2_{02}	0.03	G1	Red	Medium	8.3	7.9 ± 0.4	0.09 ± 0.006	1.8 ± 0.12	18.68
		G2	Green	Narrow	5.5	1.8 ± 0.4	0.05 ± 0.009	0.2 ± 0.04	4.135
o-H$_2^{16}$O 3_{12}-2_{21}	0.1	G1	Red	Medium	8.3	8.0 ± 0.5	0.3 ± 0.01	4.9 ± 0.16	18.74

Table A.8: Spectral Fits to Water Data: AFGL 490

| Transition	σ_{RMS}	ID	Colour	Component	Position (km/s)	Width (km/s)	Amplitude (K)	$\int T_A dv$ (K)	FWHM (km/s)
o-H$_2^{16}$O 1_{10}-1_{01}	0.02	G1	Red	Medium	-10.7 $\pm$ 0.4	5.3 $\pm$ 0.9	0.06 $\pm$ 0.01	0.8 $\pm$ 0.13	12.52
		G2	Green	Broad	-10.8 $\pm$ 0.5	15.3 $\pm$ 0.9	0.09 $\pm$ 0.01	3.5 $\pm$ 0.39	36.07
		G3	Yellow	Narrow	-11.2 $\pm$ 0.05	1.0 $\pm$ 0.07	-0.2 $\pm$ 0.01	-0.5 $\pm$ 0.03	2.302
p-H$_2^{16}$O 1_{11}-0_{00}	0.04	G1	Red	Medium	-10.7	4.4 $\pm$ 0.6	0.1 $\pm$ 0.01	1.1 $\pm$ 0.11	10.46
		G3	Yellow	Narrow	-11.2	0.8 $\pm$ 0.08	-0.2 $\pm$ 0.02	-0.5 $\pm$ 0.05	1.913
		G6	Orange	Broad	-31.0 $\pm$ 1.1	14.6 $\pm$ 1.0	-0.1 $\pm$ 0.004	-3.9 $\pm$ 0.16	34.34
p-H$_2^{16}$O 2_{02}-1_{11}	0.03	G1	Red	Broad	-10.7	16.2 $\pm$ 0.7	0.09 $\pm$ 0.004	3.6 $\pm$ 0.16	38.22
		G4	Cyan	Narrow	-13.1 $\pm$ 0.09	2.1 $\pm$ 0.1	0.2 $\pm$ 0.008	1.1 $\pm$ 0.04	4.891
		G5	Magenta	Narrow	-33.2 $\pm$ 0.2	0.5 $\pm$ 0.2	0.06 $\pm$ 0.02	0.07 $\pm$ 0.02	1.098
p-H$_2^{16}$O 2_{11}-2_{02}	0.03	G3	Yellow	Narrow	-11.2	0.5 $\pm$ 0.1	-0.08 $\pm$ 0.02	-0.1 $\pm$ 0.03	1.236
		G4	Cyan	Medium	- 13.1	2.6 $\pm$ 0.09	0.2 $\pm$ 0.007	1.4 $\pm$ 0.05	6.041
		G6	Orange	Very-Broad	-31.0	84.5 $\pm$ 2.9	0.04 $\pm$ 0.001	8.1 $\pm$ 0.2	199.0
o-H$_2^{16}$O 3_{12}-2_{21}	0.1	G1	Red	Medium	-10.7	4.0 $\pm$ 1.1	0.07 $\pm$ 0.02	0.7 $\pm$ 0.2	9.397
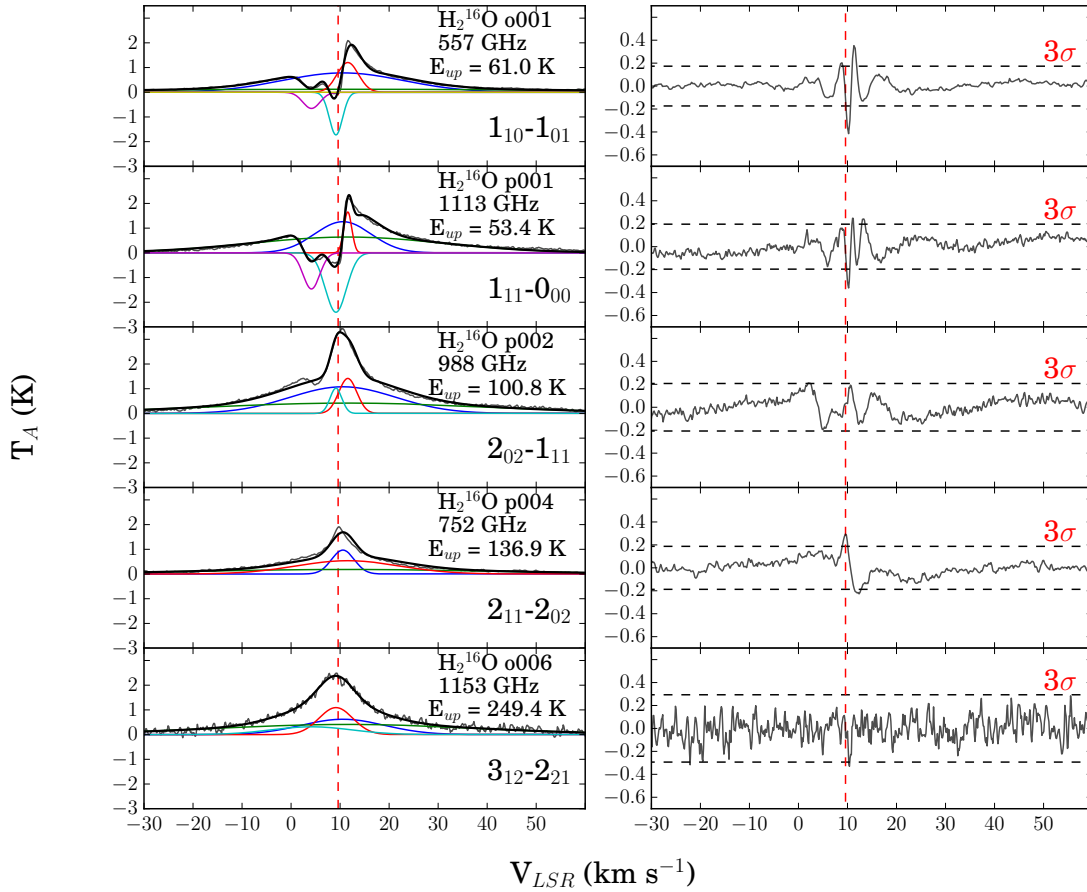
Figure A.7: NGC 2071 IR $H_2^{16}O$ Gaussian Fits. Up to 5 Gaussians were fit to these transition lines. G1 is located at $+10.6$ km s^{-1} (green), G2 at $+11.6$ km s^{-1} (red), G3 at $+11.6$ km s^{-1} (cyan), G4 at $+9.2$ km s^{-1} (magenta), and G5 at $+4.2$ km s^{-1} (yellow). Gaussians are fit at the same position in each transition, but at varying widths. See Table A.4 for further details. Local $V_{LSR} = +9.6$ km s^{-1}. Gaussian fits are subtracted from the HIFI data, yielding the residuals in the bottom panels. The 3σ boundaries around the residuals (right panels) represent the goodness of fit of the Gaussians. The majority of fits are well encased by these boundaries.
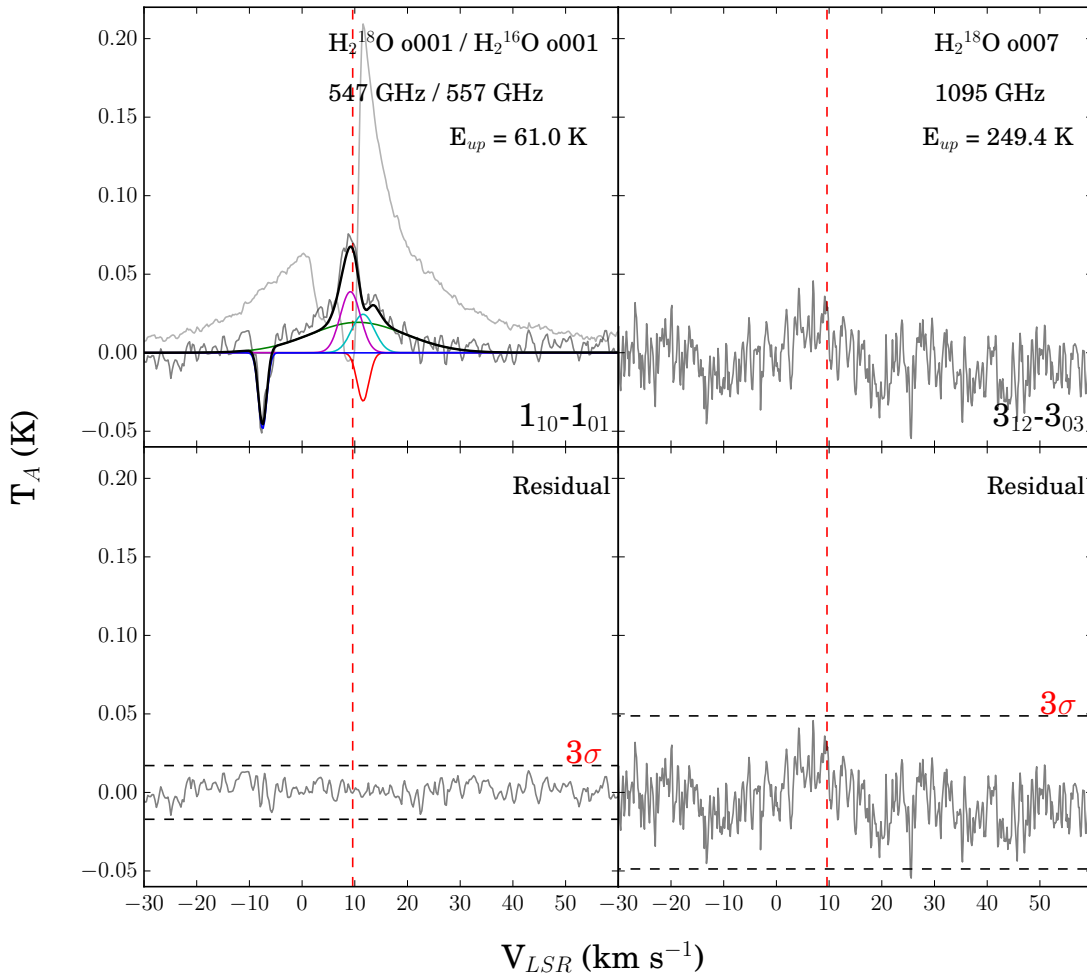
Figure A.8: NGC 2071 IR $H_2^{18}O$ Gaussian fits contrasted with $H_2^{18}O$ and $H_2^{16}O$ HIFI data (reduced to 10 % for ground state line o001). Five Gaussian fits were applied: medium G1 at +10.6 km s^{-1} (green), narrow G2 at 11.6 km s^{-1} (red), narrow G3 at 11.6 km s^{-1} (cyan), narrow G4 at 9.2 km s^{-1} (magenta), and a medium G7 at -7.5 km s^{-1} (blue). The total fit is outlined in black. Gaussians are fit for the ground state line, while the excited lines appear to be non-detections. See Table A.4 for further details. Excited o007 line considered non-detection. Local $V_{LSR} = +9.6$ km s^{-1}. Gaussian fits are subtracted from the HIFI data, yielding the residuals in the bottom panels. The 3σ boundaries around the residuals represent the goodness of fit of the Gaussians. The majority of fits are well encased by these boundaries.
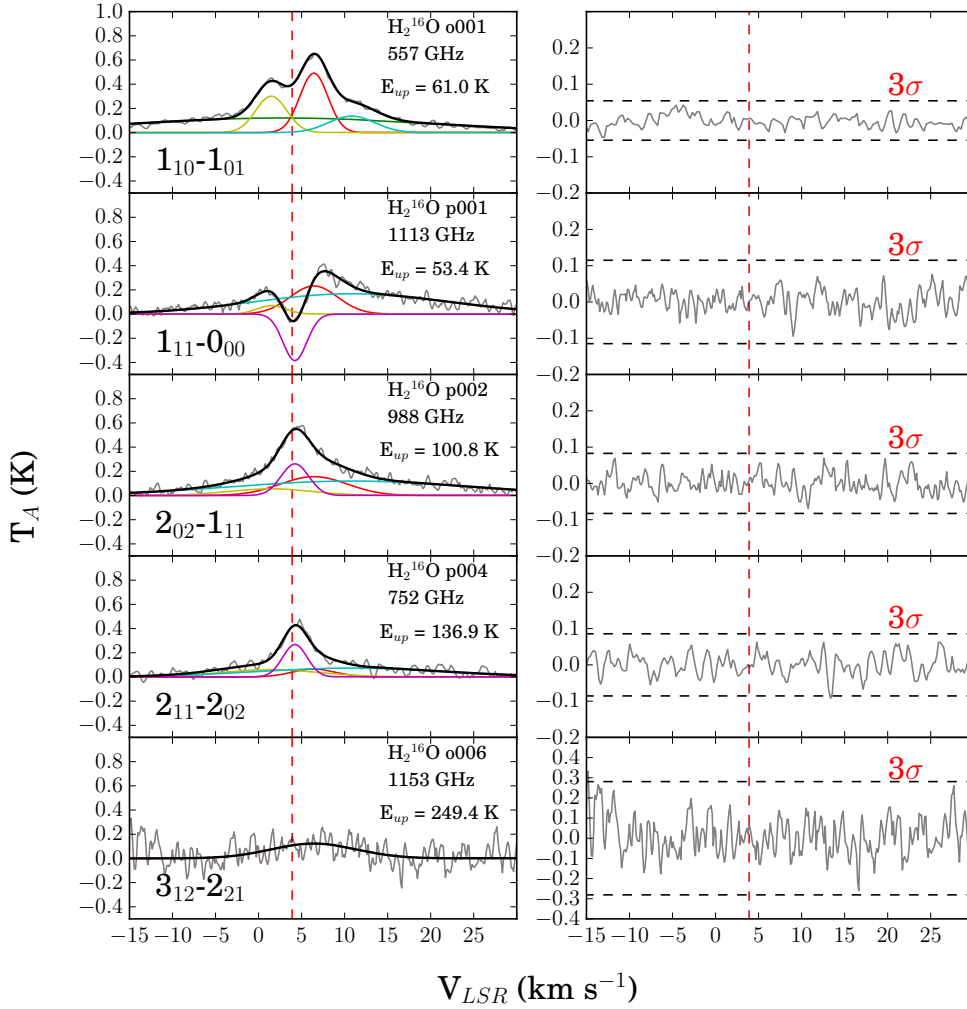
Figure A.9: Vela IRS 17 $H_2^{16}O$ Gaussian Fits contrasted with $H_2^{16}O$ HIFI data. Medium feature located at $+2.8$ km s^{-1} (green), narrow feature at $+6.5$ km s^{-1} (red), second narrow feature at $+1.5$ km s^{-1} (yellow), and third narrow feature at $+1.1$ km s^{-1} (cyan). The total fit is outlined in black. The 3_{12}-2_{21} line only has the one component at $+6.5$ km s^{-1} (red). Gaussians are fit at the same position in each transition, but at varying widths. See Table A.5 for further details. Local $V_{LSR} = +3.9$ km s^{-1}. Gaussian fits are subtracted from the HIFI data, yielding the residuals in the bottom panels. The 3σ boundaries around the residuals (right panels) represent the goodness of fit of the Gaussians. The majority of fits are well encased by these boundaries.

226
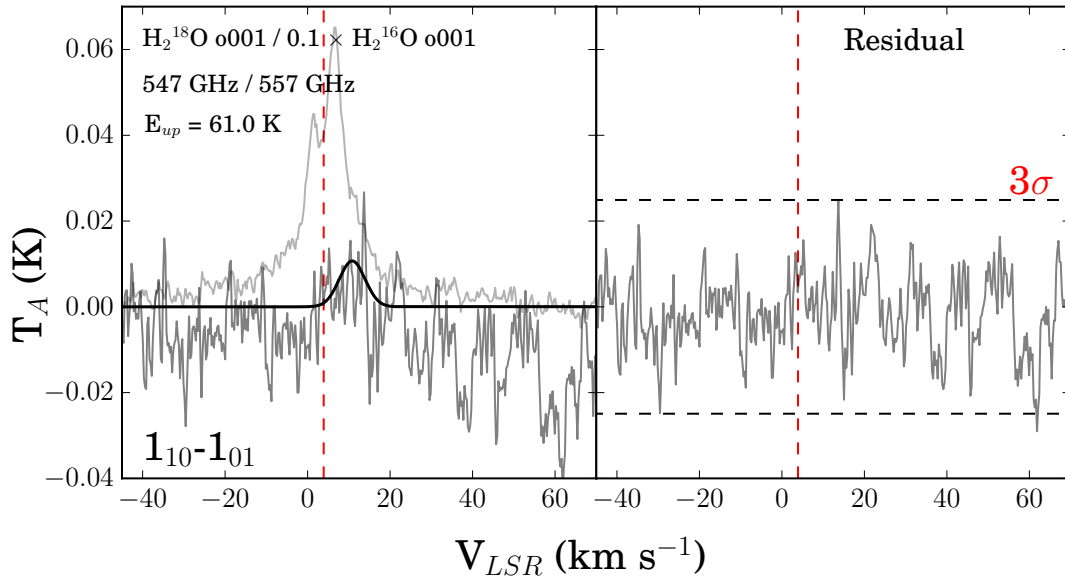
Figure A.10: Vela IRS 17 $H_2^{18}O$ Gaussian fits contrasted with $H_2^{18}O$ and $H_2^{16}O$ HIFI data, scaled to 10%. Narrow feature at $+1.1$ km s^{-1}. The total fit is outlined in black. See Table A.5 for further details. Local $V_{LSR} = +3.9$ km s^{-1}. Gaussian fits are subtracted from the HIFI data, yielding the residuals in the right panel. The 3σ boundaries around the residual represents the goodness of fit of the Gaussian. The fit is well encased by these boundary, but this line looks like it could have some instrumental aberrations or too much noise.

Figure A.11: Vela IRS 17 Gaussian components of various lines as fit by Tisi(2013). Figure extracted from Tisi(2013)

Figure A.12: Vela IRS 19 $H_2^{16}O$ Gaussian fits contrasted with $H_2^{16}O$ HIFI data (o006 scaled to 50%). This dataset was more difficult to fit. A total of 4 Gaussians were applied to the entire dataset, but only 2-3 Gaussians per line are fit. G1 is a broad feature located at +29.6 km s^{-1} (red), G2 is a second medium - very broad feature located at +18.4 km s^{-1} (Green), G3 is a narrow - medium feature located at +11.9 km s^{-1} (yellow), and G4 is a narrow feature located at +21.2 km s^{-1} (cyan). The total fit is outlined in black. Gaussians are fit at the same position in each transition the feature occurs in, but at varying widths. See Table A.6 for further details. Local $V_{LSR} = +12.2$ km s^{-1}. Gaussian fits are subtracted from the HIFI data, yielding the residuals in the bottom panels. The 3σ boundaries around the residuals represent the goodness of fit of the Gaussians. The fits are well encased by these boundaries.
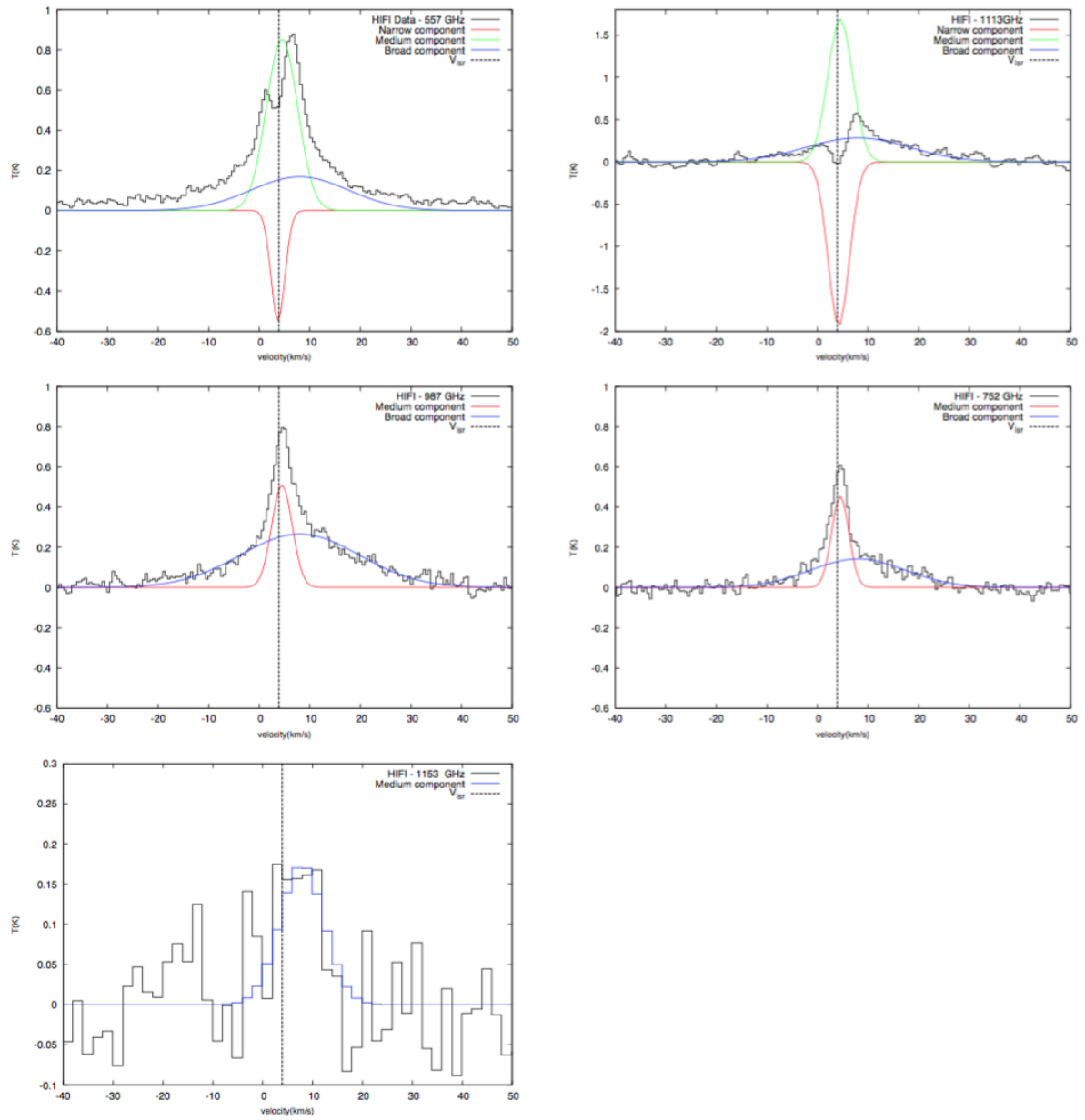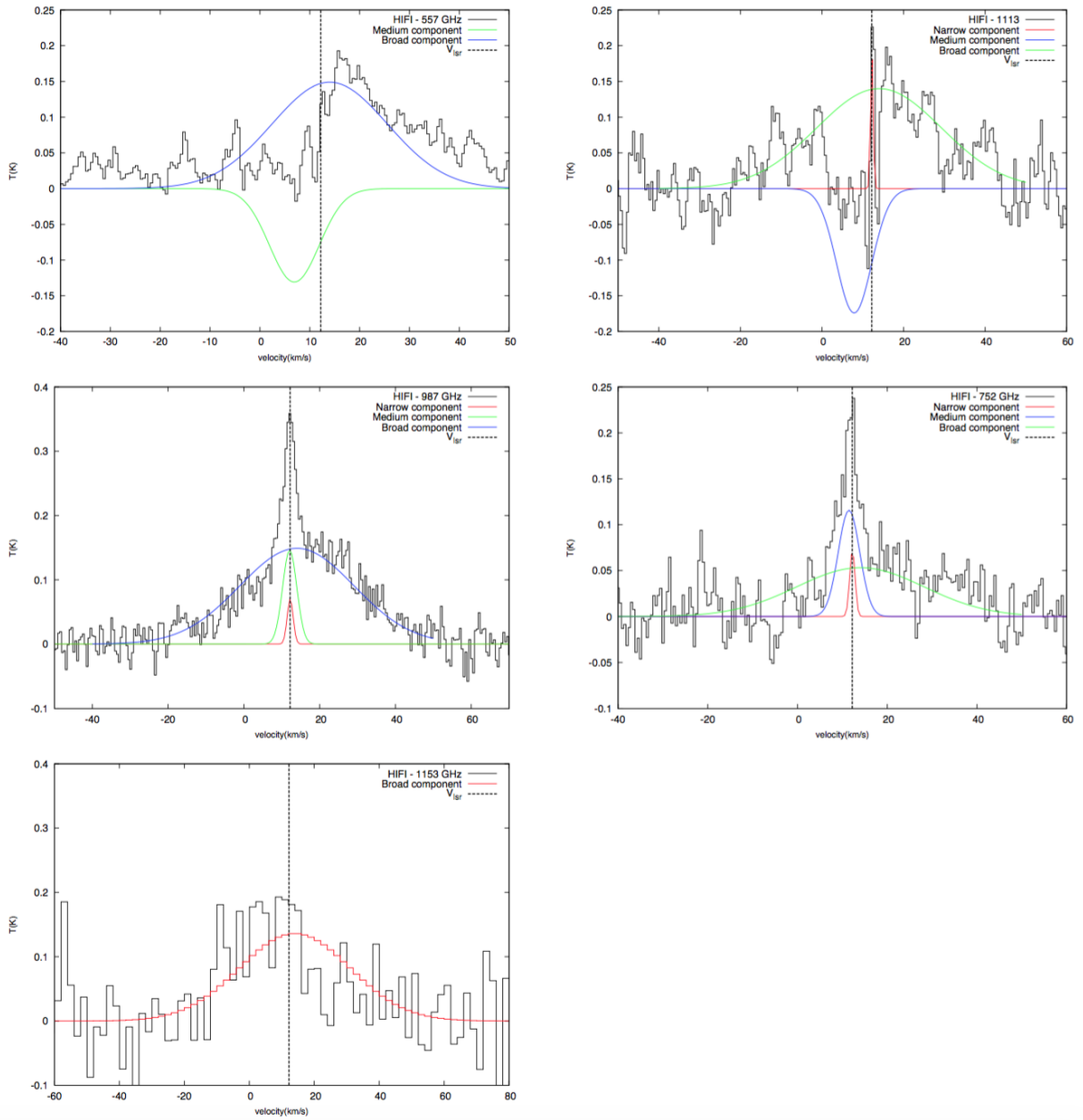
Figure A.13: Vela IRS 19 Gaussian components of various lines as fit by Tisi (2013). Figure extracted from Tisi (2013)
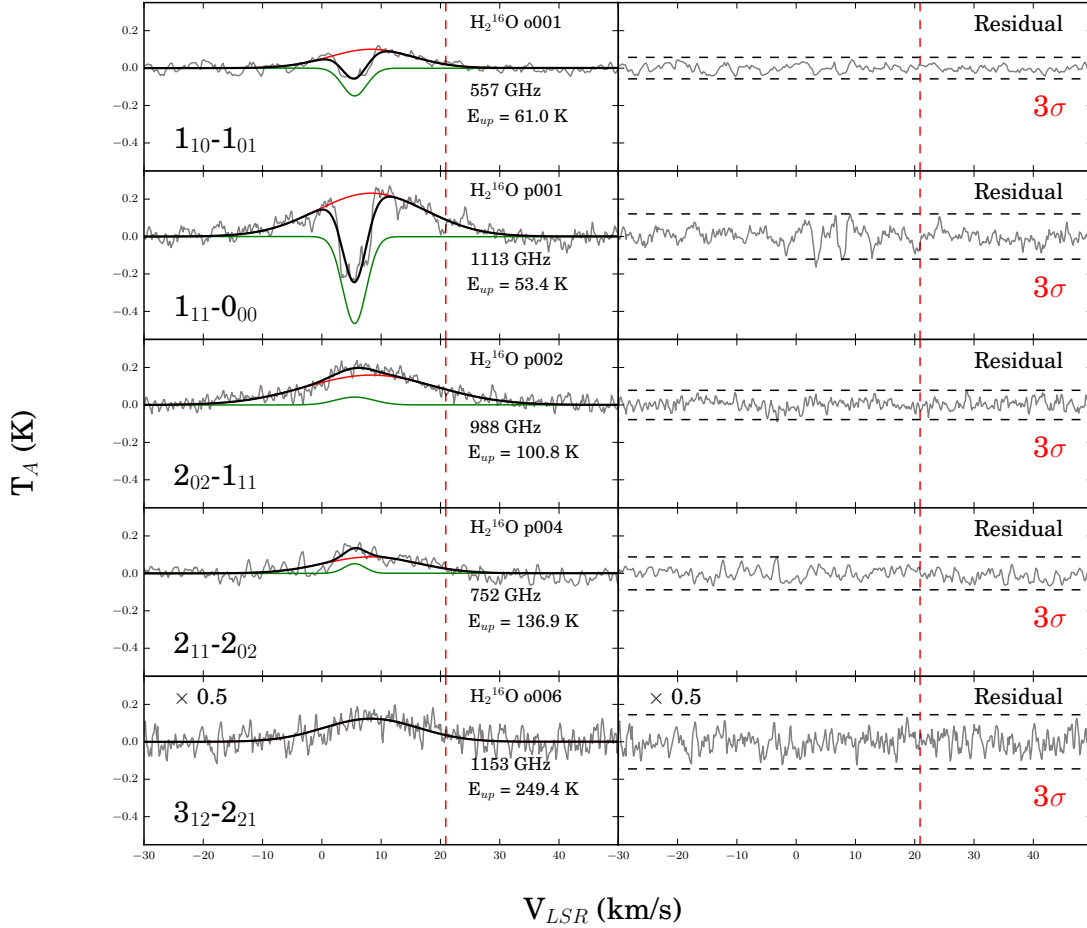
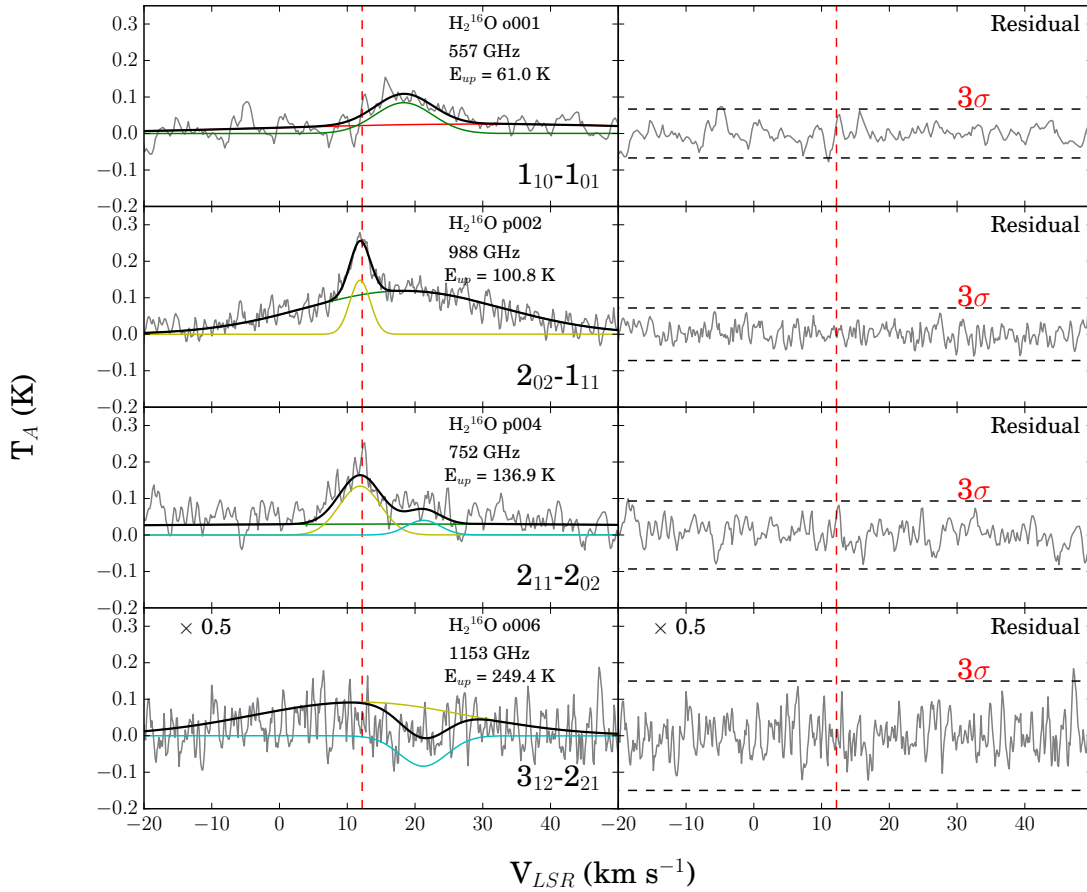Figure A.14: L1641 S3MMS1 $H_2^{16}O$ Gaussian fits contrasted with $H_2^{16}O$ HIFI data (o006 scaled to 50%). A total of 2 Gaussians were applied to the entire dataset: G1 is a medium feature located at $+8.3$ km s^{-1} (red) and G2 is a narrow feature located at $+5.5$ km s^{-1} (Green). The total fit is outlined in black. Gaussians are fit at the same position in each transition the feature occurs in, but at varying widths. See Table A.7 for further details. Local $V_{LSR} = +5.3$ km s^{-1}. Gaussian fits are subtracted from the HIFI data, yielding the residuals in the bottom panels. The 3σ boundaries around the residuals represent the goodness of fit of the Gaussians. The fits are well encased by these boundaries.
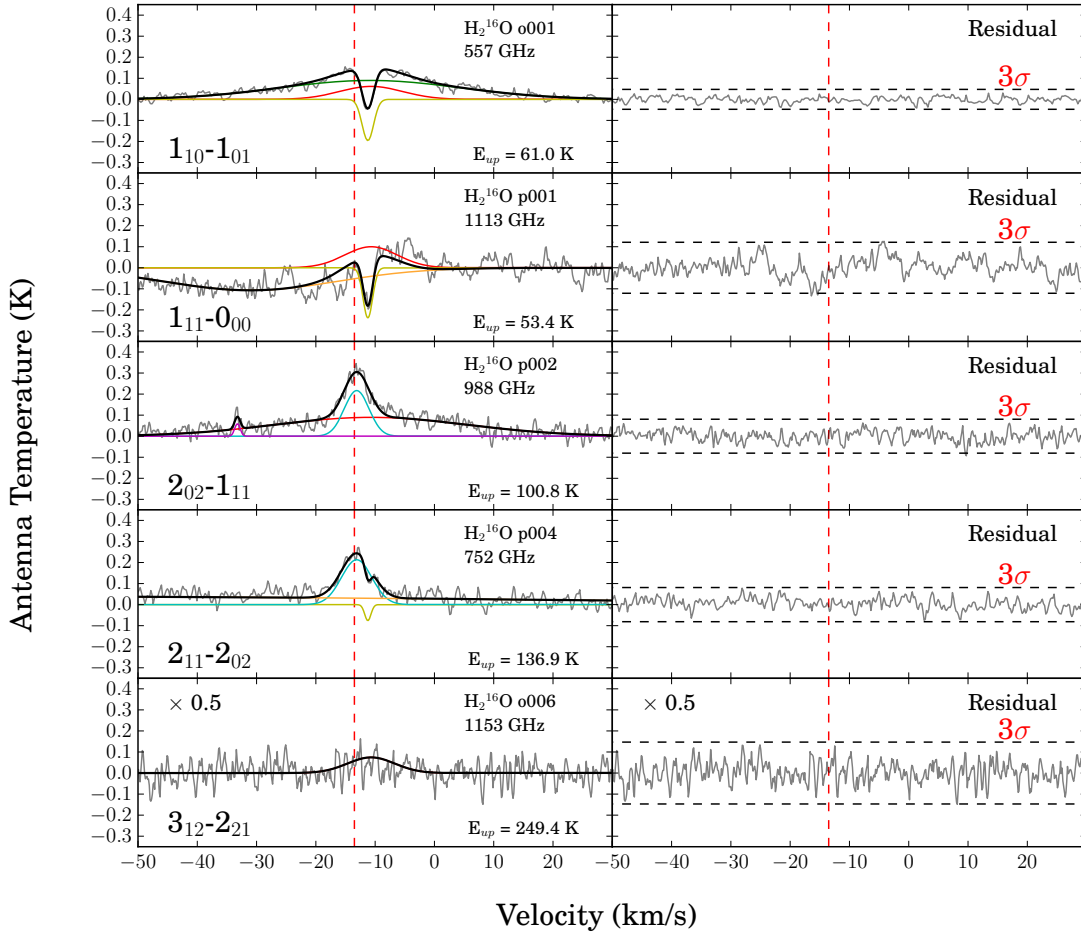
Figure A.15: AFGL 490 $H_2^{16}O$ Gaussian fits contrasted with $H_2^{16}O$ HIFI data (o006 scaled to 50%). A total of 6 Gaussians were applied to the entire dataset: G1 is a medium feature located at -10.7 km s^{-1} (red), G2 is a medium feature located at -10.8 km s^{-1} (green), G3 is a narrow feature located at -11.2 km s^{-1} (yellow), G4 is a narrow feature located at -13.1 km s^{-1} (cyan), G5 is a narrow feature located at -33.2 km s^{-1} (magenta, likely not associated with the source, but interesting to fit nonetheless), and G6 is a very broad feature located at -31.0 km s^{-1} (orange). The total fit is outlined in black. Gaussians are fit at the same position in each transition the feature occurs in, but at varying widths. See Table A.8 for further details. Local V_{LSR} = -13.5 km s^{-1}. Gaussian fits are subtracted from the HIFI data, yielding the residuals in the bottom panels. The 3σ boundaries around the residuals represent the goodness of fit of the Gaussians. The fits are well encased by these boundaries.

Appendix B

RADEX Input & Output Parameters

The RADEX program takes the following parameters as input:

1. Name of the molecular data file

2. Name of the output file

3. The frequency range for the output. This feature is merely to condense the output to only desired lines as some molecules can generate a lengthly list - the code will still run through all of the spectral lines.

4. The equivalent black body temperature of the background radiation field (usually taken to be the microwave cosmic background field, $T_{CMB} = 2.73$ K)

5. The molecular cloud kinetic temperature

6. The number and types of different colliders

7. The number density of the collider

8. The column density of the molecule: this is the parameter to vary to match the output signal level

9. The width of the molecular lines, assumed the same for all lines (also known as the Full-Width Half Maximum ΔV)

The RADEX program outputs the following:

1. the quantum numbers of the upper and lower states

2. the upper state energy (K)

3. the line frequency (GHz)

4. the excitation temperature (K) of that line. Lines are thermalized if Tex = Tkin; all lines are thermalized in the LTE case.

5. the optical depth at line center

6. T_R (K), the Rayleigh - Jeans equivalent of the intensity of the line minus the background intensity; this is also known as the antennae temperature, T_A

7. the line flux in both (K km/s)[Radio Astronomy] and (erg/cm^2·s) [Infrared Astronomy]

Appendix C

RATRAN Input & Output Parameters

This appendix outlines the input and output parameters of the radiative transfer code RATRAN. Table C.1 lists the RATRAN model file column identifiers, Table C.2 lists the input specific to AMC, and Table C.3 lists the input specific to SKY.

Table C.1: RATRAN Input Model: column identifiers

Column ID	Description
id	Shell Number
ra, rb	Inner and Outer Shell Radius (m)
za, zb	Lower and Upper Height (m) [2D ONLY]
nh	Density of Main Collision Partner (cm^{-3}) [p-H_2]
ne	Density of 2nd Collision Partner (cm^{-3}) [o-H_2]
nm	Density of Molecule (cm^{-3})
tk	Temperature of Main Collision Partner (K)
td	Dust Temperature (K)
te	Temperature of 2nd Collision Partner(K)
db	Half-Width of Line Profile (Doppler b-Parameter) (km/s)
vr	Radial Velocity (km/s)
vz	Vertical Velocity (km/s) [2D ONLY]
vr	Azimuthal Velocity (km/s) [2D ONLY]

Some important things to note:

- rb must equal r(max) for the outermost cloud shell

- ra of the innermost shell must be zero

- b = 0.6 × FWHM

Table C.2: Input to AMC (AMC.inp). (*) indicates mandatory keywords.

Input	Description
*Source_File.mdl	File Containing Input Model
*Source_File.pop	Output File
*molecule.dat	Molecular Data File
*snr	Requested Minimum Signal-to-Noise Ratio
*nphot	Minimum Number of Photons per Cell
kappa	Opacity Model
tnorm	Blackbody Temperature [K] of Intensity Normalization
velo	Velocity Model
seed	Random Number Seed
minpop	Minimum Population to Include in S/N Calculation
fixset	Convergence Requirement for First Stage
trace=on	Write History Files to Monitor Convergence
*go	Start Calculation
*c	Make New Executable for Next Calculation
Source_File2.mdl	Next Input Model File
Source_File2.out	Next Output Model File
kappa	Change Opacity Model
*go	Start Calculation
*k	Continue with Same Executable
Source_File3.mdl	Next Input Model File
Source_File3.pop	Next Output Model File
*go	Start Calculation
*q	Quit

Details regarding the above table:

- snr: Usually a signal-to-noise ratio of 10-20 is sufficient

- nphot: an nphot of 1000 is usually appropriate for an snr of 10-20. Higher values of nphot usually require higher values of snr; lower values of nphot are usually safer.

- velo: Either the file name of a user-provided velocity model or 'grid'. If 'grid' is selected, the velocity vectors are read from the 'source' input model, as seen above in Table 1.1.

- kappa: Either the file name of a user-provided description of the dust emissivity as function of frequency and position or a standard defined model. Default (no kappa defined) is no dust emission/absorption.

- tnorm: Blackbody temperature of the normalization used internally for the radiation field. tnorm is taken as t_{cmb} or 2.735 K if no value is provided. A value usually isn't required unless at wavelengths shorter than approximately 15 microns; at this wavelength, a high tnorm is required (i.e tnorm = 4000 K) such that the normalization remains finite.

- fixset: The relative accuracy of the populations after the first stage (with rays fixed). The default value 1e-6 is usually OK; only very opaque problems may need lower values.

Table C.3: SKY Input File (SKY.inp). (*) indicates mandatory keywords.

Identifier	Description
Source_File.pop	Input Model; Output from AMC
format = fits	Output Format
Source_File_SKY	Base-name for output (will have .fits extension)
trans	Transition Numbers
pix	Number of Pixels
chan	Number of Channels and Width [km/s]
distance	Distance to Source [pc]
incl	Inclination [degrees] (2D = 90, i.e. edge on)
fg	File with Table Describing Foreground
central	Central Source Radius [arcsec] and Blackbody Temperature [K]
units = K	Output Units
tnorm	Blackbody Temperature of Normalization Scheme
*go	Start Calculation
*c	Continue with New Executable
*go	Start Calculation
*k	Continue with Same Executable
*go	Start Calculation
*q	Quit

Appendix D

Constants

The following table outlines the constant values used in Chapter 3.

Table D.1: Constants used while verifying RADEX results - Ground State Water 557 GHz

Constant	Symbol	Value
Background Temperature	T_{bg}	2.728 K
Ground Level Statistical Weight	g_1	9.0
2nd Level Statistical Weight	g_2	9.0
3rd Level Statistical Weight	g_3	15.0
Ground Level Energy	E_1	23.794356 cm^{-1}
2nd Level Energy	E_2	42.371741 cm^{-1}
3rd Level Energy	E_3	79.496382 cm^{-1}
Einstein Spontaneous Emission Coefficient $(2 \rightarrow 1)$	A_{21}	3.458E-03 Hz
Einstein Spontaneous Emission Coefficient $(3 \rightarrow 1)$	A_{31}	5.593E-02 Hz
Para-Water Collision Rate $(1 \rightarrow 2)$	C_{12}	3.33e-11 cm^3 s^{-1}
Para-Water Collision Rate $(1 \rightarrow 3)$	C_{13}	3.41E-11 cm^3 s^{-1}
Para-Water Collision Rate $(2 \rightarrow 3)$	C_{23}	1.62E-11cm^3 s^{-1}
Ortho-Water Collision Rate $(1 \rightarrow 2)$	C_{12}	2.97E-10 cm^3 s^{-1}
Ortho-Water Collision Rate $(1 \rightarrow 3)$	C_{13}	1.19E-10 cm^3 s^{-1}
Ortho-Water Collision Rate $(2 \rightarrow 3)$	C_{23}	1.17E-10 cm^3 s^{-1}
Planck Constant	h	6.62607E-27 erg/Hz
Boltzmann Constant	k_B	1.38065E-16 ergs K^{-1}
Speed of Light	c	2.998E10 cm/s
Frequency	ν	556.93607 GHz
Mass of Water Molecule	M_{H218O}	18.01528 amu
Mass of Water Isotope	M_{H2O}	20.01504 amu

Appendix E

NGC 7129 FIRS 2 RATRAN Model

This section presents the NGC 7129 FIRS 2 RATRAN model radius, free-fall velocity, angular diameter, and beam dilution for $H_2^{18}O$ 557 and 995 GHz lines. The angular diameter is calculated with $\theta_{src} = d_{cloud}/D_{cloud}$ where d = diameter and D = distance to NGC 7129 FIRS 2. The beam dilution is calculated with $(\theta_{src}/\theta_{beam})^2$ where θ_{beam} is considered as the Roelfsema et al. (2012) calculated beamsizes. The RATRAN model has inner radius of 95 AU (1.421×10^{13} m) and outer radius of 18000 AU (2.69×10^{15} m). The free-fall velocity ranges from -4.6 km s^{-1} at the inner radius to -0.34 km s^{-1} at the outer radius. The beam dilution is the strongest in the inner envelope, and weakens in the outer envelope. The beam dilution is also weaker for the 557 GHz line (ground-state ortho). Table E.1 lists these parameters listed per RATRAN shell.

Table E.1: RATRAN: NGC 7129 FIRS 2 RATRAN Model - Radius, Free-Fall Velocity, Angular Diameter, and Beam Dilution ($H_2^{18}O$ o001 & p002). Bold font indicates the freeze-out radius.

Shell	Radius (10^{13} m)	Velocity	θ_{src} (rad)	$\theta_{src}('')$	$(\theta_{src}/\theta_{beam})^2$ $H_2^{18}O$ (o001)	$(\theta_{src}/\theta_{beam})^2$ $H_2^{18}O$ (p002)
1	1.421	-4.6	7.36×10^{-7}	0.152	1.54×10^{-5}	5.08×10^{-5}
2	1.496	-4.533	7.75×10^{-7}	0.160	1.71×10^{-5}	5.63×10^{-5}
3	1.525	-4.418	8.07×10^{-7}	0.166	1.84×10^{-5}	6.06×10^{-5}
4	1.555	-4.374	8.53×10^{-7}	0.176	2.07×10^{-5}	6.82×10^{-5}
5	1.646	-4.332	9.95×10^{-7}	0.205	2.80×10^{-5}	9.25×10^{-5}
6	1.919	-4.212	1.40×10^{-6}	0.289	5.57×10^{-5}	1.84×10^{-4}
7	2.708	-3.900	1.98×10^{-6}	0.408	1.11×10^{-4}	3.66×10^{-3}
8	3.822	-3.284	2.80×10^{-6}	0.578	2.23×10^{-4}	7.35×10^{-4}
9	5.400	-2.764	3.96×10^{-6}	0.817	4.45×10^{-4}	1.47×10^{-3}
10	**7.631**	**-2.325**	$\mathbf{5.59\times10^{-6}}$	**1.153**	$\mathbf{8.87\times10^{-4}}$	$\mathbf{2.93\times10^{-3}}$
11	10.786	-1.956	7.90×10^{-6}	1.629	1.77×10^{-3}	5.84×10^{-3}
12	15.244	-1.645	1.12×10^{-5}	2.31	3.56×10^{-3}	1.17×10^{-2}
13	21.557	-1.384	1.58×10^{-5}	3.25	7.05×10^{-3}	3.23×10^{-2}
14	30.474	-1.164	2.23×10^{-5}	4.60	1.41×10^{-2}	4.60×10^{-2}
15	43.099	-0.979	3.16×10^{-5}	6.52	2.84×10^{-2}	9.35×10^{-2}
16	60.947	-0.823	4.47×10^{-5}	9.22	5.67×10^{-2}	1.87×10^{-1}
17	86.185	-0.692	6.32×10^{-5}	13.04	1.13×10^{-1}	3.74×10^{-1}
18	121.864	-0.582	8.94×10^{-5}	18.44	2.27×10^{-1}	7.48×10^{-1}
19	172.354	-0.489	1.12×10^{-4}	23.10	3.56×10^{-1}	1.17
20	243.713	-0.412	1.26×10^{-4}	25.99	4.51×10^{-1}	1.49
21	256.130	-0.346	1.33×10^{-4}	27.43	5.02×10^{-1}	1.66
22	269.295	-0.338	1.40×10^{-5}	28.88	5.56×10^{-1}	1.84